



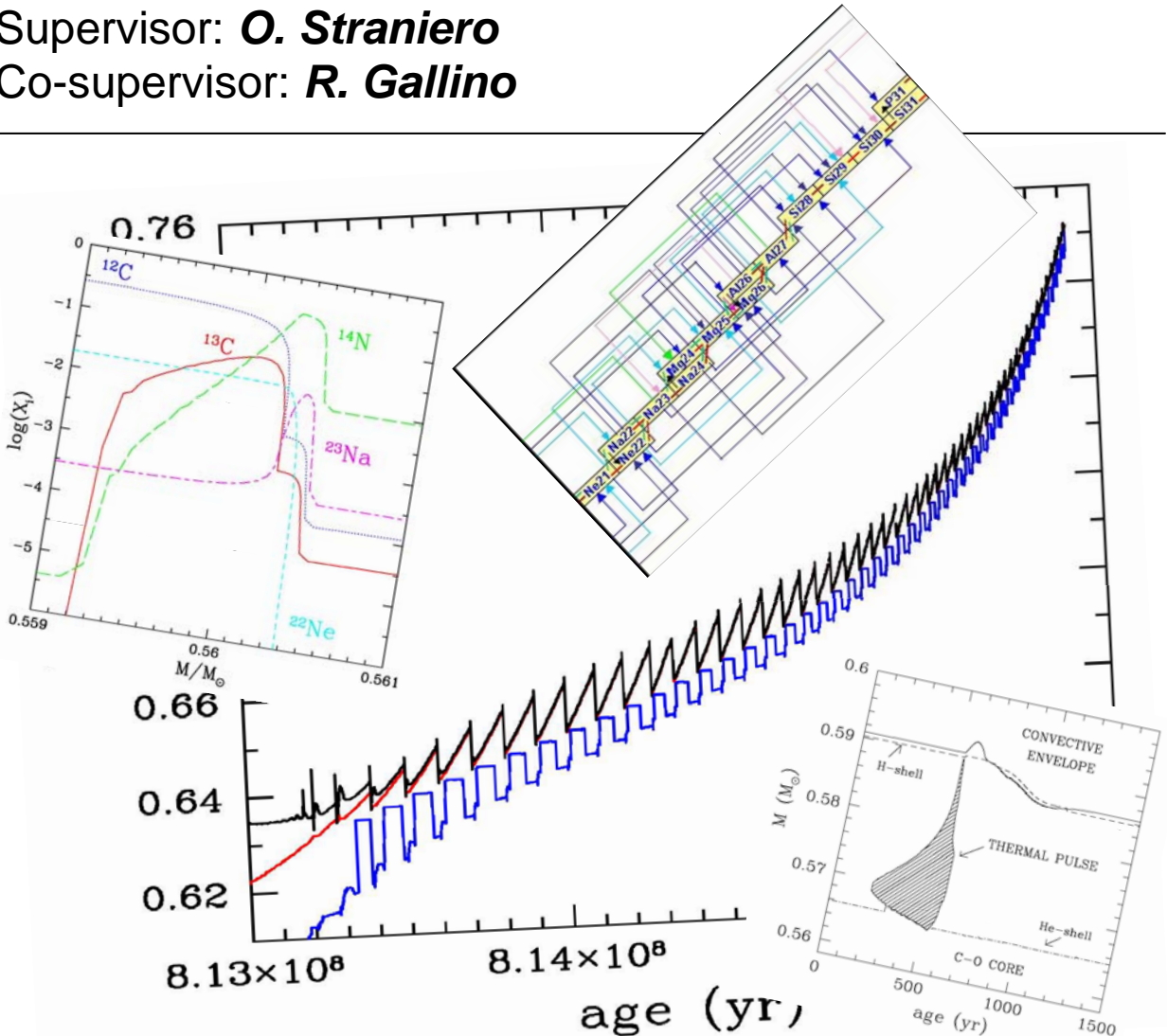
Sergio Cristallo

*PhD Thesis*

# S-process nucleosynthesis in low mass AGB Stars at different metallicities

Supervisor: **O. Straniero**

Co-supervisor: **R. Gallino**





# Contents

<b>1</b>	<b>What: the s-process</b> . . . . .	<b>1</b>
<b>2</b>	<b>Why: the failure of the classical model</b> . . . . .	<b>5</b>
2.1	A bit of history... . . . . .	7
<b>3</b>	<b>Where: the FRANEC code</b> . . . . .	<b>13</b>
3.1	Stellar equilibrium equations . . . . .	13
3.1.1	Numerical integration methods. . . . .	16
3.2	Convective zones . . . . .	17
3.2.1	The mixing length theory . . . . .	18
3.3	Input physics and initial abundances . . . . .	20
3.4	Opacities . . . . .	21
<b>4</b>	<b>When: AGB stars</b> . . . . .	<b>23</b>
4.1	Introduction . . . . .	23
4.2	Approaching the Thermally Pulsing AGB . . . . .	26
4.3	Thermally pulsing AGB . . . . .	29
4.4	The third dredge up . . . . .	31
4.5	Mass loss . . . . .	32
<b>5</b>	<b>The nuclear network</b> . . . . .	<b>37</b>
5.1	Charged particle capture reactions . . . . .	38
5.1.1	Neutron sources . . . . .	39
5.2	Neutron capture reactions . . . . .	39
5.3	$\beta$ decay reactions . . . . .	40
5.4	Isomeric states . . . . .	42
<b>6</b>	<b>The formation of the <math>^{13}\text{C}</math> pocket</b> . . . . .	<b>47</b>
6.1	The velocity profile algorithm . . . . .	49
6.2	The $^{13}\text{C}$ pocket . . . . .	54
6.3	Tests on the velocity profile algorithm . . . . .	55

<b>7</b>	<b>Thermally pulsing AGB models</b>	<b>59</b>
7.1	The Solar metallicity model	59
7.1.1	Surface enrichments	68
7.1.2	The convective $^{13}\text{C}$ burning	72
7.1.3	Early Solar System (ESS): the short-lived radioactivities problem	73
7.2	Toward lower metallicities	76
7.3	Yields	85
<b>8</b>	<b>The importance of the opacity treatment in AGB models</b>	<b>87</b>
8.1	Opacity effects at low metallicities	91
8.2	Future improvements: the molecular opacities	99
<b>9</b>	<b>Nuclear astrophysics</b>	<b>103</b>
9.1	The $^{13}\text{C}(\alpha, n)^{16}\text{O}$ reaction	104
9.2	$^{19}\text{F}$ nucleosynthesis	106
9.3	$^{23}\text{Na}$ nucleosynthesis	109
<b>10</b>	<b>Concluding remarks</b>	<b>115</b>
10.1	What we did	115
10.2	What we wish to do	116
	<b>Bibliography</b>	<b>119</b>
<b>A</b>	<b>Yields</b>	<b>129</b>
<b>B</b>	<b>Surface enrichments</b>	<b>141</b>
B.1	Solar metallicity case ( $Z=1.5\times 10^{-2}$ )	141
B.2	Intermediate metallicity case ( $Z=1\times 10^{-3}$ )	144
B.3	Low metallicity cases	147
B.3.1	$Z=1\times 10^{-4}$ ( <i>st</i> case)	147
B.3.2	$Z=1\times 10^{-4}$ ( <i>test</i> case)	150
<b>C</b>	<b>My publications</b>	<b>153</b>

# List of Tables

3.1	Adopted initial element abundances. . . . .	20
4.1	Properties of the pre-AGB phase of $M = 2 M_{\odot}$ models with different metallicities (see Table 3.1 for the adopted initial abundances). We refer to Chapter 7 for details about their AGB phase. . . . .	28
5.1	Charged particle reactions section of the FRANEC nuclear network. . . . .	45
6.1	Tests on $\beta$ parameter. Columns 2, 4, 6 and 7 are in $M_{\odot}$ units, while column 3 is in $10^{-3} M_{\odot}$ units. See text for details. . . . .	58
7.1	Data relative to a model with initial mass $M=2M_{\odot}$ ; solar metallicity case: $(C/O)_{ini} = 0.54$ , $(C/O)_{FDU} = 0.35$ , $Z=1.5 \times 10^{-2}$ . . . . .	61
7.2	Measured and predicted isotopic ratios involving short-lived isotopes. (see text for details). . . . .	75
7.3	Data relative to a model with initial mass $M=2M_{\odot}$ ; intermediate metallicity case: $(C/O)_{ini} = 0.54$ , $(C/O)_{FDU} = 0.30$ , $Z=1 \times 10^{-3}$ . . . . .	79
7.4	Data relative to a model with initial mass $M=2M_{\odot}$ ; low metallicity case: $(C/O)_{ini} = 0.54$ , $(C/O)_{FDU} = 0.26$ , $Z=1 \times 10^{-4}$ . . . . .	80
7.5	S-process indexes for the three computed models. . . . .	82
7.6	S-process indexes in a selected sample of low metallicity stars. . . . .	83
8.1	Light elements final surface overabundances for the <i>st</i> case and for the <i>test</i> case. . . . .	99
9.1	Fluorine He-intershell abundances obtained using the adopted rates or modifying some key nuclear reactions rates (see text for details). . . . .	106



# List of Figures

2.1	Nuclide abundances (relative to $N(\text{Si})=10^6$ ) as a function of the mass number. Labels in the picture identify different processes responsible for the formation of solar observed isotopes (picture from [40]). . . . .	6
2.2	Solar $s$ -process $\sigma_A N_A$ distribution. The curve has been obtained with an exponential distribution of neutron expositions (picture from [147]). . . . .	8
2.3	Solar $r$ -process $\sigma_A N_A$ distribution. The lack of a correlation between data is evident, strengthening the fact that the $s$ -process distribution is not accidental (picture from [147]). . . . .	8
2.4	Schematic diagram of the Ulrich model: shaded areas represent convective shells where neutron captures occur (from [165]). . . . .	10
3.1	Schematic diagram of the FRANEC code structure. . . . .	15
4.1	This sketch illustrates the evolution of the positions of the inner border of the convective envelope, the H-burning shell and the He-burning shell, during the thermally pulsing AGB phase. The convective regions generated by two subsequent TPs are also shown. . . . .	24
4.2	Theoretical evolutionary track in the Hertzsprung-Russell diagram of a star of initial mass $M = 2 M_\odot$ and solar metallicity (see section 7.1 for details). . . . .	25
4.3	Surface abundances variations after the occurrence of FDU episode in the $M = 2 M_\odot$ model with solar metallicity. Note that the He abundance has been divided by a factor 100 in order to match the box. . . . .	26
4.4	$3\alpha$ luminosity evolution during the off center He-flash in the $M = 2 M_\odot$ model with solar metallicity. . . . .	27
4.5	Convective episode (dashed area) in the $M = 2 M_\odot$ model with solar metallicity, during and after the 6 <sup>th</sup> TP followed by TDU. Note how the convective zone generated by the TP covers the whole He intershell. After about 200 years, the external convection penetrates inward (TDU). . . . .	30
4.6	Thermally pulsing AGB evolution of the $M = 2 M_\odot$ model with solar metallicity. Panel a): energy production rate of the H burning shell; Panel b): energy production rate of the He burning shell. . . . .	31

4.7	Mass loss rates versus period measurements (symbols) compared with the prescription proposed by [167] (line). . . . .	33
4.8	Variation versus time of the envelope mass according to different mass loss prescriptions (see text), for an AGB model of initial mass $M = 2 M_{\odot}$ with solar metallicity. . . . .	35
5.1	Nuclear network section in the Na-Mg-Al region. . . . .	38
5.2	Nuclear network sections around magic number nuclei. . . . .	41
5.3	Nuclear processes active in the region of krypton isotopes (in yellow stable isotopes, in blue the unstable ones). . . . .	43
5.4	Nuclear processes active in the region of lutetium isotopes (in yellow stable isotopes, in blue the unstable ones). . . . .	43
6.1	Radiative and adiabatic gradients at the inner border of the convective envelope during a TDU episode (Left Upper Panel: without velocity profile algorithm; Right Upper Panel: with velocity profile algorithm) and at the bottom of a convective He-shell during a TP (Lower Panel). . . . .	49
6.2	Chemical profile (upper Panel), temperature gradients (middle Panel), average velocity and pressure (lower Panel), in the region at the convective boundary during a TDU episode. . . . .	50
6.3	Variation of the relevant chemical species in the region where the $^{13}\text{C}$ pocket forms after the occurrence of the $2^{\text{nd}}$ TDU ( $M = 2M_{\odot}$ model with solar metallicity). Each Panel refers to different time steps, namely: $\Delta t = 0$ (a), $\Delta t = 3700$ (b), 14100 (c) and 39200 (d) years. . . . .	53
6.4	Abundances profiles in the $^{13}\text{C}$ pocket formed after the $2^{\text{nd}}$ TDU episode ( $M = 2M_{\odot}$ model with solar metallicity). . . . .	54
6.5	Chemical profiles at the maximum penetration of the convective envelope (left Panels) and after the formation of the $^{13}\text{C}$ pocket (right Panels) after the $2^{\text{nd}}$ TP with TDU in a $M = 2M_{\odot}$ model with $Z=1\times 10^{-4}$ . In each plot we report the H (long-dashed line), $^{12}\text{C}$ (dotted line), $^{13}\text{C}$ (solid line) and $^{14}\text{N}$ (short-dashed line) profiles. Cases with no velocity profile ( $\beta=0$ ), $\beta=0.01$ and $\beta=0.05$ are reported. . . . .	55
6.6	As in Fig. 6.5, but referring to $\beta=0.075$ , $\beta=0.09$ and $\beta=0.1$ cases. . . . .	56
6.7	As in Fig. 6.5, but referring to $\beta=0.125$ , $\beta=0.15$ and $\beta=0.2$ cases. . . . .	56
7.1	The evolution throughout the TP-AGB phase of a star with initial mass $M = 2 M_{\odot}$ and solar metallicity. . . . .	60

7.2	Evolution of the maximum temperature at the base of the convective zones generated by TPs (Panel a) and the dredged up mass per pulse (Panel b) during the AGB phase ( $M = 2M_{\odot}$ model with solar metallicity). . . . .	62
7.3	Mass loss history and derived period during the AGB phase ( $M = 2M_{\odot}$ model with solar metallicity). . . . .	63
7.4	Bolometric magnitude (upper Panel) and C/O ratio (lower Panel) along the AGB phase ( $M = 2M_{\odot}$ model with solar metallicity). . . . .	64
7.5	The <i>effective</i> (see text) mass fraction of $^{13}\text{C}$ within all the pockets ( $M = 2M_{\odot}$ model with solar metallicity). . . . .	65
7.6	Physical quantities profiles and chemical distributions (see the legend) at the moment of the maximum penetration of the convective envelope during the first TDU episode in the $M = 2M_{\odot}$ model with solar metallicity. Pressure is given in $\text{dyne}\cdot\text{cm}^{-2}$ and $H_P$ in cm. We also evidence the two regions where the $^{13}\text{C}$ pocket (horizontal dashed area) and the $^{23}\text{Na}$ pocket (vertical dashed area) form. . . . .	66
7.7	As in Fig. 7.6, but referring to the 11 <sup>th</sup> (last) $^{13}\text{C}$ pocket ( $M = 2M_{\odot}$ model with solar metallicity). . . . .	67
7.8	Pulse by pulse He intershell production factors for s-only and neutron magic nuclei with respect to the initial (solar) composition. Series refer to He intershell distributions before the first, third, sixth and eleventh (last) TP with TDU. . . . .	68
7.9	Pulse by pulse surface composition, in the usual spectroscopic notation, for the $M = 2M_{\odot}$ model with solar metallicity. . . . .	69
7.10	Observed [hs/l <sub>s</sub> ] ratio of a sample of galactic C(N) Giants [4] (blue circles), compared with our theoretical prediction (red triangle). . . . .	70
7.11	Final surface composition of the $M = 2M_{\odot}$ model with solar metallicity, compared with post-process calculations (Gallino R., <i>priv. comm.</i> ). . . . .	71
7.12	Peak neutron density evolution after the ingestion of the $^{13}\text{C}$ -pocket formed after the first TDU episode ( $M = 2M_{\odot}$ with solar metallicity). . . . .	73
7.13	TP-AGB surface evolution of $^{26}\text{Al}$ , $^{41}\text{Ca}$ , $^{60}\text{Fe}$ and $^{107}\text{Pd}$ ( $M = 2M_{\odot}$ with solar metallicity). . . . .	74
7.14	The evolution throughout the TP-AGB phase of a star with initial mass $M = 2 M_{\odot}$ and $Z=1\times 10^{-3}$ . . . . .	76
7.15	The evolution throughout the TP-AGB phase of a star with initial mass $M = 2 M_{\odot}$ and $Z=1\times 10^{-4}$ . . . . .	77
7.16	Pulse by pulse surface composition, in the usual spectroscopic notation, for the $M = 2M_{\odot}$ model with $Z = 1\times 10^{-3}$ . . . . .	81

7.17	Pulse by pulse surface composition, in the usual spectroscopic notation, for the $M = 2M_{\odot}$ model with $Z = 1 \times 10^{-4}$ . . . . .	81
7.18	Comparison between the final surface composition of the $M = 2M_{\odot}$ model with $Z=1 \times 10^{-4}$ and spectroscopic data of HD196944 [9]. . . . .	82
8.1	Logarithmic relative differences in atomic opacity coefficients obtained by comparing solar scaled and C-enhanced opacity tables in the temperature range $4.05 < \log T < 8.7$ . The comparison has been carried out on the envelope structure of the $M = 2M_{\odot}$ model with initial $Z=1 \times 10^{-4}$ , after the 3 <sup>rd</sup> (upper Panel) and the 8 <sup>th</sup> (lower Panel) TDU episodes (see text for details). . . . .	88
8.2	Logarithmic relative differences in atomic opacity coefficients obtained by comparing solar scaled and C-enhanced opacity tables of different metallicities. This test has been carried out on the envelope structure of the $M = 2M_{\odot}$ model with initial $Z=1 \times 10^{-4}$ , after the 3 <sup>rd</sup> with TDU (see text for details). . . . .	89
8.3	As in Fig. 8.2, but relative to the 8 <sup>th</sup> with TDU. . . . .	90
8.4	The evolution throughout the TP-AGB phase of a star with initial mass $M = 2 M_{\odot}$ and $Z=1 \times 10^{-4}$ . With respect to Fig. 7.15 the calculation has been performed without interpolating in metallicity the opacity coefficients. . . . .	92
8.5	Evolution of some key physical quantities in the $M = 2M_{\odot}$ model with initial metallicity $Z=1 \times 10^{-4}$ , computed with interpolation (blue dotted line, <i>st</i> case) and without interpolation (red solid line, <i>test</i> case) of the opacity coefficients. We report the total mass (upper left Panel), the surface luminosity (upper right Panel), the surface temperature (lower left Panel) and the radius (lower right Panel). . . . .	93
8.6	Mass loss history and derived period for the <i>st</i> case (blue dotted line) and the <i>test</i> case (red solid line). . . . .	94
8.7	Evolution of the maximum temperature at the base of the convective zones generated by TPs (upper Panel) and of the dredged up mass per pulse (lower Panel) during the AGB phase relative to the <i>st</i> model (blue dotted lines & triangles) and the <i>test</i> model (red solid lines & squares). . . . .	95
8.8	Final surface composition, in the usual spectroscopic notation, relative to the <i>st</i> case (blue dotted line) and to the <i>test</i> case (red solid line). . . . .	96
8.9	Chemical evolution of [ls/Fe], [hs/Fe] and [Pb/Fe ] relative to the <i>st</i> case (dotted lines) and to the <i>test</i> case (solid lines). See text for details. . . . .	97
8.10	Mass-loss rates versus period measurements (symbols) compared with our prescriptions (coloured lines). . . . .	98

8.11	Mass absorption coefficients as a function of temperature and for different C/O ratios (from [114]). . . . .	100
9.1	Different $^{13}\text{C}(\alpha, n)^{16}\text{O}$ rates as a function of temperature. The red line refers to [8], the yellow one to [51], the green one to [33] and the magenta one to [106]. . . . .	105
9.2	Fluorine abundances versus carbon abundances, both normalized by the oxygen abundance (from [95]). . . . .	107
9.3	Schematic TP-AGB structure; mechanisms responsible for the $^{23}\text{Na}$ production are evidenced. . . . .	110
9.4	Comparison between different rates of the $^{22}\text{Ne}(p, \gamma)^{23}\text{Na}$ reaction as a function of the temperature. . . . .	111
9.5	Comparison between different rates of the $^{23}\text{Na}(p, \gamma)^{24}\text{Mg}$ reaction as a function of the temperature. . . . .	112
9.6	He-intershell abundances after the $3^{rd}$ pulse with TDU obtained with the standard rates and rates provided by [77] and [78]. Data refer to the $M = 2M_{\odot}$ model with solar metallicity (left Panels) and to the $M = 2M_{\odot}$ model with $Z = 1 \times 10^{-4}$ (right Panels). . . . .	113

# The 4W rule

In my memory is still keen a childhood book reminder, in which all scientific discoveries were described by answering to four basilar questions:

- What?
- Why?
- Where?
- When?

Considering the fact I was just a child when I read these books and being the remembrance still strong, I can argue that this scheme is very efficient, so I'll use it in presenting how I spent my last three years, i.e. presenting you my PhD work.

# Chapter 1

## What: the s-process

*People usually smile when Astrophysicists assert that we are the sons of the stars, but the human life is the confirmation to this sentence: we breathe nitrogen, our bones mainly consist of carbon and calcium, fluorine is present in our teeth, our blood carries oxygen to tissues by means of the hemoglobin (an iron pigment of red blood cells).*

We just list some examples related to human body, but also common element such as aluminum, nickel, gold, silver and lead come from a previous generation of stars. Summing up, all elements have been synthesized in a star, with the exception of elements present in the Universe after the big-bang nucleosynthesis (H, He, Li). The abundances in the Solar System are due to the mixing of material ejected from stars that polluted the Universe in different epochs before the Sun formation, occurred about 5 billion years ago, after the gravitational contraction of the proto-solar cloud. Some elements formed during quiescent hydrostatic evolutionary phases; other elements have been produced during late evolutionary stages of massive stars; finally, some isotopes were synthesized during a particular phase called Asymptotic Giant Branch (AGB). Isotopes heavier than iron ( $A \geq 56$ ) are created by means of neutron capture processes. The observed heavy elements distribution shows the presence of two main components, correlated to different nucleosynthetic processes: the s (slow) process and the r (rapid) process. The r process requires high neutron densities, and it is believed to occur during explosives phases of stellar evolution (Novae, SuperNovae and/or X-rays binaries). The s process is characterized by a slow neutron capture with respect to the corresponding  $\beta$  decay: stable isotopes capture neutrons, while the radioactive ones decay ( $\beta^-$  or  $\beta^+$ ) or capture a free electron. These isotopes are mainly created in the Thermally Pulsing Asymptotic Giant Branch (TP-AGB) phase of low mass stars

( $1.5 \leq M / M_{\odot} \leq 3$ ), where freshly synthesized elements are carried out to the surface by means of a recurrent mechanism called Third Dredge Up (TDU). In this phase the stellar structure consists of a partially degenerate carbon-oxygen core, an He shell separated from an H shell by the He-intershell region and by a convective envelope. The energy required to supply the surface irradiation is mainly provided by the H burning shell, located just below the inner border of the convective envelope. This situation is recurrently interrupted by the growing up of thermonuclear runaways, driven by violent He-burning ignitions. As a consequence of a Thermal Pulse (TP), the region between the two shells (He-intershell) becomes unstable to convection for a short period, the external layers expand and, later on, the H shell burning temporarily dies down. In the He-intershell, He is partially converted into carbon. During the AGB phase, main neutron sources are the  $^{13}\text{C}(\text{a,n})^{16}\text{O}$  reaction, active in radiative conditions during the interpulse period, and the  $^{22}\text{Ne}(\text{a,n})^{25}\text{Mg}$  reaction, marginally activated within the convective shell originated by the TP. In order to obtain a sufficient amount of  $^{13}\text{C}$ , a diffusion of protons from the H-rich envelope into the C-rich radiative zone is needed: the diffused protons are captured from the abundant  $^{12}\text{C}$  via the  $^{12}\text{C}(\text{p},\gamma)^{13}\text{N}(\beta^{-})^{13}\text{C}$  nuclear chain, leading to the formation of a tiny  $^{13}\text{C}$ -pocket. When in this region the temperature reaches about  $10^8$  K, the  $^{13}\text{C}(\alpha,\text{n})^{16}\text{O}$  reaction results efficiently activated, thus producing a large amount of neutrons which are captured by the iron seeds.

The aim of this work is the study of the problematic concerning the *s*-process nucleosynthesis in low mass AGB Stars. The advance in the knowledge of the complex coupling between convective mixing and nuclear process, which allows the surface enrichment of C and *s*-process elements, is presented, together with the hypothesis concerning the physical mechanism driving the formation of the  $^{13}\text{C}$  pocket. In order to illustrate the capabilities and the limits of the theory, updated computations of a  $2 M_{\odot}$  stellar structure at different chemical compositions are reported. These models have been obtained by including into the FRANEC stellar evolution code a full nuclear network (from H up to Bi, at the termination point of the *s*-process path), upgraded with the most recent experimental (if available) and theoretical cross sections. The predicted modification of the surface composition at different metallicities occurring during the AGB evolution is shown.

After a short introduction concerning the *s*-process (see Chapter 2), we briefly describe the basic ingredients characterizing a stellar evolutionary model (Chapter 3). In Chapter 4 we resume the current status of AGB modelling, by integrating it with the new issues characterizing this work, like our evaluation of the mass loss rate. In Chapter 5 we describe

the implementation of the nuclear network, discussing the choices we made on different reaction rates. In Chapter 6 the problem of the source of neutrons is afforded in some detail, with particular emphasis to the physical process driving the formation of a  $^{13}\text{C}$  pocket in the He-rich and  $^{12}\text{C}$ -rich intershell. We also describe how the velocity profile mechanism depends on the free parameter and how the study of the s-process can minimize the uncertainty range. In Chapter 7 we present the evolution and the nucleosynthesis of the aforementioned models, comparing it with the previous extant models. In particular, we stress the fact that in the solar metallicity model, the first formed  $^{13}\text{C}$  pocket doesn't burn in radiative conditions, but it is ingested in the convective shell generated by the following TP (Section 7.1.2), opening new interesting hypothesis about the origin of radioactive isotopes in the Early Solar System (Section 7.1.3). Chapter 8 is devoted to the study of the influence of opacities on AGB models: a comparison between two low metallicity models, obtained with a different treatment of the opacity coefficients, is shown. In Chapter 9 we give a short overview on the complex interplay between nuclear physics and astrophysics, presenting some tests we computed in last three years. Finally, in Chapter 10 we report our conclusions.



## Chapter 2

### Why: the failure of the classical model

*In this Chapter we briefly discuss the problematic concerning the  $s$ -process, describing its main features and the astrophysical conditions needed for its activation. Moreover, we give an overview on the first pioneering studies devoted to this nucleosynthetic process starting from the formulation of the so-called classical model up to the most recent developments in the modelling of the  $s$ -process.*

First studies concerning the solar abundances distribution [66] were followed by detailed spectroscopic observations [159], which led to the formulation of a nucleosynthetic processes list (see Fig. 2.1) in order to reproduce the observed chemical patterns [23]. There's no way to explain the abundances of elements heavier than iron by means of nuclear charged particle reactions, being heavy nuclei cross sections strongly reduced by the repulsive Coulomb barrier, which increases with their atomic number  $Z$ . Moreover,  $^{56}\text{Fe}$  has the greatest per nucleon binding energy, therefore nuclear reactions starting from iron seeds are of endoenergetics nature. Charged particle cross section is given by:

$$\sigma(E) = \frac{S(E)}{E} \exp\left(-\frac{[0.98948 Z_1 Z_2 A^{\frac{1}{2}}]^2 \text{ MeV}}{E}\right)^{\frac{1}{2}}, \quad (2.1)$$

where the astrophysical factor  $S(E)$  slowly changes by varying the energy. The cross section  $\sigma$  (which is a measure of the probability that a reaction takes place) decreases with increasing  $Z$ , causing light elements to be burnt before heavier ones during thermonuclear processes. Therefore, during the quiescent stellar phases, the energy, mainly provided by thermal heating, cannot be responsible for the production of elements characterized by a high proton number. Proton captures on heavy elements could however occur in objects loosing their thermodynamical equilibrium, such as massive stars at the end of their evolution, when an irreversible collapse process ends with the type II Supernova explosion.

Limitations due to the Coulomb barrier overcoming disappear if dealing with neutron

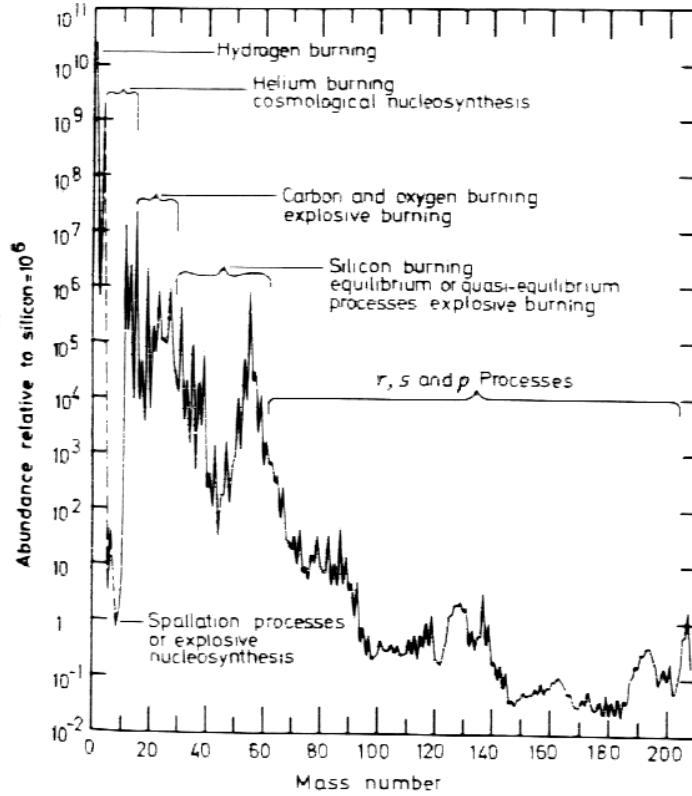


Figure 2.1 Nuclide abundances (relative to  $N(\text{Si})=10^6$ ) as a function of the mass number. Labels in the picture identify different processes responsible for the formation of solar observed isotopes (picture from [40]).

captures, occurring during hydrostatic quiescent phases, characterized by fairly low temperatures ( $KT \sim 10 \div 100$  keV). The heavy elements distribution points out the existence of three separate components, correlated to different nucleosynthetic processes:

- $s$ -process;
- $r$ -process;
- $p$ -process (which leads to the formation of proton-rich nuclei).

The aforementioned distribution is characterized by three peaks, around isotopes having neutron numbers equal to 50, 82 and 126, named magic nuclei. These isotopes show a larger stability with respect to their neighbors, behaving like noble gases (nuclei with  $Z=50$  and

$Z=82$  show similar characteristics, being however their peculiarity less evident). This is due to the fact that their nucleons completely fill nuclear energetic levels, being the energetic gap between two levels greater than energetic differences in shell internal levels. The first possible level the captured neutron can occupy is less bound than the other occupied levels, this fact giving a larger stability to this isotope with respect to its neighbors.

While the  $r$ -process ( $r$  stands for *rapid*) requests high neutron fluxes, characterized by neutron densities  $n_n \simeq 10^{22} \text{ cm}^{-3}$ , in the  $s$ -process ( $s$  stands for *slow*) the neutron content is lower ( $n_n(t) < 10^8 \text{ cm}^{-3}$ ). In such a case, stable isotopes capture free neutrons, while radioactive ones decay in their stable isobars, leading the nucleosynthesis to develop along the so-called  $\beta$  stability valley. Once defined the ratio between the mean neutron capture timescale and the mean  $\beta$  decay timescale as  $\frac{\tau_n}{\tau_\beta}$ , the nucleosynthesis chain displays along the  $\beta$  stability valley if such a ratio is bigger than 1, while if minor than 1 the nucleus absorbs more neutron moving toward heavier isotopes. In this latter case, the  $\beta$  decay stops this captures series when the binding energy is too low to permit another neutron capture; after the decay, the nucleus starts again capturing neutrons. This mechanism stops when the neutron absorber reaches its waiting point (depending on the nucleus charge), where a decay chain shifts the isotope to the stability valley.

## 2.1 A bit of history...

In Fig. 2.2 we plot the solar  $s$ -process  $\sigma_i N_i$  distribution; a monotonically decreasing profile, with evident steps in correspondence to neutron magic isotopes, results. The extreme simplicity in the  $s$ -process distribution with respect to the  $r$ -process one (see Fig. 2.3) inspired researchers in formulating numerical techniques based on analytical hints, independently on the astrophysical site: this is the main feature of the classical model.

Neutron cross sections  $\sigma_i$  are generally greater than the corresponding charged particle cross sections and increase with the atomic number. Moreover, even nuclei (even  $Z$  and  $N$ ) have lower  $\sigma$  because the resonant levels mean density is lower with respect to odd nuclei, where the captured neutron could interact more easily with the odd nucleon. Lowest neutron cross sections correspond to magic nuclei ( $N = 50, 82, 126$ ), i.e. the Y, the La and the Pb  $s$ -process peaks. The differential equation regulating the abundances of heavy nuclei is

$$\frac{dN_A}{dt} = - \langle \sigma v \rangle_A n_n(t) N_A(t) + \langle \sigma v \rangle_{A-1} n_n(t) N_{A-1}(t), \quad (2.2)$$

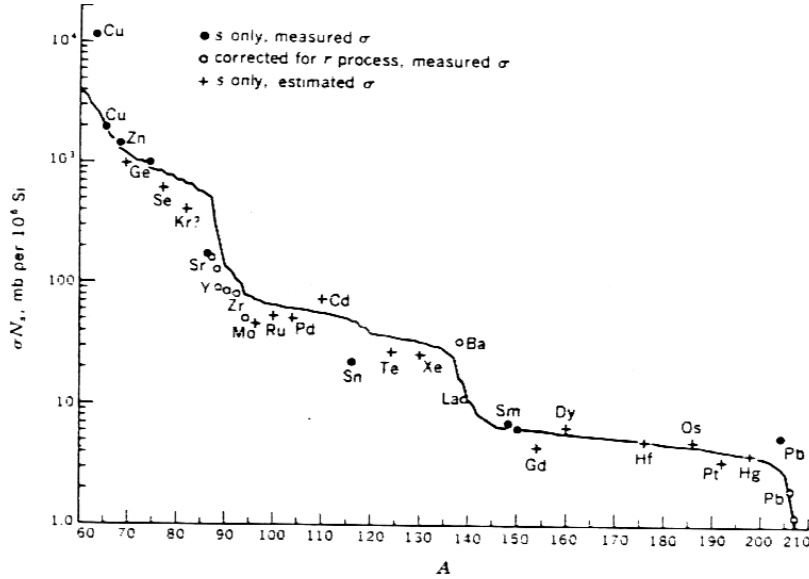


Figure 2.2 Solar  $s$ -process  $\sigma_A N_A$  distribution. The curve has been obtained with an exponential distribution of neutron expositions (picture from [147]).

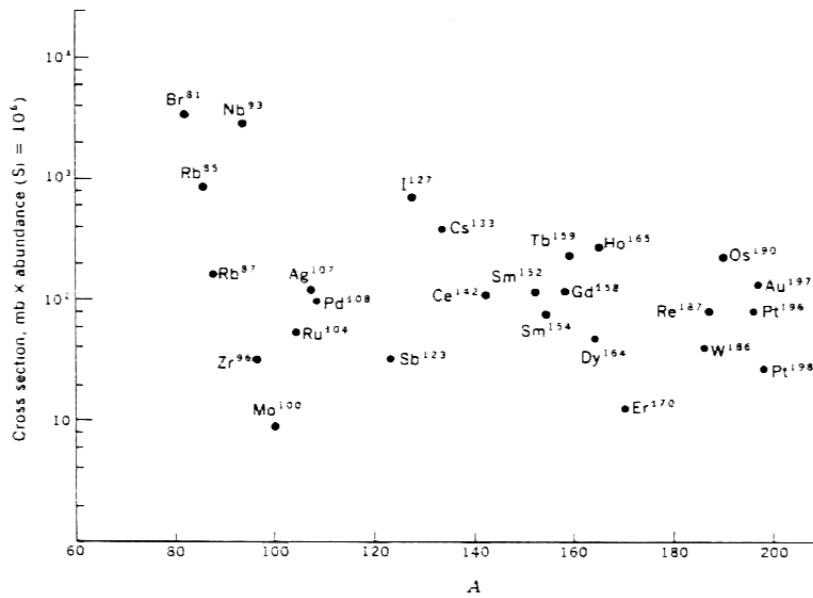


Figure 2.3 Solar  $r$ -process  $\sigma_A N_A$  distribution. The lack of a correlation between data is evident, strengthening the fact that the  $s$ -process distribution is not accidental (picture from [147]).

where  $\langle \sigma v \rangle_A$  is the destruction rate of the nucleus with atomic mass  $A$  (the  $\beta$  decay of the  $(A-1)$  isotope is assumed to be instantaneous). Maxwellian neutron cross sections are defined as

$$\langle \sigma \rangle = \frac{\langle \sigma v \rangle}{v_T} = \frac{\int_0^{+\infty} v \sigma(v) \varphi(v) dv}{v_T}, \quad (2.3)$$

where  $\varphi(v)dv$  represents the Maxwellian spectrum of velocities, given by

$$\varphi(v) = \left(\frac{4}{\pi^{1/2}}\right) \left(\frac{v}{v_T}\right)^2 \exp\left[-\left(\frac{v}{v_T}\right)^2\right] \frac{dv}{v_T}. \quad (2.4)$$

$v_T$  represents the relative thermal velocity, written as

$$v_T = \left(\frac{2\pi KT}{\mu}\right)^{1/2} \approx 1.284 \times 10^4 T^{1/2} \text{ cm sec}^{-1}, \quad (2.5)$$

where  $T$  is the gas temperature and  $\mu = \frac{M_n M_A}{(M_n + M_A)} \approx M_n = 1.674920 \times 10^{-24} \text{ g}$  (neutron mass). Because the reduced mass in equation (2.5) (labeled as  $\mu$ ) practically coincides with the neutron mass, we can assume as the right velocity the independent neutron one. Substituting it in formula (2.2), we obtain

$$\frac{dN_A}{d\tau} = -\sigma_A N_A + \sigma_{A+1} N_{A+1}, \quad (2.6)$$

where we defined the neutron exposure  $\tau$  as

$$\tau = \int n_n(t) v_T dt \text{ (mbarn}^{-1}\text{)}. \quad (2.7)$$

Considering nuclei far from closed shell configurations, the  $\sigma_A N_A$  product is practically constant (if a high neutron flux is available): this is due to the presence of magic nuclei, which stop the nucleosynthesis up to the local saturation. The constant value  $\sigma_A N_A$  is determined by the self-regulating equation 2.6; we can therefore assume as valid the following equation

$$\sigma_A \cdot N_A \approx \sigma_{A-1} \cdot N_{A-1}, \quad (2.8)$$

named local approximation. This equation is valid in regions (plateaux) between two subsequent magic nuclei (see Fig. 2.2).

A single neutron exposition can't reproduce the solar elements distribution, which could however result from a superimposition of different  $^{56}\text{Fe}$  seeds exposed to a series of neutron fluxes. A quite good reproduction can be found by adopting an exponential distribution of neutron expositions [147]:

$$\rho(\tau) = \frac{GN_{56}}{\tau_0} \exp\left(-\frac{\tau}{\tau_0}\right), \quad (2.9)$$

where  $G$  is the iron fraction exposed to neutrons,  $N_{56}$  is the initial  $^{56}\text{Fe}$  abundance and  $\tau_0$  is a parameter, named mean neutron exposure.

The exponential distribution of neutron exposures displayed in equation 2.9 can reproduce the solar abundances if three values of  $\tau_0$  (depending on the atomic mass  $A$  and corresponding to different  $s$ -process components) are adopted :

1. main component (  $90 < A < 204; \tau_0 = 0.3 \text{ mbarn}^{-1}$  );
2. weak component (  $A \leq 90; \tau_0 = 0.06 \text{ mbarn}^{-1}$  );
3. strong component (  $204 < A < 209; \tau_0 = 7.0 \text{ mbarn}^{-1}$  ).

This distribution found a full confirmation when [165] proposed his model of self-consistent  $s$ -process nucleosynthesis (see Fig. 2.4), perfectly matching with an exponential distribution. In the same paper, the convective shells characterizing the TP-AGB phase were proposed as the astrophysical site for heavy elements production. Labeling as  $M_s$  the mass

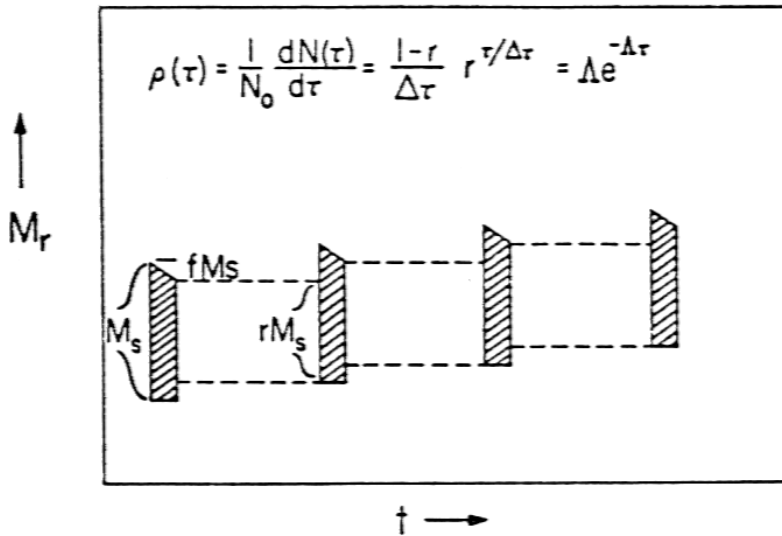


Figure 2.4 Schematic diagram of the Ulrich model: shaded areas represent convective shells where neutron captures occur (from [165]).

extension of a convective shell, only a fraction ( $r \cdot M_s$ ) of such a material is engulfed in

the following shell, while the remaining  $[(1-r) \cdot M_s]$  is directly coming from the envelope. Identifying the per pulse neutron exposition as  $\Delta\tau$ , the convective shell mass fraction  $M_s$  experiencing  $j$  subsequent expositions is  $(1-r)r^{j-1}$ . Proceeding in this way, an exponential distribution of expositions is obtained:

$$\rho(\tau) = \frac{1}{N_o} \frac{dN(\tau)}{d\tau} = \frac{(1-r)}{\Delta\tau} r^{\frac{\tau}{\Delta\tau}} = \frac{(1-r)}{\Delta\tau} \exp\left(-\frac{\tau}{\tau_0}\right), \quad (2.10)$$

where  $\tau = n\Delta\tau$  and  $\tau_0 = \frac{\Delta\tau}{-\ln r}$ .

In the classical model, no hypotheses on the site where the s-process is active were formulated. The principal neutron sources in AGB stars are the  $^{13}\text{C}(\alpha, n)^{16}\text{O}$  and the  $^{22}\text{Ne}(\alpha, n)^{25}\text{Mg}$  reactions: first studies laid on the hypothesis that both reactions were releasing neutrons inside the convective shells generated by the TPs. A first decisive improvement occurred with the works of [153], where it was demonstrated that the  $^{13}\text{C}(\alpha, n)^{16}\text{O}$  reaction is burning in radiative conditions during the interpulse period. The convective  $^{13}\text{C}$  burning model identified in an exponential distribution of neutron expositions the right theory to match observational data. That distribution changes if considering a radiative  $^{13}\text{C}$  burning, as demonstrated by [10], leading to a new formulation with respect to equation 2.9:

$$\rho(\tau) \simeq \frac{(1-r)q}{\Delta\tau} \left(1 + \frac{\tau}{\Delta\tau}\right) r^{\frac{\tau}{\Delta\tau}}. \quad (2.11)$$

In this way, the resulting neutron exposures distribution is a superposition of a few single exposures. These new improvements in the understanding of the s-process clearly shows the limitations inherent to the classical model. It is then evident the importance of modelling the s-process by carefully taking into account the astrophysical sites where this process is believed to occur. In order to do that, the use of a stellar evolutionary code is crucial.



# Chapter 3

## Where: the FRANEC code

*In this section we roughly describe how to translate a stellar structure into a stellar evolutionary code. Main topics characterizing the 1-dimensional FRANEC (Frascati RAphson Newton Evolutionary Code) code are presented. In performing these computations, we don't consider the rotation or the presence of magnetic fields.*

The comprehension of stellar physics strictly follows advances in the construction of observational instruments and the development of powerful calculators, needed to compute stellar evolutionary models. The reduced instrumental uncertainties and the refinements of stellar codes allow an even more precise and meaningful comparison between these so different approaches in solving problems related to stars. In the following Section we quickly describe the main features constituting the FRANEC code, where a full set of equations describing the physical evolution of a star is coupled with the nuclear processes fixing the temporal variation of the nuclear species. We give details on the adopted input physics and we briefly introduce how we parameterize the convection; for an exhaustive description of the code we refer to [36], [37] and [155].

### 3.1 Stellar equilibrium equations

In order to describe a stellar structure we need quantitative formulae connecting pressure, temperature and production energy terms. The complete stellar equilibrium equation system consists of four first order, non-linear and constant coefficients differential equations and of three characteristic relations:

$$\left. \begin{aligned}
\frac{dP}{dr} &= G \frac{M(r)\rho(r)}{r^2} && \text{hydrostatic equilibrium} \\
\frac{dM}{dr} &= 4\pi r^2 \rho(r) && \text{continuity equation} \\
\frac{dL}{dr} &= 4\pi r^2 \rho \epsilon(\rho, T) && \text{energy conservation} \\
\frac{dT}{dr} &= -\frac{3\kappa\rho}{4acT^3} \frac{L_r}{4\pi r^2} && \text{(radiative transport)} \\
P &= P(\rho, T) && \text{equation of state} \\
\kappa &= \kappa(\rho, T) && \text{opacity} \\
\epsilon &= \epsilon(\rho, T) && \text{energy production}
\end{aligned} \right\} \quad (3.1)$$

Temporal changes in the physics of a star are strictly connected with its energy budget: the energy lost by photons and neutrinos is continuously sustained by the gravitational energy release and the nuclear burning; these terms, coupled with mixing events, are responsible for internal and external chemical distributions modifications. The system (3.1) can't be solved in an analytic way, moreover some functions (*e.g.* the opacity) is available only in a tabular format (see Section 3.4). For these reasons, the evolution of stellar codes strictly follows hardware improvements.

The integration variable is, for the major portion of the stellar structure, the mass  $M_r$ , which is the only lagrangian variable. In superficial layers (indicatively for  $M_r \geq 0.95M_\star$ ), due to the low density,  $M_r$  starts being less sensitive to variations in the stellar structure, and the system is solved by integrating in pressure ( $P$ ). Finally, for regions more external than the photosphere, the integration is carried out on the optical deepness:

$$\tau(r) = \int_r^{+\infty} \kappa \rho dr, \quad (3.2)$$

representing the mean probability one photon has to interact before being ejected from the star. The central conditions ( $r=0$ ) is obviously ( $M_r = 0; L = 0$ ), thus leading to a singularity of the integrating variable  $M_r$ . The integration has then to be started from a stellar layer having a radius coordinate  $r'$  very small (generally  $r' \cong 10^{-5}R_\star$ ).

A particular treatment has to be reserved to the transport equation, which changes its form depending on stellar conditions (see Section 3.2).

In Figure 3.1 the logical structure of the FRANEC code is schematically reported. The first model is calculated with a fitting method and its convergence is obtained by means of a 4<sup>th</sup> order Runge-Kutta method. All variables are initialized and matrix dimensions are defined by checking the number of chemical species considered in the nuclear network. Cross sections and decay times are stored from various tables, while model peculiarities

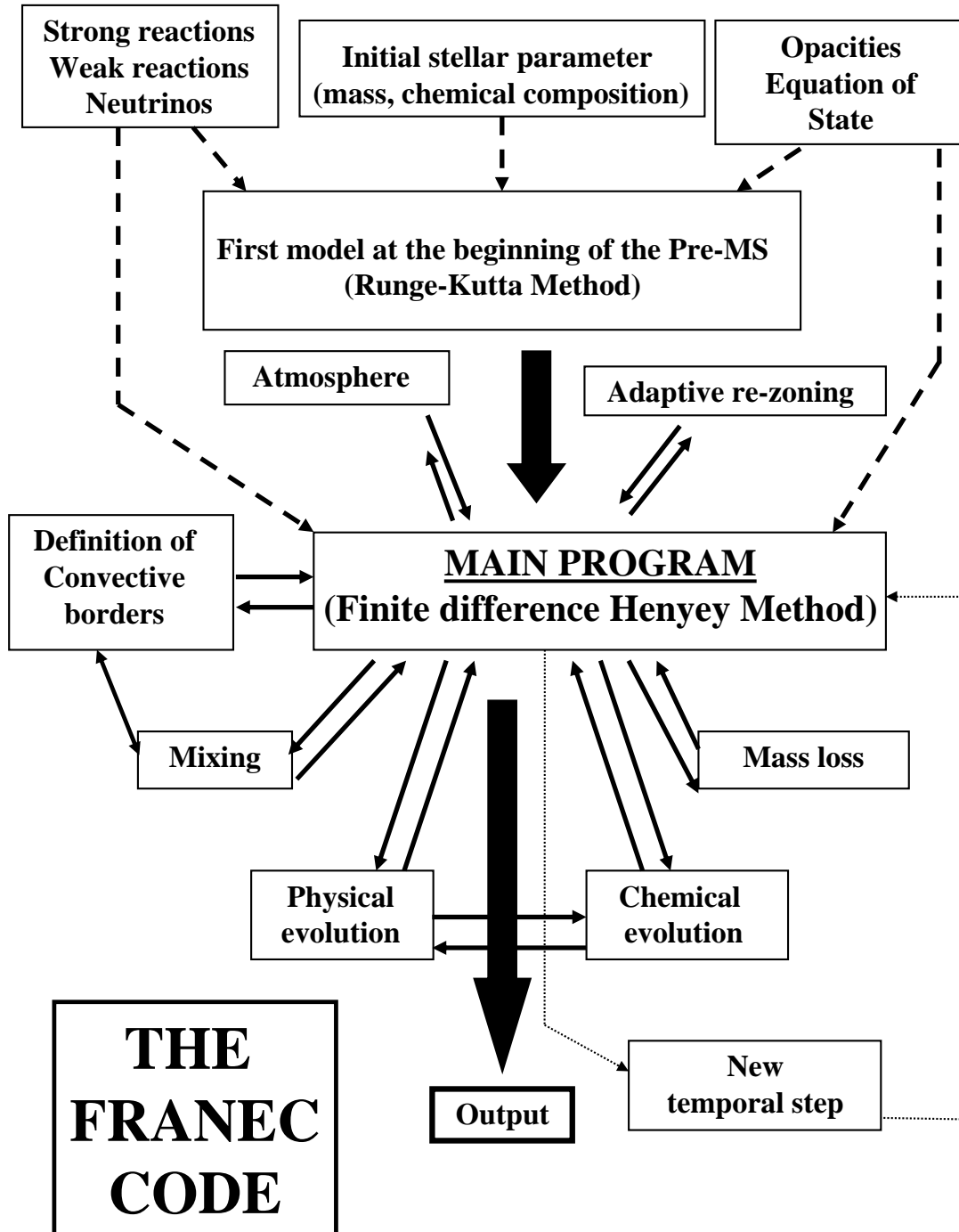


Figure 3.1 Schematic diagram of the FRANEC code structure.

and test values for the first integration are read from the initial model. Input physics, like opacity tables, initial chemical abundances and Equation of State (EOS), are stored from corresponding tables (see Section 3.3). Atmosphere conditions are calculated in a dedicated subroutine, while the amount of lost material is calculated in accordance with the adopted prescriptions (see Section 4.5). The structure is divided in spherical shells (mesh-points), whose mass distribution is regulated (each model) by a re-zoning procedure. Convective borders are defined by the Schwarzschild criterion (see Section 3.2), while the degree of mixing is determined by using the mixing length theory (see Section 3.2.1). The evolutionary time step is determined by the fact that the physical variables  $R$ ,  $L$ ,  $P$ ,  $T$ , and  $M$  do not vary by more than a fixed amount from one model to the next one. The integration is performed by using a finite increments method: the convergence is reached when the percentage corrections to the various physical and chemical quantities are smaller than  $10^{-6}$  (see next Section).

### 3.1.1 Numerical integration methods.

In order to solve the system (3.1), numerical techniques are needed, because of their capability in approximating derivatives with finite increments. In the FRANEC code, the system is solved first by imposing a set of test values ( $P(M_r), T(M_r), R(M_r), L(M_r)$ ) and by applying an iterative corrective method named NEWTON-RAPHSON. This technique is the well-known HENYEY method.

The first step consists in fixing  $m$  values of  $M_r$ , dividing the structure in close enough mesh points; the system describing the stellar structure can be written as

$$\frac{dy^h}{dx} - f_h(x, y^1, y^2, y^3, y^4) = 0. \quad (3.3)$$

where  $y^h$  ( $h = 1, 2, 3, 4$ ) are the dependent variables and  $x = M_r$  the independent one. Supposing that corresponding to  $dx = x_{j+1} - x_j$  it results  $dy^h = y_{j+1}^h - y_j^h$ , first terms of system (3.1) can be written, mesh by mesh, in the finite differences formalism:

$$F_j^h \equiv \frac{y_{j+1}^h - y_j^h}{x_{j+1} - x_j} - f_h(x_j, x_{j+1}, y_j^1, y_{j+1}^1, \dots, y_j^4, y_{j+1}^4). \quad (3.4)$$

where  $f_h$  functions are computed by calculating mean values between  $j$  e  $j+1$ . The degree of approximation in formula (3.4) grows up with reducing the  $\Delta x$  difference corresponding to  $j$  e  $j+1$  values. The (3.1) system solution must assure the condition that, for all  $j$  values,

the equation

$$F_j^h(x_j, x_{j+1}, y_j^k, y_{j+1}^k) = 0, \quad (3.5)$$

is verified. If we assign a generic trend to dependent variables we instead obtain

$$F_j^h(x_j, x_{j+1}, y_j^k, y_{j+1}^k) = c_j^h \neq 0, \quad (3.6)$$

which would be equal to 0 in case of linear derivatives. The system is then solved by modifying test values assigned to  $y_j^h$  in order to verify  $c_j^h \leq \epsilon$  for all  $j$  and for all  $h$  (an acceptable value is  $\epsilon \sim 10^{-8}$ ). Varying  $y^k$ ,  $F^h$  change following

$$\delta F_j^h = \sum_{k=1}^4 \left( \frac{\partial F_j^h}{\partial y_j^k} \delta y_j^k + \frac{\partial F_j^h}{\partial y_{j+1}^k} \delta y_{j+1}^k \right). \quad (3.7)$$

By imposing  $\delta F_j^h = -c_j^h$  (we want  $F_j^h + \delta F_j^h = 0$ ), (3.7) constitutes an algebraic system of  $(4m-4)$  linear equations, where  $m$  is the mesh point number in  $4m$  unknown  $\delta y_j^k$  ( $j=1,2,\dots,m$ ;  $k=1,2,3,4$ ). Missing relations are obtained from boundary conditions, i.e. central and superficial values.  $\delta y_j^k$  represent variation to be applied to the test values  $y_j^k$ . A solution is achieved, at the desired approximation level, by iteratively applying the newly obtained correction terms to the previous iteration results.

## 3.2 Convective zones

In stellar interiors, energy can be transported by conduction, radiation and convection. First two mechanisms are theoretically always working, even if with different efficiencies, if a temperature gradient is present. Convection is present only if stellar layers are unstable for macroscopic material transfers (convective motions). The main problem is to understand the conditions under which a convective motion starts and which is the efficiency of such a mechanism. A simple answer could be given on the basis of the work of [143], basically founded on the Archimede's argument. Under the hypothesis of no convective motions, a radiative thermal gradient, connected with the outgoing energy flux, has to raise up. If we force a material element to move, under the adiabatic assumption (justified by the fact that thermodynamic timescales are highly greater than the mechanical ones), it moves depending on its absolute adiabatic gradient  $\left| \frac{dT}{dr} \right|_{ad}$ . In other words, we have convection if the Schwarzschild criterion for the radiative stability

$$\left| \frac{dT}{dr} \right|_{rad} < \left| \frac{dT}{dr} \right|_{ad} \quad (3.8)$$

is no more fulfilled, thus leading to macroscopic material motions. This argument, valid under the adiabatic assumption, could be extended also to non-adiabatic transport, since the energy exchange with the surrounding material, tending to slow down convective motions, acts on thermodynamic timescales. Moreover, it is proportional to the temperature difference between the ambient and the convective element, which reduces with the time.

### 3.2.1 The mixing length theory

Even under the adiabatic assumption, convection can carry energy only if the local gradient is greater than the adiabatic one (*overadiabaticity conditions*). Under that hypothesis, the convective element, after covered a length  $l$ , has a temperature greater than ambient, and it is therefore able to release heat, in the quantity:

$$\delta Q = C \Delta T, \quad (3.9)$$

where  $C$  is the thermal capability and  $\Delta T$  the temperature difference between the element and the ambient, written as

$$\Delta T = \int \left[ \left( \frac{dT}{dP} \right)_{amb} - \left( \frac{dT}{dP} \right)_{ad} \right] dp = \int \delta_{ad} dp. \quad (3.10)$$

In equation 3.10,  $\delta_{ad}$  represents the superadiabaticity value.

In internal layers, the thermal capability is so high that the convective flux is largely greater than the radiative one, therefore  $\nabla_{eff} = \nabla_{ad}$  ( $\nabla_{eff}$  is the gradient characterizing the convective environment). Moving to external layers, the effective gradient diverges from the adiabatic one, however fulfilling the condition

$$\nabla_{ad} < \nabla_{eff} < \nabla_{rad}. \quad (3.11)$$

The theory describing the superadiabaticity degree of  $\nabla_{eff}$  is the so-called mixing length. If in a convective layer we define a mixing length  $l$  and a mean convective velocity  $v$ , the relationship between the superadiabaticity and the velocity is given by:

$$\nabla_{eff} = \frac{ackT_{eff}^4 + \frac{1}{2}c_p\rho vl\nabla_{ad}}{\frac{4acT^3}{3\bar{x}\rho} + \frac{1}{2}c_p\rho vl}. \quad (3.12)$$

In this formula the mixing length is assumed comparable to the pressure scale height  $H_P$ , defined as the distance where the pressure reduce its value to  $1/e$ :  $l = \alpha H_P$ , where  $\alpha$  is a free parameter, limited by the fact that a convective element can't survive for steps greater

than  $H_P$ . If  $v$  tends to 0,  $\nabla_{eff}$  tends to  $\nabla_{rad}$ , while if  $v$  is sufficiently high,  $\nabla_{eff}$  tends to  $\nabla_{ad}$ . In the same way,  $v$  could be derived as

$$v = gl \left[ \frac{H\mu}{8\kappa T} (\nabla_{eff} - \nabla_{ad}) \right]^{\frac{1}{2}}. \quad (3.13)$$

In convective zones, the mixing degree depends on the convective timescale ( $\tau_{j,k}$  between  $j$  and  $k$  adjacent mesh-points):

- if  $\tau_{nuclear} \gg \tau_{j,k}$  nuclear species present flat distributions ( $\tau_{nuclear}$  is the nuclear burning timescale);
- if  $\tau_{nuclear} < \tau_{j,k}$  nuclear species reach the local equilibrium;
- if  $\tau_{nuclear} \sim \tau_{j,k}$  the resulting distributions depend on the interplay between mixing and burning.

Another problem arises when the evolutionary time step ( $\Delta t$ ) is comparable with  $\tau_{j,k}$ :

- if  $\Delta t \leq \tau_{j,k}$  some nuclear species are not fully mixed during a temporal step;
- if  $\Delta t \gg \tau_{j,k}$  the mixing is complete.

The degree of mixing is calculated by means of the following relation:

$$X_j = X_j^o + \frac{1}{M_{conv}} \sum_k (X_k^o - X_j^o) f_{j,k} \Delta M_k \quad (3.14)$$

where the summation is extended over the whole convective zone and the superscript  $o$  refers to unmixed abundances.  $\Delta M_k$  is the mass of the mesh-point  $k$  and  $M_{conv}$  is the total mass of the convective zone. The damping factor  $f$  is:

$$f_{j,k} = \frac{\Delta t}{\tau_{j,k}} \quad (3.15)$$

if  $\Delta t < \tau_{j,k}$ , or

$$f_{j,k} = 1 \quad (3.16)$$

if  $\Delta t \geq \tau_{j,k}$ . In these formulas  $\Delta t$  is the time step and  $\tau_{j,k}$  is the mixing turnover time between the mesh-points  $j$  and  $k$ , namely:

$$\tau_{j,k} = \int_{r(j)}^{r(k)} \frac{dr}{v(r)} = \sum_{i=j,k} \frac{\Delta r_i}{v_i} \quad (3.17)$$

The mixing velocity ( $v_i$ ) is computed according to the mixing length theory. It is worth to notice that, in our code, neutrons are not mixed in convective zones, being always  $\tau_{nuclear} \ll \tau_{j,k}$ .

### 3.3 Input physics and initial abundances

In this work, we present three AGB models having the same initial mass ( $M=2M_{\odot}$ ) and different metallicities ( $Z=1.5\times 10^{-2}$ ,  $Z=1\times 10^{-3}$  and  $Z=1\times 10^{-4}$ ) therefore spanning almost the entire metal distribution of our Galaxy.

Concerning the model with  $Z=1.5\times 10^{-2}$ , the computation has been started from a homogeneous structure with a mass fraction of helium  $Y = 0.269$ . The  $Y$  and  $Z$  values have been derived from a standard solar model, by fitting the luminosity ( $L_{\odot}=3.844 \times 10^{33}$  erg/s), radius ( $R_{\odot}=6.951 \times 10^{10}$  cm) and  $(Z/X)_{\odot}$  (0.017) of the present Sun. This calibration implies  $\alpha_{m.l.}=1.9$ : we therefore adopt that value in all calculations presented in this work. The mass fractions of all the elements beyond hydrogen and helium relative to  $Z$  have been derived from [7], except for C and N [6] and O, Ne and Ar [11]. In the aforementioned papers, the solar CNO abundances have been revisited and new values result lower with respect to previous compilations [7, 69, 70]. Moreover, in order to fit the actual surface He abundance, the macroscopic settling has to be taken into account: this phenomenon reduces the heavy elements surface abundances during the evolution of the star, therefore lowering its surface He content and metallicity. For these reasons, we assume as the initial metallicity of the Sun the value  $Z=1.5\times 10^{-2}$  and hereafter we refer to this value as the solar metallicity. Table 1 lists the adopted initial mass fractions (for the most abundant elements) at the three different metallicities. Note that, for both the  $Z=1\times 10^{-3}$  and the  $Z=1\times 10^{-4}$  models, we scale the initial abundances of all the elements with the metallicity, except for hydrogen and helium (we adopt the cosmological abundance  $Y_{ini}=0.245$ ).

Element	$Z=1.5\times 10^{-2}$	$Z=1\times 10^{-3}$	$Z=1\times 10^{-4}$
H	0.716	0.754	0.755
He	0.269	0.245	0.245
C	2.47(-3)	1.65(-4)	1.65(-5)
N	1.00(-3)	6.67(-5)	6.67(-6)
O	6.12(-3)	4.08(-4)	4.08(-5)

Table 3.1 Adopted initial element abundances.

In our calculations, electron screening is taken into account by following prescriptions from [46] and [68] for the weak and intermediate regimes, while from [89] and [90] for the strong one. For the description of the adopted equation of state, we refer to [152], updated by [126]. Above  $10^6$  K, the matter is assumed to be completely ionized, while below that

value, partial ionization is taken into account. In the high-temperature regime, the electron degeneracy, relativistic effects, electron-positron pair creation, and Coulomb interactions contributions are considered, while below the threshold temperature value, the ionization stages are derived from the classical Saha equation. We refer to [117] and [118] for the energy loss due to photoneutrinos, pair and plasma neutrinos. Bremsstrahlung neutrinos are taken from [47], corrected by [136].

### 3.4 Opacities

The energy irradiated by a star, mainly consisting of photons, covers a wide energy range (from X band to radiowaves). Photons created in the internal layers of a star suffer for a series of interactions with the surrounding material, whose net effect is the isotropisation of the flux. The capability of a material to interact with the radiation is called opacity and its efficiency is expressed by the well-know coefficient  $\kappa$ . This coefficient is defined as the inverse of the photon free mean path and it depends not only on the temperature and the density (the higher the velocity and the density of the particles are, the higher the probability a photon would interact with them is), but also on the chemical composition (the higher the mean weight is, the higher the opacity is) and the frequency. This latter dependency is solved by calculating a mean opacity coefficient over the entire frequency range, named Rosseland mean opacity. A photon produced in the core of a star is then continuously absorbed and emitted, this perdurable interaction producing a net flux toward the external layers. In regions where the opacity is very high, the material warms up and when the temperature gradient is high, macroscopic motions start mixing the region, which results then dominated by convection (see Section 3.2). Dominant opacity sources are reported in the following list (we fix the items order by first considering contributions at higher temperatures):

- continuous sources;
- atomic lines opacities;
- molecular sources;
- grains opacity.

At high temperatures, contributions to the global opacity come from electronic scattering (Thomson scattering if dealing with non-relativistic matter or Compton scattering in the

relativistic case), bound-bound (b-b) processes, bound-free (b-f) processes and free-free (f-f) processes. If the temperature decreases below 4500 K, an additional opacity source is represented by oxygen composite molecules (TiO, VO, H<sub>2</sub>O, ZrO) or carbon composite molecules (C<sub>2</sub>, CH, CN and SiC), depending on which, oxygen or carbon, is the most abundant element. In previous two categories we did not mention the CO molecule, because its contribution to opacity is independent on the C/O ratio, being its binding energy so large that all the atoms of the least abundant element (C or O) are locked to form that molecule. For temperatures lower than 1500 K the presence of small solid dust particles further enhances the opacities, therefore the contributions from condensates have to be accounted for in the determination of the optical thickness of the material. Finally, in regions characterized by high densities, the conductive opacities contribution represents a non-negligible fraction of the total opacity.

The determination of all these coefficients may results computationally not feasible because of their frequency dependence, so it is often useful to use pre-tabulated mean opacity tables. Tables of radiative opacity have been derived by means of the web facility provided by the OPAL group (<http://www-phys.llnl.gov/Research/OPAL/opal.html>). These opacity tables extend down to  $\log T = 4.05$ , therefore additional low temperature opacity are needed: we use tables provided by [5]. Conductive opacities are taken from [125]. The opacity change caused by the variation of the internal chemical composition, due to nuclear burning, convective mixing and microscopic diffusion, has been taken into account by linearly interpolating between tables with different  $Z$  and  $Y$ . Such a procedure guarantees an accurate determination of the surface abundance variations, provided that the relative distribution of the heavy elements remains almost unchanged. Unfortunately, this is not the case of AGB stars during the TP-AGB phase, when TDU episodes occur. In this case, in fact, the relative isotopic distributions results deeply modified, in particular the <sup>12</sup>C mass fraction is greatly enhanced. We refer to Section 7.2 and Chapter 8 for a detailed analysis of this problem.

# Chapter 4

## When: AGB stars

*In this Chapter we review the present status in the modelling of low mass AGB stars. In particular, the evolutionary phases before the TP-AGB phase are described. Moreover, we give details on our current choice concerning the mass loss rate, considered one of the main uncertainty sources in the study of AGB stars.*

### 4.1 Introduction

It was in 1868 when the Jesuit astronomer Father Angelo Secchi first recognized in the peculiar spectrum of some red giants the signature of carbon enhancement [146]. This new class includes stars belonging to the Disk of the Milky Way, called by Secchi "red carbon stars" and nowadays named C(N-Type) stars, that are evolved low mass red giants with photospheric  $C/O > 1$ . In the Hertzsprung-Russell diagram, they are located near the tip of the asymptotic giant branch (AGB) and represent the end point of the evolutionary sequence of a star that starts the AGB as an M giant (typically  $C/O < 0.5$ ) and progressively modifies its surface composition, passing through the MS, S and C(N) stages. The internal structure of these giant stars is made of three regions: a compact C-O core, a thin He-rich and C-rich mantel (He intershell) and an expanded H-rich envelope. As usual for red giant stars, the envelope is largely unstable against convection. Carbon is synthesized by the  $3\alpha$  reactions that burn at the base of an He-rich layer surrounding the core. The first question for the theoreticians was the search for a process capable to move the C from the deep interior of the star to the surface ([86], [111], [154]). Modern studies have clarified that the dredge up of C is due to the combination of two distinct convective episodes. The first is responsible for an efficient mixing of the whole He-rich layer and the second partially overlaps the zone previously mixed by the first convective episode and extends to

the stellar surface. As a consequence of these two convective episodes, other products of the nucleosynthesis occurring within the He-rich mantle, besides  $^{12}\text{C}$ , should appear at the surface. As a matter of fact, MS, S, C(N) and post-AGB stars are enriched in s-process elements, like Sr, Y, Zr, and Ba, La, Ce, Nd corresponding to the light and heavy s-abundance peaks, as early encoded by [23]. Detection of unstable  $^{99}\text{Tc}$ , whose half life is "only"  $2.1 \times 10^5$  yr, demonstrates that this enhancement cannot be due to an anomalous pollution of the pristine material from which these stars were born, but that the s process must be at work in their interiors [115]. In addition, it was realized that only relatively faint AGB stars become C-rich and that the brightest AGBs are N-rich [173]. This evidence supports the hypothesis that C(N)-stars have low mass progenitors. In massive AGBs, indeed, the CN-cycle taking place at the base of the external convective layer converts most of the C dredged up into N. As recalled in Chapter 2, recent studies have demonstrated that the

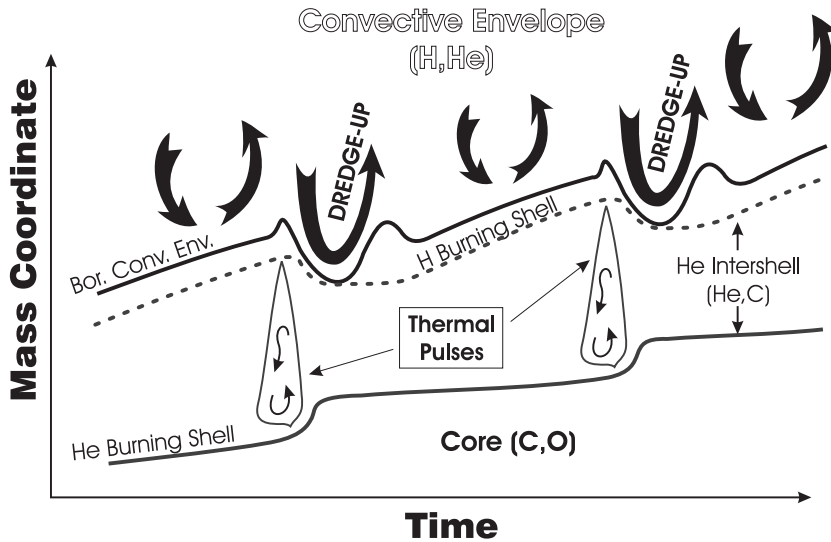


Figure 4.1 This sketch illustrates the evolution of the positions of the inner border of the convective envelope, the H-burning shell and the He-burning shell, during the thermally pulsing AGB phase. The convective regions generated by two subsequent TPs are also shown.

AGB stars with  $M < 3 M_{\odot}$  are the major contributors to the galactic production of the isotopes belonging to the main component of the s process, involving isotopes with atomic mass beyond  $A \sim 80$  (see for a review [172]). Clayton [40] first pointed out that a multiple neutron exposure, rather than a single exposure, is needed to reproduce the main component and [165] suggested that this condition could occur in the He-rich layer of an AGB

star. A few years before, indeed, [145] discovered that during the late AGB the He burning shell is recurrently switched on and off. At each He re-ignition, a thermonuclear runaway (TP) occurs and the rapid release of nuclear energy induces the formation of an extended convective region, where the products of the nucleosynthesis are fully mixed. (see figure 4.1).

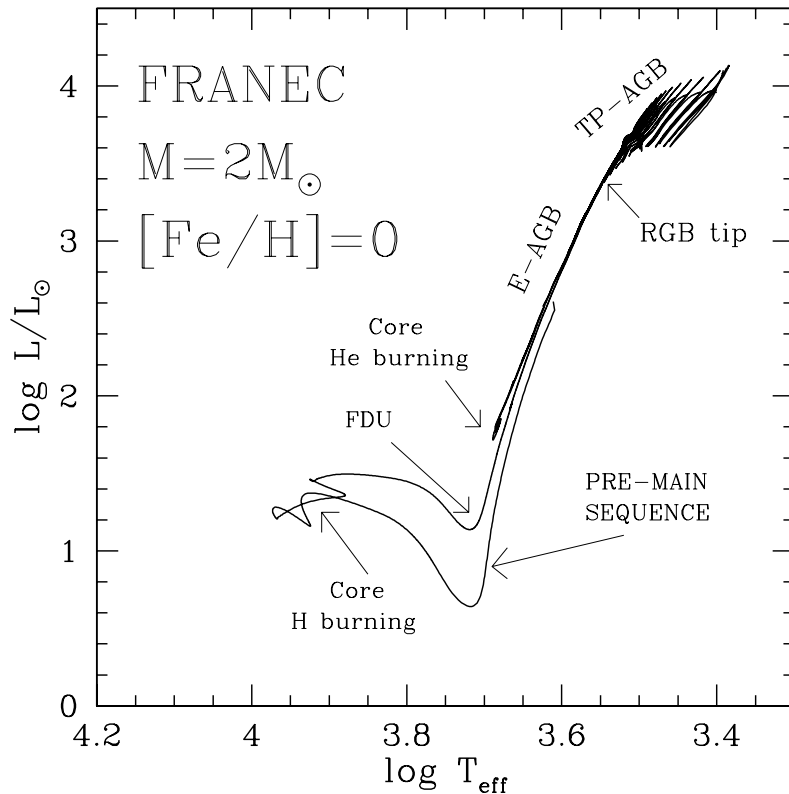


Figure 4.2 Theoretical evolutionary track in the Hertzsprung-Russell diagram of a star of initial mass  $M = 2 M_{\odot}$  and solar metallicity (see section 7.1 for details).

Two promising neutron sources for the build up of the heavy s-process isotopes were early recognized ([28], [29]): the  $^{22}\text{Ne}(\alpha, n)^{25}\text{Mg}$  reaction and the  $^{13}\text{C}(\alpha, n)^{16}\text{O}$  reaction. On the basis of detailed AGB stellar models, it has been understood that the major source of neutrons in low mass AGB stars is provided by the  $^{13}\text{C}(\alpha, n)^{16}\text{O}$  reaction. The s-process nucleosynthesis mostly occurs during the relatively long interpulse period (namely the time elapsed between two subsequent TPs), in a thin radiative layer at the top of the He intershell ( $\sim 10^{-3} M_{\odot}$ ), when the temperature ranges between 80 and  $100 \times 10^6$  K

[153]. A second neutron burst giving rise to a small neutron exposure, but with a high peak neutron density, is released by the marginal activation of the  $^{22}\text{Ne}$  neutron source in the convective TPs, modifying the final s-process composition at branchings along the s path depending on the neutron density or on temperature.

## 4.2 Approaching the Thermally Pulsing AGB

The evolutionary track in the HR diagram calculated for a  $2 M_{\odot}$  star of solar metallicity is reported in Figure 4.2. The initial model is fully convective and corresponds to the pre-main sequence contraction phase, with a central temperature of about  $10^5$  K. The model has been evolved from the pre-main sequence, through core H burning, the red giant branch (RGB), the off-center He flash and the He burning, up to the AGB.

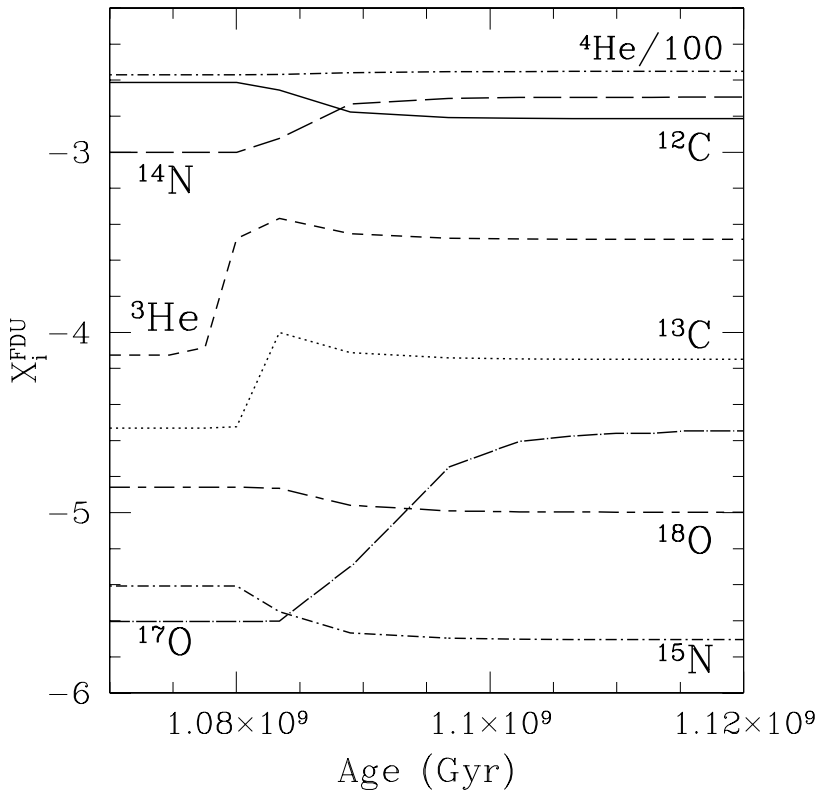


Figure 4.3 Surface abundances variations after the occurrence of FDU episode in the  $M = 2 M_{\odot}$  model with solar metallicity. Note that the He abundance has been divided by a factor 100 in order to match the box.

After the star leaves the main sequence and first becomes a red giant, the convective envelope penetrates in the radiative region above the H shell, enriching the surface composition with the ashes of proton captures occurred in this deep zone during the main sequence (first dredge up, FDU); with respect to the pristine composition,  $^4\text{He}$ ,  $^3\text{He}$ ,  $^{13}\text{C}$ ,  $^{17}\text{O}$ , and  $^{14}\text{N}$  are enhanced, while  $^{12}\text{C}$ ,  $^{15}\text{N}$  and  $^{18}\text{O}$  are depleted (see Fig. 4.3). Light

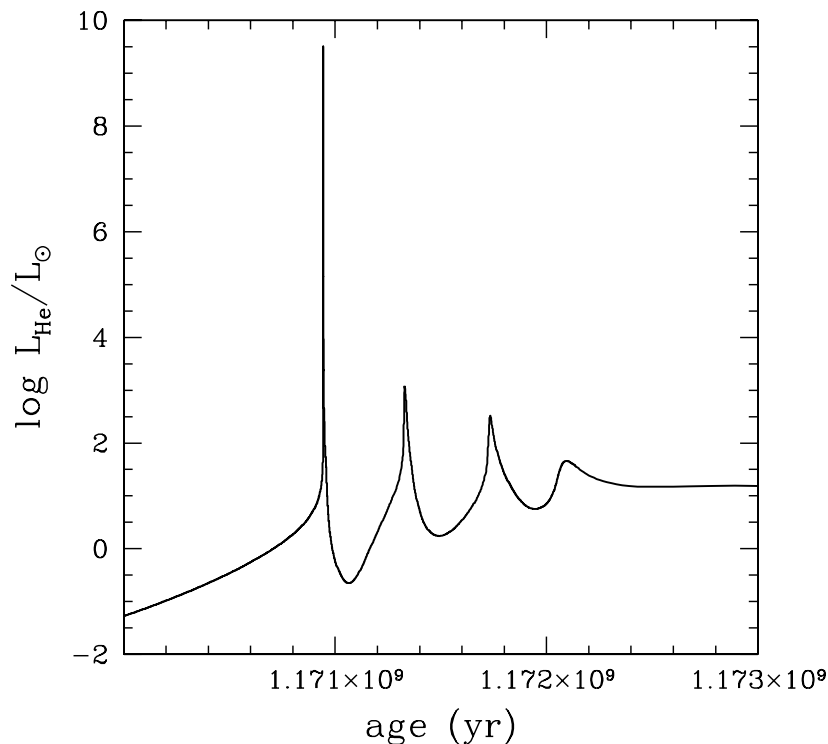


Figure 4.4  $3\alpha$  luminosity evolution during the off center He-flash in the  $M = 2 M_{\odot}$  model with solar metallicity.

elements, Li and Be, are practically extinguished. The upper mass limit for the occurrence of the first dredge up increases with the metallicity. At  $Z=0.02$ , all stars entering the AGB have experienced the first dredge up episode, but this only occurs for  $M < 3 M_{\odot}$  and  $M < 2.5 M_{\odot}$  when  $Z=0.001$  and  $Z=0.0001$ , respectively ([21], [49]). After the FDU, the star climbs along the RGB up to the tip and a violent off-center He-flash develops (see Fig. 4.4): when the electronic degeneration is removed, a strong thermonuclear runaway develops, whose luminosity is more than  $3 \times 10^9 L_{\odot}$ . After a couple of weaker flashes,

the core He-burning starts (blue loop in the HR diagram of Fig. 4.2). In Table 4.1 we

$Z$	$\Delta t_{\text{H}}$	$M^{cc}$	$\text{He}_{\text{FDU}}$	$\log L_{\text{tip}}^{\text{RGB}}$	$M_{\text{H}}^{\text{ini}}$	$\Delta t_{\text{He}}$	$M_{\text{H}}^{\text{end}}$
$1.5 \times 10^{-2}$	1008	0.293	0.281	3.365	0.470	111	0.521
$1 \times 10^{-3}$	644	0.365	0.263	3.119	0.454	100	0.587
$1 \times 10^{-4}$	562	0.386	0.269	2.560	0.369	121	0.620

Table 4.1 Properties of the pre-AGB phase of  $M = 2 M_{\odot}$  models with different metallicities (see Table 3.1 for the adopted initial abundances). We refer to Chapter 7 for details about their AGB phase.

report the fundamental properties of the evolutionary sequences (up to core He-burning) for 3 different models with the same initial mass ( $M=2M_{\odot}$ ) and different metallicities ( $Z=Z_{\odot}$ ,  $Z=\times 10^{-3}$  and  $Z=1 \times 10^{-4}$ ). We tabulate, by column, the following quantities: (1) the model metallicity, (2) the core H-burning lifetime (in Myr), (3) the maximum size of the convective core during central H burning, (4) the surface He mass fraction after the FDU, (5) the tip luminosity of the first RGB (in solar luminosities), (6) the mass of the H-exhausted core at the beginning of the He core burning, (7) the core He-burning lifetime (in Myr) and (8) the mass of the H-exhausted core at the end of the core He burning. All masses are in solar masses units.

In stars less massive than  $\sim 10 M_{\odot}$ , central He burning leaves a compact C-O core. After He exhaustion, the central density rapidly increases (above  $10^5$  and up to  $10^8$  g/cm $^{-3}$ ), electrons become highly degenerate and a huge energy loss by plasma neutrinos takes place. The neutrino energy depletion is only partially supplied by the release of gravitational energy from the core contraction, and the thermal content of the core is used to balance the deficit. The resulting cooling starts from the center, where the density is higher, and the maximum temperature moves progressively outward. It exists a maximum mass, called  $M_{\text{up}}$ , for which the whole core cools down, a fact that prevents carbon ignition. The precise value of  $M_{\text{up}}$  depends on the chemical composition: it is  $\sim 7 M_{\odot}$  for population I stars (of nearly solar composition) and for very metal-poor stars (population III), while it is smaller ( $\sim 6 M_{\odot}$ ) for population II (halo) stars. Stars with mass slightly larger than  $M_{\text{up}}$  suffer a violent carbon ignition in degenerate condition ([48], [137]). Stars with smaller mass enter the TP-AGB phase (see [49] for an updated presentation of the pre-AGB evolution).

During the first part of the Asymptotic Giant Branch (called early-AGB), the He shell burning progressively moves outward and the mass of the C-O core increases. In low mass stars, the H burning maintains an entropy barrier that limits the internal boundary of the

external convective layer. In contrast, in massive AGB stars, owing to the huge energy flux coming out from the He burning zone, the base of the H-rich envelope expands and cools, so that the H burning dies down. In this case, the external convection penetrates inward, within the H-depleted zone. This is the second dredge up (SDU), found in stellar models with  $M > 3\text{--}5 M_{\odot}$ , depending on the chemical composition<sup>1</sup>. As a consequence of the SDU, a further increase of the surface abundances of helium and nitrogen is expected in massive AGBs. In addition, the SDU reduces the H-depleted region and prevents the formation of massive white dwarfs.

Finally, when the He burning shell gets closer to the H/He discontinuity, it dies down and, after a rapid contraction, the H burning shell fully supplies the surface energy loss.

### 4.3 Thermally pulsing AGB

The temporary stop of the He burning shell marks the beginning of the TP-AGB phase. The first thermal pulse occurs when the H burning shell accumulates enough He below it, so that the He-rich zone is compressed and heated, and He reignites. Despite the degree of electron degeneracy of the He-rich material is weak, a thermonuclear runaway occurs, because the thermodynamical time scale needed to locally expand the gas is much longer than the nuclear burning time scale of the  $3\alpha$  reaction [144]. Owing to the fast release of nuclear energy, the local temperature increases and the He burning luminosity blows up, in extreme cases to  $10^9 L_{\odot}$ . The thermonuclear runaway drives the formation of a convective zone that extends from the region of the He burning to the H/He discontinuity (see Figure 4.5). At the base of this convective shell an incomplete He burning takes place and the products of the  $3\alpha$  reaction (essentially carbon) are mixed over the whole intershell. At the quenching of a thermal instability, the resulting mass fraction of C in the top layer of the He intershell is  $X(^{12}\text{C}) \sim 0.25$ . When the expansion has progressed far enough, the temperature of the He shell decreases and a quiescent He burning phase begins. The variations of the H and He burning luminosities for the  $2 M_{\odot}$  model with  $Z = Z_{\odot}$  are reported in Figure 4.6. The expansion powered by the thermal instability pushes outward the layers of material located above the He burning shell. The temperature and the density at the base of the H-rich envelope decrease and the H burning shell dies down. In these conditions, a TDU episode is strongly favored. Indeed, at the interface between the envelope and the mantel, owing to the large energy flux coming from below,

---

<sup>1</sup>the lower the metallicity, the smaller the minimum mass for the occurrence of the second dredge up.

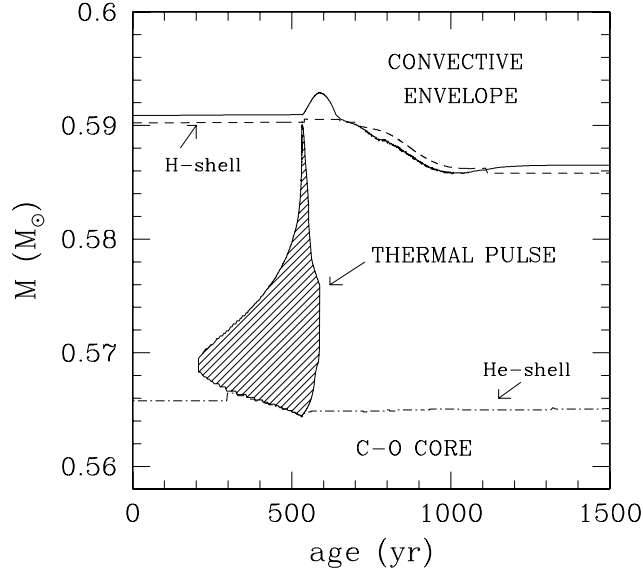


Figure 4.5 Convective episode (dashed area) in the  $M = 2 M_{\odot}$  model with solar metallicity, during and after the 6<sup>th</sup> TP followed by TDU. Note how the convective zone generated by the TP covers the whole He intershell. After about 200 years, the external convection penetrates inward (TDU).

the local temperature gradient increases. On the other hand, due to the low density, the ratio of the gas pressure to the radiation pressure decreases and the adiabatic temperature gradient approaches its minimum allowed value for a fully ionized gas plus radiation (i.e.  $(d\log T/d\log P)_{ad} = 0.25$ ). Then the Schwarzschild criterion for the convective instability (see Section 3.2) is more easily fulfilled and the envelope may penetrate (in mass) within the He intershell. The propagation of the convective instability is self-sustained due to the increase of the local opacity that occurs because fresh H (high opacity) is brought by convection into the He-rich layers (low opacity). If the dredge up is deep enough to overlap the region previously mixed by the convective zone generated by the TP, helium, carbon and heavy s elements are brought to the surface. A C(N) star may eventually form as a consequence of a series of recurrent TDU episodes ([85], [111], [154]).

Between two subsequent pulses (interpulse phase), the H burning shell supplies the energy radiated by the stellar surface and the luminosity of the star basically depends on the mass of the H-exhausted core,  $M_H$ . In other words, a direct correlation exists between

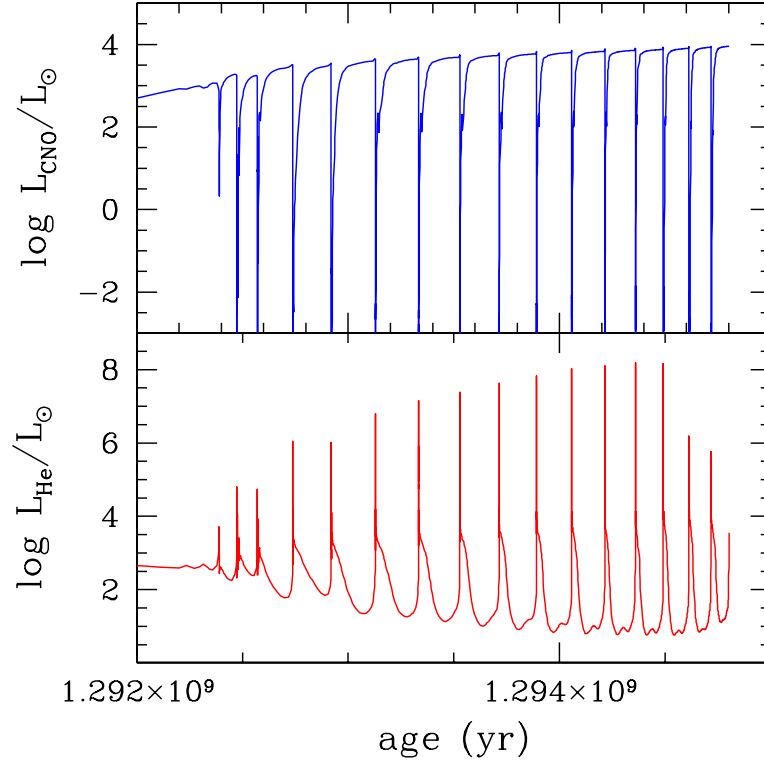


Figure 4.6 Thermally pulsing AGB evolution of the  $M = 2 M_{\odot}$  model with solar metallicity. Panel a): energy production rate of the H burning shell; Panel b): energy production rate of the He burning shell.

the core mass and the stellar luminosity ([123], [87])<sup>2</sup>. As the H burning shell advances in mass, the internal boundary of the convective envelope recedes, but always remains very close to the region where the thermonuclear reactions are switched on.

#### 4.4 The third dredge up

The products of the s-process nucleosynthesis as well as those of the He burning can be actually observed only if the TDU takes place. The TDU is driven by the expansion of the envelope powered by a thermal pulse. It is deeper when the strength of the pulse,

<sup>2</sup>The classical core mass-luminosity relation, as reported by [87], relates the maximum luminosity reached toward the end of the interpulse phase and the mass of the H-exhausted core, namely:  $L_{max} = 5.925 \times 10^4 (M_H - 0.495)$ .

as measured by the maximum luminosity attained by the He burning, is stronger. In principle, the strength of the pulse depends on temperature and density of the He-rich layer at the epoch of the ignition. The higher is the density and the temperature at He ignition, the stronger the thermal pulse is. For this reason, since He is accumulated by the thermonuclear fusion occurring in the H burning shell at the base of the envelope, the H burning rate is among the most important quantities regulating the physical conditions of the point where He ignites. It follows that the third dredge up is influenced by the parameters affecting the H-burning rate such as, in particular, the metallicity, the mass of the H-exhausted core and the mass of the envelope ([183], [87], [156]). As a general rule, a slower H burning implies a higher density of the He-rich layer and, therefore, a stronger TP ensues. Such an occurrence suggests a few important considerations:

i) along the AGB, the mass of H-depleted material that is dredged up in a single episode ( $\delta M_{\text{TDU}}$ ) initially increases, because the core mass increases, reaches a maximum and then decreases, when the mass loss erodes a substantial fraction of the envelope;

ii) for given core and envelope masses, the TDU is deeper in low metallicity stars, because the H burning is less efficient (see Chapter 7);

iii) there is a minimum envelope mass for which the TDU takes place. This minimum depends on the core mass and on the chemical composition of the envelope; we found that the TDU ceases when the envelope mass becomes smaller than  $0.3 \div 0.5 M_{\odot}$  [156] (see Chapter 7). This implies that in stars of initial mass below a given threshold ( $M < 1.2 M_{\odot}$ ), the residual envelope mass at the beginning of the thermally pulsing AGB is already too small and the TDU cannot take place. As a matter of fact, AGB stars belonging to the Galactic Globular Clusters, whose initial mass are of the order of  $0.8 - 0.9 M_{\odot}$ , do not show the enhancement of C and s-elements, which is the signature of the TDU [151]. Similarly, at variance with their metal-rich disk counterparts, halo post-AGB stars do not show any significant enhancement of the s-elements [63].

## 4.5 Mass loss

During the AGB, the star may become unstable against large amplitude pulsations. Pulsations induce a compression of the gas and the resulting increase of the density of the cool atmospheric layers favors the formation of complex molecules and dust grains, which trap the outgoing radiation flux driving a strong wind. Mass loss could also be influenced by the environment, as in close binary systems or in crowded stellar populations, like the central

region of Globular Clusters. Mass loss erodes the envelope causing important changes in the stellar properties. The duration of the AGB, the strength of the pulse, the efficiency of the TDU are a few examples of the quantities affected by the mass loss. The correct evaluation of the mass loss rate is also required to estimate the degree of chemical pollution of the interstellar medium ascribed to AGB stars.

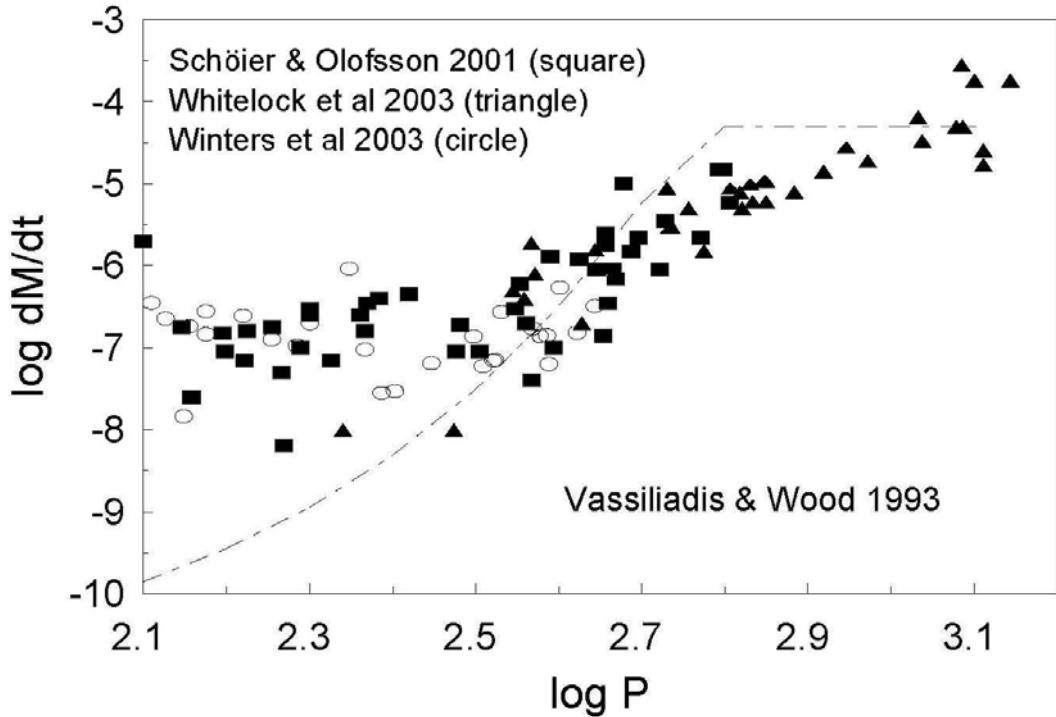


Figure 4.7 Mass loss rates versus period measurements (symbols) compared with the prescription proposed by [167] (line).

The AGB mass loss rate may be estimated from infrared color indices or from molecular CO rotational lines measurements. The available data indicate that it ranges between  $10^{-8}$  and  $10^{-4} M_{\odot}/\text{yr}$ . In variable AGB stars, the larger the period the larger the mass loss is. No other correlations between mass loss and stellar parameters (luminosity, mass, composition) have been clearly identified (see e.g. [178]). The poor knowledge of the actual mass loss rate is one of the major uncertainties of AGB stellar models. Much effort has been devoted to derive a suitable prescription for this phenomenon to be used

in calculations of AGB evolutionary models. The Reimers' formula<sup>3</sup> was introduced to describe the mass loss in population II red giants [132] and the  $\eta$  parameter was calibrated according to the luminosity and color distribution of bright globular clusters stars ( $\eta \sim 0.4$ , [134]). Unfortunately an equally stringent constraint for the calibration of the mass loss rate in AGB stars is lacking. In principle, the mass loss rate may be adjusted in order to reproduce the observed luminosity functions of the AGB stellar population, or that of a sub-sample of AGBs, like the C(N)-stars. Another important constraint can be derived from the initial to final mass relation [177]. On the basis of synthetic AGB models, [71] suggested that a Reimers' mass loss formula, with the parameter  $\eta = 5$ , provides a suitable reproduction of these observational constraints. Their method, however, only indicates the average mass loss rate, whereas the mass loss history remains largely unknown. Indeed [72] showed how different mass loss prescriptions may equally fulfil the same constraints. Our tests, which make use of detailed stellar models to reproduce similar observational constraints, show that the mass loss rate suggested by [71] may be adequate only for the more massive and/or more evolved AGB stars, but in low mass AGBs it is definitely too high.

A possible alternative method to estimate the mass loss rate is based on the observed correlation with the pulsational period [167]. Since the evolution of the pulsational period depends on the variations of radius, luminosity and mass, this relation provides a simple method to estimate the evolution of the total stellar mass from basic stellar parameters. In Figure 4.7 we collected data for the mass loss rate versus period, as measured by various authors for O-rich ([180], open circles) and C-rich ([178],[142], triangles and squares) AGB stars. Beside the evident spread of the data, three different regimes can be recognized:

- i)  $P < 300$  days: moderate mass loss (roughly between  $10^{-8}$  and  $3 \times 10^{-7} M_{\odot}/\text{yr}$ );
- ii)  $300 < P < 1000$  days: exponential increase of the mass loss;
- iii)  $P > 1000$  days: the mass loss approaches a maximum ( $\sim 5 \times 10^{-5} M_{\odot}/\text{yr}$ ), which roughly coincides with the expected radiation-pressure-driven limit [167].

The dot-dashed line in the figure represents the prescription proposed by [167]. It clearly underestimates the mass loss rate of short period variables, whilst for  $P$  ranging between 500 and 1000 days the mass loss appears too high by an order of magnitude. Thus, we have worked out a new relation, which provides a better calibration of the mass loss-period relation, namely:

---

<sup>3</sup> $\dot{M}(M_{\odot}/\text{yr}) = 1.34 \times 10^{-5} \cdot \eta \cdot \frac{L^{\frac{3}{2}}}{M \cdot T_{\text{eff}}^2}$ , where  $L$  and  $M$  are in solar units and the  $L$  effective temperature in K.

- for  $\log P < 2.5$

$$\dot{M} = 1.34 \times 10^{-5} \cdot \eta \cdot \frac{L^{\frac{3}{2}}}{M \cdot T_{\text{eff}}^2} (\eta = 0.4) ;$$

- for  $2.5 \leq \log P \leq 3.1$

$$\dot{M} = \max \left\{ \begin{array}{l} 1.34 \times 10^{-5} \cdot \eta \cdot \frac{L^{\frac{3}{2}}}{M \cdot T_{\text{eff}}^2} (\eta = 0.4) \\ 10^{[-101.6 + 63.26 \cdot \log P - 10.282 \cdot (\log P)^2]} \end{array} \right. ;$$

- for  $\log P > 3.1$

$$\dot{M} = 5 \times 10^{-5} .$$

According to long period variables data [73], we derive the pulsational period for the model by using the period- $M_K$  relation proposed by [178]. The bolometric corrections (needed to calculate  $M_K$ ) are estimated by adopting the temperature- $M_K$  relation calculated by [53] by fitting spectra of very bright M-giant stars in the Solar neighborhood. This prescription

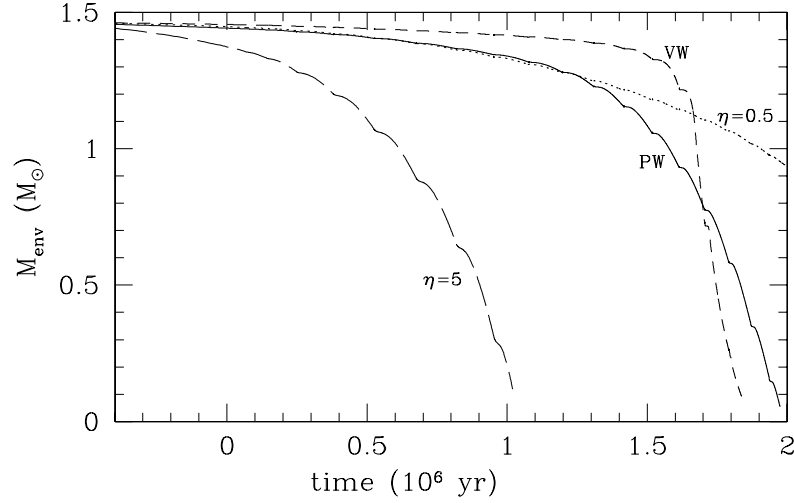


Figure 4.8 Variation versus time of the envelope mass according to different mass loss prescriptions (see text), for an AGB model of initial mass  $M = 2 M_{\odot}$  with solar metallicity.

has been used in our latest calculations of low mass AGB stellar models (see Section 7.1, Section 7.2 and the discussion at the end of Section 8.1). In Figure 4.5 we report the evolution of the envelope mass ( $M_{\text{env}}$ ) of a  $2 M_{\odot}$  AGB stellar model, as obtained under different prescriptions for the mass loss, namely: Reimers ( $\eta = 5$ ), Reimers ( $\eta = 0.5$ ),

Vassiliadis & Wood (VW) and our new calibration of the mass loss-period relation (PW). The 0 of the temporal scale corresponds to the beginning of the TP-AGB phase. Note how the mass loss history depends on the rate prescription. While the Reimers' formula provides a constant increase of the mass loss, the Vassiliadis and Wood rate leads to a negligible mass loss for the major part of the AGB evolution, with a sudden increase to the radiation-pressure-driven limit toward the end. Our prescription resembles a moderate Reimers' ( $\eta = 0.5$ ) mass loss rate for the first 1.2 Myr and switches to the stronger  $\eta = 5$  in the late TP-AGB phase. Note how the different prescriptions affect the duration of the AGB and, in turn, the AGB luminosity function and the estimated contribution of AGB stars to the Galactic chemical evolution. Finally, let us stress that in the observational sample used to calibrate the mass loss rate no indication about the star's metallicity is present: we therefore lack of a reliable mass loss estimate at low metallicities. In order to fill the gap, we follow prescriptions from [22], who consider the shift of the superwind effect to higher luminosity in very low metallicity variable stars.

## Chapter 5

# The nuclear network

*In this Chapter we present the nuclear network adopted in the framework of the FRANEC code: we currently follow the nucleosynthesis of about 500 isotopes (from H to the Pb-Bi-Po ending point) linked by more than 750 reactions. This network, the same already used in the post-process calculations [59], is continuously upgraded according to the latest theoretical and experimental nuclear physics improvements.*

The simultaneous solution of the stellar structure equations and a full network including all the relevant isotopes up to the termination point of the s-process path (Pb-Bi) requires a relevant computational power. For this reason, a post-process nucleosynthesis calculation, based on AGB stellar models computed with a restricted nuclear network, was generally preferred. In spite of these limitations, this approach provided a very important improvement with respect to prior calculations, based on the so-called classical analysis of the s process (see discussion in [10]). The coupling of a stellar code with a complete nuclear network has not been feasible so far, but this limitation has been overcome thanks to last computer generations. AGB model presented in this work are therefore calculated by using an extended set of nuclear processes including all chemical species involved in the s-process nucleosynthesis. In the following Sections we summarize the reactions inserted in the network, by describing our choices and by listing the adopted references.

## 5.1 Charged particle capture reactions

Reaction rates of isotopes involving charged particles are generally taken from the NACRE compilation [8]. For those reactions not included in that database, we use the rates tabulated by [33] and [127], with some exceptions (see Table 5.1 for a complete list of the adopted reaction rates). In Fig. 5.1 we report a section of the nuclear database in the

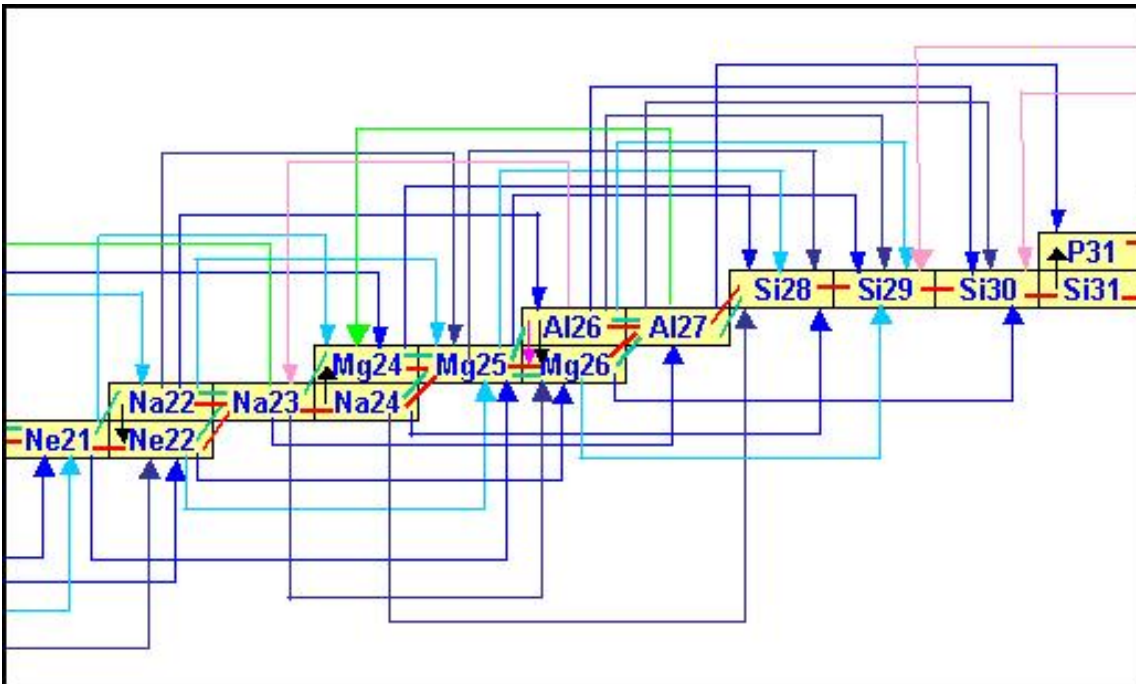


Figure 5.1 Nuclear network section in the Na-Mg-Al region.

Na-Mg-Al region. Nuclear processes are represented with different colors; weak interactions are plotted as black arrows.

Between charged particle reactions, the choice of the  $^{14}\text{N}(p,\gamma)^{15}\text{O}$  is of particular importance. In our network, we use the result of the recent measurement obtained by the LUNA collaboration [88]. Being the bottleneck of the CNO cycle, this reaction regulates the He deposition on the intershell of an AGB star and in turn affects the pulse strength and the efficiency of the TDU (see the discussion in section 4.4). The new low energy astrophysical factor ( $S(0)=1.7$  MeV barn) is about 40% lower than that suggested by NACRE.

### 5.1.1 Neutron sources

A subthreshold resonance makes difficult the low energy extrapolation of the  $^{13}\text{C}(\alpha, n)^{16}\text{O}$  reaction rate. We adopt the rate suggested by [51]. We also investigate the effects of different rates ([106], [8]) and we find a negligible modification of the final surface isotopic distribution. In Section 9.1 we give details concerning this test.

The  $^{22}\text{Ne}(\alpha, n)^{25}\text{Mg}$  rate is even more complex, owing to the possible existence of unknown low energy resonances [105]. We adopt the value suggested by [93].

## 5.2 Neutron capture reactions

Neutron captures belong to the two body  $i + j \longrightarrow k + l$  reaction class ( $i$  represents the seed nucleus,  $j$  the neutron,  $k$  is the newly synthesized  $A+1$  nucleus and  $l$  a  $\gamma$ -ray). Labeling as  $N_{pair}$  the pair number  $i$ - $j$ , it results

$$N_{pair} = \frac{N_i N_j}{n_i! n_j!} = \frac{N_i N_j}{1 + \delta_{ij}} , \quad (5.1)$$

(where  $n_i$  is the particle number of element  $i$  involved in the reaction). Defining  $N(v)dv$  as the neutron-nucleus pairs whose relative velocity is between  $v$  and  $v + dv$ , the number of reactions per time unit and per nucleus  $A$  is

$$N_{reactions} = \int N(v) \sigma v dv , \quad (5.2)$$

being  $\sigma$  the radiative neutron cross section. If we define  $\tilde{n}(v) = \frac{N(v)}{N_{pair}}$ , under the assumption that

$$\int \tilde{n}(v) dv = 1 , \quad (5.3)$$

we obtain

$$N_{reactions} = N_{pair} \int_0^{+\infty} \tilde{n}(v) \sigma v dv , \quad (5.4)$$

or (in astrophysical notation)

$$N_{reactions} = N_{pair} \langle \sigma v \rangle_{ij} . \quad (5.5)$$

Being

$$\frac{N_i}{V} = \rho N_{Av} \frac{X_i}{A_i}, \quad (5.6)$$

and indicating with  $Y_i = \frac{X_i}{A_i}$  the number fractions and with  $N_{Av}$  the Avogadro's number, the reactions number per time unit and per mass unit is:

$$R_{ij} = \frac{Y_i Y_j}{N_i! N_j!} N_{Av}^2 \rho < \sigma v >_{ij}. \quad (5.7)$$

With  $n$ -capture reactions we mean  $(n, \gamma)$ ,  $(n, \alpha)$  and  $(n, p)$  processes. For the  $(n, \gamma)$  reactions, we adopt, as reference compilation, the recommended rates by [12] (hereafter BK2000). In that paper, experimental and theoretical data are critically revised and the reaction rates are listed as a function of the thermal energy from 5 to 100 keV. We recall that the typical thermal energy at which the  $s$ -process nucleosynthesis occurs in AGB stars are 8 keV for the  $^{13}\text{C}(\alpha, n)^{16}\text{O}$  reaction and 23 keV for the  $^{22}\text{Ne}(\alpha, n)^{25}\text{Mg}$  reaction. For the few reactions not included in BK2000, we use the theoretical calculations of [127].

Starting from this database, we have upgraded the network with the most recent experimental results. With regard to Si isotopes we refer to [76], Cl isotopes to [75],  $^{60}\text{Ni}$  to [43],  $^{62}\text{Ni}$  to [128],  $^{88}\text{Sr}$  to [103], Kr isotopes to [60], Xe isotopes to [130], Cd isotopes to [181], Cs isotopes to [124],  $^{139}\text{La}$  to [121], Pm isotopes to [131],  $^{151}\text{Sm}$  to [2], Eu isotopes to [17] and finally Pt isotopes to [104]. The rates of  $(n, \alpha)$  and  $(n, p)$  reactions involving heavy isotopes are taken from RT2000. We adopt the  $(n, \alpha)$  and  $(n, p)$  rates on light isotopes from various authors. In particular: the  $^{14}\text{N}(n, p)^{14}\text{C}$  is taken from [101], the  $^{17}\text{O}(n, \alpha)^{14}\text{C}$  from [171], the  $^{26}\text{Al}(n, p)^{26}\text{Mg}$  from [102], the  $^{26}\text{Al}(n, \alpha)^{23}\text{Na}$  from [170] and the  $^{33}\text{S}(n, \alpha)^{30}\text{Si}$  from [141]. The  $^{35}\text{Cl}(n, p)^{35}\text{S}$  rate has been derived from [52], the  $^{36}\text{Cl}(n, p)^{36}\text{S}$  and the  $^{36}\text{Cl}(n, \alpha)^{33}\text{P}$  from [169], the  $^{37}\text{Ar}(n, p)^{37}\text{Cl}$  and the  $^{37}\text{Ar}(n, \alpha)^{34}\text{S}$  from [64]. The  $^{39}\text{Ar}(n, \alpha)^{36}\text{S}$  is from [65], while the  $^{41}\text{Ca}(n, p)^{41}\text{K}$  and the  $^{41}\text{Ca}(n, \alpha)^{38}\text{Ar}$  rates are from [168]. In Fig. 5.2 we report three network sections around magic nuclei, corresponding to the  $s$ -process bottlenecks (see Chapter 2): with respect to Fig. 5.1, only neutron capture processes (red lines) and weak interactions (black arrows) appear. At the  $s$ -process ending point (i.e. in the Pb-Bi region)  $\alpha$  decays start being efficient.

### 5.3 $\beta$ decay reactions

During  $s$ -process nucleosynthesis, main competitors to neutron captures are  $\beta$  decays and electronic captures:

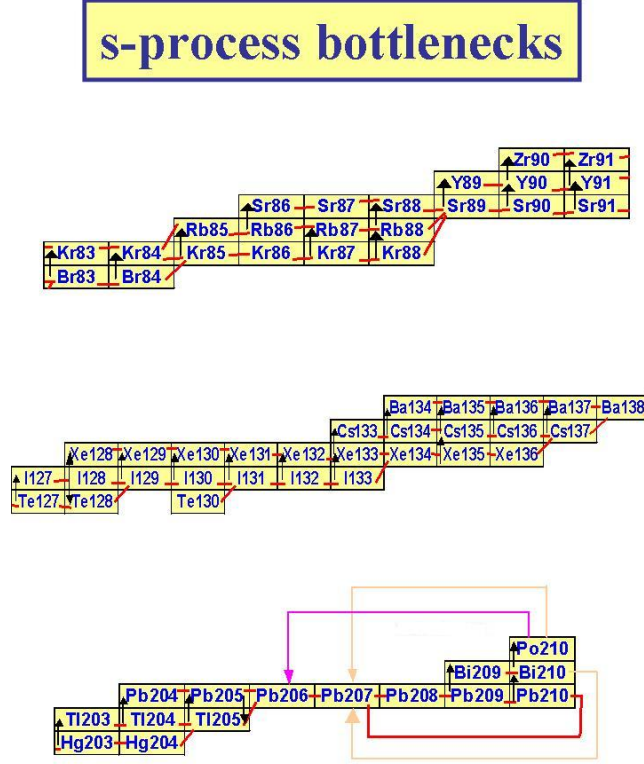


Figure 5.2 Nuclear network sections around magic number nuclei.

$$N_A(Z, N) \xrightarrow{\beta^-} N_A(Z + 1, N - 1) + e^- + \bar{\nu}_e, \quad (5.8)$$

$$N_A(Z, N) \xrightarrow{\beta^+} N_A(Z - 1, N + 1) + e^+ + \nu_e. \quad (5.9)$$

$$N_A(Z, N) + e^- \xrightarrow{\beta^+} N_A(Z - 1, N + 1) + \nu_e. \quad (5.10)$$

Labeling as  $N_i$  the particle number suffering a  $\beta$  decay and with  $\lambda_i = \frac{1}{\tau_i}$  their decay probability ( $\tau_i$  is their half time), at the time t the surviving particle number is

$$N_i(t) = N_i(0) \exp -(\lambda_i t), \quad (5.11)$$

while the per second decay is

$$A = \left| \frac{dN_i}{dt} \right| = N_i \lambda_i. \quad (5.12)$$

The  $\beta$  decay rate is then:

$$R_i = N_{Av} Y_i \lambda_i . \quad (5.13)$$

Weak interaction rates (electron captures, and  $\beta$  decays) are interpolated as a function of the temperature and electron density. At temperatures lower than  $10^6$  K we assume a constant value equal to the terrestrial one. For isotopes up to  $^{37}\text{Ar}$ , data have been taken from [122], with the exception of  $^7\text{Be}$  [33] and the isomeric state of  $^{26}\text{Al}$ , for which we refer to [41]. Concerning the unstable isotopes between  $^{39}\text{Ar}$  and  $^{45}\text{Ca}$  we use prescriptions by [57], while between  $^{45}\text{Ca}$  and  $^{64}\text{Cu}$  (excluding  $^{63}\text{Ni}$ ) we follow [109]. For  $^{63}\text{Ni}$  and heavier isotopes we use the rates tabulated in [160], with the exceptions of  $^{79}\text{Se}$  and  $^{176}\text{Lu}$ , for which we refer respectively to [99] and [100]. For the few rates not included in any compilation, we use the terrestrial value.

If the  $\beta$  decay rate is comparable with the neutron capture one, in the  $s$ -process appear a branching, whose treatment results very difficult, considered the eventual dependencies on temperature and neutron density. It is therefore extremely important to know the branching factor, given by:

$$f_- = \frac{\lambda_\beta}{\lambda_\beta + \lambda_n} , \quad (5.14)$$

where  $\lambda_\beta = \frac{\ln 2}{t_{\frac{1}{2}}}$  is the  $\beta$  decay rate ( $t_{\frac{1}{2}}$  represents the isotope half time) and  $\lambda_n$  the neutron capture rate:  $\lambda_n = n_n \sigma v_T$ .

## 5.4 Isomeric states

Isomeric states are excited levels having a lifetime largely longer than a normal excited level. The existence of isomeric states of unthermalized isotopes leads to ramifications of the  $s$ -process flux ([174], [175]). In particular, branching points originated by the isomeric state of  $^{26}\text{Al}$ ,  $^{85}\text{Kr}$ ,  $^{176}\text{Lu}$  and  $^{180}\text{Ta}$  require particular attention.

Concerning  $^{26}\text{Al}$ , the proton capture on  $^{25}\text{Mg}$  is split in two distinct reactions: the first produces the ground state  $^{26}\text{Al}^g$  (with terrestrial half life  $T_{1/2} = 7.16 \times 10^5$  yr) and the second creates the isomer  $^{26}\text{Al}^m$  that almost instantaneously decays into  $^{26}\text{Mg}$ . Therefore, the isomeric state  $^{26}\text{Al}^m$  and the ground state  $^{26}\text{Al}^g$  have to be treated as separate particles, if not thermalised.

Concerning  $^{85}\text{Kr}$  (see Fig. 5.3) ground and isomeric states result completely independent if the neutron density  $n_n > 10^7 \text{ cm}^{-3}$ : it is then necessary to treat isomeric and

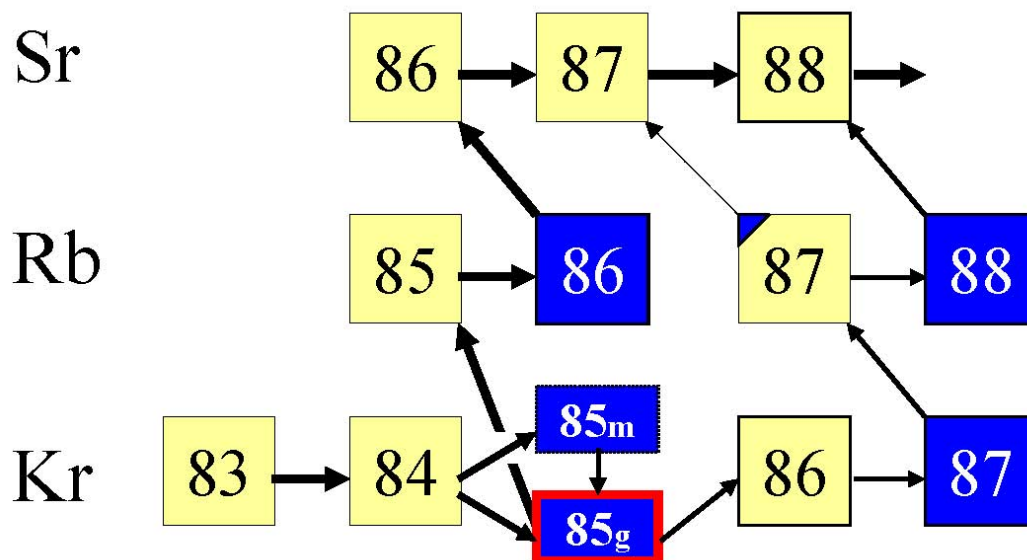


Figure 5.3 Nuclear processes active in the region of krypton isotopes (in yellow stable isotopes, in blue the unstable ones).

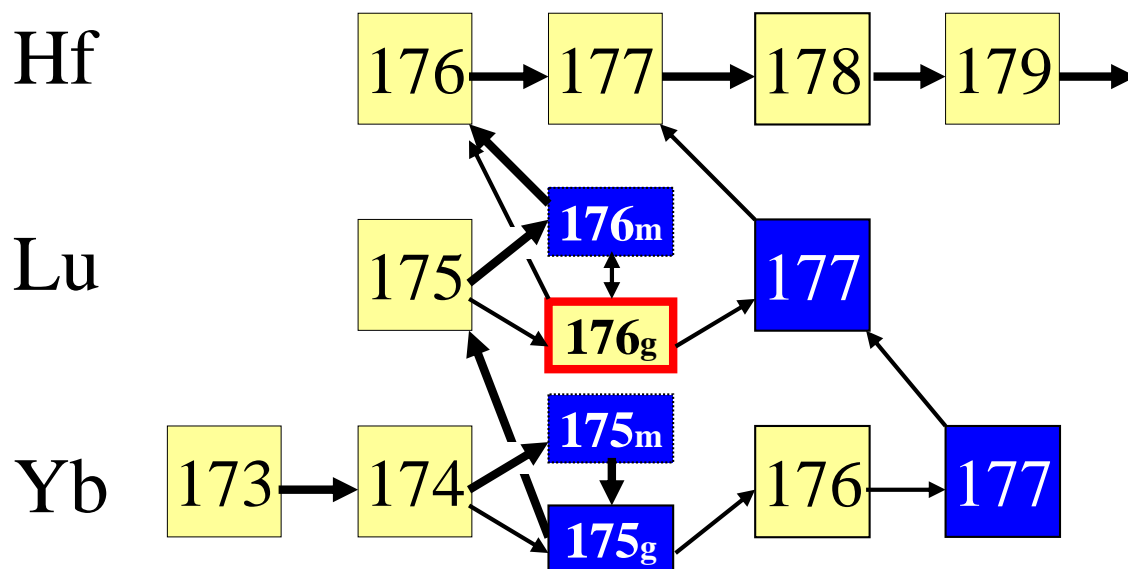


Figure 5.4 Nuclear processes active in the region of lutetium isotopes (in yellow stable isotopes, in blue the unstable ones).

ground states as two separate isotopes. The neutron capture of  $^{84}\text{Kr}$  to  $^{85}\text{Kr}^m$  has a 50% probability with respect the total cross section (at 30 keV, [15]).  $^{85}\text{Kr}^m$  has a non-zero probability to decay by internal conversion to its ground state (of 20%), thus leading to the following isomeric ratio (IR):

$$IR = \frac{\sigma(^{84}\text{Kr}(n, \gamma)^{85}\text{Kr}^m)}{\sigma_{tot}(^{84}\text{Kr}(n, \gamma)^{85}\text{Kr})} = 0.42 . \quad (5.15)$$

Note that the  $\beta^-$  half life of  $^{85}\text{Kr}^m$  is 4.48 h, while that of  $^{85}\text{Kr}^g$  is 10.76 yr.

The situation in the (Yb,Lu,Hf) region is even more complex, but it represents a sensitive s-process thermometer because of the presence of two s-only isotopes ( $^{176}\text{Lu}$  and  $^{176}\text{Hf}$ ), shielded against the r-process  $\beta$  decay chain by their stable isobar  $^{176}\text{Yb}$  (see Fig. 5.4). Isomeric and ground state interact by thermally induced transitions, depending on the stellar environment temperature: around  $3 \times 10^8$  K an enhanced feeding of the ground state is expected [182].

We adopt this isomeric ratio:

$$IR = \frac{\sigma(^{175}\text{Lu}(n, \gamma)^{176}\text{Lu}^m)}{\sigma_{tot}(^{175}\text{Lu}(n, \gamma)^{176}\text{Lu})} = 0.2, \quad (5.16)$$

with the exception of a restricted temperature range ( $2.3 \times 10^8 < T < 4.6 \times 10^8$ ), where we assumed an effective IR=0.25 (Gallino R., *private communication*). A detailed analysis of this branching using new experimental determinations of IR( $^{176}\text{Lu}$ ) is underway (Gallino R., *private communication*).

Finally, for the complex treatment of the branching between isomeric and ground state of  $^{180}\text{Ta}$ , we refer to [119].

$\text{H}(p,\nu)^2\text{H}$	[8]	$^{19}\text{F}(\alpha,p)^{22}\text{Ne}$	[164]
$^2\text{H}(p,\gamma)^3\text{He}$	[8]	$^{19}\text{F}(\alpha,n)^{22}\text{Na}$	[33]
$^3\text{He}(^3\text{He},\alpha)2\text{H}$	[8]	$^{20}\text{Ne}(p,\gamma)^{21}\text{Na}$	[8]
$^3\text{He}(\alpha,\gamma)^7\text{Be}$	[8]	$^{20}\text{Ne}(\alpha,\gamma)^{24}\text{Mg}$	[8]
$^4\text{He}(\alpha,\alpha)^{12}\text{C}$	[33]	$^{21}\text{Ne}(p,\gamma)^{22}\text{Na}$	[8]
$^6\text{Li}(p,\gamma)^7\text{Be}$	[8]	$^{21}\text{Ne}(\alpha,\gamma)^{25}\text{Mg}$	[33]
$^6\text{Li}(p,^3\text{He})^4\text{He}$	[8]	$^{21}\text{Ne}(\alpha,n)^{24}\text{Mg}$	[8]
$^7\text{Li}(p,\alpha)^4\text{He}$	[8]	$^{22}\text{Ne}(p,\gamma)^{23}\text{Na}$	[8]
$^7\text{Be}(p,\gamma)^8\text{B}$	[8]	$^{22}\text{Ne}(\alpha,n)^{25}\text{Mg}$	[93]
$^9\text{Be}(p,\gamma)^{10}\text{B}$	[8]	$^{22}\text{Ne}(\alpha,\gamma)^{26}\text{Mg}$	[96]
$^9\text{Be}(p,\alpha)^6\text{Li}$	[8]	$^{22}\text{Na}(p,\gamma)^{23}\text{Mg}$	[8]
$^{10}\text{B}(p,\gamma)^{11}\text{C}$	[8]	$^{22}\text{Na}(\alpha,\gamma)^{26}\text{Al}_g$	[161]
$^{10}\text{B}(p,\alpha)^7\text{Be}$	[8]	$^{22}\text{Na}(\alpha,p)^{25}\text{Mg}$	[127]
$^{11}\text{B}(p,\gamma)^{12}\text{C}$	[8]	$^{22}\text{Na}(\alpha,n)^{25}\text{Al}$	[127]
$^{11}\text{B}(p,\alpha)^2^4\text{He}$	[8]	$^{23}\text{Na}(p,\gamma)^{24}\text{Mg}$	[8]
$^{12}\text{C}(p,\gamma)^{13}\text{N}$	[8]	$^{23}\text{Na}(\alpha,\gamma)^{27}\text{Al}$	[127]
$^{12}\text{C}(\alpha,\gamma)^{16}\text{O}$	[107]	$^{23}\text{Na}(\alpha,p)^{26}\text{Mg}$	[127]
$^{13}\text{C}(p,\gamma)^{14}\text{N}$	[8]	$^{23}\text{Na}(p,\alpha)^{20}\text{Ne}$	[8]
$^{13}\text{C}(\alpha,n)^{16}\text{O}$	[51]	$^{24}\text{Na}(p,\gamma)^{25}\text{Mg}$	[127]
$^{14}\text{C}(p,\gamma)^{15}\text{N}$	[33]	$^{24}\text{Na}(\alpha,\gamma)^{28}\text{Al}$	[127]
$^{14}\text{C}(\alpha,\gamma)^{18}\text{O}$	[33]	$^{24}\text{Na}(\alpha,p)^{27}\text{Mg}$	[127]
$^{14}\text{N}(p,\gamma)^{15}\text{O}$	[88]	$^{24}\text{Mg}(p,\gamma)^{25}\text{Al}$	[8]
$^{14}\text{N}(\alpha,\gamma)^{18}\text{F}$	[67]	$^{24}\text{Mg}(\alpha,\gamma)^{28}\text{Si}$	[33]
$^{14}\text{N}(\alpha,p)^{17}\text{O}$	[33]	$^{25}\text{Mg}(p,\gamma)^{26}\text{Al}_g$	[8]
$^{15}\text{N}(p,\gamma)^{16}\text{O}$	[8]	$^{25}\text{Mg}(p,\gamma)^{26}\text{Al}_m$	[8]
$^{15}\text{N}(p,\alpha)^{12}\text{C}$	[8]	$^{25}\text{Mg}(\alpha,\gamma)^{29}\text{Si}$	[33]
$^{15}\text{N}(\alpha,\gamma)^{19}\text{F}$	[8]	$^{25}\text{Mg}(\alpha,p)^{28}\text{Al}$	[33]
$^{16}\text{O}(p,\gamma)^{17}\text{F}$	[8]	$^{25}\text{Mg}(\alpha,n)^{28}\text{Si}$	[8]
$^{16}\text{O}(\alpha,\gamma)^{20}\text{Ne}$	[8]	$^{26}\text{Mg}(p,\gamma)^{26}\text{Al}$	[8]
$^{17}\text{O}(p,\alpha)^{14}\text{N}$	[8]	$^{26}\text{Mg}(\alpha,\gamma)^{30}\text{Si}$	[33]
$^{17}\text{O}(p,\gamma)^{18}\text{F}$	[8]	$^{26}\text{Mg}(\alpha,n)^{29}\text{Si}$	[8]
$^{17}\text{O}(\alpha,\gamma)^{21}\text{Ne}$	[33]	$^{26}\text{Al}_g(p,\gamma)^{27}\text{Si}$	[8]
$^{17}\text{O}(\alpha,n)^{20}\text{Ne}$	[8]	$^{26}\text{Al}_g(\alpha,p)^{29}\text{Si}$	[161]
$^{18}\text{O}(p,\gamma)^{19}\text{F}$	[8]	$^{26}\text{Al}_g(\alpha,n)^{29}\text{P}$	[161]
$^{18}\text{O}(p,\alpha)^{15}\text{N}$	[8]	$^{26}\text{Al}_g(\alpha,\gamma)^{30}\text{P}$	[161]
$^{18}\text{O}(\alpha,\gamma)^{22}\text{Ne}$	[96]	$^{27}\text{Al}(p,\gamma)^{28}\text{Si}$	[8]
$^{18}\text{O}(\alpha,n)^{21}\text{Ne}$	[8]	$^{27}\text{Al}(p,\alpha)^{24}\text{Mg}$	[8]
$^{19}\text{F}(p,\gamma)^{20}\text{Ne}$	[8]	$^{27}\text{Al}(\alpha,\gamma)^{31}\text{P}$	[127]
$^{19}\text{F}(p,\alpha)^{16}\text{O}$	[8]	$^{27}\text{Al}(\alpha,p)^{30}\text{Si}$	[127]

Table 5.1 Charged particle reactions section of the FRANEC nuclear network.



## Chapter 6

### The formation of the $^{13}\text{C}$ pocket

*A major improvement in our stellar evolution code is the introduction of a physical algorithm for the treatment of the convective/radiative interfaces. In such a way we succeed to overcome the discontinuity in the thermal gradients that otherwise would result at the border of the H-rich convective envelope and the inner radiative C and He-rich intershell region. Furthermore, the partial diffusion of protons in the top layers of the He shell gives naturally rise to the subsequent formation of a  $^{13}\text{C}$ -rich tiny layer: the so-called  $^{13}\text{C}$  pocket. This pocket results partially overlapped with an outer  $^{14}\text{N}$  pocket, followed by a further minor  $^{23}\text{Na}$  pocket, both of primary origin. Moreover, we test the dependency of the newly introduced algorithm from the free parameter  $\beta$ , implicit in its formulation.*

As outlined in previous Chapters, in TP-AGBs two major neutron sources may operate within the intershell: the  $^{22}\text{Ne}(\alpha, n)^{25}\text{Mg}$  and the  $^{13}\text{C}(\alpha, n)^{16}\text{O}$  reactions.

The amount of  $^{14}\text{N}$  left by the H burning at the top of the intershell is practically equal to the sum of the abundances (by number) of the C-N-O in the envelope. During the early phase of the convective thermal pulse, the material within the intershell is fully mixed and the  $^{14}\text{N}$  is totally converted into  $^{22}\text{Ne}$  throughout the chain  $^{14}\text{N}(\alpha, \gamma)^{18}\text{F}(\beta^+ \nu)^{18}\text{O}(\alpha, \gamma)^{22}\text{Ne}$ . Near the peak of the thermonuclear runaway, if the temperature is high enough (i.e.  $\sim 3.5 \times 10^8$  K), the  $^{22}\text{Ne}(\alpha, n)^{25}\text{Mg}$  reaction may provide a significant neutron flux. Iben ([82]) first demonstrated that this condition is fulfilled in intermediate mass stars. Actually, in low mass stars ( $M < 3 M_{\odot}$ ), the temperature at the base of the convective zone generated by the TP barely attains  $3 \times 10^8$  K (see Tables 7.1, 7.3 and 7.4 in Chapter 7) and the  $^{22}\text{Ne}$  neutron source is marginally activated ([84], [154], [59]).

In low mass AGB stars, an alternative neutron source is provided by the  $^{13}\text{C}(\alpha, n)^{16}\text{O}$  reaction: its activation requires a substantially lower temperature, namely  $\sim 90 \times 10^6$  K, easily attained in the He intershell. Note that between two subsequent TPs, the H burning shell leaves some  $^{13}\text{C}$  in the upper region of the He-rich intershell. The burning of this  $^{13}\text{C}$ , however, produces a negligible neutron flux, even if, as a consequence of the TDU, the CNO in the envelope may grow up to 10 times the solar abundance. This occurs because, in the material processed by the CNO burning, the  $^{14}\text{N}$  is, in any case, two orders of magnitude more abundant than the  $^{13}\text{C}$ . In practice, all the neutrons released by the  $^{13}\text{C}$  left by the H burning are captured by the abundant  $^{14}\text{N}$ . Then, an alternative source of  $^{13}\text{C}$  is needed, in a zone where  $^{14}\text{N}$  is depleted. In nature,  $^{13}\text{C}$  is produced via  $^{12}\text{C}(p, \gamma)^{13}\text{N}(\beta^+ \nu)^{13}\text{C}$ . After each TP, the material within the He-rich intershell is plenty of  $^{12}\text{C}$  and all the  $^{14}\text{N}$  has been converted into  $^{22}\text{Ne}$ , but it is also H depleted. So, the problem is how to inject a few protons into the He-rich intershell.

Sackmann et al. [138] suggested that the convective zone generated by the thermal pulse could extend beyond the H/He discontinuity. In this case, protons are ingested downward, where the temperature is so high that the reaction chain  $^{12}\text{C}(p, \gamma)^{13}\text{N}(\beta^+ \nu)^{13}\text{C}(\alpha, n)^{16}\text{O}$  would release neutrons. Against this hypothesis, [83] argued that during the thermonuclear runaway the H burning shell remains active and generates an entropy barrier that prevents the penetration of the convective instability into the H-rich envelope. Extant AGB stellar models show that only in very metal-poor stars, owing to the lack of CNO, ingestion of protons in the convective pulse may occur ([56], [92], [157], [158]). More favorable conditions for the formation of a  $^{13}\text{C}$  pocket within the intershell are realized at the epoch of the TDU and during the so-called post-flash dip, the period that immediately follows the TDU [87]. Indeed, as a consequence of the TDU, a sharp discontinuity between the H-rich envelope and the He- and C-rich intershell forms. This condition is maintained until H burning is reignited. The time elapsed from the maximum penetration of the convective envelope and H reignition is about  $10^4$  yr (for a star of  $2 M_{\odot}$ ). During this period, different physical mechanisms may contribute to the downward diffusion of a few protons into the underlying radiative layer. In such a case, at H reignition the top layers of the He intershell heat up and a  $^{13}\text{C}$  pocket forms. Roughly speaking, the required mixing process must be able to diffuse about  $5 \times 10^{-5} M_{\odot}$  of H within a region as large as  $\sim 10^{-3} M_{\odot}$ . Note that an excess of protons must be avoided, because in that case the production of  $^{13}\text{C}$  is followed by the production of  $^{14}\text{N}$  (via  $^{13}\text{C}(p, \gamma)^{14}\text{N}$  reaction). Straniero et al. [153] demonstrated that the  $^{13}\text{C}$  formed in this way is fully consumed by the  $^{13}\text{C}(\alpha, n)^{16}\text{O}$  reaction in radiative

conditions during the interpulse phase, when the temperature reaches  $\sim 90 \times 10^6$  K, giving rise to a substantial neutron exposure with a maximum neutron density of  $10^7 \text{ cm}^{-3}$ . The expected s-process nucleosynthesis has been first calculated by [59].

## 6.1 The velocity profile algorithm

Among the various attempts to find the possible mechanism responsible for the formation of the  $^{13}\text{C}$  pocket, [85] evaluated the timescale of the atomic diffusion driven by the sharp composition gradient left by the penetrating convective envelope at the time of the TDU and concluded that this is a promising possibility to diffuse enough protons from the envelope into the He-rich intershell. More recently [79], inspired by hydrodynamical simulations

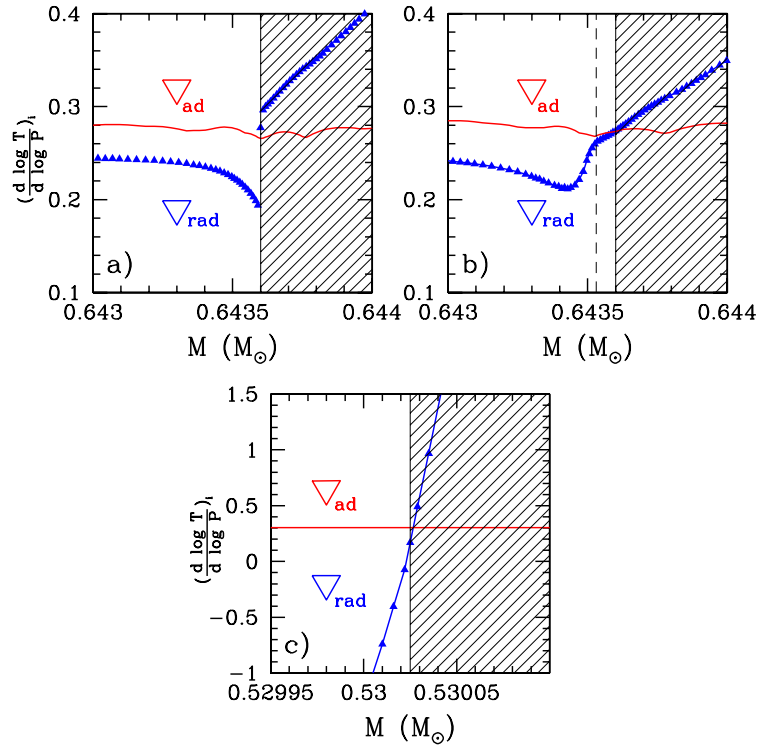


Figure 6.1 Radiative and adiabatic gradients at the inner border of the convective envelope during a TDU episode (Left Upper Panel: without velocity profile algorithm; Right Upper Panel: with velocity profile algorithm) and at the bottom of a convective He-shell during a TP (Lower Panel).

of [54], invoked mechanical overshoot of material from the bottom of the convective envelope into the underlying stable region. AGB models taking into account stellar rotation were calculated by [110] and a certain mixing of protons into the intershell at the epoch of the TDU was found. However, this rotationally induced mixing does not stop when the

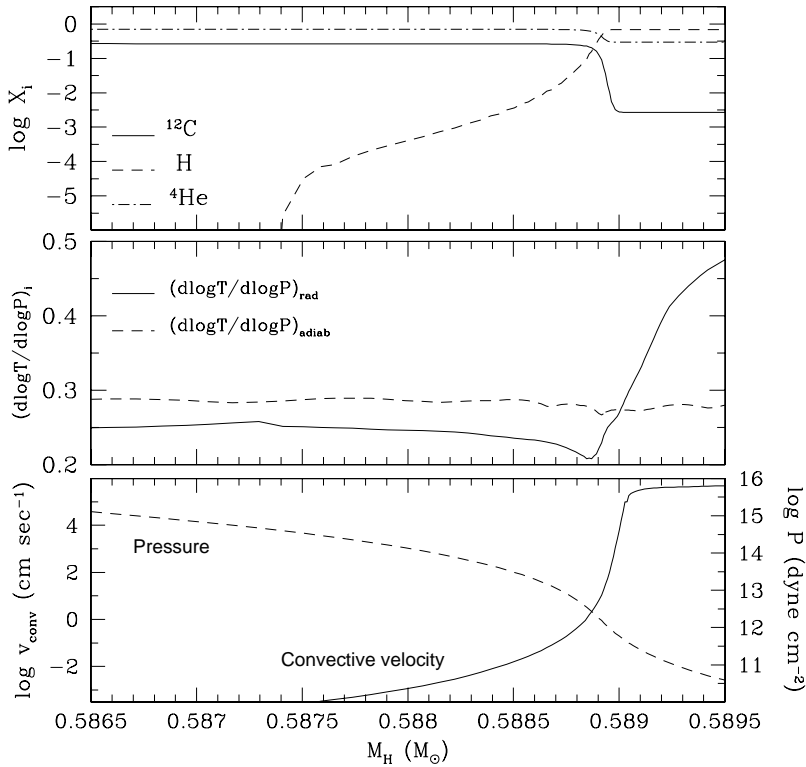


Figure 6.2 Chemical profile (upper Panel), temperature gradients (middle Panel), average velocity and pressure (lower Panel), in the region at the convective boundary during a TDU episode.

convective envelope recedes, but it continues during the interpulse period causing the contamination of the  $^{13}\text{C}$  pocket with too much  $^{14}\text{N}$ . Gravity waves have been investigated to explain the formation of the  $^{13}\text{C}$  pocket by [44], and [27] show that a magnetic field of  $10^8$  gauss, comparable with the one measured in white dwarfs, may induce a deep circulation below the convective envelope at the epoch of the TDU, allowing the required diffusion of protons into the intershell.

Owing to the lack of a reliable description of the physical phenomena that govern the

diffusion of protons into the He intershell, in the current AGB nucleosynthesis calculations the amount of  $^{13}\text{C}$  is assumed as free parameter (see [59]). In the model presented here we adopt a simple approach based on an argument early discussed by [14] (see also [31], [55]). When the TDU takes place, the opacity of the envelope (H-rich) is significantly larger than the opacity of the underlying H-exhausted (and He-rich) region. This fact causes an abrupt change of the temperature gradient at the inner border of the penetrating convective envelope. In this condition, the convective boundary becomes unstable, because any perturbation causing an excess of mixing immediately leads to an increase of the opacity and, in turn, to an increase of the temperature gradient. This occurrence favors a deeper penetration of the convective instability or, in other words, a deeper dredge up. A similar mechanism is responsible for the growth of the convective core during central He burning ([123], [30]). A different view of the same phenomenon concerns the evaluation of the average convective velocity. In the framework of the mixing length theory, this velocity is proportional to the difference between the radiative temperature gradient (i.e. the gradient necessary to carry out the total energy flux if convection would be inhibited) and the adiabatic temperature gradient. For this reason, the average convective velocity usually drops to 0 at the stable boundary of a convective layer, where the temperature gradient coincides with the adiabatic one. However, when convection penetrates in a region of lower opacity (this happens during a third dredge up episode), the difference between the actual temperature gradient and the adiabatic gradient grows above 0 and a positive average convective velocity is found at the inner border of the convective envelope, which, for this reason, becomes unstable. In principle, as soon as He is mixed with the envelope, the opacity and, in turn, the difference between the radiative and the adiabatic temperature gradients are reduced. However, the mass of the convective envelope is usually much larger than the amount of the dredged up material and the relaxing effect of the additional mixing is, in practice, negligible ([55], [32]). Then, a simple thermodynamic criterion cannot be used to determine the real extension of the convective instability. For sure, the steep pressure gradient that develops immediately below the formal border of the convective envelope limits the penetration of the instability, so that the average convective velocity should rapidly drop to 0. In order to mimic this behavior, we assume that in the region underlying the formal convective boundary, the average velocity follows an exponential decline, namely

$$v = v_{bce} \exp\left(-\frac{d}{\beta H_P}\right), \quad (6.1)$$

where  $d$  is the distance from the formal convective boundary,  $v_{bce}$  is the velocity of the most internal convective mesh,  $H_P$  is the pressure scale height at the formal border of the convective envelope (defined by the Schwarzschild criterion) and  $\beta$  is a free parameter. Note that this formula is similar to the "overshoot" proposed by [79]. However, in this case, since  $v_{bce}$  is usually 0, it produces a negligible amount of extra mixing, except during a dredge up. In Figure 6.1 we plot the radiative and the adiabatic gradients in two different evolutionary phases: panel a) and b) show the gradients at the inner border of the convective envelope during a TDU episode, while panel c) depicts the situation at the bottom of a convective shell generated by a TP. Model shown in panel a) has been calculated by simply applying the Schwarzschild criterion: the expected discontinuity in the radiative border clearly appears. This abrupt step in the radiative gradient results smoothed (panel b) if we use Formula 6.1 in calculating the convective velocities below the inner border of the convective envelope. In this case, the profile results smoothed, as a consequence of the diffused protons from the envelope, which enhance the opacity in the underlying layers. The drop of the radiative gradient plotted in panel b) is however shifted toward the interior with respect the convective border defined by the Schwarzschild criterion: this is due to the fact that the velocity profile algorithm implies full convection in the closest region below this formal border. The vertical dashed line in panel b) represents the mass coordinate where the hydrogen profile starts significantly decreasing with respect the envelope value. In panel c) we report the gradients at the bottom of a convective shell generated by a TP: the radiative gradient doesn't present discontinuities. This behavior therefore confirms that the exponentially decaying profile of the convective velocities has to be applied only at the inner border of the convective envelope (or more generally to H-rich convective shells). This algorithm allows us to account for the partial mixing that occurs when the time step is reduced to or below the mixing timescale. In practice, when the TDU takes place, complete mixing is obtained within the fully convective zone, while the region immediately below, where the convective turnover time scale is larger, is only partially mixed. We refer to this region as the Velocity Profile Zone (hereafter VPZ). Figure 6.2 shows the chemical profile, the radiative and adiabatic temperature gradients, the average velocity and the pressure, in the region around the convective boundary, in a model of  $2 M_{\odot}$  with solar metallicity, during a dredge up episode (see Section 7.1 for details). The three major effects of the introduction of this exponential decay of the convective velocity are: i) the convective boundary is more stable against perturbation; ii) a smooth profile of protons within the intershell is left by the TDU; iii) a more efficient TDU results (see next

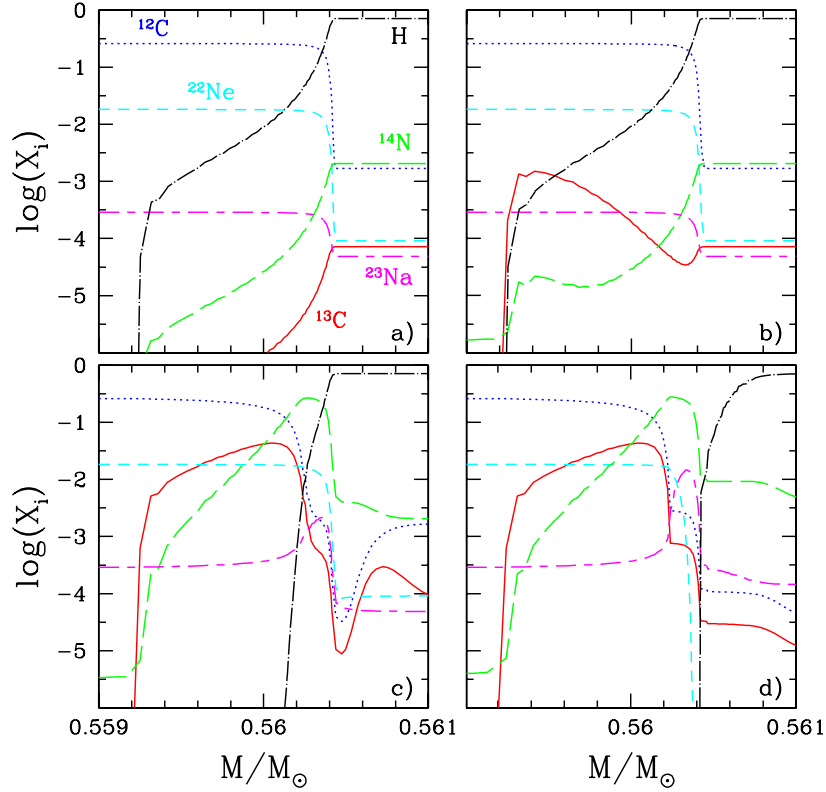


Figure 6.3 Variation of the relevant chemical species in the region where the  $^{13}\text{C}$  pocket forms after the occurrence of the  $2^{\text{nd}}$  TDU ( $M = 2M_\odot$  model with solar metallicity). Each Panel refers to different time steps, namely:  $\Delta t = 0$  (a),  $\Delta t = 3700$  (b), 14100 (c) and 39200 (d) years.

Section). As a consequence of ii), a  $^{13}\text{C}$  pocket almost  $^{14}\text{N}$ -free forms in this zone. After a few tests, we found that in order to get a suitable amount of  $^{13}\text{C}$  in the pocket, the  $\beta$  parameter should be of the order of 0.1 (see Section 6.3).

Concerning the third point, the increase in the TDU efficiency is due to the fact that, being the velocity profile algorithm partially mixing hydrogen from the envelope in the He- and C-rich intershell, the penetrating envelope attain zones enriched in H with respect to the case without the velocity profile. As a first consequence the opacity of that region becomes greater and consequently the radiative gradient results enhanced, increasing in such a way the difference between the radiative and the adiabatic temperature gradients and consequently leading to higher values for convective velocities at the inner border of the convective envelope.

## 6.2 The $^{13}\text{C}$ pocket

Figure 6.3 illustrates the various steps of the formation of a  $^{13}\text{C}$  pocket in a model with initial mass  $M=2M_{\odot}$  and solar metallicity (see Section 7.1 for details). Once the convective envelope reached the maximum penetration (panel a), the temperature in the underlying regions starts increasing (panel b) and protons (black dot-long-dashed profile) start being captured by the abundant  $^{12}\text{C}$  (blue dotted line) and by the freshly synthesized  $^{13}\text{C}$  (red solid line), leading to the production of  $^{14}\text{N}$  (green long-dashed line). The formation of the  $^{13}\text{C}$  and  $^{14}\text{N}$  pockets is followed (panel c) by the growth of a  $^{23}\text{Na}$ -rich layer (magenta short-dashed long-dashed line). In panel d the H-shell reactivates and the convective envelope recedes. In Fig. 6.4 we plot the chemical profiles of trace isotopes in the region around the  $^{13}\text{C}$  pocket. The  $^{13}\text{C}$  pocket (red solid line) partially overlaps with a more external

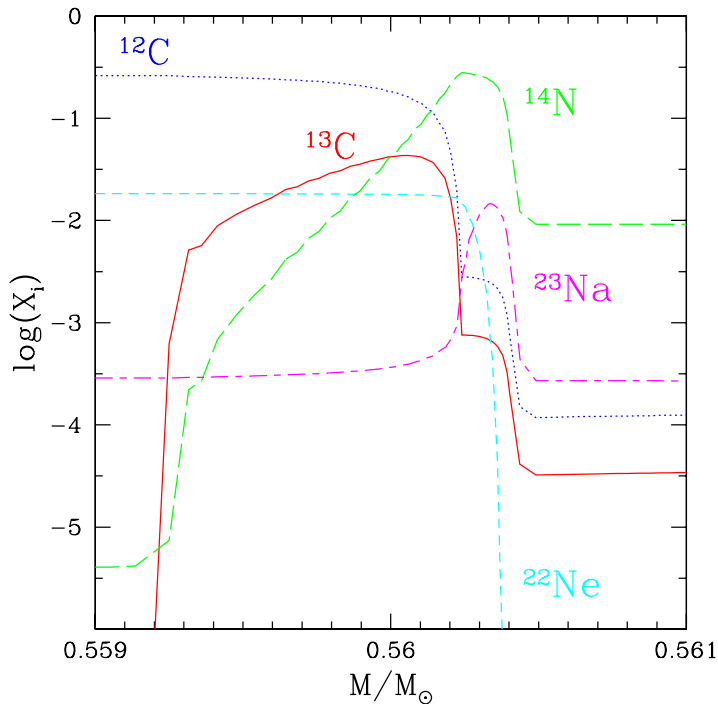


Figure 6.4 Abundances profiles in the  $^{13}\text{C}$  pocket formed after the  $2^{nd}$  TDU episode ( $M = 2M_{\odot}$  model with solar metallicity).

$^{14}\text{N}$  pocket (green long-dashed line). The maximum of the  $^{14}\text{N}$  coincides with the region where the protons diffused from the convective envelope at the epoch of the TDU were abundant enough to allow a full CN cycle. This is also the region where the  $^{23}\text{Na}$  (magenta short-dashed-long-dashed line) has been efficiently produced by the  $^{22}\text{Ne}(p,\gamma)^{23}\text{Na}$  reaction.

Indeed, at the end of the previous TP, the mass fraction of  $^{22}\text{Ne}$  (cyan short-dashed line) in the top layer of the He-rich intershell is of the order of  $2 \times 10^{-2}$  and, around the  $^{14}\text{N}$  maximum, this  $^{22}\text{Ne}$  is almost completely converted into  $^{23}\text{Na}$ , leading to the formation of a tiny  $^{23}\text{Na}$  pocket. In Section 9.3 we evaluate the efficiency of this mechanism in producing sodium and we compare it with other possible  $^{23}\text{Na}$  sources in AGB stars.

### 6.3 Tests on the velocity profile algorithm

The introduction of the exponentially decaying profile of convective velocities automatically implies an assumption on the value of the free parameter  $\beta$ . In the models presented in this work, we assume a value  $\beta=0.1$  and in order to justify such a choice we perform some tests on the  $Z=1 \times 10^{-4}$  model. We calculate the same sequence TP-Interpulse-TP, starting from the first TP followed by TDU, and we evaluate the consequences of changing this parameter in the range  $0 < \beta < 0.2$ . In Fig.6.5, Fig.6.6 and Fig.6.7 we present the

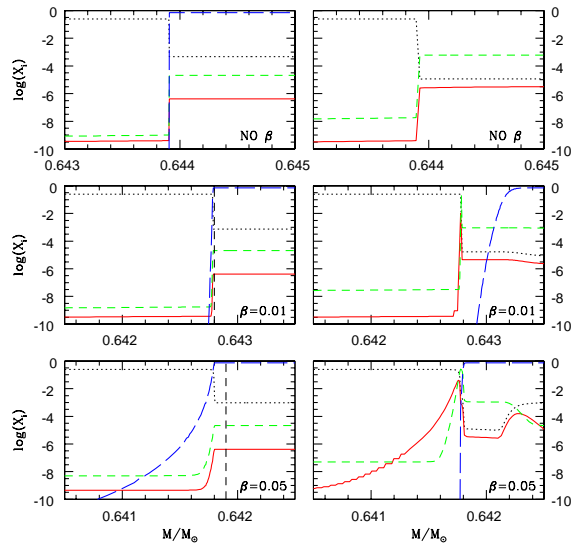


Figure 6.5 Chemical profiles at the maximum penetration of the convective envelope (left Panels) and after the formation of the  $^{13}\text{C}$  pocket (right Panels) after the 2<sup>nd</sup> TP with TDU in a  $M = 2M_{\odot}$  model with  $Z=1 \times 10^{-4}$ . In each plot we report the H (long-dashed line),  $^{12}\text{C}$  (dotted line),  $^{13}\text{C}$  (solid line) and  $^{14}\text{N}$  (short-dashed line) profiles. Cases with no velocity profile ( $\beta=0$ ),  $\beta=0.01$  and  $\beta=0.05$  are reported.

results: in the left panel of each plot we report the profiles of  $^{12}\text{C}$  (dotted line),  $^{13}\text{C}$  (solid

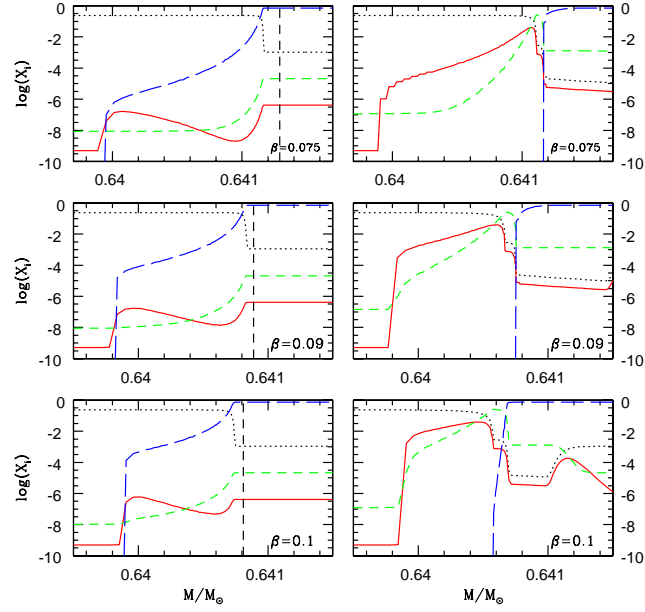


Figure 6.6 As in Fig. 6.5, but referring to  $\beta=0.075$ ,  $\beta=0.09$  and  $\beta=0.1$  cases.

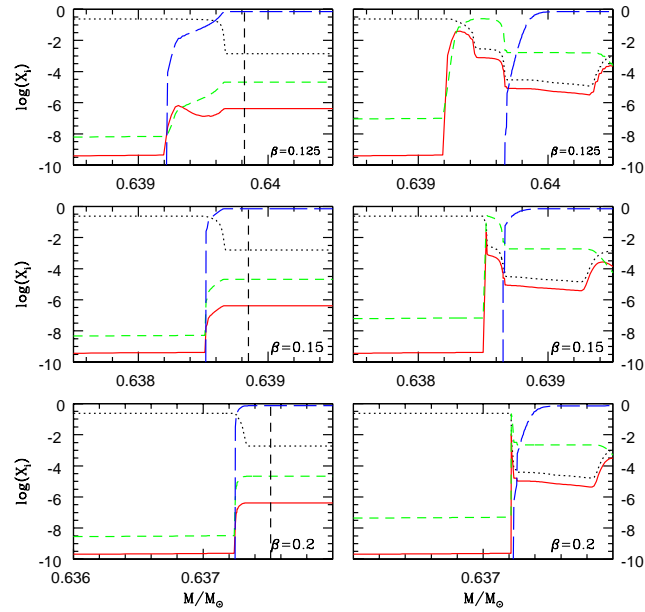


Figure 6.7 As in Fig. 6.5, but referring to  $\beta=0.125$ ,  $\beta=0.15$  and  $\beta=0.2$  cases.

line),  $^{14}\text{N}$  (short dashed line) and H (long dashed line) at the moment of the maximum penetration of the convective envelope. The vertical short-dashed black line in each left panel represents the inner border of the convective envelope as defined by the Schwarzschild criterion. As already outlined in Section 6.1, the most external part of the VPZ results almost fully mixed, due to the still high values of the convective velocities below the formal border of the convective envelope. In right panels we plot the same mass regions once the envelope has receded and the  $^{13}\text{C}$  pocket has already formed. In Table 6.1 we tabulate the corresponding physical quantities, that is (from left to right) the value of the  $\beta$  parameter, the deepest mass coordinate reached by the inner border of the envelope during the TDU, the amount of dredged up material, the extension in mass of the newly formed  $^{13}\text{C}$  pocket, the product  $\beta \times H_P$  (where  $H_P$  is the pressure scale height at the bottom of the convective envelope), the amount of hydrogen diffused in the VPZ and finally the resulting effective  $^{13}\text{C}_{eff}$  left in the VPZ, defined as

$$X(^{13}\text{C}_{eff}) = X(^{13}\text{C}) - X(^{14}\text{N}) \times \frac{14}{13}. \quad (6.2)$$

A first noticeable evidence is the strong dependence of the TDU efficiency from  $\beta$ : the amount of material interested by a single TDU episode increases by more than a factor 3 (see column 3 in Table 6.1) from the case without overshooting and the extreme case  $\beta=0.2$ . This is expected because, increasing the  $\beta$  value, the amount of extramixed hydrogen is monotonically increasing, raising up opacities in the upper layers of the He-intershell: in this way a deeper penetration of the convection envelope naturally develops (see Section 6.1). In contrast, the  $^{13}\text{C}$  available for the heavy elements nucleosynthesis ( $^{13}\text{C}_{eff}$  in equation 6.2) grows up with increasing  $\beta$ , reaches a maximum in correspondence of  $\beta=0.1$  and then decreases down to negative values. This results from a combination of two different physical processes: the growing of the  $^{13}\text{C}_{eff}$  is a direct consequence of the greater efficiency of the velocity profile algorithm, while its decreasing for large  $\beta$  values is due to the fact that the convection efficiency in the VPZ starts to be too high. This leads the most external layers of the He-intershell being fully mixed and consequently showing an envelope-like H abundance, instead of the H profile needed for the formation of the  $^{13}\text{C}$  pocket. The negative values tabulated for the two tests with the highest  $\beta$  are due to the complete overlapping between the  $^{13}\text{C}$  and the  $^{14}\text{N}$  pockets. In this case, all neutrons released by the  $^{13}\text{C}(\alpha, n)^{16}\text{O}$  reaction are captured by the abundant  $^{14}\text{N}$  via the  $^{14}\text{N}(n, p)^{14}\text{C}$  reaction, *de facto* erasing the source for the heavy elements nucleosynthesis.

Summing up, we propose an efficient way to calibrate the free parameter affecting the velocity profile algorithm, confining its possible values in a narrower range, and we adjust

it in order to obtain the maximum  $^{13}\text{C}$  pocket. It has however to be reminded that, in

$\beta$	$M_{Deep}$	$M_{TDU}$	$\Delta M$	$\beta \times H_P$ [cm]	$\Sigma_H$	$\Sigma_{^{13}\text{C}}$
NO	0.64400	1.90	-	-	-	-
0.01	0.64282	2.80	7.20E-05	5.16E+07	2.01E-05	5.55E-08
0.05	0.64189	3.32	8.40E-04	3.10E+08	2.35E-05	6.07E-07
0.075	0.64128	3.63	1.39E-03	5.28E+08	4.01E-05	2.31E-06
0.09	0.64089	3.81	1.11E-03	5.44E+08	5.48E-05	4.65E-06
0.1	0.64081	4.10	9.53E-04	6.19E+08	6.63E-05	5.48E-06
0.125	0.63982	4.59	6.22E-04	1.05E+09	1.49E-04	5.61E-07
0.15	0.63885	5.15	3.20E-04	1.37E+09	1.72E-04	< 0
0.2	0.63749	6.12	2.40E-04	1.72E+09	2.07E-04	< 0

Table 6.1 Tests on  $\beta$  parameter. Columns 2, 4, 6 and 7 are in  $M_\odot$  units, while column 3 is in  $10^{-3} M_\odot$  units. See text for details.

general, observations show an important scatter of s-process abundances at any metallicity [26]. This scatter reveals a spread of the effective amount of  $^{13}\text{C}$  in the pocket, perhaps due to differences in the stellar parameters, such as the initial mass or the mass loss rate, or to the chaotic nature of the process responsible of the proton injection into the He intershell. Recent studies [80, 150] demonstrate that the effects induced by rotation during the interpulse period after a TP can induce a spread of the abundances in the layers right below the inner border of the convective envelope. This would be the direct consequence of the shear between the rapid solid body rotation of the core and the slow rotating differential envelope. We could then hypothesize that different rotational efficiencies could partially mix the  $^{13}\text{C}$  pocket with the  $^{14}\text{N}$  one, leading to lower values of  $^{13}\text{C}_{eff}$ , and giving naturally rise to the desired spread of the  $^{13}\text{C}$  pocket efficiencies.

We recall that the calibration we carry out is efficient in the context of the FRANEC code. It is therefore useless to compare the  $\beta=0.1$  value of our velocity profile algorithm with the ones proposed by [54] and [79], since they parameterize the convection by means of a different numerical procedure. Our aim is only to reduce the range of uncertainty which actually overwhelms this free parameter by evaluating the effects induced on the formation of the  $^{13}\text{C}$ -pocket (which governs the following s-process nucleosynthesis). Moreover, another big warning must be raised: the calibration we perform is efficient for low mass AGB stars. For larger masses, a lower value of the  $\beta$  free parameter is probably requested (see e.g. [38]), due to the fact that the entire He-intershell structure is shrinking, passing from  $\Delta M \sim 10^{-2} M_\odot$  down to  $\Delta M \sim 10^{-3} M_\odot$ . We will investigate these hypotheses in future works.

# Chapter 7

## Thermally pulsing AGB models

*In order to illustrate the capabilities and the limits of our code, an updated computation of a  $2 M_{\odot}$  stellar structure with different chemical compositions is reported. These models have been obtained by including into the stellar evolution code the full nuclear network described in Section 5. The predicted modifications of the surface composition occurring during the AGB evolution are shown.*

Data presented in this section refer to three different stellar models, having the same initial mass ( $2 M_{\odot}$ ) and different metallicities:  $Z=1.5 \times 10^{-2}$ ,  $Z=1 \times 10^{-3}$  and  $Z=1 \times 10^{-4}$ . We operated this choice because this mass value is representative of low mass AGB stars and the three metallicities span almost the entire metal distribution of our Galaxy. The physical evolution and the nucleosynthesis characterizing each model are analysed in Sections 7.1 and 7.2, while in Section 7.3 we present the global yields.

### 7.1 The Solar metallicity model

We used the network and the mixing algorithm described in previous Chapters to calculate the evolutionary sequence of a  $2 M_{\odot}$  star of solar metallicity. Before the first TP, a Reimers' formula for the mass loss ( $\eta = 0.4$ ) has been assumed. During the thermally pulsing AGB phase, we adopt the mass loss rate prescription discussed in Section 4.5. The calculation has been stopped when the envelope mass is reduced down to  $\sim 0.35 M_{\odot}$ , the corresponding total mass being  $M_{tot}^* \sim 1.0 M_{\odot}$ ; at this epoch, the envelope composition is freezed, because TDU episodes already ceased.

In Fig.7.1 we plot the TP-AGB phase of the model, when the stellar structure is characterized by a partially degenerate C-O core, a mutually excluding H and He burning shells

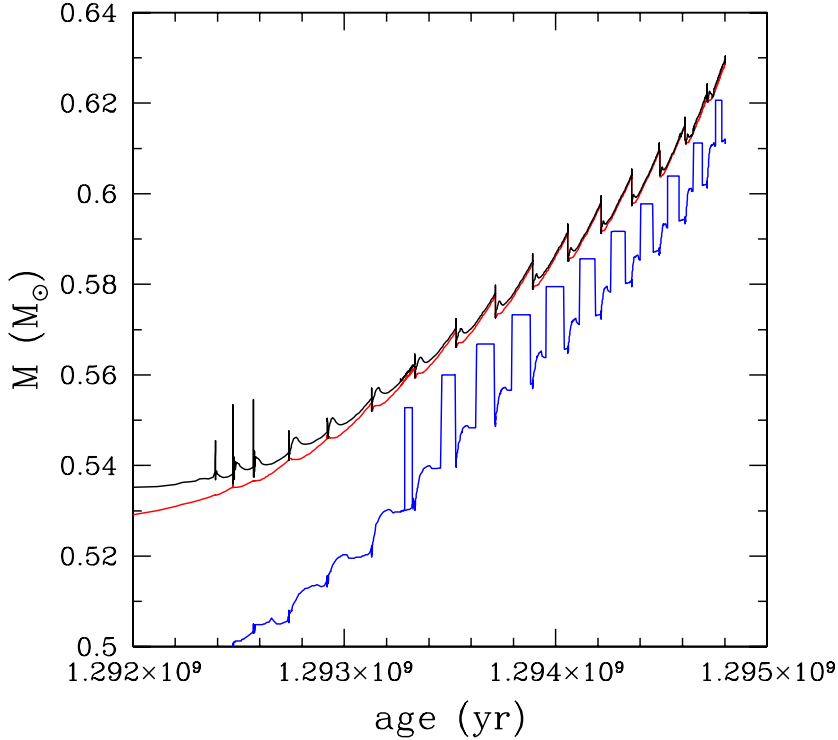


Figure 7.1 The evolution throughout the TP-AGB phase of a star with initial mass  $M = 2 M_{\odot}$  and solar metallicity.

and by a fully convective envelope. The three lines of each plot illustrate the evolution of the positions, in mass coordinates, of (top to bottom): the inner border of the convective envelope (dark line), the maximum energy production within the H-burning shell (red line) and the maximum energy production within the He-intershell (blue line). The outward shift of the location of the maximum energy production within the intershell, in Figure 7.1, marks the onset of the  $^{13}\text{C}$  burning during the interpulse. The most energetic mesh in the intershell region is normally identified by the He-burning shell, but when the  $^{13}\text{C}$  starts burning (releasing neutrons) its energy contribution is larger than the  $3\alpha$  reaction one. Note that the He-burning shell is practically switched off during the interpulse phase. We take into account the energy release due to the following neutron capture by adding 5 MeV (assumed as a mean energy value) to the energetics of the  $^{13}\text{C}(\alpha, n)^{16}\text{O}$  reaction. In Table 7.1 we report some physical quantities characterizing the TP phase.

TDU	$M_{tot}$	$M_H$	$M_{env}$	$M_{TDU}$	$\Delta M_{Pulse}$	$\Delta M_H$
1	1.88E+00	5.54E-01	1.33E+00	4.00E-04	3.33E-02	7.50E-03
2	1.87E+00	5.61E-01	1.31E+00	2.10E-03	3.12E-02	8.20E-03
3	1.85E+00	5.70E-01	1.28E+00	3.50E-03	2.97E-02	9.10E-03
4	1.83E+00	5.77E-01	1.25E+00	4.60E-03	2.84E-02	1.02E-02
5	1.80E+00	5.85E-01	1.22E+00	5.60E-03	2.73E-02	1.08E-02
6	1.76E+00	5.91E-01	1.17E+00	6.20E-03	2.61E-02	1.11E-02
7	1.69E+00	5.98E-01	1.09E+00	6.30E-03	2.50E-02	1.17E-02
8	1.59E+00	6.04E-01	9.86E-01	6.20E-03	2.39E-02	1.21E-02
9	1.46E+00	6.10E-01	8.50E-01	5.80E-03	2.29E-02	1.16E-02
10	1.29E+00	6.15E-01	6.75E-01	4.20E-03	2.14E-02	1.09E-02
11	1.13E+00	6.21E-01	5.09E-01	9.00E-04	1.93E-02	9.70E-03
TOT.				4.58E-02		

TDU	$\lambda$	$r$	$\Delta t_{ip}$	$T_{max}^{TP}$	$Z_{sup}$	C/O
1	5.33E-02	6.19E-01	2.06E+05	2.46E+08	1.49E-02	0.33
2	2.56E-01	7.47E-01	1.94E+05	2.53E+08	1.50E-02	0.37
3	3.85E-01	6.63E-01	1.85E+05	2.61E+08	1.55E-02	0.46
4	4.51E-01	6.16E-01	1.77E+05	2.68E+08	1.63E-02	0.62
5	5.19E-01	5.75E-01	1.67E+05	2.75E+08	1.72E-02	0.80
6	5.59E-01	5.36E-01	1.57E+05	2.80E+08	1.83E-02	1.01
7	5.38E-01	5.12E-01	1.45E+05	2.85E+08	1.95E-02	1.24
8	5.12E-01	4.93E-01	1.33E+05	2.88E+08	2.07E-02	1.47
9	5.00E-01	4.80E-01	1.21E+05	2.90E+08	2.20E-02	1.72
10	3.85E-01	4.77E-01	1.03E+05	2.92E+08	2.30E-02	1.92
11	9.28E-02	4.97E-01	8.36E+04	2.89E+08	2.30E-02	1.93

Table 7.1 Data relative to a model with initial mass  $M=2M_{\odot}$ ; solar metallicity case:  $(C/O)_{ini} = 0.54$ ,  $(C/O)_{FDU} = 0.35$ ,  $Z=1.5 \times 10^{-2}$ .

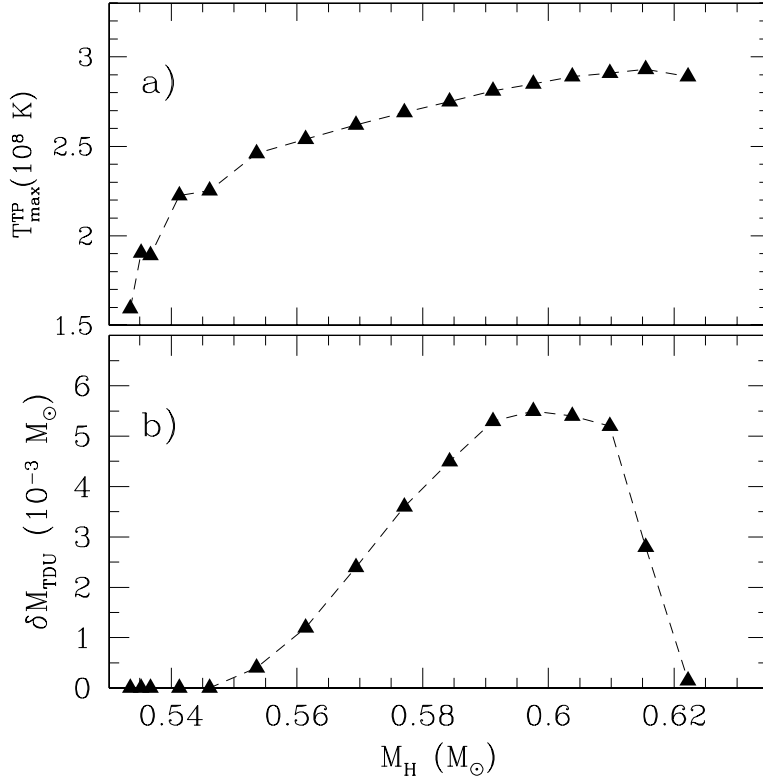


Figure 7.2 Evolution of the maximum temperature at the base of the convective zones generated by TPs (Panel a) and the dredged up mass per pulse (Panel b) during the AGB phase ( $M = 2M_\odot$  model with solar metallicity).

In the upper part we tabulate (from left to right): *i*) number of TDU episodes, *ii*) total mass of the star, *iii*) core mass before the occurrence of TDU episodes, *iv*) mass of the convective envelope, *v*) mass of material interested by TDU episodes, *vi*) extension in mass of the convective shell generated by the TPs, *vii*) mass burnt by the H-shell during the previous interpulse period. In the lower part we report (from left to right): *i*) number of TDU episodes, *ii*)  $\lambda$  factors (defined as the ratio between the material suffering TDU and the H-burning ashes of the previous interpulse period), *iii*) overlap factors  $r$  between two subsequent TPs (defined as the ratio between the portion of the convective pulse interested by the nucleosynthesis of previous pulses and the total mass of the convective pulse), *iv*) duration of the interpulse phases, *v*) maximum temperature attained at the bottom of the convective pulses, *vi*) surface metallicity and *vii*) C/O surface ratio. In the Table caption

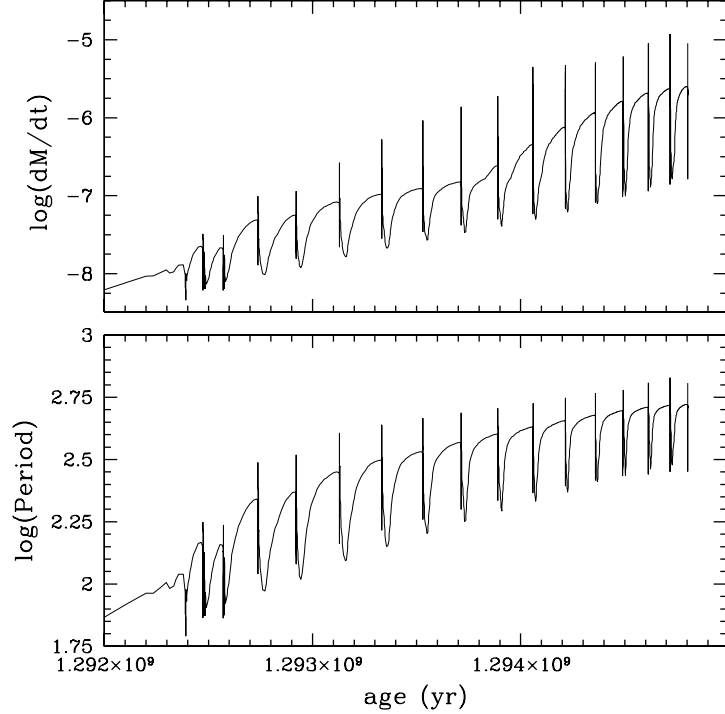


Figure 7.3 Mass loss history and derived period during the AGB phase ( $M = 2M_{\odot}$  model with solar metallicity).

we report the initial (C/O) ratio, the (C/O) ratio after the First Dredge Up (FDU) and the initial metallicity. Moreover, in the last row of the upper part, we report the total amount of dredged up material. Note that in this Table we only report data concerning pulses followed by TDU: some pulses without TDU develop in the early AGB Phase, as depicted in Fig. 7.1. The first TDU episode in fact occurs after six TPs, when the core mass is  $0.55 M_{\odot}$ . The evolution of  $T_{max}^{TP}$  (the maximum temperature at the base of the convective zone generated by the TP) and  $\delta M_{TDU}$  (the amount of mass dredged up) are reported in Figure 7.2. As expected, the deepness of the TDU initially increases, due to the increase of the core mass. Then, during the TP-AGB phase, the effect of the envelope erosion becomes important, and the dredge up efficiency decreases, dropping to 0 after the last computed TP. The possible activation of the  $^{22}\text{Ne}(\alpha, n)^{25}\text{Mg}$  reaction critically depends on  $T_{max}^{TP}$  that, for this reason, represents a key quantity for the comprehension of the nucleosynthesis occurring in AGB stars. It is obviously related to the maximum He burning luminosity.  $T_{max}^{TP}$  initially increases and attains a nearly asymptotic upper limit, of

about  $2.9 \times 10^8$  K. At such a low temperature the  $^{22}\text{Ne}(\alpha, n)^{25}\text{Mg}$  is marginally activated, providing minor neutron exposures.

In Fig. 7.3 we report the mass loss history (upper panel) and the derived period (lower panel) of the model. The transition between the two mass loss regimes (see Section 4.5) occurs when the pulsational period exceeds  $\log P > 2.5$ , as showed by the slope change in the mass loss rate curve.

The final C/O is 1.93, while it becomes larger than 1 when the core mass is about  $0.58 M_{\odot}$  and the luminosity is  $\log L/L_{\odot} = 3.85$ , which corresponds to a bolometric magnitude of  $-4.9$  mag (see Figure 7.4). Our result is in good agreement with the recent work of [74], who analysed a sample of galactic C-stars at infrared (IR) wavelengths. Their derived C-star luminosity function results peaked at  $M_{bol} \sim 4.8$ , *de facto* erasing the debated inconsistencies on the brightness of C-stars between observations and theoretical predictions.

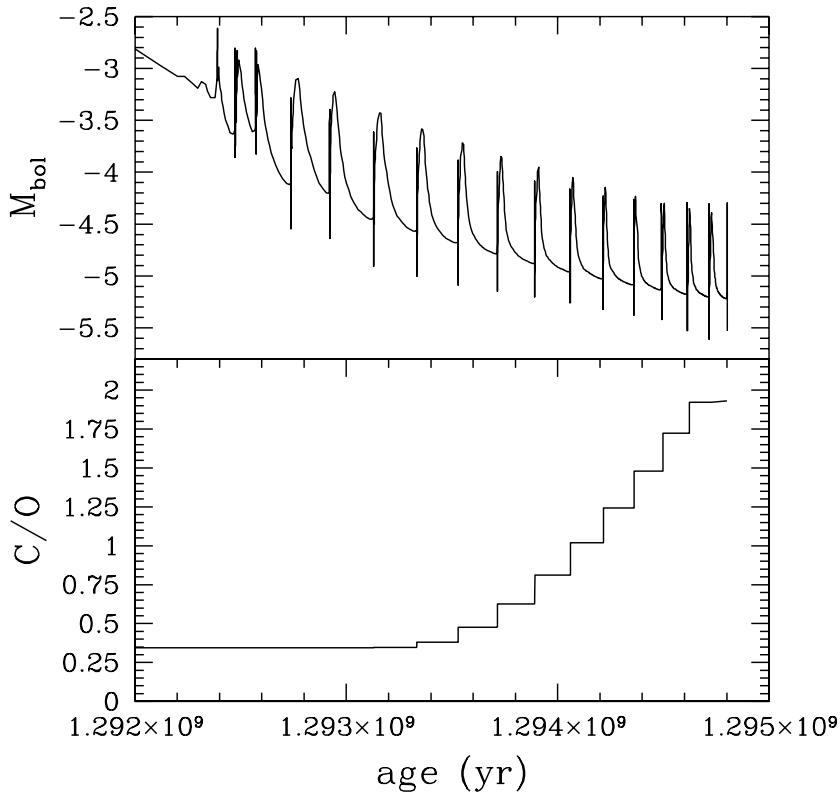


Figure 7.4 Bolometric magnitude (upper Panel) and C/O ratio (lower Panel) along the AGB phase ( $M = 2M_{\odot}$  model with solar metallicity).

As described in Section 6.2, a  $^{13}\text{C}$  pocket forms after each TDU episode. The  $^{13}\text{C}$  in the first pocket is only partially burnt during the interpulse and the residual is engulfed into the convective zone generated by the subsequent TP. This phenomenon therefore leads

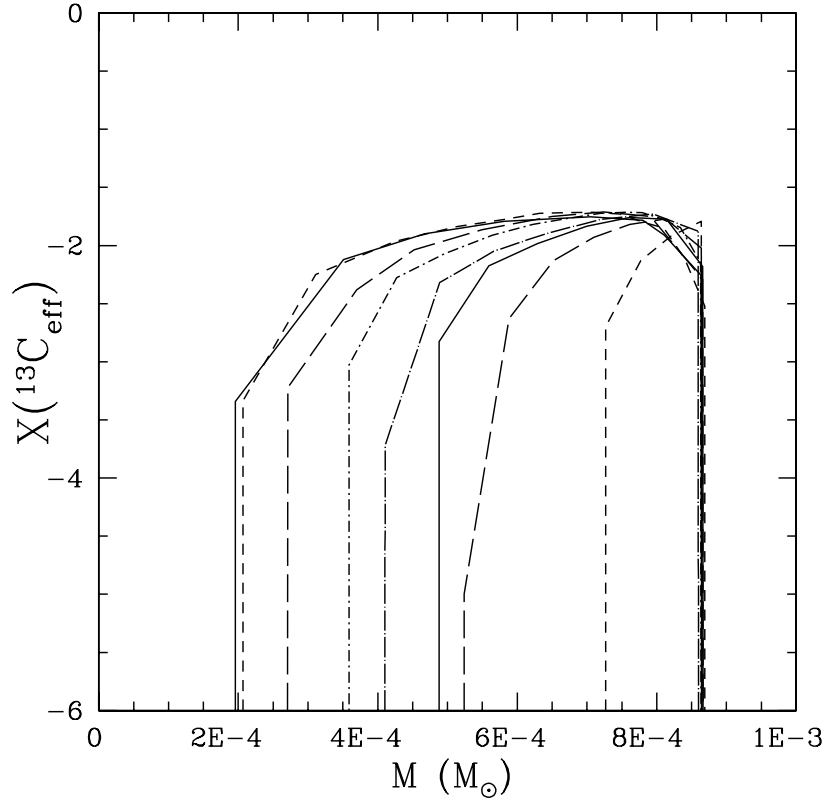


Figure 7.5 The *effective* (see text) mass fraction of  $^{13}\text{C}$  within all the pockets ( $M = 2M_{\odot}$  model with solar metallicity).

to a convective  $^{13}\text{C}$  burning, with quite interesting consequences on the nucleosynthesis of neutron-rich isotopes (see Section 7.1.3). In all other cases, the  $^{13}\text{C}$  is fully consumed during the interpulse. The resulting nucleosynthesis is characterized by a rather low neutron density, never exceeding  $10^7$  neutrons/cm $^3$ ; a typical neutron exposure reached during a radiative  $^{13}\text{C}$  burning (weighted over the whole pocket) is very powerful:  $\delta\tau \sim 0.25$  mbarn $^{-1}$ . The s-rich pocket is then engulfed and diluted by the convective zone generated by the TP and, later on, partly dredged up by the next TDU. The maximum neutron density is attained in the more internal layer of the  $^{13}\text{C}$  pocket, where the  $^{14}\text{N}$  is less abundant. The *effective* abundances of  $^{13}\text{C}$  in all the pockets we found (defined as  $X_{\text{eff}}(^{13}\text{C}) = X(^{13}\text{C}) -$

$X(^{14}\text{N}) \times 13/14$ ) are reported in Figure 7.5. Each pocket has been shifted in mass in order to superimpose their external borders; the 0 point of the abscissa is arbitrary. The extension of the pockets decreases with time, the first one being the largest ( $\Delta M \sim 6.5 \times 10^{-4} M_{\odot}$ , about 6 times greater than the last one). We lay emphasis on this point by com-

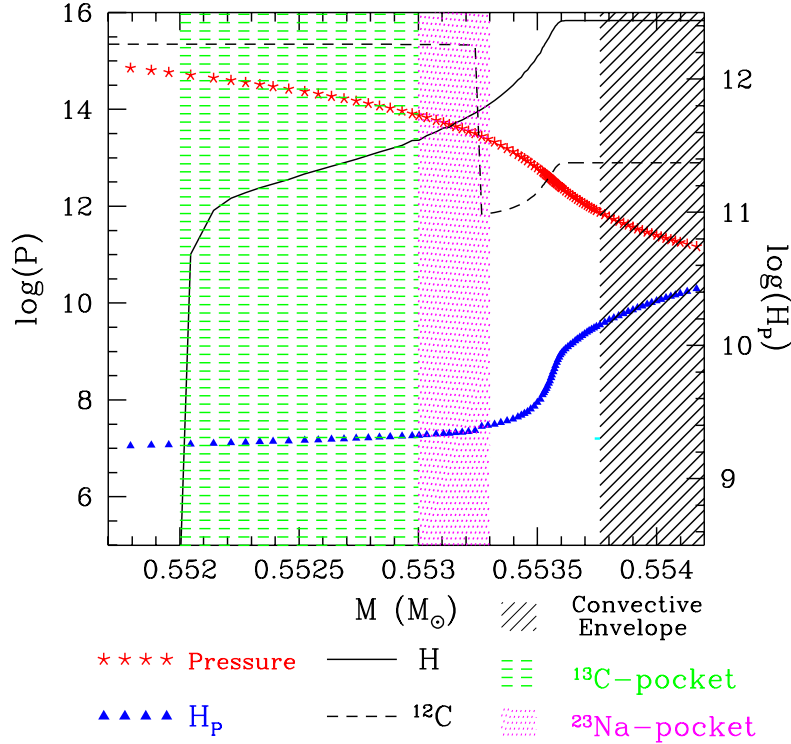


Figure 7.6 Physical quantities profiles and chemical distributions (see the legend) at the moment of the maximum penetration of the convective envelope during the first TDU episode in the  $M = 2M_{\odot}$  model with solar metallicity. Pressure is given in  $\text{dyne}\cdot\text{cm}^{-2}$  and  $H_P$  in cm. We also evidence the two regions where the  $^{13}\text{C}$  pocket (horizontal dashed area) and the  $^{23}\text{Na}$  pocket (vertical dashed area) form.

menting Fig. 7.6 and Fig. 7.7, which depict the moment of the maximum penetration of the convective envelope, during the first and the last (11<sup>th</sup>) TDU episode, respectively. The solid and the dashed lines refer to hydrogen and  $^{12}\text{C}$  profiles respectively, the slanting dashed area is the convective envelope (the inner border of this area is defined by the Schwarzschild criterion). The horizontal and the vertical dashed areas represent the layers where the  $^{13}\text{C}$  and the  $^{23}\text{Na}$  pockets form (see Section 6.2), when the envelope recedes and the H-shell restarts burning. Starred line reproduces the pressure profile, while triangles

are placed along the  $H_P$  distribution. The reduction of the pocket extension is due to the fact that while the pressure in the He core changes of one order of magnitude passing from the 1<sup>st</sup> to the 11<sup>th</sup> TDU episode, it undergoes a strong reduction in the envelope (about 5 order of magnitudes), due to the expansion of the structure along the AGB track. The

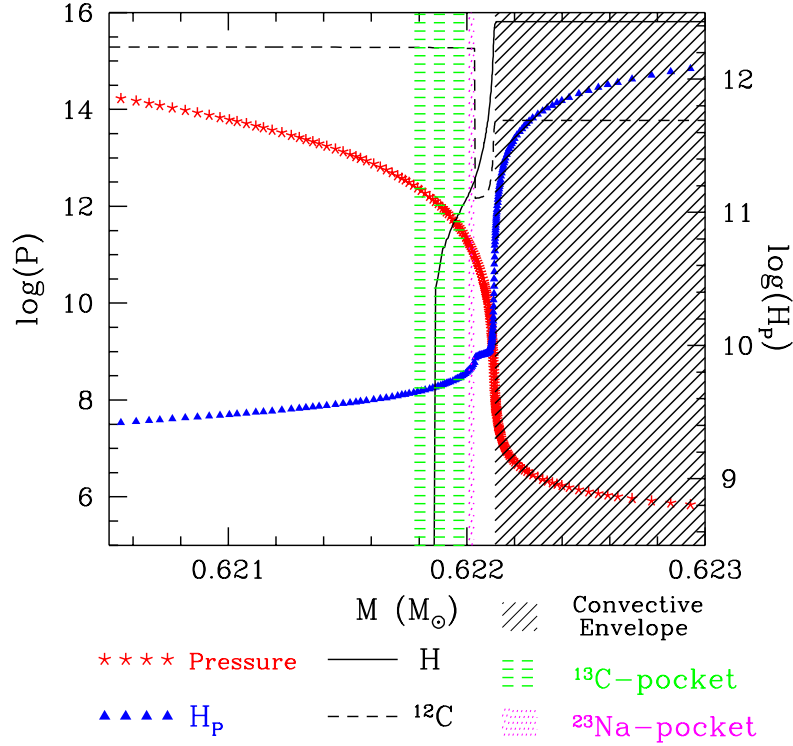


Figure 7.7 As in Fig. 7.6, but referring to the 11<sup>th</sup> (last)  $^{13}\text{C}$  pocket ( $M = 2M_{\odot}$  model with solar metallicity).

star radius increases in fact from  $200 R_{\odot}$  to more than  $500 R_{\odot}$ , while the mass decreases from  $1.88 M_{\odot}$  down to  $1.13 M_{\odot}$  (see Table 7.1). This huge difference between the external and the internal pressure strongly affects the efficiency of the velocity profile mechanism, leading to the formation of more and more narrow pockets. The size reduction of the pockets has a direct consequence on the overabundances in the He intershell, that is the production factor of the various chemical species with respect the initial abundances. In Fig. 7.8 we report the production factors defined as the ratio  $N_j^s/N_j^{\odot}$ , where  $N_j^s$  stands for the He intershell isotopic abundance and  $N_j^{\odot}$  for the initial one. The plot clearly shows that the overabundances reach a maximum around the 6<sup>th</sup> TDU and then decrease down to the level defined by the 11<sup>th</sup> TDU. This is due to the fact that while the extension of

the  $^{13}\text{C}$  pocket is decreasing pulse by pulse, the mass burnt by the H-shell in the interpulse period is slightly increasing for the entire duration of the AGB phase (see Table 7.1). This

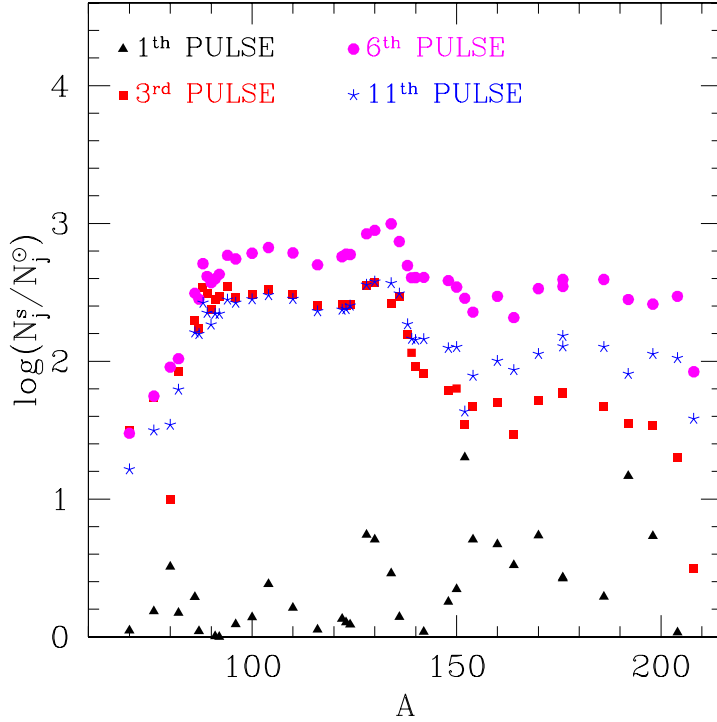


Figure 7.8 Pulse by pulse He intershell production factors for s-only and neutron magic nuclei with respect to the initial (solar) composition. Series refer to He intershell distributions before the first, third, sixth and eleventh (last) TP with TDU.

implies that the s-process nucleosynthesis inside the pocket is no more able to compensate the dilution of the s-enriched material within the material left in the ashes of the H-burning shell, leading the intershell overabundances to decrease.

### 7.1.1 Surface enrichments

The ashes of neutron-capture nucleosynthesis allowed by the  $^{13}\text{C}$  burning are spread within the He intershell by the convective shells generated by TPs. Later on, as a consequence of the TDU, the envelope composition is polluted with the products of the s process. The surface compositions resulting after each TDU episode are reported in Figure 7.9 (see Appendix B.1 for detailed pulse by pulse data). We use the standard spectroscopic

notation<sup>1</sup>. Among the light elements, note the logarithmic enhancements of C (0.56 dex), N (0.30 dex), F (0.49 dex), Ne (0.22 dex) and Na (0.17 dex). We recall that C is the main product of the  $3\alpha$ -burning. The nitrogen enhancement in the envelope is totally due to the first dredge up. In fact, the  $^{14}\text{N}$  left by the H burning within the intershell is fully converted into  $^{22}\text{Ne}$  during the convective TP, giving rise to the resulting Ne enhancement. Fluorine is synthesized in the convective shell generated by the thermal pulse via the  $^{15}\text{N}(\alpha, \gamma)^{19}\text{F}$  reaction (see Section 9.2). The Na enhancement is mainly due to proton capture on  $^{22}\text{Ne}$  (see Section 9.3). Concerning the s-process nucleosynthesis, all the elements (from Sr to Pb) result enhanced. We find that the abundance of Sr, Y and Zr at the first s peak,

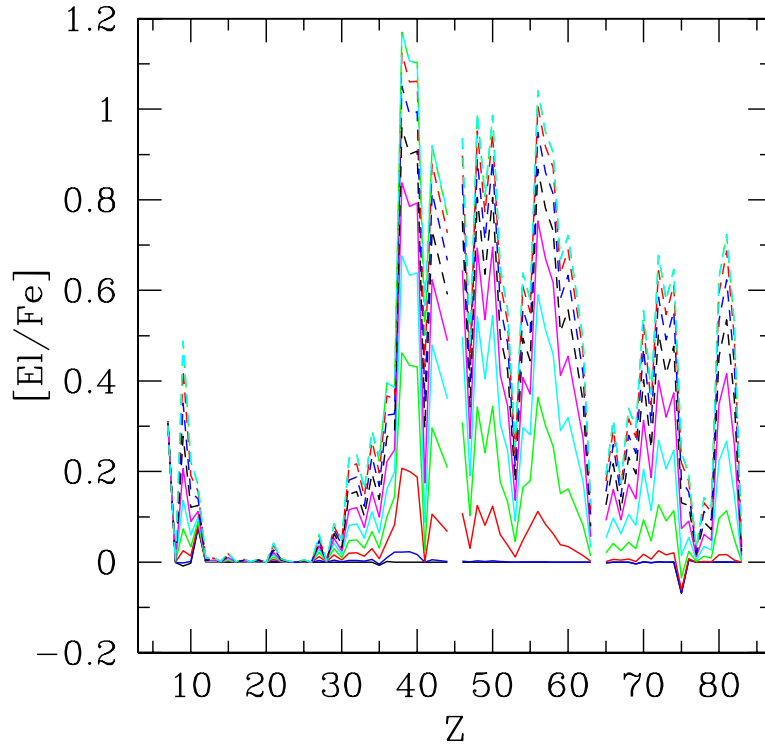
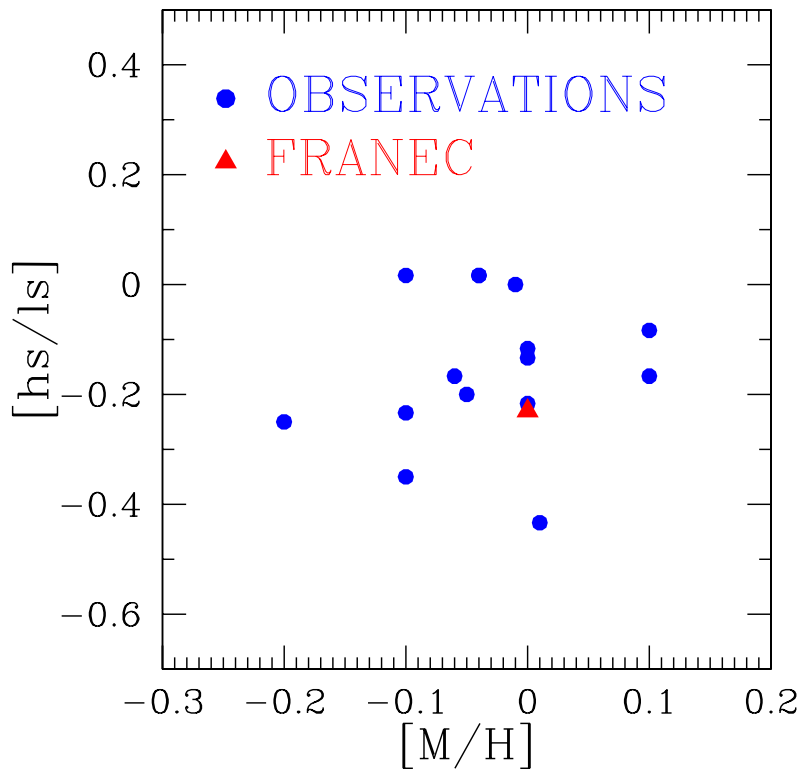


Figure 7.9 Pulse by pulse surface composition, in the usual spectroscopic notation, for the  $M = 2M_{\odot}$  model with solar metallicity.

the so-called ls elements (*light s elements*), is comparable with the one of the hs elements (*heavy s elements*) Ba, La, Ce, Pr, Nd at the second s peak. Lead is underproduced with

<sup>1</sup> $[\text{El}/\text{Fe}] = \log(N(\text{El})/N(\text{Fe})) - \log(N(\text{El})/N(\text{Fe}))_{\odot}$ . The label El stands for the generic element.

respect to barium, as expected for AGB stars of this metallicity. In Figure 7.10, the  $[\text{hs}/\text{ls}]$  attained in the envelope when  $C/O=1$  is compared to those measured in galactic C(N) Giants [4]: our theoretical value lays in the range spanned by observational data. Note that, for a given metallicity, this intrinsic index is indicative of the mean neutron exposure that characterizes the s-process distribution and it is independent of the fact that the observed s-enhanced star is an intrinsic AGB or a main sequence or a giant star (extrinsic AGB).



be mentioned that [20] recently propose a narrower spread of the  $^{13}\text{C}$  pockets (a factor 3 instead of more than one order of magnitude proposed by [26]) by carrying out population synthesis simulations with a rapid synthetic evolution code.

Even if it is evident that a single modelling is not able to cover the observed range, we note that the standard case (ST, see [59]) was shown to reproduce the main s-process component in the solar system for low mass AGB stars and half-solar metallicity: in that model the  $^{13}\text{C}$  pocket efficiency was assumed identical for all TPs followed by TDU. In

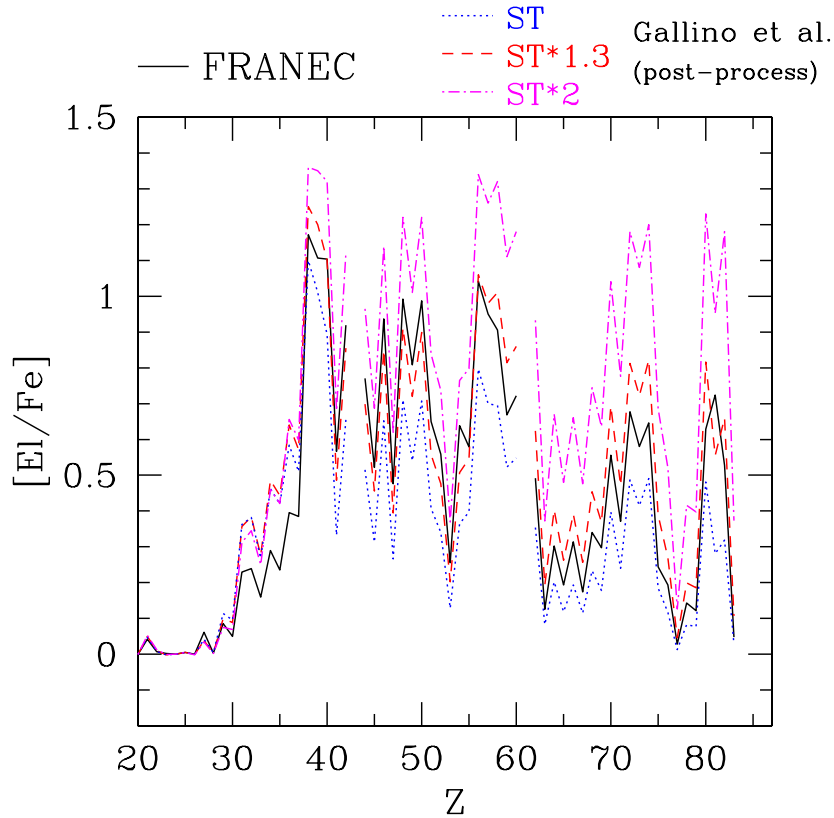


Figure 7.11 Final surface composition of the  $M = 2M_{\odot}$  model with solar metallicity, compared with post-process calculations (Gallino R., *priv. comm.*).

order to evaluate the efficiency of the adopted velocity profile algorithm (see Chapter 6), we compare our surface enrichment distribution with the most recent post-process calculations (Gallino R., *private communication*) performed over a  $M=2M_{\odot}$  model with  $Z=2\times 10^{-2}$  [156], characterized by a Reimers' mass-loss rate with  $\eta=0.5$ . By varying the efficiency of their  $^{13}\text{C}$  pocket [59], we find that our model is approximately equivalent to their  $\text{ST}\times 1.3$  case (see Fig. 7.11). A general agreement results from the comparison, but a different profile in the two curves (dark solid line and red dashed line) appears

corresponding to the thallium overabundance. This difference has to be ascribed to our more detailed treatment of the weak processes determining the  $^{205}\text{Tl}$  and  $^{205}\text{Pb}$  abundances with respect to the post-process calculation, where the temporal delay between the extinction of the convective shell generated by the thermal pulse and the occurrence of the following TDU episode is not taken into account (see [116] for the analysis of this problem). Note that the average enhancement of s-process elements is roughly the same, even if the plotted distributions result from completely different evolutions along the AGB phase: we obtain 11 pulses followed by TDU, while the post-process calculation is characterized by 22 pulses followed by TDU (see [156]). However, we recall that the introduction of the velocity profile algorithm makes our TDU more efficient with respect to previous calculations (see Section 6.1): this feature counterbalances the decreased number of TDU episodes, which is mainly determined by the adopted mass-loss rate (see the discussion at the end of Section 8.1).

We stress the fact that our resulting  $^{13}\text{C}$  pocket is not so different from the  $\text{ST}\times 2$  case of [59], which represents an upper limit: ingestion of a larger abundance of protons would favor the  $^{14}\text{N}$  production by proton capture on  $^{13}\text{C}$ . The presence of physical processes up to date not considered in our code (see discussion in Section 6.3) could result in a spread of the pocket efficiency, therefore allowing us to span in the  $^{13}\text{C}$  pocket range requested by observations.

### 7.1.2 The convective $^{13}\text{C}$ burning

As pointed out in previous Sections, the  $^{13}\text{C}$  formed after each third dredge up episode is usually completely consumed by  $\alpha$  captures before the onset of the subsequent TP, releasing neutrons. This is the most efficient neutron source in low mass AGB stars, and the resulting s-process nucleosynthesis is at the origin of the solar main component. However, in the solar metallicity model, we find that the temperature of the first formed  $^{13}\text{C}$  pocket remains too low during the interpulse and the  $^{13}\text{C}$  is not completely burnt, being partially engulfed in the convective zone generated by the following TP. The  $^{13}\text{C}$  burning takes place at the bottom of the convective shell ( $T_8 \sim 1.6$ ) producing a maximum neutron density  $n_n = 3.3 \times 10^{11}$  neutrons/cm<sup>3</sup>, about 30 times larger than the neutron density released by the subsequent  $^{22}\text{Ne}$  neutron burst (see Fig. 7.12). These numbers refer to the maximum neutron density attained at the bottom of the convective shell generated by the TP, while the average neutron density within the shell is one order of magnitude lower (see [58]). The contribution to the nucleosynthesis from this anomalous convective  $^{13}\text{C}$  burning reveals interesting peculiarities. In particular, some branchings, which remain closed during a

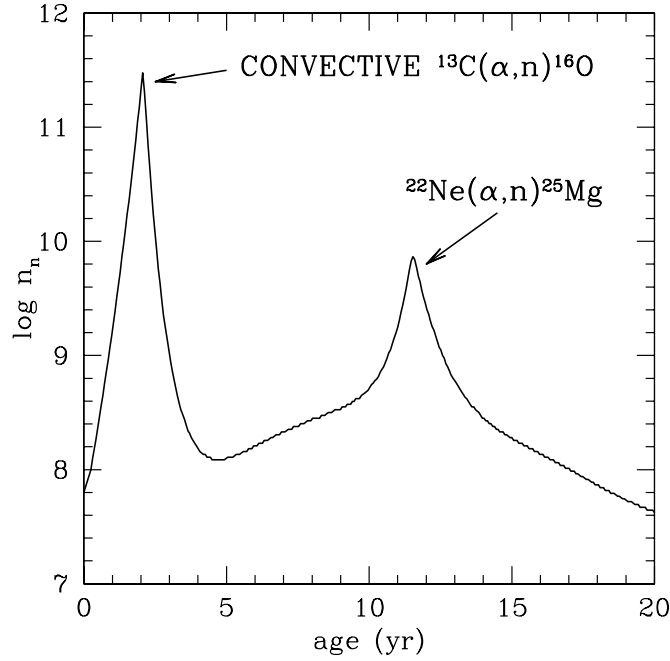


Figure 7.12 Peak neutron density evolution after the ingestion of the  $^{13}\text{C}$ -pocket formed after the first TDU episode ( $M = 2M_{\odot}$  with solar metallicity).

standard radiative  $^{13}\text{C}$  burning and are marginally activated during the  $^{22}\text{Ne}(\alpha, n)^{25}\text{Mg}$  burning, are now open. In a very short temporal step ( $\Delta T < 3$  years, see Fig. 7.12) we obtain a consistent production of neutron-rich isotopes normally by-passed by the standard radiative  $^{13}\text{C}$  s-process, among which  $^{60}\text{Fe}$ ,  $^{86}\text{Kr}$ ,  $^{87}\text{Rb}$  and  $^{96}\text{Zr}$ .

### 7.1.3 Early Solar System (ESS): the short-lived radioactivities problem

In this Section, we want to verify the hypothesis that a single low mass AGB star had contaminated the protosolar nebula right before its collapse (as suggested by [176]), by comparing the measured early solar system abundances of different short-lived isotopes to the predicted surface composition of our solar metallicity model. Before explaining the procedure we follow, we describe the nucleosynthetic processes responsible of stellar surface enrichments of  $^{26}\text{Al}$ ,  $^{41}\text{Ca}$ ,  $^{60}\text{Fe}$  and  $^{107}\text{Pd}$ .

Ground state  $^{26}\text{Al}$  has a half-life of  $7.16 \times 10^5$  years and is efficiently produced in the H-burning shell by proton captures on  $^{25}\text{Mg}$ . The surface is firstly enriched of freshly synthesized  $^{26}\text{Al}$  when the convective envelope partially erodes the H-burning shell (first bump in the  $^{26}\text{Al}$  profile in Fig. 7.13) and, later on, as a consequence of TDU episodes. Note that

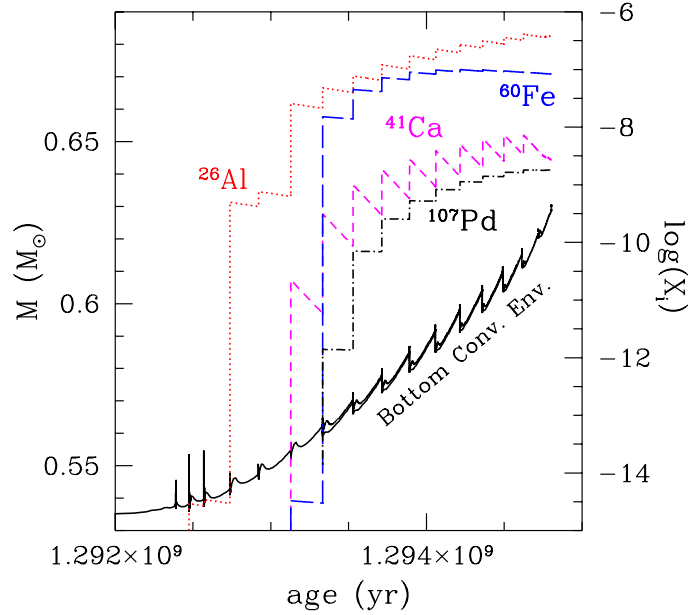


Figure 7.13 TP-AGB surface evolution of  $^{26}\text{Al}$ ,  $^{41}\text{Ca}$ ,  $^{60}\text{Fe}$  and  $^{107}\text{Pd}$  ( $M = 2M_{\odot}$  with solar metallicity).

a stellar layer exposed to a neutron flux is substantially depleted in  $^{26}\text{Al}$ , because of the large neutron-capture cross section of this isotope. This happens during both the radiative and convective  $^{13}\text{C}$  burnings as well as during the convective  $^{22}\text{Ne}$  burnings. When the temperature at the bottom of the convective shells generated by TPs exceeds  $T_8 \sim 2.7$ , the  $^{26}\text{Al}(n,p)^{26}\text{Mg}$  reaction efficiently destroys the  $^{26}\text{Al}$ . In our solar metallicity model this condition is attained only toward the end of the AGB phase, so that  $^{26}\text{Al}$  left in the H-burning shell ashes is largely preserved (with the exception of the thin layer where the radiative  $^{13}\text{C}$  burning takes place). For this reason we found a substantial surface enhancement of  $^{26}\text{Al}$ .

The appearance at the surface of  $^{41}\text{Ca}$  and  $^{60}\text{Fe}$  is simultaneous with the occurrence of the first TDU episode (see Fig. 7.13). As already recalled, the high  $^{60}\text{Fe}$  production we obtain is a direct consequence of the engulfment into the convective zone generated by the next TP of the  $^{13}\text{C}$  contained in the first  $^{13}\text{C}$ -pocket. The final surface isotopic ratio  $^{60}\text{Fe}/^{56}\text{Fe}$  we obtain in the solar metallicity model is equal to  $6.5 \times 10^{-5}$ , about 15 times higher than the value obtained in the case of the *standard* radiative  $^{13}\text{C}$ -burning (see for a comparison Table 4 of [176]). On the contrary, in the  $Z=1 \times 10^{-4}$  model, no cool  $^{13}\text{C}$  pockets are found (see Section 7.2).

Concerning the  $^{41}\text{Ca}$  nucleosynthesis, the equilibrium value between production and destruction terms ( $^{41}\text{Ca}/^{40}\text{Ca}\sim 10^{-2}$ ) is normally attained when a consistent amount of neutrons is available. Thus, an excess of  $^{41}\text{Ca}$  can only be obtained in the case of a very small neutron flux. This occurs when the  $^{13}\text{C}$  left in the He-rich intershell by the H-burning during the Early-AGB phase is burnt by  $\alpha$  captures at the beginning of the thermally-pulsing phase, before the occurrence of the first TDU episode.

The  $^{107}\text{Pd}$  is mainly synthesized during the *standard* radiative  $^{13}\text{C}$  burning inside  $^{13}\text{C}$ -pockets, when isotopes are exposed to large neutron exposures. The more the number of radiative  $^{13}\text{C}$  burning episodes is, the larger the  $^{107}\text{Pd}$  abundance in the envelope is.

Under the hypothesis that the protosolar nebula was contaminated by a single AGB star, we follow the procedure described in [176]: we adjust the isotopic ratios at the end of our model by assuming a dilution factor ( $f$ ) and a delay time ( $\Delta$ ) between the end of the AGB phase and the beginning of the pollution process (see Table 7.2). We use the  $\Delta$  assumed in [176] (see their Table 5) and we tune the dilution factor in order to match the Pd isotopic ratio. We find too low Al, Ca and Fe isotopic ratios with respect to ESS measurements.

The situation is completely different if we analyse the "relative" isotopic enhancements just after the  $2^{nd}$  TDU: at that epoch the internal layers has suffered a unique low neutron exposure due to the convective  $^{13}\text{C}$  burning ( $\delta\tau \sim 0.05 \text{ mbarn}^{-1}$ ), avoiding in such a way the later contribution from radiative  $^{13}\text{C}$  burnings (which strongly increase the Pd isotopic ratio). We report in Table 7.2 (column 4) the isotopic ratios after the  $2^{nd}$  TDU, obtained by adjusting again the two free parameters. We found an agreement for Ca, Fe and Pd isotopic ratios, but a too low  $^{26}\text{Al}/^{27}\text{Al}$  turns out. We could however invoke the occurrence

Isot. Ratio	ESS Inventory	END AGB <sup>(a)</sup>	$2^{nd}$ TDU <sup>(b)</sup>
$^{26}\text{Al}/^{27}\text{Al}$	$5 \times 10^{-5}$	$3.3 \times 10^{-7}$	$1.0 \times 10^{-5}$
$^{41}\text{Ca}/^{40}\text{Ca}$	$1.5 \times 10^{-8}$	$5.2 \times 10^{-11}$	$1.5 \times 10^{-8}$
$^{60}\text{Fe}/^{56}\text{Fe}$	$(2 \div 20) \times 10^{-7}$	$4.4 \times 10^{-9}$	$1.9 \times 10^{-7}$
$^{107}\text{Pd}/^{108}\text{Pd}$	$2.0 \times 10^{-5}$	$\equiv 2.0 \times 10^{-5}$	$\equiv 2.0 \times 10^{-5}$

<sup>(a)</sup>  $f_1=1.6 \times 10^{-4}$ ;  $\Delta_1=0.68 \text{ Myr}$ .

<sup>(b)</sup>  $f_2=1.9 \times 10^{-2}$ ;  $\Delta_2=0.25 \text{ Myr}$ .

Table 7.2 Measured and predicted isotopic ratios involving short-lived isotopes. (see text for details).

of Cool Bottom Process (CBP), a slow deep circulation taking place in the radiative region

located between the H-burning shell and the inner border of the convective envelope. This mechanism, supposed to work both during the RGB [35] as well during the AGB phase [120] of low mass stars, efficiently produces  $^{26}\text{Al}$  at the base of the convective envelope, therefore enhancing its surface abundance.

Our guess is that the astrophysical source polluting the ESS was a lower mass AGB star ( $1.3\div 1.5 M_{\odot}$ ): in that case the number and the strength of the TDU episodes would decrease and the final isotopic distribution could be similar to the one obtained after the 2<sup>nd</sup> TDU episode of our  $M = 2 M_{\odot}$  (provided the occurrence of the first convective  $^{13}\text{C}$  burning, needed to increase the  $^{60}\text{Fe}$  abundance). This hypothesis, based on strong *ad hoc* assumptions, has however to be verified by a full stellar model.

## 7.2 Toward lower metallicities

In the last years, a large number of high-resolution spectroscopic observations of very metal-poor C- and s-rich stars has been carried out. The present generation of halo stars

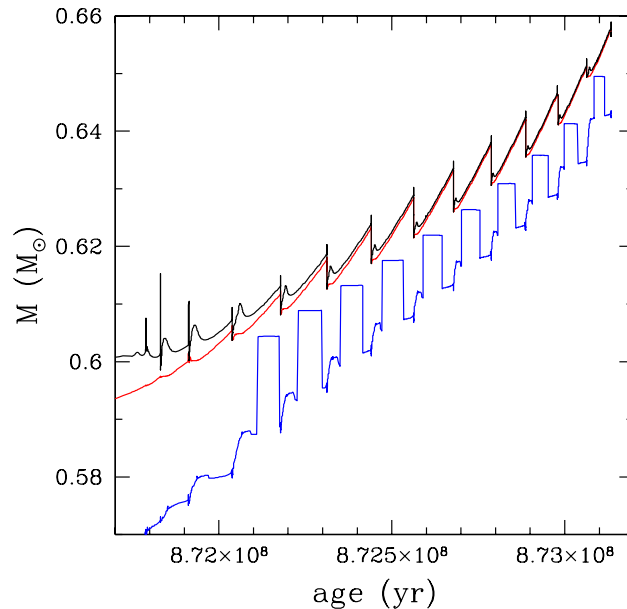


Figure 7.14 The evolution throughout the TP-AGB phase of a star with initial mass  $M = 2 M_{\odot}$  and  $Z=1\times 10^{-3}$ .

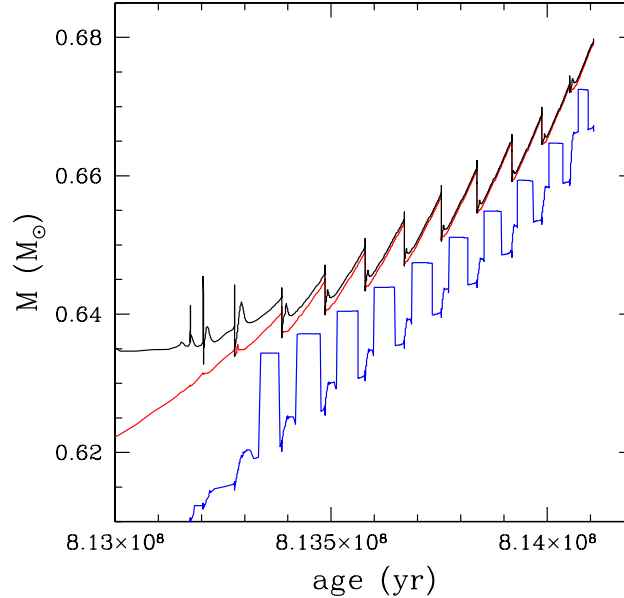


Figure 7.15 The evolution throughout the TP-AGB phase of a star with initial mass  $M = 2 M_{\odot}$  and  $Z=1 \times 10^{-4}$ .

is old ( $\sim 14$  Gyr) and, therefore, is made of low mass objects ( $M < 0.9 M_{\odot}$ ). Then, when a low mass star reaches the AGB, its envelope is so small that the TDU never takes place. However, available spectroscopic surveys for very metal-poor stars ([16], [39]) found that  $\sim 20\%$  to  $30\%$  of the candidates ( $[\text{Fe}/\text{H}] < -2.5$ ) are carbon rich. These stars are probably low mass dwarfs or giants, with a lifetime comparable with the age of the Galaxy, belonging to binary systems. It is possible that in most cases the C enhancement is the result of an ancient accretion process (by stellar wind or Roche lobe overflow [95]) from a more massive AGB companion (now a white dwarf). In such a case, also the products of the neutron capture nucleosynthesis were accreted onto the secondary star. High-resolution spectroscopy of metal-poor C-rich stars largely confirms such a qualitative expectation. However, the precise prediction of the heavy element enhancements at the surface of the secondary star is more complex than previously sketched. We have to recall that we are looking at the intershell material that was mixed with the envelope of the primary AGB stars during the various TDU episodes and, later on, further diluted within the pristine material of the envelope of the secondary star. If this secondary star (actually

the C-rich object presently detected), is evolved off the main sequence, this late dilution may be particularly efficient. In addition, the amount of mass accreted depends on the orbital parameters of the system that are, in most cases, unknown.

In order to investigate the s-process distributions of low metallicity AGB stars, we have calculated an intermediate ( $Z=1\times 10^{-3}$ ) and a low metallicity model ( $Z=1\times 10^{-4}$ ), representative of Galactic halo stars. We follow the same presentation scheme adopted for the solar model. In Fig. 7.14 and 7.15 we report the TP-AGB evolution of the two models, while in Tables 7.3 and 7.4 we tabulate the corresponding physical quantities (columns have the same meanings as in Table 7.1). The  $Z=1\times 10^{-3}$  model has been stopped when the envelope mass was reduced down to  $M_{env}^{end} \sim 0.343M_{\odot}$ , being the final total mass  $M_{tot}^* \sim 1M_{\odot}$  (the last TDU episode occurs when  $M_{env} = 0.579M_{\odot}$ ). Concerning the  $Z=1\times 10^{-4}$  calculation, we stop the evolution when  $M_{env}^{end} \sim 0.196M_{\odot}$  and  $M_{tot}^* \sim 0.9M_{\odot}$  (the last TDU episode occurs when  $M_{env} = 0.457M_{\odot}$ ). In both cases the final envelope composition is therefore frozen.

In low mass AGBs, the  $^{13}\text{C}(\alpha, n)^{16}\text{O}$  (the main source of neutrons) is primary-like, i.e. not directly affected by the metallicity of the pristine material. Nevertheless, the iron seeds scale with the metallicity, so that the lower the metallicity the larger is the number of neutrons available per seed. As a result, at low metallicities, most of the seeds are converted into  $^{208}\text{Pb}$ , at the termination point of the s-process fluence. In metal-poor AGB star experiencing a few TDU episodes, a consistent enhancement of lead is therefore expected [61, 24]. Trends illustrated in Fig. 7.16 and Fig. 7.17 confirm the previous sentence: a consistent lead production is found in both models, leading to a final  $[\text{Pb}/\text{Fe}]$  equal to 2.56 and 2.61, in the  $Z=1\times 10^{-3}$  and the  $Z=1\times 10^{-4}$  models, respectively (see Appendixes B.2 and B.3.1 for detailed data pulse by pulse).

Another peculiarity of low metallicity models is the strong carbon surface enrichment: this is the direct consequence of the occurrence of TDU episodes, when the convective envelope penetrates into the  $^{12}\text{C}$ -rich He-intershell. The lower the metallicity is, the larger surface carbon overabundances are found:  $[\text{C}/\text{Fe}] \sim 1.7$  at  $Z=1\times 10^{-3}$  and  $[\text{C}/\text{Fe}] \sim 2.6$  at  $Z=1\times 10^{-4}$ . Similar large overabundances are not found for nitrogen: we in fact obtain  $[\text{N}/\text{Fe}] \sim 0.4$  and  $[\text{N}/\text{Fe}] \sim 0.6$  respectively. On the contrary, a lot of observed low metallicity s-rich stars usually show N-rich surface envelopes. The enhancement of nitrogen could be due to the hot bottom burning, but this would exclude low mass AGB stars that have a too cool temperature at the base of the convective envelope. The activation of the CBP process during the AGB (see Section 7.1.3) could contribute to the systematic occurrence

TDU	$M_{tot}$	$M_H$	$M_{env}$	$M_{TDU}$	$\Delta M_{Pulse}$	$\Delta M_H$
1	1.93E+00	6.05E-01	1.33E+00	5.00E-04	2.52E-02	5.20E-03
2	1.92E+00	6.12E-01	1.31E+00	2.50E-03	2.37E-02	7.00E-03
3	1.91E+00	6.18E-01	1.29E+00	4.20E-03	2.28E-02	8.30E-03
4	1.89E+00	6.23E-01	1.27E+00	5.40E-03	2.20E-02	9.50E-03
5	1.88E+00	6.28E-01	1.25E+00	6.10E-03	2.13E-02	1.04E-02
6	1.84E+00	6.33E-01	1.21E+00	6.40E-03	2.05E-02	1.10E-02
7	1.77E+00	6.38E-01	1.13E+00	6.50E-03	1.98E-02	1.11E-02
8	1.65E+00	6.42E-01	1.01E+00	6.20E-03	1.90E-02	1.10E-02
9	1.46E+00	6.46E-01	8.14E-01	5.10E-03	1.81E-02	1.05E-02
10	1.23E+00	6.51E-01	5.79E-01	1.40E-03	1.76E-02	9.60E-03
TOT.				4.43E-02		

TDU	$\lambda$	$r$	$\Delta t_{ip}$	$T_{max}^{TP}$	$Z_{sup}$	C/O
1	9.61E-02	6.15E-01	1.23E+05	2.49E+08	1.05E-03	0.4
2	3.57E-01	7.26E-01	1.39E+05	2.64E+08	1.48E-03	1.7
3	5.06E-01	6.36E-01	1.34E+05	2.75E+08	2.30E-03	3.9
4	5.68E-01	5.68E-01	1.28E+05	2.84E+08	3.36E-03	6.4
5	5.87E-01	5.16E-01	1.22E+05	2.92E+08	4.56E-03	8.9
6	5.82E-01	4.68E-01	1.15E+05	2.97E+08	5.80E-03	11.2
7	5.86E-01	4.55E-01	1.08E+05	3.01E+08	7.09E-03	12.5
8	5.64E-01	4.32E-01	1.00E+05	3.04E+08	8.39E-03	15.6
9	4.86E-01	4.14E-01	9.23E+04	3.05E+08	9.72E-03	17.6
10	1.46E-01	4.49E-01	8.37E+04	3.02E+08	1.03E-02	18.4

Table 7.3 Data relative to a model with initial mass  $M=2M_{\odot}$ ; intermediate metallicity case:  $(C/O)_{ini} = 0.54$ ,  $(C/O)_{FDU} = 0.30$ ,  $Z=1 \times 10^{-3}$ .

TDU	$M_{tot}$	$M_H$	$M_{env}$	$M_{TDU}$	$\Delta M_{Pulse}$	$\Delta M_H$
1	1.96E+00	6.40E-01	1.32E+00	2.70E-03	1.91E-02	5.20E-03
2	1.95E+00	6.45E-01	1.31E+00	4.10E-03	1.90E-02	7.20E-03
3	1.94E+00	6.49E-01	1.29E+00	4.80E-03	1.84E-02	8.20E-03
4	1.92E+00	6.53E-01	1.27E+00	5.50E-03	1.79E-02	9.00E-03
5	1.88E+00	6.57E-01	1.22E+00	5.80E-03	1.74E-02	9.40E-03
6	1.79E+00	6.61E-01	1.13E+00	5.80E-03	1.69E-02	9.50E-03
7	1.63E+00	6.65E-01	9.65E-01	5.20E-03	1.63E-02	9.50E-03
8	1.41E+00	6.69E-01	7.40E-01	3.70E-03	1.55E-02	9.10E-03
9	1.13E+00	6.73E-01	4.57E-01	4.00E-04	1.44E-02	8.10E-03
TOT.				3.80E-02		

TDU	$\lambda$	$r$	$\Delta t_{ip}$	$T_{max}^{TP}$	$Z_{sup}$	C/O
1	5.19E-01	7.12E-01	1.10E+05	2.64E+08	5.05E-04	11.6
2	5.69E-01	6.32E-01	1.00E+05	2.77E+08	1.22E-03	22
3	5.85E-01	5.54E-01	9.37E+04	2.87E+08	2.15E-03	28.1
4	6.11E-01	5.08E-01	9.10E+04	2.95E+08	3.20E-03	31.9
5	6.17E-01	4.66E-01	8.68E+04	3.01E+08	4.31E-03	34.7
6	6.10E-01	4.32E-01	8.26E+04	3.06E+08	5.48E-03	37.5
7	5.47E-01	4.02E-01	7.78E+04	3.07E+08	6.66E-03	39.8
8	4.07E-01	4.13E-01	7.17E+04	3.10E+08	7.78E-03	42
9	4.94E-02	4.38E-01	6.46E+04	3.09E+08	8.04E-03	42.6

Table 7.4 Data relative to a model with initial mass  $M=2M_{\odot}$ ; low metallicity case:  $(C/O)_{ini} = 0.54$ ,  $(C/O)_{FDU} = 0.26$ ,  $Z=1\times 10^{-4}$ .

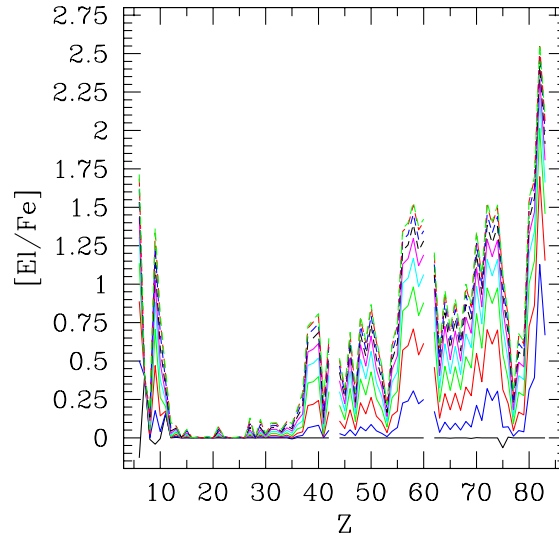


Figure 7.16 Pulse by pulse surface composition, in the usual spectroscopic notation, for the  $M = 2M_{\odot}$  model with  $Z = 1 \times 10^{-3}$ .

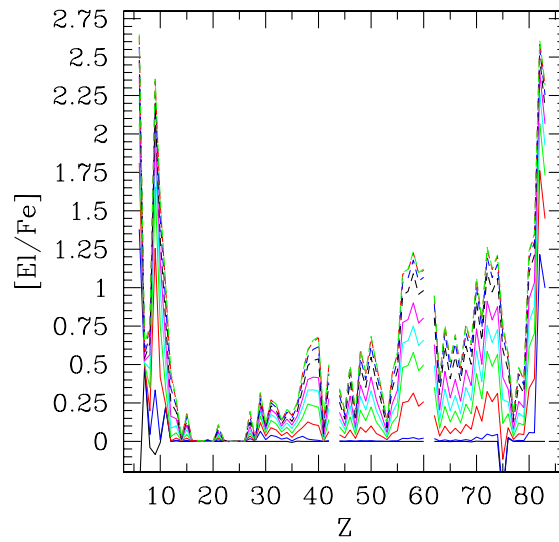


Figure 7.17 Pulse by pulse surface composition, in the usual spectroscopic notation, for the  $M = 2M_{\odot}$  model with  $Z = 1 \times 10^{-4}$ .

of the nitrogen overabundance. This effect is not taken into account in our calculations, but it could have dramatic consequences on the determination of the opacity coefficients (see Section 8.2). Moreover, [81] (see also [56]) suggested that the scarcity of CNO in very

Metallicity	[ls/Fe]	[hs/Fe]	[hs/ls]	[Pb/Fe]	[Pb/hs]
$1.5 \times 10^{-2}$	1.12	0.86	-0.26	0.53	-0.33
$1 \times 10^{-3}$	0.77	1.42	0.65	2.56	1.14
$1 \times 10^{-4}$	0.65	1.13	0.48	2.61	1.48

Table 7.5 S-process indexes for the three computed models.

metal-poor stars may allow the convective zone generated by the first strong TP to ingest some protons from the envelope. In this case, a hot CN cycle takes place within the He-rich intershell and consistent amounts of  $^{13}\text{C}$  and  $^{14}\text{N}$  are produced. More recently [92], on the basis of detailed stellar models computations, proposed that a peculiar s-process nucleosynthesis, characterized by a high neutron density, could be activated by  $\alpha$ -capture on the freshly synthesized  $^{13}\text{C}$ . The detailed s-process nucleosynthesis for a low mass ( $M=1.5M_{\odot}$ )

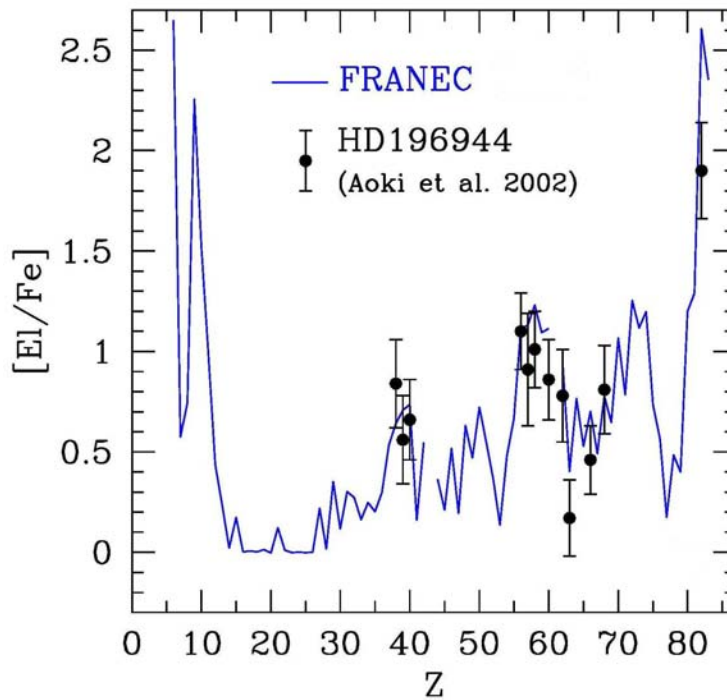


Figure 7.18 Comparison between the final surface composition of the  $M = 2M_{\odot}$  model with  $Z=1 \times 10^{-4}$  and spectroscopic data of HD196944 [9].

Star	[Fe/H]	[ls/Fe]	[hs/Fe]	[hs/ls]	[Pb/Fe]	[Pb/hs]
CS 22880-074 <sup>(a)</sup>	-1.93	0.16	1.16	1.00	1.90	0.74
CS 22898-027 <sup>(a)</sup>	-2.26	0.87	2.14	1.27	2.84	0.70
CS 29526-110 <sup>(a)</sup>	-2.38	1.11	1.90	0.79	3.30	1.40
CS 31062-050 <sup>(a)</sup>	-2.31	1.02	2.23	1.21	2.90	0.67
CS 31062-050 <sup>(b)</sup>	-2.41	0.67	2.02	1.35	2.81	0.79
HD 196944 <sup>(a)</sup>	-2.25	0.61	0.89	0.28	1.90	1.01
HD 196944 <sup>(c)</sup>	-2.40	0.60	0.85	0.25	2.10	1.25
HD 187861 <sup>(c)</sup>	-2.30	1.30	1.98	0.68	3.30	1.32
HD 198269 <sup>(c)</sup>	-2.20	0.40	1.38	0.98	2.40	1.02
HD 201626 <sup>(c)</sup>	-2.10	0.90	1.65	0.75	2.60	0.95
HD 224959 <sup>(c)</sup>	-2.20	1.00	2.02	1.02	3.10	1.08
V-Ari <sup>(c)</sup>	-2.40	1.10	1.60	0.50	1.20	-0.40
HE 2148-1247 <sup>(d)</sup>	-2.30	1.15	2.23	1.08	3.12	0.89
CS 22948-27 <sup>(e)</sup>	-2.47	1.00	2.25	1.25	2.72	0.47

<sup>(a)</sup> Aoki et al. 2002 [9]

<sup>(b)</sup> Johnson & Bolte 2004 [94]

<sup>(c)</sup> Van Eck et al. 2003 [166]

<sup>(d)</sup> Cohen et al. 2003 [42]

<sup>(e)</sup> Barbuy et al. 2005 [13]

Table 7.6 S-process indexes in a selected sample of low metallicity stars.

and very metal-poor ( $Z=5\times 10^{-5}$ ) AGB model has been calculated by [157]. They found that the ingestion of proton into the convective intershell region and the subsequent deep TDU provide the required mechanism to explain the N enhancement, but the high neutron density is maintained only for a very short time (few days), with negligible consequences on the overall surface overabundances.

Another interesting feature emerging from these low metallicity models is the increasing fluorine overabundance with decreasing the metallicity ( $[F/Fe]=1.4$  at  $Z=1\times 10^{-3}$  and  $[F/Fe]=2.4$  at  $Z=1\times 10^{-4}$ ). This effect is due to the primarity of the  $^{13}\text{C}$  pocket with respect to the H-burning ashes (see Section 9.2 for details). This result adds support to the fact that AGB stars are an important source of Galactic fluorine (see [133]).

The sodium surface enrichment presents features similar to fluorine, resulting  $[Na/Fe]=0.44$  at  $Z=1\times 10^{-3}$  and  $[Na/Fe]=1.0$  at  $Z=1\times 10^{-4}$ . Recent determinations of two reaction rates involved in the  $^{23}\text{Na}$  nucleosynthesis ([77],[78]) could however decrease these values (see Section 9.3).

Far from concluding that a single choice of the many model parameters ( $M$ ,  $Z$ , convective

efficiency, mass loss, etc.) can reproduce the observed abundance spread of low metallicity stars, in Fig. 7.18 we tentatively compare the final distribution of our  $Z=1\times 10^{-4}$  model with the abundances of HD196944 [9]. A general agreement for ls and hs elements is found, but a too low theoretical [Pb/Fe] results. It has however to be noticed that low metallicity s-process enriched stars show consistent enhancements in the hs elements, spanning in the range  $0.8 < [\text{hs}/\text{Fe}] < 2.3$  (for a comparison between spectroscopic data and theoretical s-process distribution in these stars see [18], [19], [91] and [62]). In Table 7.5 we resume the final s-process indexes characterizing the  $Z=1\times 10^{-3}$  and the  $Z=1\times 10^{-4}$  models (for the sake of clarity we also tabulate data relative to the solar metallicity model), while in Table 7.6 we report the observational counterpart, relative to a sample of low metallicity stars. The adopted criterion to identify the sample reported in this latter Table is  $Z_{star} \sim 1\times 10^{-4}$ , corresponding to  $[\text{Fe}/\text{H}] \simeq -2.2$  (we fix a range of  $\pm 0.3$  dex, in the logarithmic scale). Even if our final [hs/Fe] value lays within the observed range, the majority of these stars show larger values with respect to our theoretical expectation. This could be ascribed to the fact that, in our model, the  $^{13}\text{C}$  pocket becomes more and more narrow with increasing the TP number, thus leading to a reduced s-process production within the He intershell along the AGB phase (we already evidenced this phenomenon in Section 7.1, describing the solar metallicity model). A second, more reliable, explanation could be identified in the small number of TPs, which is mainly determined by the adopted mass loss rate. We already motivated our choice in Section 4.5, but we want to point out the effect of the adopted interpolation in metallicity of the opacity coefficients (see Section 3.3). While in the  $Z=Z_{\odot}$  model the envelope metallicity slightly changes (see Table 7.1), in the  $Z=1\times 10^{-4}$  model it results drastically modified (a factor 4 just after two TPs with TDU, see Table 7.4). The interpolation of the opacity coefficient is efficient if the relative metal distribution is preserved, but it has to be reminded that, in the  $Z=1\times 10^{-4}$  model, the heavy elements distribution after the first TDU results quite entirely (99%) composed by  $^{12}\text{C}$  (after the first TDU episode, the envelope  $\text{C}/\text{O} > 11$ ).

Therefore, in order to evaluate the validity of our opacity treatment, we need to study the effects induced by a variation of the relative element composition on the opacity coefficients. In Chapter 8 we present these tests in detail.

### 7.3 Yields

One of the aims of this work is to provide a complete and uniform set of low mass AGB yields, comprehensive of all chemical species, starting from hydrogen up to the Pb-Bi s-process ending point. In Appendix A we present our results, without comparing our data with extant compilations. This choice rises from two basic considerations:

- the small number of computed models (we didn't span in the mass range at all);
- the different initial compositions (we adopt a depleted CNO with respect to data presented by [7], this implying a different solar metallicity with respect to the majority of the extant compilations. Moreover, we didn't analyse at all the metallicity range of the Magellanic Clouds).

According to the definition of stellar yield [162], we can write (in solar mass units):

$$M_y(k) = \int_0^{\tau(M_i)} [X(k) - X^0(k)] \frac{dM}{dt} dt \quad (7.1)$$

where  $dM/dt$  is the adopted mass loss rate, while  $X(k)$  and  $X^0(k)$  stand for the current and the initial abundance of the element  $k$  respectively. In calculating the yields, we hypothesize that the star is losing its entire envelope at the end of the AGB phase by means a single strong and quick mass loss episode.



## Chapter 8

# The importance of the opacity treatment in AGB models

*In this Chapter we discuss the effects induced by a different treatment of the opacity coefficients in the cool envelopes of AGB stars. In particular, we discriminate the contribution from different elements to atomic opacities. We follow the TP-AGB evolution of a  $Z = 1 \times 10^{-4}$  model, computed by using in the envelope opacity coefficients at fixed metallicity, and we compare the results with the low metallicity model presented in the previous Chapter. Moreover, we comment the effects due to molecular opacities in low temperatures regions ( $10^4 < T < 10^3 K$ ), characterizing the convective external layers of AGB stars.*

Main contributors to atomic opacities are carbon and iron: in order to understand which source dominates in the envelopes of AGB stars, we perform some tests by varying their relative abundances. By means of the OPAL web-site facility we downloaded opacity tables with scaled solar composition and tables where we set the carbon amount equal to the 99% of the metal content: consequently, the abundances of the other elements roughly result divided by a factor 100. For each set we dispose of tables at different metallicities (from  $Z=0$  to  $Z=0.04$ ), containing opacity coefficients calculated with different hydrogen mass fractions (from  $X=0$  to  $X=1$ ). These coefficients are tabulated as a function of temperature (we deal with atomic opacities, therefore the temperature range is  $4.05 < \log T < 8.7$ ) and density (the adopted variable is  $R = \rho / T_6^3$ , where  $T_6$  is the temperature in units of millions degrees). We then extract from our  $Z=1 \times 10^{-4}$  model an envelope structure (by calculating the  $R$  values needed to identify the right opacity coefficient) after the occurrence of the

$3^{rd}$  and the  $8^{th}$  TDU episodes. The surface metallicities are  $Z \sim 2 \times 10^{-3}$  and  $Z \sim 8 \times 10^{-3}$  respectively (see Table 7.4), while the hydrogen abundance is  $X \sim 0.7$  in both cases.

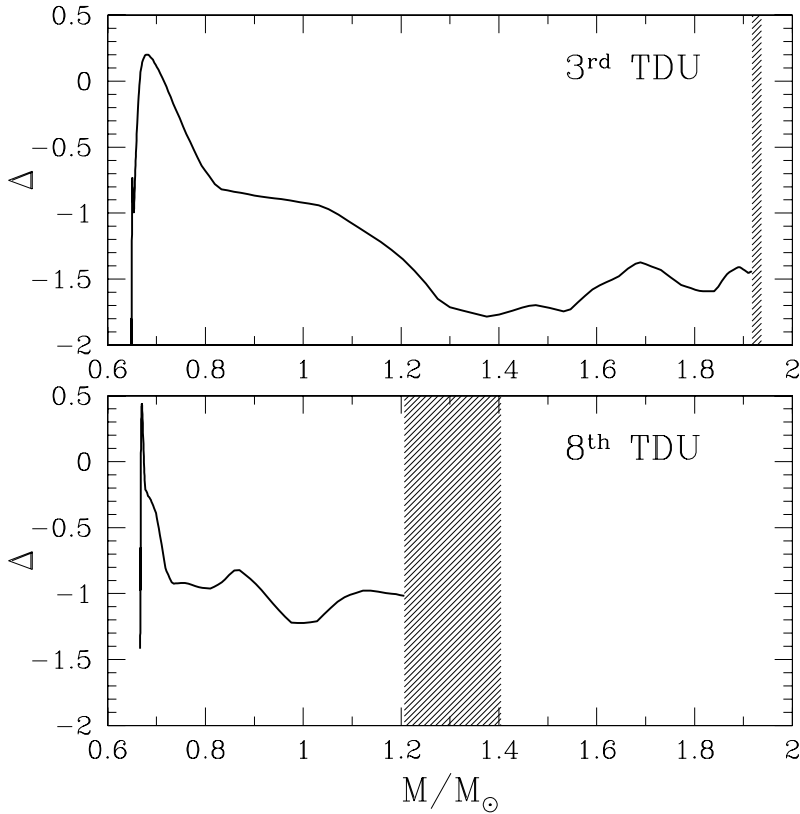


Figure 8.1 Logarithmic relative differences in atomic opacity coefficients obtained by comparing solar scaled and C-enhanced opacity tables in the temperature range  $4.05 < \log T < 8.7$ . The comparison has been carried out on the envelope structure of the  $M = 2M_{\odot}$  model with initial  $Z = 1 \times 10^{-4}$ , after the  $3^{rd}$  (upper Panel) and the  $8^{th}$  (lower Panel) TDU episodes (see text for details).

In Figure 8.1 we plot the differences in opacity coefficients, obtained by using scaled solar tables (with metal contents close to the two envelope compositions) with the corresponding C-enhanced ones. Shaded areas represent the external layers, characterized by temperatures lower than 11220 K ( $\log T = 4.05$ ): while after the  $3^{rd}$  TDU episode the envelope is almost entirely hotter than 11220 K, after the  $8^{th}$  TDU low temperatures cover about the 25% of its extension (note that in this latter model the total mass of the star

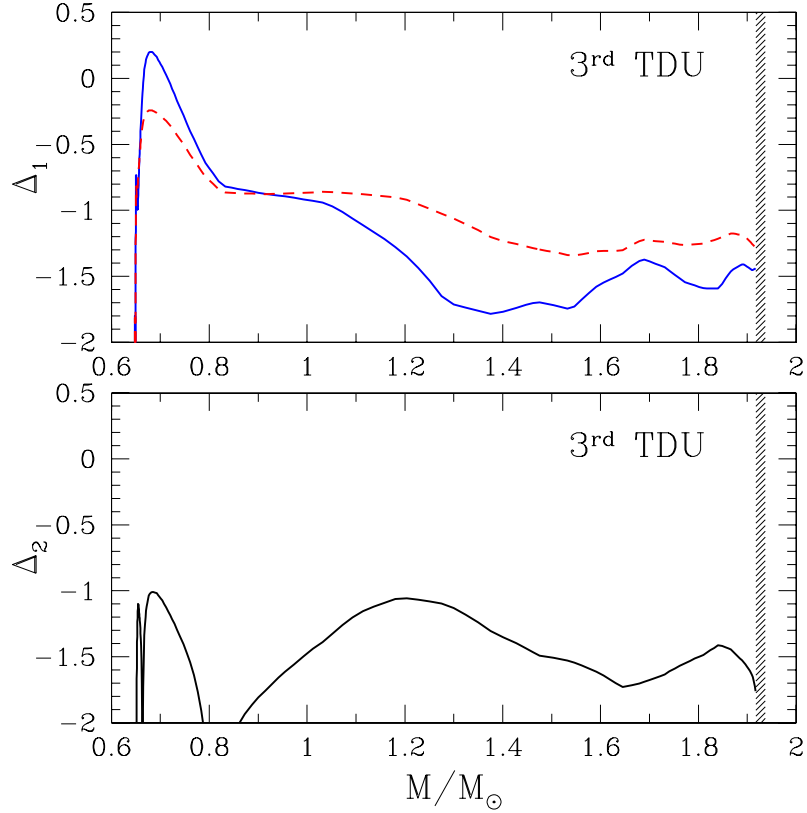


Figure 8.2 Logarithmic relative differences in atomic opacity coefficients obtained by comparing solar scaled and C-enhanced opacity tables of different metallicities. This test has been carried out on the envelope structure of the  $M = 2M_{\odot}$  model with initial  $Z=1\times 10^{-4}$ , after the 3<sup>rd</sup> with TDU (see text for details).

has been already eroded by radiative winds). We define  $\Delta$  as:

$$\Delta = \log \left( \left| \frac{\kappa_{c.en.} - \kappa_{so.s.}}{\kappa_{c.en.}} \right| \right) \quad (8.1)$$

where indexes *so.s.* and *c.en.* refer to solar scaled and C-enhanced tables, respectively. The opacities obtained by enhancing the carbon, but maintaining fixed the metallicity, are lower with respect to the solar scaled tables. Differences up to a factor 4 are found in the inner regions of the convective envelope. It has to be mentioned that, at fixed metallicity, the iron amount in the solar scaled tables is about a factor 100 more abundant with respect to the C-enhanced ones, therefore the resulting larger opacities could be directly correlated to iron abundance.

In order to check this hypothesis, we calculate, in the envelope structure after the 3<sup>rd</sup> TDU

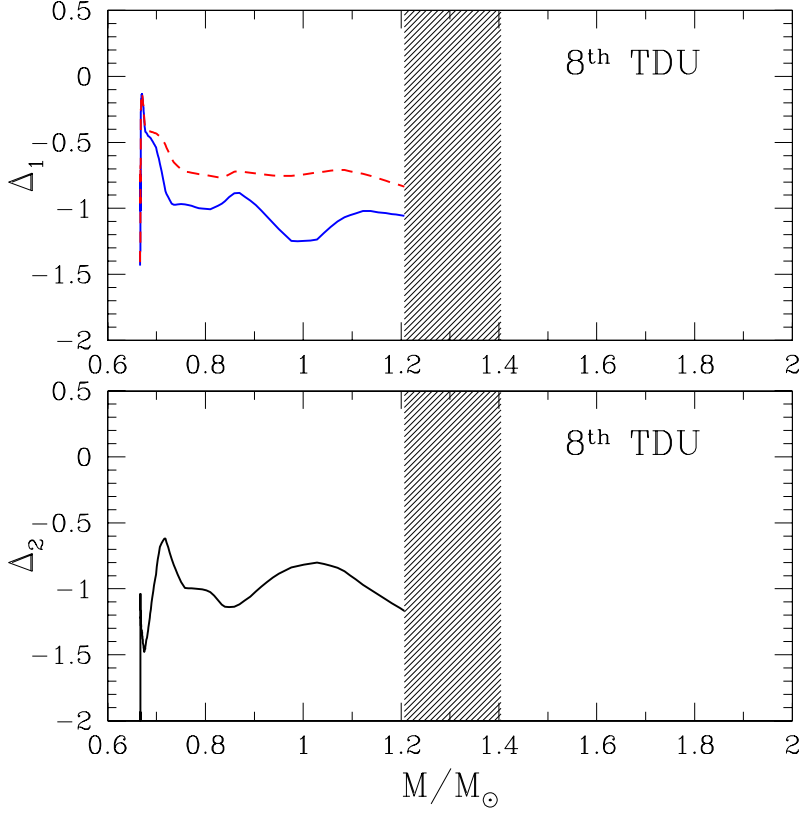


Figure 8.3 As in Fig. 8.2, but relative to the 8<sup>th</sup> with TDU.

episode, opacity differences obtained by comparing a solar scaled table at  $Z=2\times 10^{-3}$  with respect to:

- i)* a solar scaled table at  $Z=1\times 10^{-4}$  (upper panel of Figure 8.2, red dashed line);
- ii)* a C-enhanced table at  $Z=2\times 10^{-3}$  (upper panel of Figure 8.2, blue solid line).

$\Delta_1$  values are calculated as in equation 8.1:

$$\Delta_1 = \log \left( \left| \frac{\kappa_{z1m4} - \kappa_{z2m3}}{\kappa_{z1m4}} \right| \right) \quad \text{red dashed line} \quad (8.2)$$

$$\Delta_1 = \log \left( \left| \frac{\kappa_{z2m3,C-en} - \kappa_{z2m3}}{\kappa_{z2m3,C-en}} \right| \right) \quad \text{blue solid line.} \quad (8.3)$$

Moreover, in the lower panel of same figure we calculated the differences between the scaled solar table at  $Z=1\times 10^{-4}$  and the C-enhanced one at  $Z=2\times 10^{-3}$ :

$$\Delta_2 = \log \left( \frac{\kappa_{z2m3,C-en} - \kappa_{z1m4}}{\kappa_{z2m3,C-en}} \right). \quad (8.4)$$

In this latter comparison we find differences lower than 10% (equivalent to  $\Delta_2 < -1$ ). Let us notice that the iron amount in the two tables is very similar (the carbon enhancement implies in fact a reduction for other chemical species): this means that the carbon enhancement has negligible effects on the atomic opacity, which therefore results strongly dependent on the iron content. A similar comparison has been carried out for the 8<sup>th</sup> TDU case (Figure 8.3): differences between a  $Z=1\times 10^{-4}$  solar scaled table and a C-enhanced one at  $Z=8\times 10^{-3}$  are lower than 25%, corroborating the result obtained in the previous test. We can therefore conclude that, in this range of temperatures, the main contribution to opacity comes from iron, which dominates over carbon.

The interpolation in metallicity of the opacity coefficients in the envelope of giant stars could therefore be inadequate when TDU episodes occur, because the iron amount in the envelope is practically constant, while the metallicity increases, due to the large amount of dredged up  $^{12}\text{C}$ . Summing up, our opacity treatment seems to overestimate the atomic contribution to opacity in the envelope of TP-AGB stars. It is therefore worth to compute a model without interpolating the opacity coefficients (i.e. adopting, in the envelope, a table at fixed metallicity) and compare it with respect to the model described in Section 7.2.

## 8.1 Opacity effects at low metallicities

In this Section we present a comparison between two models with initial mass  $M=2M_{\odot}$  and  $Z=1\times 10^{-4}$ . The first one has been already presented in Section 7.2 (hereafter *st* case), while the second has been computed by using, in the envelope, the opacity coefficients at  $Z=1\times 10^{-4}$ , corresponding to the initial metallicity, for the entire evolution (hereafter *test* case). The computation starts from an advanced model, given that the envelope metallicity doesn't significantly change before the first TDU episode. We stop the *test* model when the envelope composition freezes out ( $M_{env} \sim 0.32 M_{\odot}$ ,  $M_{tot}^* \sim 1.1 M_{\odot}$ ). We report in Appendix A and Appendix B.3.2 the yields and the surface enrichments relative to the *test* case, respectively.

In Fig. 8.4 we report the TP-AGB phase of the *test* case: its duration is longer (about a factor 2 with respect to the *st* model), this implying a natural increase in the number of TPs followed by TDU (N=49 with respect to the 9 found in the *st* model). In order to understand the physical reasons of so different evolutions, we compare some key physical quantities characterizing the two models during the AGB phase (see Fig. 8.5), in this

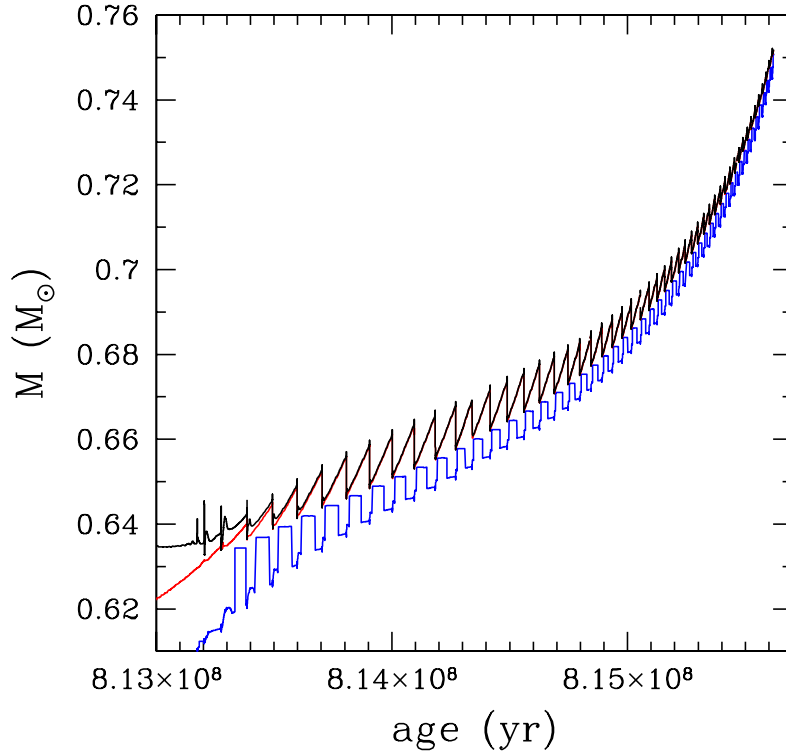


Figure 8.4 The evolution throughout the TP-AGB phase of a star with initial mass  $M = 2 M_{\odot}$  and  $Z=1 \times 10^{-4}$ . With respect to Fig. 7.15 the calculation has been performed without interpolating in metallicity the opacity coefficients.

particular instance: the total mass (upper left panel), the surface luminosity (upper right panel), the surface temperature (lower left panel) and the radius (lower right panel). Blue dotted lines relate to the *st* case, while red solid lines refer to the *test* case (the black solid line in each panel represents the common evolution of two models before the occurrence of the first TDU episode). We argue that the mass loss rate of the *test* model is less efficient with respect to the *st* case, while the surface luminosity is practically the same in the two models (it exclusively depends on the core mass [123]). On the contrary, surface temperatures and radii show completely different behaviors, the *test* case resulting always hotter and less expanded. We report in Fig. 8.6 the mass loss rate history and the derived period for the two cases. The reason for this great difference in the mass loss rate has to be

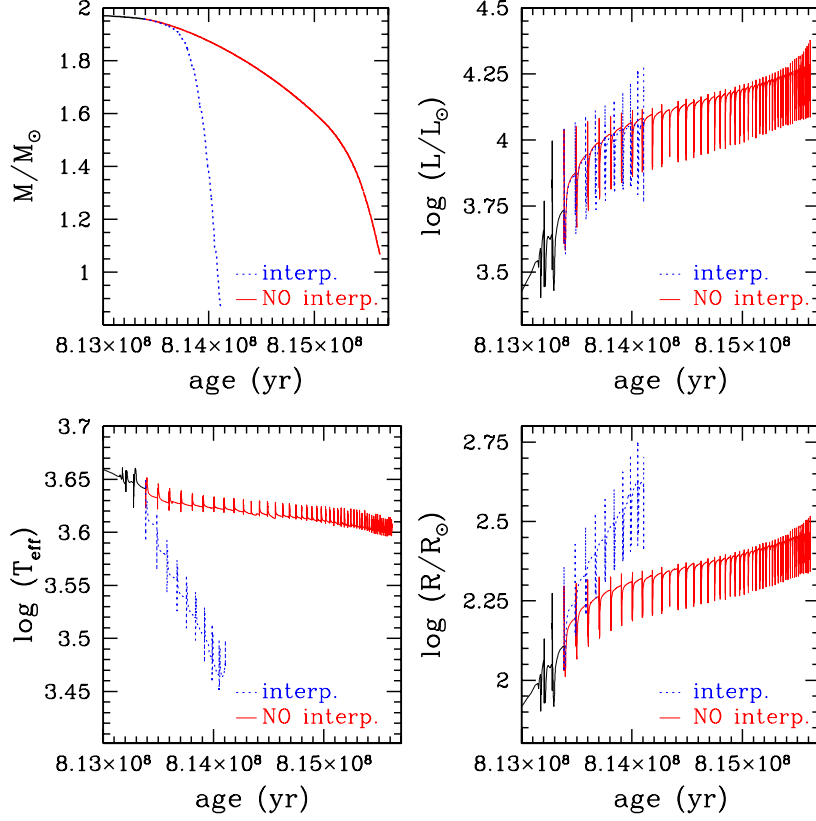


Figure 8.5 Evolution of some key physical quantities in the  $M = 2M_{\odot}$  model with initial metallicity  $Z=1\times 10^{-4}$ , computed with interpolation (blue dotted line, *st* case) and without interpolation (red solid line, *test* case) of the opacity coefficients. We report the total mass (upper left Panel), the surface luminosity (upper right Panel), the surface temperature (lower left Panel) and the radius (lower right Panel).

searched in the surface temperature evolution (see the lower left panel in Fig. 8.5). In fact, the new resulting surface temperature evolution affects both the adopted mass loss regimes, either the Reimers' formulation or the mass loss-period calibration. Concerning the first parameterization, the larger surface temperature found in the *test* case implies a lower mass rate, being  $\dot{M}_{\text{Reimers}} \propto T_{\text{eff}}^{-2}$  (the luminosity is practically constant in the two models). The mass loss rate derived by the mass loss-period calibration results depressed because of the adopted temperature- $M_K$  relation [53]: the larger the temperature is, the lower the period is, therefore leading to a lower mass loss rate (see Section 4.5). Consequently, the transition to this latter mass loss regime from the Reimers' one occurs later in the AGB evolution (see the slope change of the red solid line in the upper panel of Fig. 8.6).

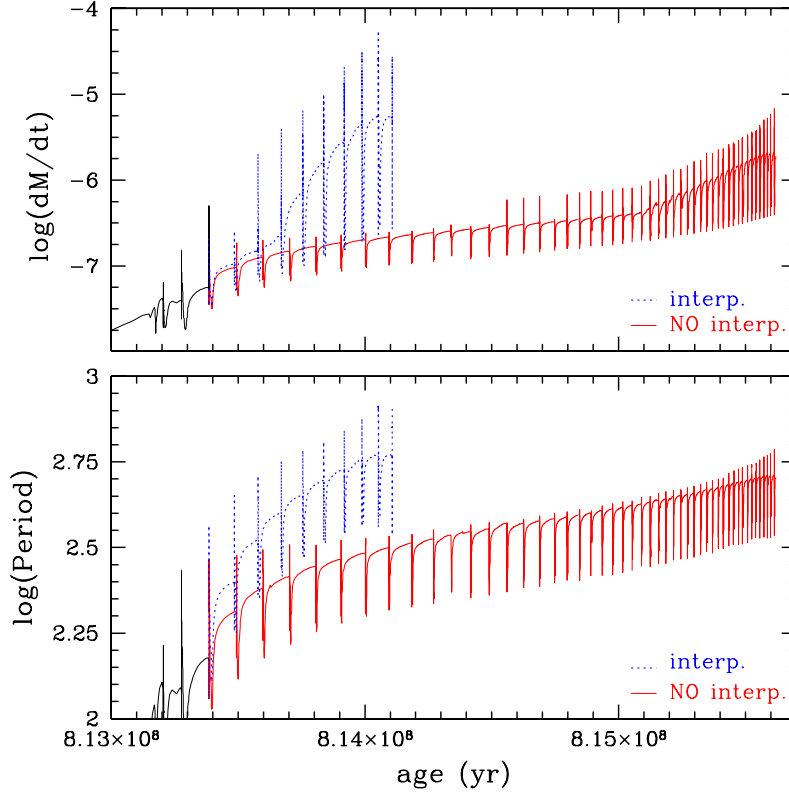


Figure 8.6 Mass loss history and derived period for the *st* case (blue dotted line) and the *test* case (red solid line).

As a consequence of so different mass-loss rate histories, in the *test* case we find a large increase of the total dredged up material during the AGB phase ( $\Delta M_{TDU}^{tot} = 1.86 \times 10^{-1} M_{\odot}$ ) with respect to the *st* case ( $\Delta M_{TDU}^{tot} = 3.80 \times 10^{-2} M_{\odot}$ , see Table 7.4 of Section 7.2). In Fig. 8.7 we report the evolution of the maximum temperature at the base of the convective zones generated by TPs (upper panel) and the dredged up mass per pulse (lower panel) during the AGB phase relative to the two cases. It appears clear how the faster reduction of the envelope mass in the *st* case strongly affects the evolution of  $\delta M_{TDU}$ , reducing the maximum attained value and depressing the further decreasing tail (evident in the *test* model). Moreover, note that the temperature attained at the base of the convective shell generated by a thermal instability is generally greater, for the same core masses, in the *test* case with respect to the *st* case: this is due to the  $T_{max}^{TP}$  dependence on the envelope mass [156].

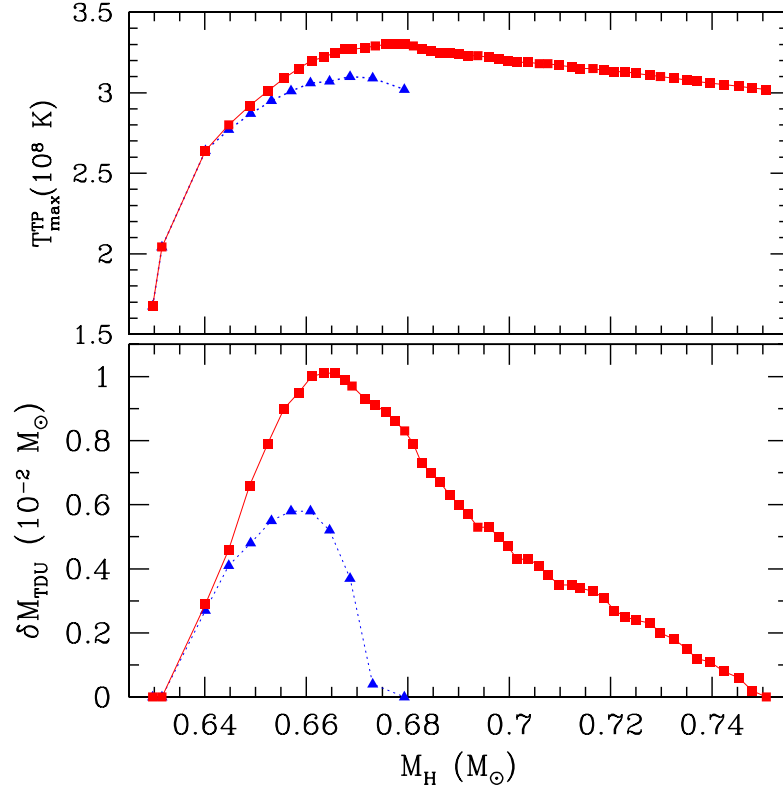


Figure 8.7 Evolution of the maximum temperature at the base of the convective zones generated by TPs (upper Panel) and of the dredged up mass per pulse (lower Panel) during the AGB phase relative to the *st* model (blue dotted lines & triangles) and the *test* model (red solid lines & squares).

The difference in mass loss rates also implies dramatic consequences on the chemical evolution of the model. In Fig. 8.8 we compare the final enhancement distributions obtained for the *test* case (red solid line) with the one characterizing the *st* case (blue dotted line): the light elements (from C to Al) and the s-process heavy elements result highly enhanced in this latter test we performed. In Table 8.1 we tabulate data corresponding to light elements. The larger carbon, oxygen, fluorine and neon surface enrichments are the direct consequences of the increased number of TDU episodes (see previous Chapters and Section 9.2 for a description of the nuclear processes at their origin). The strong final nitrogen enhancement ( $[N/Fe]=1.48$ ) is instead due to the envelope erosion, during TDU episodes, of the H shell and the underlying layers, occurring when the H-burning is switched off. This region, whose extension is  $\Delta M_{\text{tot}} \sim 10^{-4} M_\odot$ , is even more enriched in  $^{14}\text{N}$  during

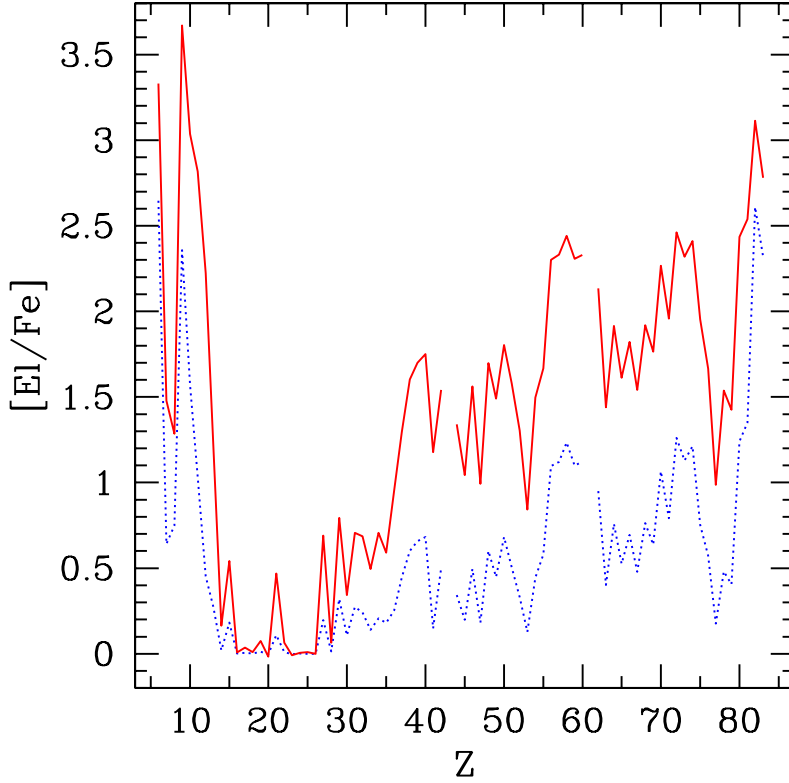


Figure 8.8 Final surface composition, in the usual spectroscopic notation, relative to the *st* case (blue dotted line) and to the *test* case (red solid line).

the AGB phase, due to the increase of  $^{12}\text{C}$  in the envelope and its conversion to  $^{14}\text{N}$  operated by the CNO cycle within the H-burning shell. The increased number of TDU episodes in the *test* case implies also a larger magnesium surface abundance: such enhancement is mainly due to neutron capture processes and to the activation of the  $^{22}\text{Ne}(\alpha, n)^{25}\text{Mg}$  and the  $^{22}\text{Ne}(\alpha, \gamma)^{26}\text{Mg}$  reactions in the He-intershell; moreover, an additional contribution to  $^{24}\text{Mg}$  comes from the proton capture on  $^{23}\text{Na}$ , occurring in the H-burning shell. Finally, the larger aluminum overabundance has to be ascribed to the same mechanism responsible for the  $^{14}\text{N}$  enhancement, involving in this case proton captures on  $^{25}\text{Mg}$  and  $^{26}\text{Al}$ . We refer to Section 9.3 for the discussion concerning the production of  $^{23}\text{Na}$  at low metallicities.

In Fig. 8.9 we show  $[\text{ls}/\text{Fe}]$  (red curves),  $[\text{hs}/\text{Fe}]$  (blue curves) and  $[\text{Pb}/\text{Fe}]$  (black curves) of the two models: dotted lines refer to the *st* case, while the solid ones to the *test* case. The resulting final overabundances in this latter model are about one order of magnitude

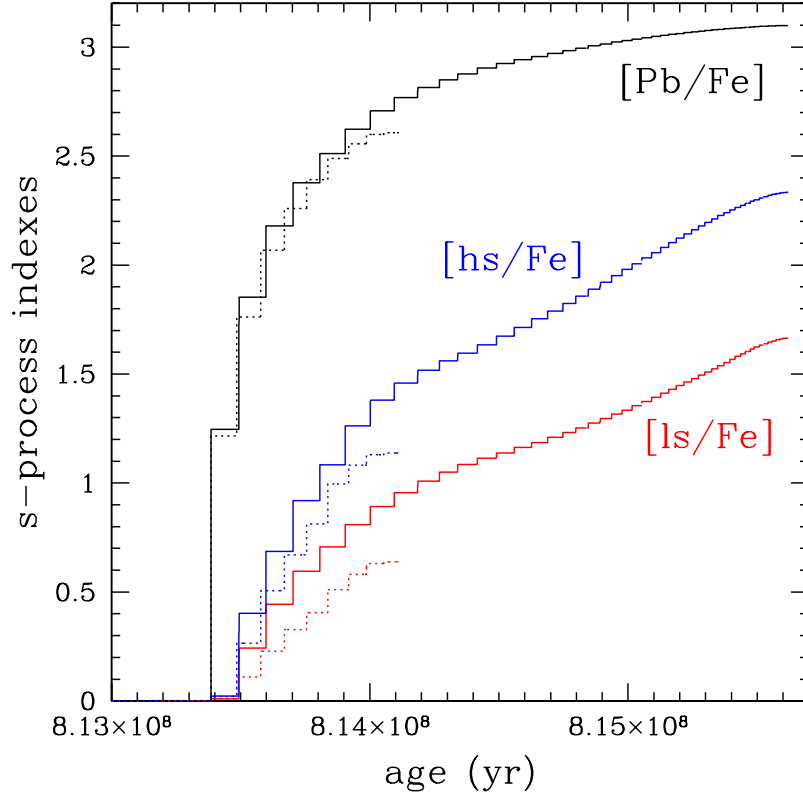


Figure 8.9 Chemical evolution of  $[ls/Fe]$ ,  $[hs/Fe]$  and  $[Pb/Fe]$  relative to the *st* case (dotted lines) and to the *test* case (solid lines). See text for details.

larger with respect to the ones found in the *st* case; in particular, the final  $[hs/Fe] \sim 2.3$  is consistent with the highest values obtained for s-process enriched halo stars (see discussion in Section 7.2). The surface abundances found in the *test* case seem therefore to suggest that the model computed with opacity tables at fixed metallicity is more efficient in reproducing spectroscopic data at low metallicities.

There are however observational counterparts supporting the opposite conclusion, driven by the study of C-stars in Dwarf Spheroidal Galaxies (DSGs); we refer in particular to experimental and theoretical works on the Draco DSG. In this galaxy, whose metallicity presents a quite large dispersion ( $-3.0 < [Fe/H] < -1.5$ , see [148]), a restricted number of C-stars has been observed [149] and their effective temperatures, estimated by means of infrared photometry [1], lay in the range  $3.5 < \log T < 3.6$ . A meaningful example is represented by D461, whose surface temperature is estimated to be  $\log T \sim 3.55$  [50]. Note

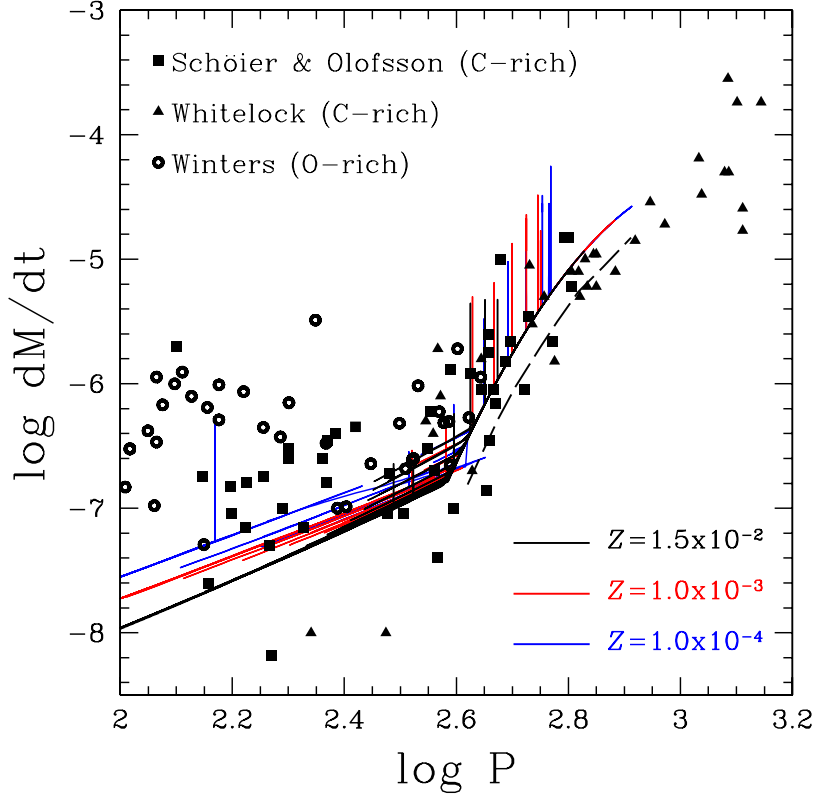


Figure 8.10 Mass-loss rates versus period measurements (symbols) compared with our prescriptions (coloured lines).

that this value is not reachable with the *test* case (see left lower panel in Fig. 8.5).

It therefore results that the effect due to the metallicity enrichment of the convective envelopes in AGB stars has to be taken into account in the opacity treatment, but the test we carried out seems to indicate that we are overestimating it.

Finally, it has to be stressed that the low number of thermal pulses with respect to previous calculations (see e.g. [156]) is a consequence not only of the opacity coefficients treatment, but it depends also on the adopted mass-loss rate. Observational data reported in Fig. 4.7 and discussed in Section 4.5 show a large scatter, which cannot obviously be reproduced if using a single theoretical fitting curve. In fact, the choice of a weaker mass-loss rate (*e.g.* a factor 2 lower) still lay within the observed spread. In Fig. 8.10 we report the same observational data of Fig. 4.7, but compared with our adopted mass-loss rates at the three different metallicities. It results evident from the plot that a consistent number of

Element	<i>st</i> case	<i>test</i> case
C	2.64	3.33
N	0.64	1.48
O	0.75	1.29
F	2.36	3.67
Ne	1.56	3.04
Na	1.03	2.82
Mg	0.45	2.22
Al	0.27	1.21

Table 8.1 Light elements final surface overabundances for the *st* case and for the *test* case.

stars in the range  $2.6 < \log P < 2.9$  show lower mass loss rates with respect our theoretical curve, while the highest regimes are covered by the growing up of strong and fast mass loss spikes (consequence of the rapid luminosity increase due to the development of a thermal pulses, see upper right panel of Fig. 8.5). It has to be noted that the probability to observe an AGB star during the very short high luminosity phase following a TP is quite reduced, but this fact is counterbalanced by the larger surface flux, which could act as a selection criterion. In Fig. 8.10 we also draw a fourth curve (black long-dashed line), which represents our mass-loss rate divided by a factor 2: with this choice also the lowest rates would be accounted for by the theoretical curve. It is therefore necessary to investigate with a new set of models which are the effect of reducing the adopted mass-loss on the number of thermal pulses and to evaluate the consequences on the following chemical evolution.

## 8.2 Future improvements: the molecular opacities

The discrepancies outlined in the previous Section turn our attention to a problem not yet considered in this work: the molecular contribution to opacity. As already explained, dashed areas in Figures 8.1, 8.2 and 8.3 represent cool envelope regions, not covered from the tables provided by the OPAL web-facility. In these temperature regimes, molecules are the dominant opacity source. In the tables we are currently using, the effects due to the presence of molecules are taken into account [5] but, unfortunately, no tables with a variable carbon (and nitrogen) mass fraction are currently available. This is a great handicap in modelling AGB stars. In fact, when the C/O ratio grows above 1, the contribution due to some carbonaceous molecules, like CN and C<sub>2</sub>, is about one order of magnitude

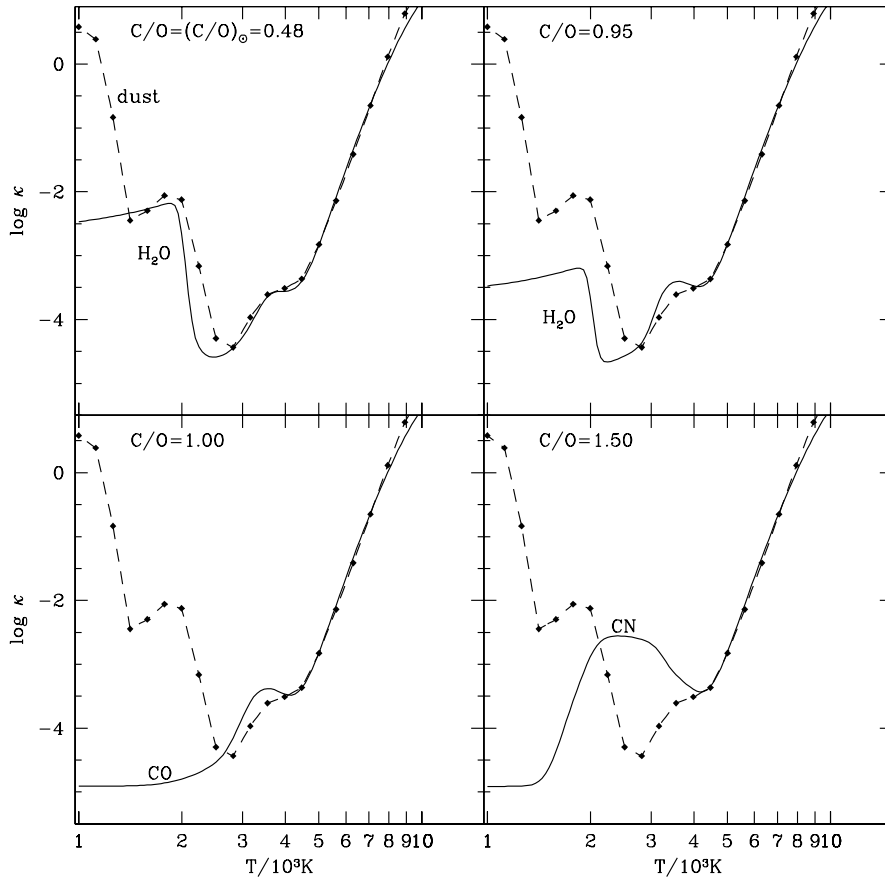


Figure 8.11 Mass absorption coefficients as a function of temperature and for different C/O ratios (from [114]).

greater with respect to the other opacity contributors. In Fig. 8.11, taken from [114], the mass absorption coefficients as a function of temperature and for different C/O ratios are reported. Solid lines represent calculations obtained by varying the C/O values, while the dashed lines are from [5] (obtained with a scaled solar C/O=0.48). Dominant molecular species are labeled nearby the corresponding opacity peaks. In the lower right panel the contribution of the CN molecule in the region between  $10^3$  and  $10^4$  K dominates over the other species [114]. Consequently, along the AGB phase the effects due to the presence of this molecule are even more dramatic with increasing the C/O ratio. In order to form this molecule, C and N are obviously needed.

While carbon is dredged up to the surface by means of TDU episodes, in our models the surface nitrogen abundance results modified only by the FDU episode (see Sections 7.1 and

7.2), without presenting any enhancement during the AGB phase. However, in the *test* case described in the previous Section we obtain a non negligible nitrogen enhancement, thus leading to the possibility to form a large number of CN molecules. Moreover, if we suppose the existence of extramixing processes like the CBP (see Section 7.1.3), the nitrogen abundance in the envelope would result further enhanced and, consequently, the contribution from the CN molecule could consistently increase the opacity.

In the future we will investigate this hypothesis, when opacity tables at different C/O ratio will be available.



## Chapter 9

# Nuclear astrophysics

*In this Chapter we point out the effect of varying some nuclear reaction rates in the nucleosynthesis of light and heavy elements. In particular, we deal with the  $^{13}\text{C}(\alpha,n)^{16}\text{O}$  reaction and with the production of  $^{19}\text{F}$  and  $^{23}\text{Na}$ .*

Up to date, a lot of problems concerning the evolution of the stars are still open. We can list for instance the production of solar neutrinos, the dynamics of late stages of massive stars evolution and, of course, the mechanisms regulating the nucleosynthesis of heavy elements during the s-process and the r-process. Nuclear physics finds a natural link with Astrophysics in the study of these problems, by analysing, in a laboratory context, the efficiency of nuclear reactions: this means to determine cross sections involved in nuclear processes at low energies. In stellar internal layers, the mean kinetic energy of particles constituting a plasma is some keV, while the repulsive Coulomb barrier between two light nuclei is around the MeV, so fusion nuclear reactions occur only by means of the tunnel effect, whose probability to occur is exponentially decreasing with decreasing the energy. In the past, nuclear cross section have been measured at higher energies with respect to the typical temperatures characterizing stellar interiors. Then, in order to obtain the cross section in the keV energy range, an extrapolation is needed, because, as mentioned before, the direct measurement at low energy is too difficult and it requires too long experimental time. As reported in formula 2.1 (see Chapter 2), the cross section can be written as the product between an exponential term (representing the Coulomb penetration factor, quickly varying with the energy) and the astrophysical factor  $S(E)$ , weakly dependent on the energy. This latter term represents the pure nuclear contribution to the investigated reaction. The progresses in experimental technologies recently permitted to measure  $S(E)$

down to the keV range, reaching the Gamow peak of the studied reaction. Between experiments devoted to the determination of cross sections of astrophysical interest, the LUNA collaboration has to be mentioned. This project, whose acronym stands for Laboratory for Underground Nuclear Astrophysics, is carried out at Gran Sasso National Laboratories (LNGS), where the natural shield offered by 1.5 Km of rocks is able to reduce the background due to cosmic rays of more than 6 orders of magnitude. The most important reaction rate measured with the LUNA facility is the  $^{14}\text{N}(p,\gamma)^{15}\text{O}$ , whose determination has strong implications on the evolution of low mass stars (see Section 5.1).

In this Section we present some tests we perform on low mass AGB models by adopting different prescriptions concerning some key nuclear reactions rates. In particular, we discuss the effects on AGB nucleosynthesis induced by varying the  $^{13}\text{C}(\alpha,n)^{16}\text{O}$  reaction (Section 9.1) and the reaction rates regulating the production of  $^{19}\text{F}$  (Section 9.2) and  $^{23}\text{Na}$  (Section 9.3).

## 9.1 The $^{13}\text{C}(\alpha,n)^{16}\text{O}$ reaction

The most important neutron source in AGB is, as recalled in previous Sections, the  $^{13}\text{C}(\alpha,n)^{16}\text{O}$  reaction. A direct measurement of this reaction at low energies is very difficult, therefore indirect methods are requested. A possibility is represented by the study of the direct  $\alpha$ -transfer reaction  $^{13}\text{C}(^6\text{Li},d)^{17}\text{O}$ , but the presence of a subthreshold resonance state at 6.356 MeV in  $^{17}\text{O}$  could cause a huge enhancement of the cross section, as suggested by [45]. The astrophysical S factor proposed by [51] show a possible increase at the low energy tail: for this reason they derived a reaction rate by assuming a strong enhancement properly due to this sub-threshold state. This new feature implies some differences with respect the rate proposed by [33], who didn't take into account the sub-threshold resonance. A treatment similar to [33] has been followed by [106] and [97], who assumed a large reduced width of the sub-threshold state, justifying such a choice by the lack of experimental evidence that support a large resonance alpha strength. Basing of the data sample presented by [51], but using different extrapolation parameters in the low energy region, [8] proposed a different S(E) factor, about 50% greater than the value recommended by [51].

It is then evident how the low energies extrapolation of the S-factor is affected by a significant uncertainty. We assume as a standard choice the rate reported by [51]. In Fig.

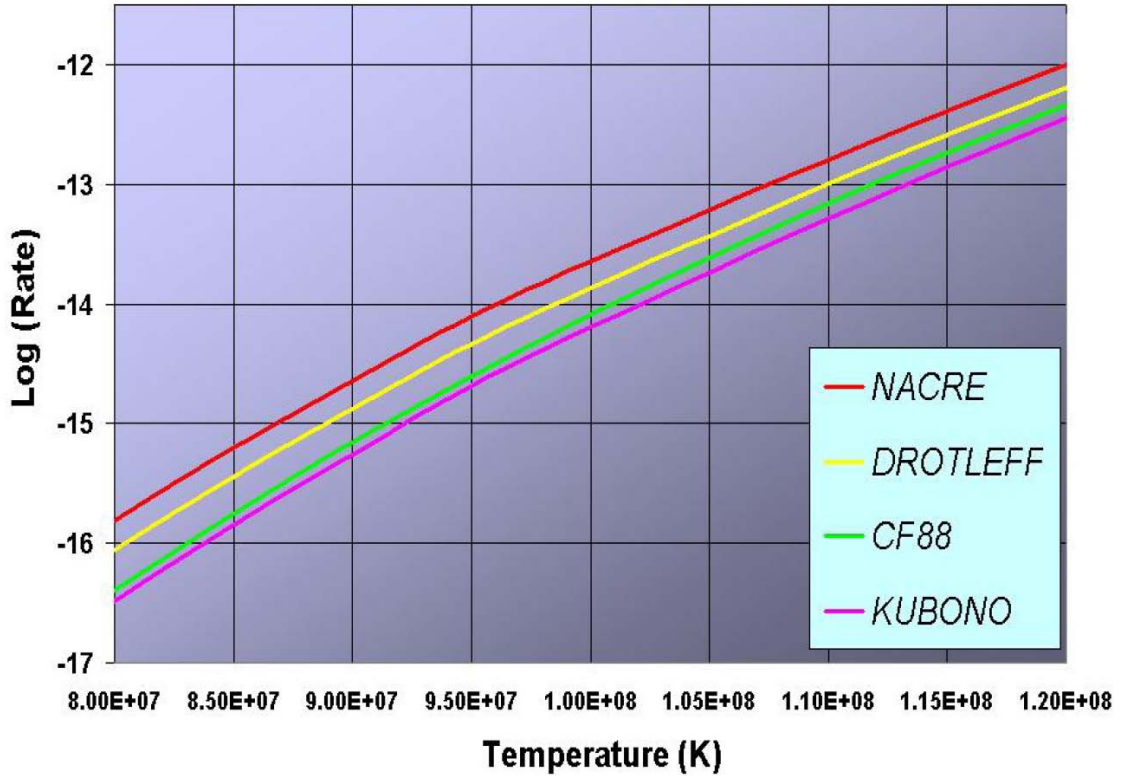


Figure 9.1 Different  $^{13}\text{C}(\alpha,n)^{16}\text{O}$  rates as a function of temperature. The red line refers to [8], the yellow one to [51], the green one to [33] and the magenta one to [106].

9.1 we plot the rates proposed by different authors as a function of temperature. According to these values, we calculate the same model ( $M = 2 M_{\odot}$ ,  $Z = Z_{\odot}$ ) by varying the  $^{13}\text{C}(\alpha,n)^{16}\text{O}$  by a factor 4. The substitution of the standard rate [51] with the value proposed by [106] or [8] only slightly affects the surface overabundances. We found a maximum difference of 25%, affecting a few isotopes, being these variations in any case smaller than typical spectroscopic error bars. The only isotope strongly affected by a different choice of the  $^{13}\text{C}(\alpha,n)^{16}\text{O}$  rate is the  $^{60}\text{Fe}$ . The resulting surface abundances using [51] or [8] differ less than (5÷6)%, while the production of  $^{60}\text{Fe}$  increases up to a factor 20 if adopting the rate proposed by [106]. In fact, using a lower rate for the  $^{13}\text{C}(\alpha,n)^{16}\text{O}$  reaction, the amount of  $^{13}\text{C}$  present in the first  $^{13}\text{C}$ -pocket and ingested in the following convective shells increases, leading to higher neutron densities and consequently to a huge production of  $^{60}\text{Fe}$ , as described in Section 7.1.3.

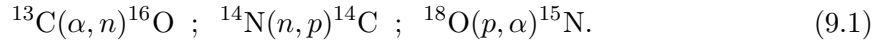
It has however to be noticed that a recent reanalysis of the same rate [98] leads to different

results with respect to [106], implying a good agreement with the value presented by [51].

## 9.2 $^{19}\text{F}$ nucleosynthesis

In this Section we study the nuclear processes responsible for the fluorine nucleosynthesis, testing the effects induced by varying some key nuclear rates regulating its production. The aim of this study is therefore to explore the impact of these nuclear reaction rates on the  $^{19}\text{F}$  yields at solar and low metallicities ( $Z=1\times 10^{-4}$ ), trying to give a solution to the current disagreement between theoretical predictions of fluorine enhancements in giant stars and observational data [95]. Spectroscopic measurements of different types of nearby solar metallicity Giant stars show in fact a high spread in the  $[\text{F}/\text{O}]$  ratio, spanning from 0.5 up to 1.5 (see Fig. 9.2), while theoretical models can only account for values below 1 [113].

The  $^{19}\text{F}$  nucleosynthesis is strictly connected to the presence, in the He-intershell, of  $^{15}\text{N}$ , because of the following nucleosynthetic path:



The  $^{15}\text{N}$  is subsequently diluted in the TP and it suffers an  $\alpha$ -capture forming  $^{19}\text{F}$ . This

$Z=1.5\times 10^{-2}$ model		
CASE	$^{19}\text{F}$	$^{19}\text{F}$ % var.
Adopted rates	$2.30\times 10^{-5}$	—
$^{15}\text{N}(p, \alpha)^{12}\text{C} / 2$	$2.45\times 10^{-5}$	+6.5%
$^{18}\text{O}(p, \alpha)^{15}\text{N} \times 2$	$2.38\times 10^{-5}$	+3.5%
$^{14}\text{C}(\alpha, \gamma)^{18}\text{O} / 2$	$2.19\times 10^{-5}$	-4.8%

$Z=10^{-4}$ model		
CASE	$^{19}\text{F}$	$^{19}\text{F}$ % var.
Adopted rates	$1.92\times 10^{-5}$	—
$^{15}\text{N}(p, \alpha)^{12}\text{C} / 2$	$2.30\times 10^{-5}$	+19.8%
$^{18}\text{O}(p, \alpha)^{15}\text{N} \times 2$	$2.21\times 10^{-5}$	+15.1%
$^{14}\text{C}(\alpha, \gamma)^{18}\text{O} / 2$	$1.63\times 10^{-5}$	-15.1%

Table 9.1 Fluorine He-intershell abundances obtained using the adopted rates or modifying some key nuclear reactions rates (see text for details).

nuclear chain works in two different environments: inside the  $^{13}\text{C}$  pocket (when  $^{13}\text{C}$  burns in radiative condition) or in the convective shell generated by the TP (when the equilibrium

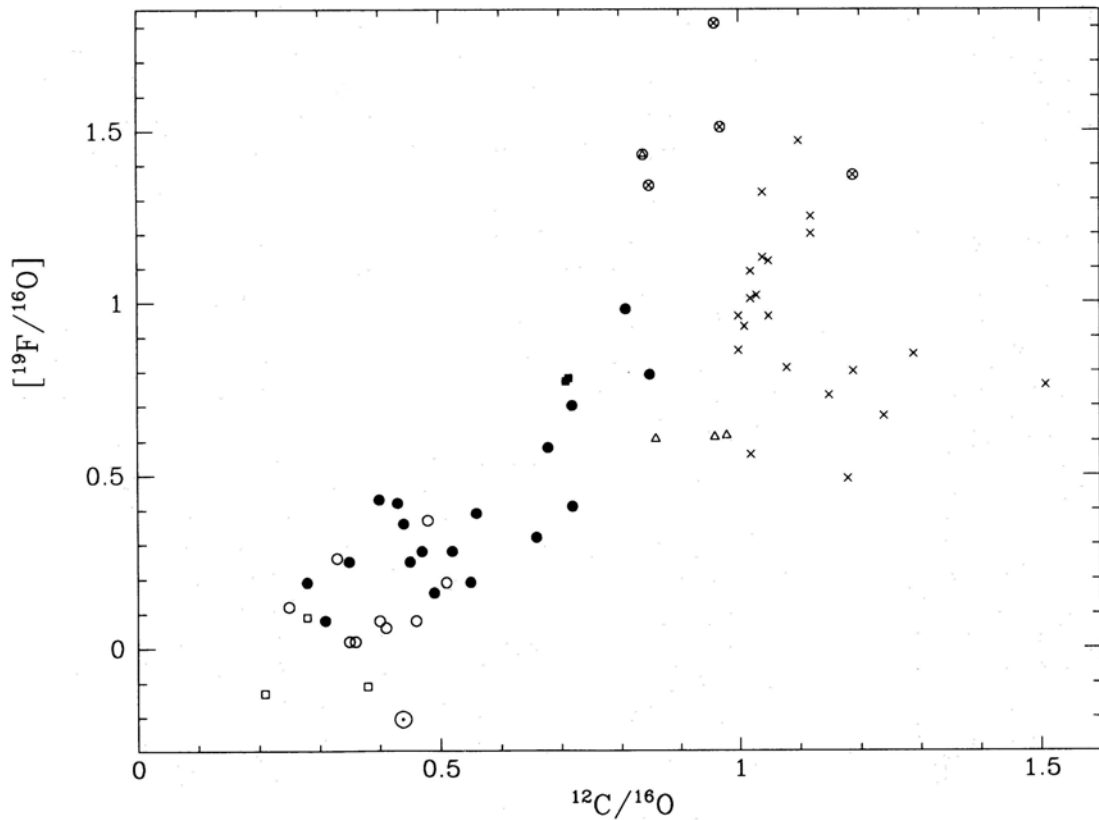


Figure 9.2 Fluorine abundances versus carbon abundances, both normalized by the oxygen abundance (from [95]).

$^{13}\text{C}$ , left in the H-ashes, is engulfed in the TP). The first mechanism is of primary origin (due to the primarity of the  $^{13}\text{C}$  pocket), while the second one depends on the envelope metallicity: the larger the total CNO abundance is, the larger the  $^{13}\text{C}$  equilibrium abundance left in the H burning shell ashes is. This latter mechanism is in fact dominant in the solar metallicity model, where the  $^{13}\text{C}$  equilibrium abundance is quite large: its mass fraction starts from  $3.7 \times 10^{-5}$  after the first pulse with TDU and increases up to  $8.4 \times 10^{-5}$  at the end of the AGB phase. We find that the contribution to  $^{19}\text{F}$  from the  $^{13}\text{C}$  present in the H-burning ashes is responsible for the 65% of the synthesized fluorine. On the contrary, in the  $Z=1 \times 10^{-4}$  model the contribution from the equilibrium  $^{13}\text{C}$  is lower (it grows from  $2.7 \times 10^{-6}$  up to  $4.3 \times 10^{-5}$ ) and its contribution to the fluorine nucleosynthesis is therefore of secondary importance.

This situation changes in the *test* case of Section 8.1, due to the increased number of TDU episodes, which leads to a larger total CNO abundance in the envelope. In this case, the contribution from the equilibrium  $^{13}\text{C}$  in the H-burning ashes results dominant, increasing the fluorine overabundance of a factor 20 with respect the *st* case (see Table 8.1 in Section 8.1).

For both metallicities, we calculate the effects of varying some key nuclear rates in the  $^{19}\text{F}$  production; in particular we change:

- $^{15}\text{N}(\text{p},\alpha)^{12}\text{C}$ ;
- $^{18}\text{O}(\text{p},\alpha)^{15}\text{N}$ ;
- $^{14}\text{C}(\alpha,\gamma)^{18}\text{O}$ .

The  $^{15}\text{N}(\text{p},\alpha)^{12}\text{C}$  reaction has been measured by [185] and [129] between  $E=0.07$  and 0.76 MeV, while data between  $E=0.76$  and 1.6 MeV are from [140]. We test the effect of varying this rate by dividing its value for a factor 2.

The  $^{18}\text{O}(\text{p},\alpha)^{15}\text{N}$  reaction is characterized by more than 50 resonances between  $E=20$  and 6746 keV (see [8]), being the less energetic one ( $E=20$  keV) the major source of uncertainty. Possible contributions from low energy resonances were presented by [179] and by [34]. We evaluate the effects of varying this rate by multiplying its value by a factor 2.

Finally, the adopted value for the  $^{14}\text{C}(\alpha,\gamma)^{18}\text{O}$  reaction is that one proposed by [33]. The determination of this rate appears particularly difficult due to the presence of a  $1^-$  sub-threshold state at  $E=6.198$  MeV [67]. Recently, a new reanalysis of this rate has been presented by [113]. We compute a test by dividing the adopted value by a factor 2 (this roughly corresponds to the upper limit proposed by [113]). All the studied reactions affect the synthesis of  $^{15}\text{N}$  (and consequently of  $^{19}\text{F}$ ), including this latter rate. In particular, the efficiency of the  $^{14}\text{C}(\alpha,\gamma)^{18}\text{O}$  regulates the production of  $^{15}\text{N}$  during the neutron release governed by the  $^{13}\text{C}(\alpha,\text{n})^{16}\text{O}$ , because it produces  $^{18}\text{O}$  simultaneously with the protons from the  $^{14}\text{N}(\text{n},\text{p})^{14}\text{C}$  reaction.

As reported in Table 9.1, major changes occur in the low metallicity model (variations are of the order of 20% with respect to the 5% found in the solar metallicity model). In fact, the reaction rates variations affect results mainly during the interpulse phase, where  $^{13}\text{C}$  burns at temperatures around  $9\times 10^7$  K and the nucleosynthesis is working in radiative conditions. In this environment, the rates variations have important effects on the  $^{15}\text{N}$  production, while in the convective shell the efficiency of these rates is already high, due to the larger temperature reached at the bottom of the mixed zone. In low metallicity models

the contribution of the  $^{13}\text{C}$  present in the pocket is relatively more important with respect to the  $^{13}\text{C}$  left in the H ashes, therefore we expect larger variations at low metallicities. In the solar metallicity model, changes of nuclear reaction rates regulating the fluorine production imply little variations on its surface abundance, therefore confirming the final value obtained with the adopted rates:  $[\text{F}/\text{O}] \sim 0.5$ . Consequently, our model are not able to cover the entire spectroscopic range presented by [95]. [113] hypothesized that data furnished by [95] could be out of date or that possible effects due to a Non Local Thermal Equilibrium (NLTE) or to a 3D treatment could modify the observed surface  $^{19}\text{F}$  abundances. Another possibility is the inclusion in the stellar code of extra mixing processes at the base of the convective envelope, such as the CBP (see Section 7.1.3).

### 9.3 $^{23}\text{Na}$ nucleosynthesis

As recalled in previous Chapters, the s-process is responsible for the observed enhancements of elements heavier than iron in AGB stars; nonetheless, neutron captures affect also the nucleosynthesis of light elements, which are normally produced through proton and  $\alpha$  captures:  $^{23}\text{Na}$  belongs to this category.

In TP-AGB stars, sodium is mainly synthesized by proton captures on  $^{22}\text{Ne}$ . In Fig. 9.3 we report a scheme of the internal layers constituting an AGB star. From the top to the bottom, we plot the convective envelope, the H-burning shell, separated from the He-shell by the He-intershell, and the degenerate C-O core. The proton diffusion from the envelope obtained by introducing the convective velocity profile (see Section 6) is represented by the sprinkled area and labeled as 'P', while the region interested by the  $^{13}\text{C}$ -pocket is drawn as a black thick line. Two convective shells generated by TPs are plotted for the sake of clarity. The numbered arrows identify the activation of nuclear processes synthesizing  $^{23}\text{Na}$ : in our models, in fact, sodium is produced in different phases. The first burst occurs during the formation of the  $^{13}\text{C}$  pocket (number 1) by means of the  $^{22}\text{Ne}(p,\gamma)^{23}\text{Na}$  reaction, as already pointed out in Section 6.2. In the solar metallicity case, the  $^{23}\text{Na}$  production is dominated by this mechanism.

In the  $Z=1\times 10^{-4}$  model, a second source of  $^{23}\text{Na}$  is represented by the neutron capture on  $^{22}\text{Ne}$ , which occurs both during the radiative  $^{13}\text{C}$  burning (mechanism number 2) and during the convective  $^{22}\text{Ne}$  burning (mechanism number 3). These additional sources contribute to 13% and 35% of the total sodium production, respectively.

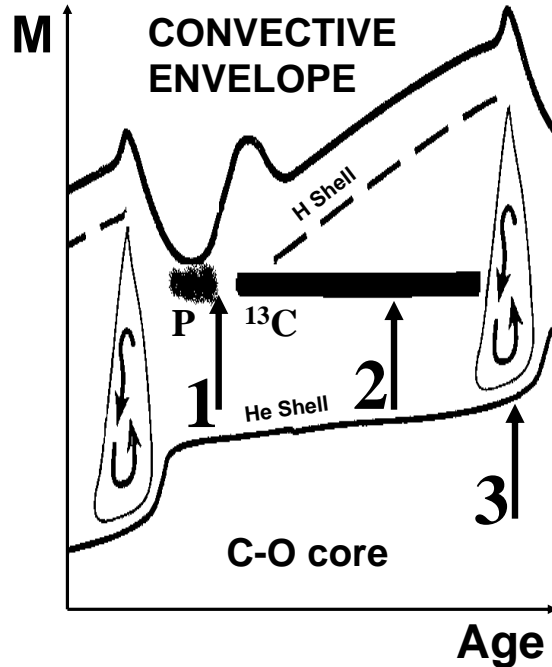


Figure 9.3 Schematic TP-AGB structure; mechanisms responsible for the  $^{23}\text{Na}$  production are evidenced.

While our solar metallicity model shows a negligible  $^{23}\text{Na}$  surface enrichment (+25%, equivalent to 0.1 dex) during the AGB phase, at the end of the  $Z=1 \times 10^{-4}$  model we found a sodium surface enhancement by more than a factor 10 ( $[\text{Na}/\text{Fe}] \sim 1$ ).

Recent measurements of  $^{22}\text{Ne}(p,\gamma)^{23}\text{Na}$  [77] and  $^{23}\text{Na}(p,\gamma)^{24}\text{Mg}$  reaction rates [78] significantly reduce the values quoted in the NACRE compilation [8] around  $10^8$  K (see Figures 9.4 and 9.5). We then calculate a series of TPs in the  $Z=Z_{\odot}$  and in the  $Z=1 \times 10^{-4}$  models with rates from ([77],[78]) and we compare the resulting intershell sodium mass fraction with the one obtained with the NACRE rates [8].

In Fig. 9.6 we plot the neon and sodium abundances in the He-intershell after the  $3^{rd}$  pulse with TDU, obtained with the adopted rates [8] and rates provided by [77] and [78]. Left panels refer to the solar metallicity model, the right ones to the  $Z=1 \times 10^{-4}$  model. Lower panels show the He-intershell abundances profiles obtained with the standard adopted rates ([8]) while the upper panel depict the abundances obtained by using rates provided by [77] and [78]. In all panels we report the  $^{12}\text{C}$  abundance (dotted line), the  $^{13}\text{C}$  one (sort-dashed

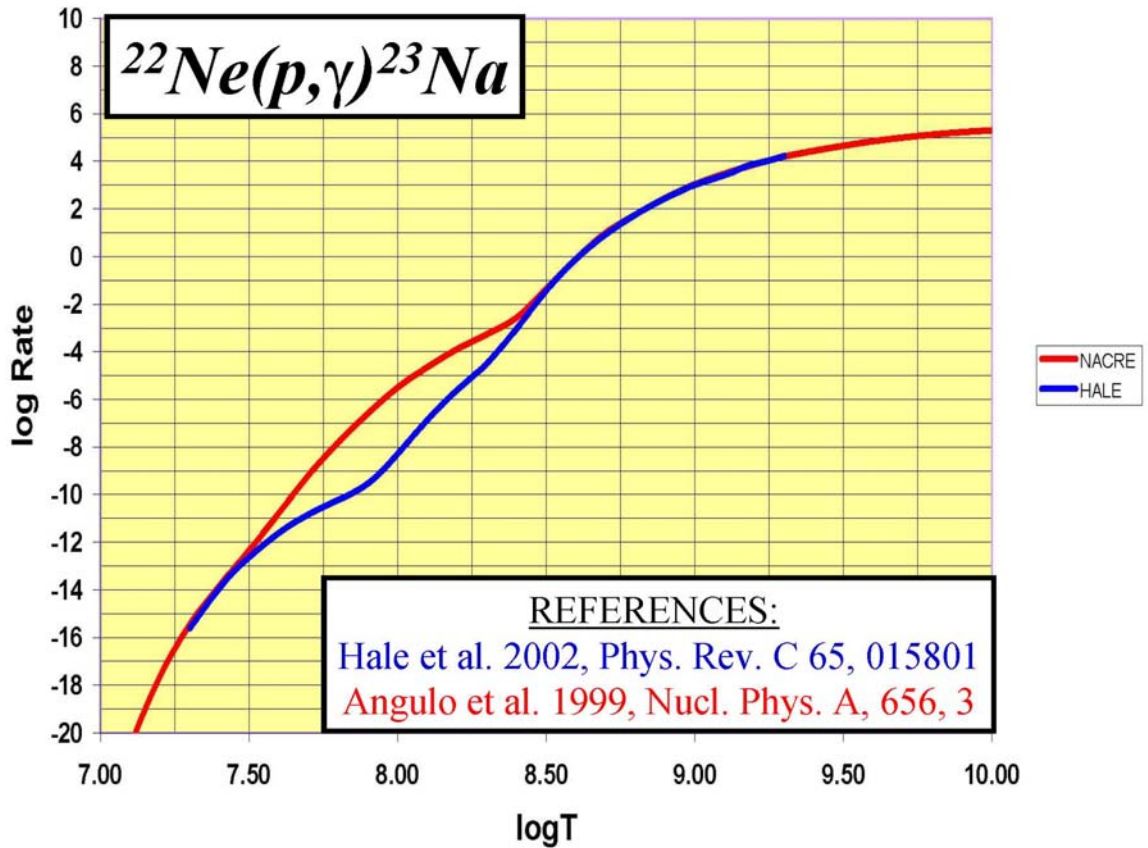


Figure 9.4 Comparison between different rates of the  $^{22}\text{Ne}(p,\gamma)^{23}\text{Na}$  reaction as a function of the temperature.

line), the  $^{22}\text{Ne}$  one (long-dashed line), the  $^{23}\text{Na}$  one (solid line) and the hydrogen one (asterisks).

In the solar metallicity model, a lower  $^{23}\text{Na}$  pocket is found when using rates from [77] and [78], leading however to negligible variations with respect to the adopted rates [8]. The lower  $^{22}\text{Ne}$  abundance found in the H-burning ashes doesn't affect the global  $^{22}\text{Ne}$  production, because of its primary origin.

In the  $Z=1\times 10^{-4}$  model, the reduction of the first reaction rate depresses the abundance peak of the  $^{23}\text{Na}$  pocket as in the solar metallicity model. This effect is marginally counterbalanced by the reduction of the second reaction rate, which leads to a larger  $^{23}\text{Na}$  abundance in the H-burning shell ashes (see top right panel in Fig. 9.6). A variation of about  $-30\%$  is found. This considerable difference is not emerging from the solar metallicity model because the sodium initial abundance is larger with respect to the  $Z=1\times 10^{-4}$  model one. The different sensitivities of the two models with respect to the rates variation

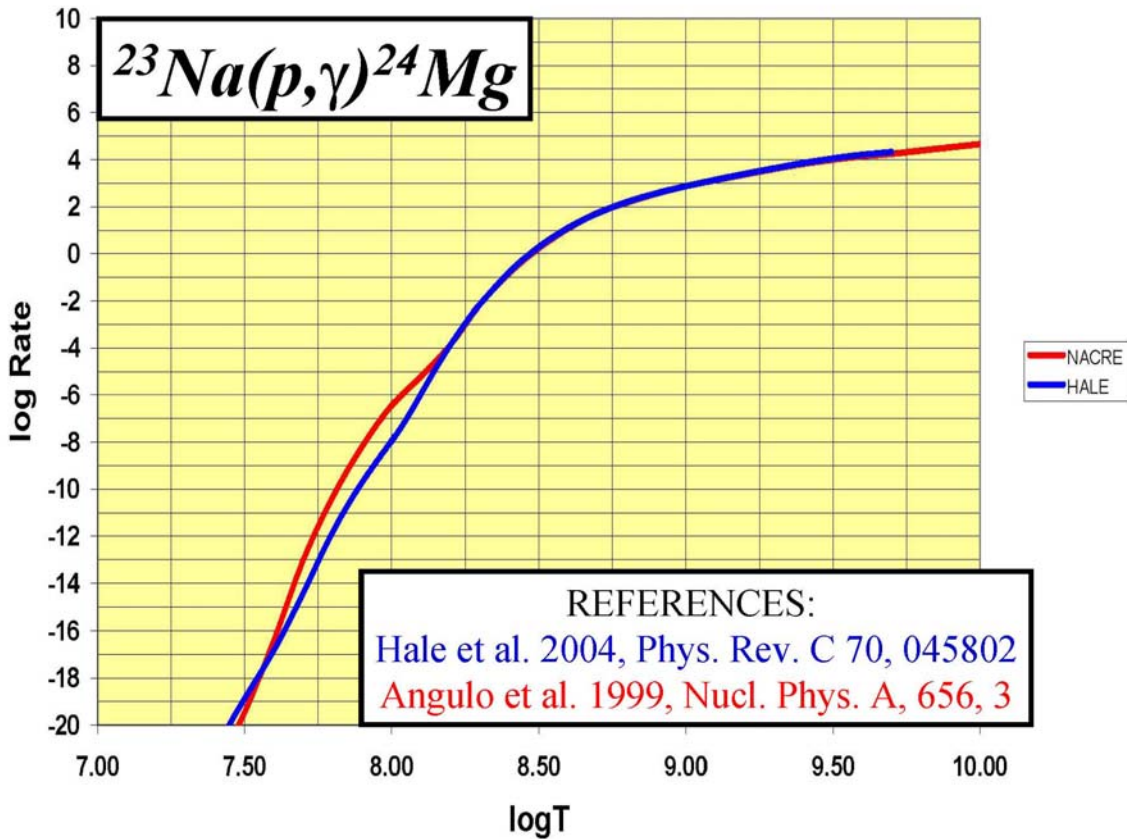


Figure 9.5 Comparison between different rates of the  $^{23}\text{Na}(p,\gamma)^{24}\text{Mg}$  reaction as a function of the temperature.

have therefore to be ascribed to a dilution effect. In this way, the reduction of the  $^{23}\text{Na}$  pocket, affecting both models with the same efficiency (due to its primary origin), is more evident at low metallicities.

Moreover, we verify that the correction of a misprint in the  $^{23}\text{Na}(n,\gamma)^{24}\text{Na}$  reaction rate (5 keV data tabulated in [12]) implies a further decrease of the sodium abundance by about 15% in the  $Z=1\times 10^{-4}$  model. This correction makes the contribution of the neutron capture on  $^{22}\text{Ne}$  during radiative  $^{13}\text{C}$  burning negligible, while it does not affect the  $\sim 23$  keV neutron capture occurring in the convective  $^{22}\text{Ne}$  burning. As a whole, we estimate that with these changes of the relevant reaction rates the final sodium overabundance in our  $Z=1\times 10^{-4}$  model would be  $[\text{Na}/\text{Fe}]\sim 0.7$ , that is a factor 2 lower than predictions presented in Section 7.2.

Finally, it has to be stressed that a different treatment of the opacity in the envelope of a low

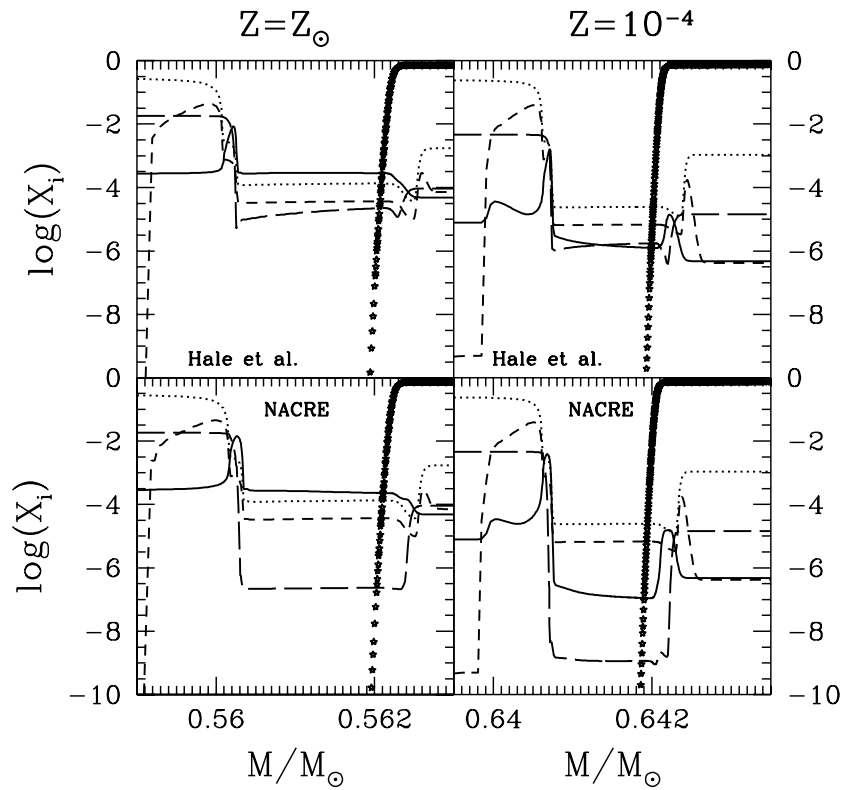


Figure 9.6 He-intershell abundances after the 3<sup>rd</sup> pulse with TDU obtained with the standard rates and rates provided by [77] and [78]. Data refer to the  $M = 2M_{\odot}$  model with solar metallicity (left Panels) and to the  $M = 2M_{\odot}$  model with  $Z = 1 \times 10^{-4}$  (right Panels).

metallicity AGB star (*test* case) implies a great enhancement in the final sodium overabundance with respect the standard (*st*) case (see Table 8.1 in Section 8.1). This large increase (almost a factor 50) is due to the contribution coming from the  $^{22}\text{Ne}(n,\gamma)^{23}\text{Ne}(\beta^-)^{23}\text{Na}$  nucleosynthetic chain, which results efficiently activated when the temperature at the bottom of the convective region generated by a TP reaches  $T \sim 3.2 \times 10^8$  K. This condition is easily fulfilled in the *test* case (see Fig. 8.7 in Section 8.1), while it is barely attained in the *st* case, in which proton capture on  $^{22}\text{Ne}$  dominates over the corresponding neutron capture.



# Chapter 10

## Concluding remarks

### 10.1 What we did

In this PhD Thesis we presented the nucleosynthesis and the evolution of low mass AGB stars, by computing three different models with the same initial mass ( $M=2 M_{\odot}$ ) and different metallicities ( $Z=1.5\times 10^{-2}$ , equivalent to the initial metal amount of the Sun,  $Z=1\times 10^{-3}$  and  $Z=1\times 10^{-4}$ ).

In the first part we described the main features of the s-process (Chapter 1), illustrating the motivations at the base of this work (Chapter 2). In Chapter 3 we described main characteristics of our stellar evolutionary code (FRANEC), stressing in particular the treatment of convection and the adopted input physics, while in Chapter 4 we reviewed the theoretical investigation of nucleosynthesis and evolution of low mass AGB stars.

In Chapter 5 we described the procedure followed in constructing a full nuclear network (from H to Bi), in which about 500 isotopes are linked by more than 700 reactions. We upgraded our database by using the most recent experimental and theoretical reaction rates, involving both strong and weak interactions.

The introduction of an exponentially decaying profile of velocity below the convective envelope during Third Dredge Up episodes allows a small amount of protons to diffuse in the C-rich He intershell, leading to the formation of a  $^{13}\text{C}$ -rich layer (Chapter 6). The resulting  $^{13}\text{C}$  pocket partially overlaps with a more external  $^{14}\text{N}$  pocket, followed by a further minor  $^{23}\text{Na}$  pocket. All these pockets are of primary origin: no dependence on the initial metallicity has in fact been evidenced. The mass extension of the  $^{13}\text{C}$  pocket decreases along the AGB phase, simultaneously with the shrinking of the He-intershell region, starting from  $\Delta M_{^{13}\text{C}}^{eff} \sim 6 \times 10^{-4} M_{\odot}$  down to  $2 \times 10^{-4} M_{\odot}$ . We also tested the sensitivity of the velocity profile algorithm by varying the  $\beta$  free parameter, implicit in

its formulation. We motivated the choice of our standard value ( $\beta=0.1$ ) by analysing the resulting  $^{13}\text{C}$  pocket at varying  $\beta$ . However, our aim is not to give an absolute value, but to narrow the uncertainty implied by the use of a free parameter.

The evolution and the nucleosynthesis of the three computed model are presented in Chapter 7. We followed the AGB evolutions up to the envelope composition freezes out; the final elemental distributions are representative of the ones expected for the intrinsic carbon stars observed in the disk and in the halo of the Milky Way. A comparison with available spectroscopic analysis shows a reasonable agreement with solar metallicity, while points out some problems in the modelling of AGB stars at low metallicities. Concerning the solar metallicity case, we formulated a new hypothesis on the origin of short-lived radioactive isotopes at the epoch of the Early Solar System formation.

For the first time in the literature, we furnished a uniform set of yields at different metallicities, containing all the chemical species (see Appendix A).

As demonstrated in Chapter 8, a different treatment of the opacity coefficients in the cool envelopes of low mass AGB stars has dramatic effects on their mass-loss rate, therefore implying large changes in their final surface overabundances. The tests we carried out lead us to conclude that, at the moment, these problems cannot be solved, because of the lack of opacity tables calculated with different C/O ratios.

Finally, in Chapter 9 we pointed out our membership to the nuclear astrophysics tribe, by discussing how the variations of some nuclear reaction rates affect the nucleosynthesis of light and heavy elements.

## 10.2 What we wish to do

The present work demonstrates that, nowadays, the computational power allows the coupling between a stellar evolutionary code and a full nuclear network. A different treatment of the internal border of the convective envelope with respect to the Schwarzschild criterion allows the formation of the so-called  $^{13}\text{C}$  pocket. It has however to be reminded that the algorithm we introduced is dependent on a free parameter, that we calibrated for low mass AGB stars: a lower value is probably requested in computing models with initial larger masses. In the future we'll therefore investigate this hypothesis by calculating models of more massive AGB stars ( $4 < M/M_{\odot} < 9$ ).

Moreover, we are interested in studying solar metallicity models with initial mass  $M \sim (1.3 \div 1.5)M/M_{\odot}$ , in order to verify our guess on the origin of short-lived radioactive

isotopes at the epoch of the formation of the Early Solar System.

We propose our mechanism as a valid tool for the creation of a self-consistent s-process model, but also other physical mechanisms have to be taken into account, among which the introduction of rotation in our code is of primary importance. Rotation could in fact have important effects on the formation of the  $^{13}\text{C}$  pocket [80, 150] and, coupled with our velocity profile algorithm, could give naturally rise to the desired spread in the  $^{13}\text{C}$  pocket efficiencies. Other promising mechanisms have however to be considered, like gravity waves or magnetic fields: recently, the work of [27] verified that the required magnetic fields strengths are in the range foreseen for the formation of the  $^{13}\text{C}$  pocket.

Finally, the importance of the adopted mass loss rate and of molecules contribution to opacity has been pointed out. While the first problem will be analyzed by calculating new models with a reduced mass loss, the second one could be solved only when opacity tables with enhanced carbon and nitrogen abundances will be available.

We therefore conclude that we still have a lot of work to do, but our efforts are always sustained by the wise latin words:

***PER ASPERA AD ASTRA...***



# Bibliography

- [1] Aaronson, M., & Mould, J.: 1985, *ApJ* **290**, 191.
- [2] Abbondanno, U. and 113 coauthors: 2004, *Phys. Rev. Lett.* **93**, 1103.
- [3] Abia, C., Busso, M., Gallino, R., Domínguez, I., Straniero, O., Isern, J.: 2001, *ApJ* **559**, 1117.
- [4] Abia, C. and 8 coauthors: 2002, *ApJ* **579**, 817.
- [5] Alexander, D.R., & Ferguson, J.W.: 1994, *ApJ* **437**, 879.
- [6] Allende Prieto C., Lambert D.L., Asplund M.: 2002, *ApJ* **573**, L137.
- [7] Anders, E., Grevesse, N.: 1989, *Geochim. Cosmochim. Acta* **53**, 197.
- [8] Angulo, C. and 27 coauthors: 1999, *Nucl. Phys. A* **656**, 3.
- [9] Aoki, W., Ryan, S.G., Norris, J.E., Beers, T.C., Ando, H., Tsangarides, S.: 2002, *ApJ* **580**, 1149.
- [10] Arlandini, C., Käppeler, F., Wisshak, K., Gallino, R., Lugaro, M., Busso, M., Straniero, O.: 1999, *ApJ* **525**, 886.
- [11] Asplund, M., Grevesse, N., Sauval, A.J., Allende Prieto, C., Kiselman, D.: 2004, *A&A* **417**, 751.
- [12] Bao, Z.Y., & Käppeler, F.: 2000, *Atom. Data Nucl. Data Tables* **76**, 70.
- [13] Barbuy, B., Spite, M., Spite, F., Hill, V., Cayrel, R., Plez, B., Petitjean, P.: 2005, *A&A* **429**, 1031.
- [14] Becker, S.A., & Iben, I.Jr.: 1979, *ApJ* **232**, 831.
- [15] Beer, H.: 1991, *ApJ* **375**, 823.
- [16] Beers, T.C.: 1999, in *ASP. Conf. Ser.* **165**, 202.

- [17] Best, J. and 8 coauthors: 2001, *Phys. Rev. C* **64**, 0115801.
- [18] Bisterzo, S., Gallino, R., Straniero, O., Aoki, W., Ryan, S., Beers, T.C.: 2006, OMEG05 Symposium, in press
- [19] Bisterzo, S., Gallino, R., Straniero, O., Ivans, I.I., Käppeler, F., Aoki, W.: 2006, *Mem. SAIt*, in press
- [20] Bonacic Marinovic, A., Izzard, R.I., Lugaro, M., Pols, O.R.: *astroph* 0603757
- [21] Boothroyd, A.J., Sackmann, I.-J.: 1999, *ApJ* **510**, 232.
- [22] Bowen, G.H., & Willson, L.A.: 1991, *ApJ* **375**, L53.
- [23] Burbidge, E.M., Burbidge, G.R., Fowler, W.A., Hoyle, F.: 1957, *Rev. Mod. Phys.* **29**, 547.
- [24] Busso, M., Gallino, R., Wasserburg, G. J.: 1999, *ARA&A* **37**, 239.
- [25] Busso, M., Gallino, R., Lugaro, M., Straniero, O., Smith, V.V., Lambert, D.L.: 2000, *Mem. SAIt* **71**, 805.
- [26] Busso, M., Gallino, R., Lambert, D.L., Travaglio, C., Smith, V.V.: 2001, *ApJ* **557**, 802.
- [27] Busso, M., Nucci, M.C., Chieffi, A., Straniero, O.: 2004, *Mem. SAIt*, **75**, 648.
- [28] Cameron, A.G.W.: 1954, *Phys. Rep.* **93**, 932.
- [29] Cameron, A.G.W.: 1960, *AJ* **65**, 485.
- [30] Castellani, V., Giannone, P., Renzini, A.: 1971, *Ap&SS* **10**, 340.
- [31] Castellani, V., Chieffi, A., Straniero, O.: 1992, *ApJ* **78**, S517.
- [32] Castellani, V., Marconi, M., Straniero, O.: 1996, *A&A* **340**, 160.
- [33] Caughlan, G.R., & Fowler, W.A.: 1988, *Atom. Data Nucl. Data Tables* **40**, 283.
- [34] Champagne, A.E., & Pitt, M.L.: 1986, *Nucl. Phys. A* **457**, 367.
- [35] Charbonnel, C.: 1995, *ApJ* **453**, L41.
- [36] Chieffi, A., & Straniero, O.: 1989, *ApJ* **71**, 47S.

- [37] Chieffi, A., Limongi, M., Straniero, O.: 1998, *ApJ* **502**, 737.
- [38] Chieffi, A., Domínguez, I., Limongi, M., Straniero, O.: 2001, *ApJ* **554**, 1159.
- [39] Christlieb, N.: 2003, *Rev. Mod. Astron.* **16**, 191.
- [40] Clayton, D.D.: 1968, in *Principles of Stellar Evolution and Nucleosynthesis*, Chicago: The Univ. of Chicago Press.
- [41] Coc, A., Porquet, M.G., Nowacki, F.: 2000, *Phys. Rev. C* **61**, 015801.
- [42] Cohen, J.G., Christlieb, N., Quian, Y.Z., Wasserburg, G.J.: 2003, *ApJ* **588**, 1082.
- [43] Corvi, F., Fioni, G., Günsing, F., Mutti, P., Zanini, L.: 2002, *Nucl. Phys. A* **697**, 581.
- [44] Denissenkov, P.A., & Tout, C.A.: 2003, *MNRAS* **340**, 722.
- [45] Descouvemont, P.: 1987, *Phys. Rev. C* **36**, 2206.
- [46] Dewitt, H.E., Graboske, H.C., Cooper, M.S.: 1973, *ApJ* **181**, 439.
- [47] Dicus, D.A., Kolb, E.W., Schramm, D.N., Tubbs, D.L.: 1976, *ApJ* **210**, 481.
- [48] Domínguez, I., Tornambé, A., Isern, J.: 1993, *ApJ* **419**, 268.
- [49] Domínguez, I., Chieffi, A., Limongi, M., Straniero, O.: 1999, *ApJ* **524**, 226.
- [50] Domínguez, I., Abia, C., Straniero, O., Cristallo, S., Pavlenko, Ya-V.: 2004, *A&A* **422**, 1045.
- [51] Drotleff, H.W. and 8 coauthors: 1993, *ApJ* **414**, 735.
- [52] Druyts, S., Wagemans, C., Geltenbort, P.: 1994, *Nucl. Phys. A* **573**, 291.
- [53] Fluks, M.A., Plez, B., The, P.S., de Winter, D., Westerlund, B.E., Steenman, H.C.: 1994, *A&AS* **105**, 311.
- [54] Freytag, B., Ludwig, H.-G., Steffen, M.: 1996, *A&A* **313**, 497.
- [55] Frost, C.A., & Lattanzio, J.C.: 1996, *ApJ* **473**, 383.
- [56] Fujimoto, M.Y., Ikeda, Y., Iben, I.Jr.: 2000, *ApJ* **529**, L25.
- [57] Fuller, G.M., Fowler, W.A., Newman, M.J.: 1982, *ApJS* **48**, 279.

- [58] Gallino, R., Busso, M., Picchio, G., Raiteri, C.M., Renzini, A.: 1988, *ApJ* **334**, 45L.
- [59] Gallino, R., Arlandini, C., Busso, M., Lugaro, M., Travaglio, C., Straniero, O., Chieffi, A., Limongi, M.: 1998, *ApJ* **497**, 388.
- [60] Gallino, R. and 8 coauthors: 2002, in the Proceedings of the *11<sup>th</sup> Workshop on Nuclear Astrophysics*, eds. W. Hillebrandt & E. Müller, Garching: MPA/P13, 205.
- [61] Gallino, R., Arnone, E., Pignatari, M., Straniero, O.: 2005, *Mem. SAIt* **75**, 700.
- [62] Gallino, R., Wasserburg, G.J., Busso, M., Straniero, O.: 2005, *IAUS* **228**, 461.
- [63] Giridhar, S., Lambert, D.L., Gonzalez, G.: 2000, *ApJ* **531**, 521.
- [64] Goeminne, G., Wagemans, C., Wagemans, J., Geltenbort, P., Loiselet, M., Gaelens, M., Denecke, B., Koester, U.: 2001, *Nucl. Phys. A* **688**, 233.
- [65] Goeminne, G.: 2001, PhD Thesis
- [66] Goldschmidt, V.M.: 1937, *Math. Naturew. Kl.* **4**, 99.
- [67] Görres, J., Graff, S., Wiescher, M., Azuma, R.E., Barnes, C.A., Wang, T.R.: 1992, *Nucl. Phys. A* **548**, 414.
- [68] Graboske, H.C., Dewitt, H.E., Grossman, A.S., Cooper, M.S.: 1973, *ApJ* **181**, 457.
- [69] Grevesse, N., & Noels, A.: 1993, in *Origin and evolution of the elements*, ed. N. Prantzos, E. Vangioni-Flam, & M. Cassé, Cambridge University Press, 15
- [70] Grevesse, N., & Sauval, A.J.: 1998, *Space Sci. Rev.* **85**, 161.
- [71] Groenewegen, M.A.T., & de Jong, T.: 1993, *A&A* **267**, 410.
- [72] Groenewegen, M.A.T., & de Jong, T.: 1994, *A&A* **282**, 127.
- [73] Groenewegen, M.A.T., & Whitelock, P.: 1996, *MNRAS* **281**, 1347.
- [74] Guandalini, R., Busso, M., Ciprini, S., Silvestro, G., Persi, P.: 2006, *A&A* **445**, 1069.
- [75] Guber, K.H., Sayer, R.O., Valentine, T.E., Leal, L.C., Spencer, R.R., Harvey, J.A., Koehler, P.E., Rauscher, T.: 2002, *Phys. Rev. C* **65**, 058801.
- [76] Guber, K.H., Koehler, P.E., Derrien, H., Valentine, T.E., Leal, L.C., Sayer, R.O., Rauscher, T.: 2003, *Phys. Rev. C* **67**, 062802.

- [77] Hale, S.E., Champagne, A.E., Iliadis, C., Hansper, V.Y., Powell, D.C., Blackmon, J.C.: 2002, *Phys. Rev. C* **65**, 015801.
- [78] Hale, S.E., Champagne, A.E., Iliadis, C., Hansper, V.Y., Powell, D.C., Blackmon, J.C.: 2004, *Phys. Rev. C* **70**, 045802.
- [79] Herwig, F., Blöcker, T., Schönberner, D., El Eid, M.: 1997, *A&A* **324**, L81.
- [80] Herwig, F., Langer, N., Lugaro, M.: 2003, *ApJ* **593**, 1056.
- [81] Hollowell, D., Iben, I.Jr., Fujimoto, M.Y.: 1990, *ApJ* **351**, 245.
- [82] Iben, I.Jr.: 1975, *ApJ* **196**, 525.
- [83] Iben, I.Jr.: 1976, *ApJ* **208**, 165.
- [84] Iben, I.Jr., & Truran, J.W.: 1978, *ApJ* **220**, 980.
- [85] Iben, I.Jr.: 1982, *ApJ* **260**, 821.
- [86] Iben, I.Jr.: 1983, *ApJ* **275**, 65.
- [87] Iben, I.Jr., & Renzini, A.: 1983, *ARA&A* **21**, 271.
- [88] Imbriani, G. and 33 coauthors: 2005, *Eur. Phys. J. A* **25**, 455.
- [89] Itoh, N., Totsuji, H., Ichimaru, S.: 1977, *ApJ* **218**, 477.
- [90] Itoh, N., Totsuji, H., Ichimaru, S., Dewitt, H.E.: 1979, *ApJ* **234**, 1079.
- [91] Ivans, I.I., Sneden, C., Gallino, R., Cowan, J.J., Preston, G.W.: 2005, *ApJ* **627**, 145.
- [92] Iwamoto, N., Kajino, T., Mathews, G.J., Fujimoto, M.Y., Aoki, W.: 2004, *ApJ* **602**, 377.
- [93] Jaeger, M., Kunz, R., Mayer, A., Hammer, J.W., Staudt, G., Kratz, K.-L., Pfeiffer, B.: 2001, *Phys. Rev. Lett* **87**, 202501.
- [94] Johnson, J.A. & Bolte, M.: 2004, *ApJ* **605**, 462.
- [95] Jorissen, A., Smith, V.V., Lambert, D.L. 1992, *A&A* **261**, 164
- [96] Käppeler, F. and 10 coauthors: 1994, *ApJ* **437**, 396.
- [97] Kato, S. and 15 coauthors: 2003, *Nucl. Phys. A* **718**, 189.

- [98] Keeley, N., Kemper, K., Khoa, D.T.: 2003, *Nucl. Phys. A* **726**, 159.
- [99] Klay, N., & Käppeler, F.: 1988, *Phys. Rev. C* **38**, 295.
- [100] Klay, N., Käppeler, F., Beer, H., Schatz, G.: 1991, *Phys. Rev. C* **44**, 2839.
- [101] Koehler, P.E., & O'Brien, H.A.: 1989, *Phys. Rev. C* **39**, 1655.
- [102] Koehler, P.E., Kavanagh, R.W., Vogelaar, R.B., Gledenov, Yu.M., Popov, Yu.P.: 1997, *Phys. Rev. C* **56**, 1138.
- [103] Koehler, P.E. and 10 coauthors: 2000, *Phys. Rev. C* **62**, 055803.
- [104] Koehler, P.E., Harvey, J.A., Guber, K.H., Winters, R.R., Raman, S.: 2002, *J. Nucl. Sci. & Technology Suppl.* **2**, 546.
- [105] Koehler, P.E.: 2002, *Phys. Rev. C* **66**, 055805.
- [106] Kubono, S. and 15 coauthors: 2003, *Phys. Rev. Lett.* **90**, 062501.
- [107] Kunz, R., Fey, M., Jaeger, M., Mayer, A., Hammer, J.W., Staudt, G., Harissopulos, S., Paradellis, T.: 2002, *ApJ* **567**, 643.
- [108] Lambert, D.L., Smith, V.V., Busso, M., Gallino, R., Straniero, O.: 1995, *ApJ* **450**, 302.
- [109] Langanke, K., Martinez Pinedo, G.: 2000, *Nucl. Phys. A* **673**, 481.
- [110] Langer, N., Heger, A., Wellstein, S., Herwig, F.: 1999, *A&A* **346**, L37.
- [111] Lattanzio, J.: 1989, *ApJ* **344**, L25.
- [112] Lugaro, M., Davis, A.M., Gallino, R., Pellin, M.J., Straniero, O., Käppeler, F.: 2003, *ApJ* **563**, 186.
- [113] Lugaro, M., Ugalde, C., Karakas, A., Görres, J., Wiescher, M., Lattanzio, J., Cannon, R.: 2004, *615* **934L**, .
- [114] Marigo, P.: 2002, *A&A* **387**, 507.
- [115] Merrill, P.W.: 1952, *ApJ* **116**, 21.
- [116] Mowlavi, N., Goriely, S., Arnould, M.: 1998, *A&A* **330**, 206.

- [117] Munakata, H., Kohyama, Y., Itoh, N.: 1985, *ApJ* **296**, 197.
- [118] Munakata, H.: 1986, *ApJ* **304**, 580.
- [119] Nemeth, Zs., Käppeler, F., Reffo, G.: 1992, *ApJ* **392**, 277.
- [120] Nollett, K.M., Busso, M., Wasserburg, G.J.: 2003, *ApJ* **582**, 1036.
- [121] O'Brien, S., Dababneh, S., Heil, M., Käppeler, F., Plag, R., Reifarth, R., Gallino, R., Pignatari, M.: 2003, *Phys. Rev. C* **68**, 035801.
- [122] Oda, T., Hino, M., Muto, K., Takahara, M., Sato, K.: 1994, *Atom. Data Nucl. Data Tables* **56**, 231.
- [123] Paczynski, B.: 1970, *Acta Astron.* **20**, 47.
- [124] Patronis, N. and 9 coauthors: 2004, *Phys. Rev. C* **69**, 025803.
- [125] Potekhin, A.Y.: 1999, *A&A* **351**, 787.
- [126] Prada Moroni, P., & Straniero, O.: 2002, *ApJ* **581**, 585.
- [127] Rauscher, T., & Thielemann, F.K.: 2000, *Atom. Data Nucl. Data Tables* **75**, 1.
- [128] Rauscher, T., & Guber, K.H.: 2002, *Phys. Rev. C* **66**, 028802.
- [129] Redder, A., Becker, H.W., Lorenz-Wirzba, H., Rolfs, C., Schmalbrock, P., Trautvetter, H.P.: 1982, *Z. Phys. A* **305**, 325.
- [130] Reifarth, R. and 8 coauthors: 2002, *Phys. Rev. C* **66**, 064603.
- [131] Reifarth, R. and 9 coauthors: 2003, *ApJ* **582**, 1251.
- [132] Reimers, D.: 1975, *Mem. Soc. R. Sci. Liege, 6<sup>e</sup> Ser.* **8**, 369.
- [133] Renda, A., Fenner, Y., Gibson, B.K., Karakas, A.I., Lattanzio, J.C., Campbell, S., Chieffi, A., Cunha, K., Smith, V.V.: 2004, *MNRAS* **354**, 575.
- [134] Renzini, A.: 1981, in *Physical Processes in Red Giants*, eds. I. Iben Jr., A. Renzini, Dordrecht: Reidel, 431.
- [135] Reyniers, M., Van Winckel, H., Gallino, R., Straniero, O.: 2004, *A&A* **417**, 269.
- [136] Richardson, M.B., van Horn, H.M., Ratcliff, K.F., Malone, R.C.: 1982, *ApJ* **255**, 624.

- [137] Ritossa, C., Garcia-Berro, E., Iben, I.Jr.: 1996, *ApJ* **460**, 489.
- [138] Sackmann, I.-J, Smith, R.L., Despain, K.H.: 1974, *ApJ* **187**, 555.
- [139] Savina, M.R., Davis, A. M., Tripa, C.E., Pellin, M.J., Gallino, R., Lewis, R.S., Amari, S.: 2004, *Science* **303**, 649.
- [140] Schardt, A., Fowler, W.A., Lauritsen, C.C.: 1952, *Phys. Rev. C* **86**, 527.
- [141] Schatz, H., Jaag, S., Linker, G., Steininger, R., Käppeler, F., Koehler, P.E., Graff, S.M., Wiescher, M.: 1995, *Phys. Rev. C* **51**, 379.
- [142] Schöier, F.L., & Olofsson, H.: 2001, *A&AS* **368**, 969.
- [143] Schwarzschild, M.: 1958, *Structure and Evolution of the Stars*, Princeton: Princeton University Press.
- [144] Schwarzschild, M., & Härm, R.: 1965, *ApJ* **142**, 855.
- [145] Schwarzschild, M., & Härm, R.: 1967, *ApJ* **150**, 961.
- [146] Secchi, A.: 1868, *Astronomische Nachrichten* **1737**, 9.
- [147] Seeger, P.A., Fowler, W.A., Clayton, D.D.: 1965, *Astrophys. J. Suppl.* **11**, 121.
- [148] Shetrone, M.D., Bolte, M., Stetson, P.B.: 1998, *AJ* **115**, 1888.
- [149] Shetrone, M.D., Côte, P., Stetson, P.B.: 2001, *PASP* **113**, 1122.
- [150] Siess, L., Goriely, S, Langer, N.: 2004, *A&A* **415**, 1089.
- [151] Sneden, C., Ivans, I.I., Kraft, R.P.: 2000, *Mem. SAIt* **71**, 657.
- [152] Straniero, O.: 1988 *A&AS* **76**, 157.
- [153] Straniero, O., Gallino, R., Busso, M., Chieffi, A., Limongi, M., Salaris, M.: 1995, *ApJ* **440**, L85.
- [154] Straniero, O., Chieffi, A., Limongi, M., Gallino, R., Busso, M., Arlandini, C.: 1997, *ApJ* **478**, 332.
- [155] Straniero, O., Chieffi, A., Limongi, M.: 1997, *ApJ* **490**, 425.
- [156] Straniero, O., Domínguez, I, Cristallo, S., Gallino, R.: 2003, *PASA* **20**, 389.

- [157] Straniero, O., Cristallo, S., Gallino, R., Domínguez, I.: 2004, *Mem. SAIt*, **75**, 665.
- [158] Suda, T., Aikawa, M., Machida, M.N., Fujimoto, M.Y., Iben, I.Jr.: 2004, *ApJS* **611**, 476.
- [159] Suess. H.E. & Urey, H.C.: 1956, *Rev. Mod. Phys.*, **28**, 53.
- [160] Takahashi, K., & Yokoi, K.: 1987, *Atom. Data Nucl. Data Tables* **36**, 375.
- [161] Thielemann, F.K., Truran, J.W., Arnould, M.: 1986, *Adv. Nucl. Astrophys.:* Proceedings of the Second IAP Workshop, Paris, France, 525.
- [162] Tinsley B.M.: 1980, *Fundam. of Cosmic Phys.* **5**, 287.
- [163] Travaglio, C., Gallino, R., Arnone, E., Cowan, J., Jordan, F., Sneden, C.: 2004, *ApJ* **601**, 864.
- [164] Ugalde., C. and 8 coauthors: 2005, *Nucl. Phys. A* **758**, 577.
- [165] Ulrich, R.K.: 1973, in *Explosive Nucleosynthesis*, eds. Schramm D.N. & Arnett W.D., Austin: University Texas Press, 139.
- [166] Van Eck, S., Goriely, S., Jorissen, A., Plez, B.: 2003, *A&A* **404**, 291.
- [167] Vassiliadis, E., & Wood, P.R.: 1993, *ApJ* **413**, 641.
- [168] Wagemans, C., Bieber, R., Weigmann, H., Geltenbort, P.: 1998, *Phys. Rev. C* **57**, 1766.
- [169] Wagemans, C., Goeminne, G., de Smet, L., Wagemans, J.: 2003, *Nucl. Phys. A* **719**, 127.
- [170] Wagemans, J., Wagemans, C., Goeminne, G., Geltenbort, P., Moens, A.: 2001, *Nucl. Phys. A* **696**, 31.
- [171] Wagemans, J., Wagemans, C., Goeminne, G., Serot, O., Loiselet, M., Gaelens, M.: 2002, *Phys. Rev. C* **65**, 034614.
- [172] Wallerstein, G. and 14 coauthors: 1997, *Rev. Mod. Phys.* **69**, 995.
- [173] Wallerstein, G., & Knapp, G.R.: 1998, *ARA&A* **36**, 369.
- [174] Ward, R.A., Newman, M.J., Clayton, D.D.: 1976, *ApJS* **31**, 33.

- [175] Ward, R.A., & Newman, M.J.: 1978, *ApJ* **219**, 195.
- [176] Wasserburg, J.J., Busso, M., Gallino, R., Nollett, K.M.: *Nucl. Phys. A*, in press
- [177] Weidemann, V.: 2000, *A&A* **363**, 647.
- [178] Whitelock, P.A., Feast, M.W., van Loon, J.Th., Zijlstra, A.A.: 2003, *MNRAS* **342**, 86.
- [179] Wiescher, M., & Kettner, K.U.: 1982, *ApJ* **263**, 891.
- [180] Winters, J.M., Le Bertre, T., Jeong, K.S., Nyman, L.-A., Epchtein, N.: 2003, *A&A* **409**, 715.
- [181] Wisshak, K., Voss, F., Käppeler, F., Kazakov, L.: 2002, *Phys. Rev. C* **66**, 025801.
- [182] Wisshak, K., Voss, F., Käppeler, F., Kazakov, L.: 2006, *Phys. Rev. C* **73**, 015807.
- [183] Wood, P.R.: 1981, in *Physical Processes in Red Giants*, eds. I. Iben Jr., A. Renzini, Dordrecht: Reidel, 135.
- [184] Zinner, E.: 1999, *Ann. Rev. Earth Planet. Sci.* **26**, 147.
- [185] Zyskind, J.L., & Parker, P.D.: 1979, *Nucl. Phys. A* **320**, 404.

# Appendix A

## Yields

Hereafter we report the yields (in  $M_{\odot}$  units) for a  $M=2M_{\odot}$  star with different metallicities:  $Z=Z_{\odot}$  (corresponding to  $1.5 \times 10^{-2}$ , see Section 7.1),  $Z=1 \times 10^{-3}$  (see Section 7.2) and  $Z=1 \times 10^{-4}$  (the *st* case described in Section 7.2 and the *test* case presented in Section 8.1).

Isotope	$Z = 1.5 \times 10^{-2}$	$Z = 1 \times 10^{-3}$	$Z = 1 \times 10^{-4}$ ( <i>st</i> )	$Z = 1 \times 10^{-4}$ ( <i>test</i> )
$^1\text{H}$	-4.29E-02	-5.73E-02	-6.12E-02	-1.84E-01
$^2\text{H}$	-3.31E-05	-3.42E-05	-3.36E-05	-3.12E-05
$^3\text{He}$	3.75E-04	2.82E-04	1.97E-04	1.50E-04
$^4\text{He}$	3.42E-02	4.72E-02	5.25E-02	1.45E-01
$^6\text{Li}$	-1.06E-09	-7.01E-11	-6.89E-12	-6.40E-12
$^7\text{Li}$	-1.51E-08	-9.49E-10	-4.43E-11	5.86E-11
$^7\text{Be}$	7.37E-19	1.74E-17	1.59E-17	6.85E-17
$^9\text{Be}$	-2.65E-10	-1.80E-11	-1.76E-12	-1.64E-12
$^{10}\text{B}$	-1.34E-09	-9.15E-11	-9.05E-12	-8.44E-12
$^{11}\text{B}$	-5.75E-09	-3.97E-10	-3.96E-11	-3.69E-11
$^{12}\text{C}$	6.04E-03	9.04E-03	7.94E-03	3.07E-02
$^{13}\text{C}$	5.43E-05	3.35E-06	4.58E-07	2.84E-06
$^{14}\text{C}$	5.31E-11	4.56E-10	4.72E-10	1.00E-08
$^{14}\text{N}$	1.36E-03	1.40E-04	2.58E-05	1.21E-04
$^{15}\text{N}$	-2.80E-06	-2.15E-07	-2.12E-08	-1.20E-08
$^{16}\text{O}$	-1.05E-04	2.21E-04	2.08E-04	6.58E-04
$^{17}\text{O}$	3.40E-05	7.55E-06	9.62E-07	7.92E-07
$^{18}\text{O}$	-5.76E-06	-5.14E-07	-5.57E-08	1.39E-07

Isotope	$Z = 1.5 \times 10^{-2}$	$Z = 1 \times 10^{-3}$	$Z = 1 \times 10^{-4}$ ( <i>st</i> )	$Z = 1 \times 10^{-4}$ ( <i>test</i> )
<sup>19</sup> F	9.34E-07	7.48E-07	7.78E-07	1.15E-05
<sup>20</sup> Ne	-2.02E-05	3.55E-07	1.23E-06	1.73E-04
<sup>21</sup> Ne	5.17E-08	1.22E-07	1.20E-07	3.30E-06
<sup>22</sup> Ne	8.24E-04	4.66E-04	3.11E-04	6.71E-03
<sup>23</sup> Na	2.11E-05	5.14E-06	2.67E-06	1.18E-04
<sup>24</sup> Mg	7.96E-07	6.32E-06	3.18E-06	3.53E-04
<sup>25</sup> Mg	-1.16E-06	3.57E-06	3.07E-06	1.43E-04
<sup>26</sup> Mg	8.91E-07	2.87E-06	2.99E-06	1.04E-04
<sup>26</sup> Al	3.92E-07	3.46E-08	1.40E-08	2.60E-07
<sup>27</sup> Al	-6.33E-08	1.02E-06	4.12E-07	5.01E-06
<sup>28</sup> Si	-1.33E-05	1.10E-07	2.21E-07	1.64E-06
<sup>29</sup> Si	-5.97E-07	4.10E-08	1.83E-08	1.27E-07
<sup>30</sup> Si	1.36E-07	1.26E-07	3.46E-08	1.86E-07
<sup>32</sup> Si	1.03E-16	7.07E-15	1.01E-14	3.93E-15
<sup>31</sup> P	2.78E-07	9.27E-08	3.54E-08	1.37E-07
<sup>32</sup> P	3.06E-20	2.09E-18	2.97E-18	1.16E-18
<sup>32</sup> S	-7.54E-06	-1.16E-07	-8.12E-09	-7.18E-08
<sup>33</sup> S	3.69E-08	1.49E-08	1.50E-09	7.93E-09
<sup>34</sup> S	-1.76E-07	2.82E-08	5.75E-09	2.50E-08
<sup>36</sup> S	2.23E-08	4.14E-09	8.78E-10	3.11E-09
<sup>35</sup> Cl	-9.55E-08	-3.36E-09	-4.18E-10	-2.17E-09
<sup>36</sup> Cl	1.37E-09	2.30E-10	2.19E-11	6.54E-11
<sup>37</sup> Cl	7.80E-08	7.13E-09	7.12E-10	3.94E-09
<sup>36</sup> Ar	-8.72E-07	-3.18E-08	-4.45E-09	-2.25E-08
<sup>38</sup> Ar	4.00E-08	2.50E-08	3.60E-09	1.93E-08
<sup>39</sup> Ar	1.23E-13	2.10E-12	5.02E-13	3.01E-13
<sup>40</sup> Ar	1.74E-08	1.53E-09	4.99E-10	1.80E-09
<sup>39</sup> K	-5.31E-08	-3.97E-11	2.37E-10	7.86E-10
<sup>40</sup> K	6.53E-09	9.97E-10	9.51E-11	6.01E-10

Isotope	$Z = 1.5 \times 10^{-2}$	$Z = 1 \times 10^{-3}$	$Z = 1 \times 10^{-4}$ ( <i>st</i> )	$Z = 1 \times 10^{-4}$ ( <i>test</i> )
<sup>41</sup> K	4.01E-08	4.90E-09	4.39E-10	2.69E-09
<sup>40</sup> Ca	-1.57E-06	-4.88E-08	-7.09E-09	-3.52E-08
<sup>41</sup> Ca	3.97E-09	4.81E-10	4.39E-11	1.35E-10
<sup>42</sup> Ca	1.77E-08	3.31E-09	4.26E-10	2.30E-09
<sup>43</sup> Ca	3.12E-09	6.64E-10	1.04E-10	5.69E-10
<sup>44</sup> Ca	-6.74E-09	5.65E-10	1.78E-10	7.70E-10
<sup>46</sup> Ca	1.89E-09	1.75E-10	8.24E-11	3.24E-10
<sup>48</sup> Ca	-3.02E-09	-3.21E-11	-4.02E-12	-1.81E-11
<sup>45</sup> Sc	4.09E-09	6.27E-10	9.44E-11	5.30E-10
<sup>46</sup> Ti	3.10E-09	2.42E-10	4.54E-11	1.49E-10
<sup>47</sup> Ti	-4.68E-09	-2.26E-10	-7.31E-12	-8.43E-11
<sup>48</sup> Ti	-6.39E-08	-3.83E-09	-4.18E-10	-2.35E-09
<sup>49</sup> Ti	1.69E-08	2.90E-09	2.60E-10	1.52E-09
<sup>50</sup> Ti	4.37E-08	5.93E-09	6.03E-10	3.46E-09
<sup>50</sup> V	-3.34E-11	-2.31E-12	-2.41E-13	-1.35E-12
<sup>51</sup> V	-6.67E-09	-5.48E-11	-3.27E-11	-1.40E-10
<sup>50</sup> Cr	-2.74E-08	-1.89E-09	-1.96E-10	-1.10E-09
<sup>52</sup> Cr	-3.67E-07	-9.86E-09	-1.57E-09	-7.89E-09
<sup>53</sup> Cr	-4.75E-08	-8.74E-10	-1.40E-10	-5.72E-10
<sup>54</sup> Cr	4.87E-08	1.01E-08	1.28E-09	7.33E-09
<sup>55</sup> Mn	-1.29E-07	1.22E-08	-6.46E-10	-1.36E-09
<sup>54</sup> Fe	-2.30E-06	-1.40E-07	-1.59E-08	-8.72E-08
<sup>55</sup> Fe	7.09E-15	2.78E-13	1.98E-14	3.93E-14
<sup>56</sup> Fe	-2.92E-05	-1.03E-06	-1.50E-07	-7.89E-07
<sup>57</sup> Fe	1.27E-06	3.78E-07	3.21E-08	2.03E-07
<sup>58</sup> Fe	2.22E-06	4.65E-07	6.68E-08	3.86E-07
<sup>60</sup> Fe	1.06E-07	9.30E-09	6.78E-09	2.20E-08
<sup>59</sup> Co	5.68E-07	9.46E-08	1.57E-08	9.04E-08
<sup>60</sup> Co	3.71E-13	3.27E-14	2.38E-14	7.72E-14

Isotope	$Z = 1.5 \times 10^{-2}$	$Z = 1 \times 10^{-3}$	$Z = 1 \times 10^{-4}$ ( <i>st</i> )	$Z = 1 \times 10^{-4}$ ( <i>test</i> )
<sup>58</sup> Ni	-1.64E-06	-1.07E-07	-1.20E-08	-6.69E-08
<sup>59</sup> Ni	2.10E-08	3.38E-09	2.21E-10	8.58E-10
<sup>60</sup> Ni	-1.08E-07	3.67E-08	8.28E-09	4.53E-08
<sup>61</sup> Ni	1.82E-07	2.82E-08	5.15E-09	2.56E-08
<sup>62</sup> Ni	2.90E-07	3.57E-08	9.42E-09	3.91E-08
<sup>63</sup> Ni	4.17E-14	1.79E-12	6.83E-13	5.77E-13
<sup>64</sup> Ni	3.51E-07	1.64E-08	9.30E-09	3.05E-08
<sup>63</sup> Cu	1.18E-07	1.74E-08	6.05E-09	2.48E-08
<sup>65</sup> Cu	1.03E-07	4.87E-09	2.28E-09	7.28E-09
<sup>64</sup> Zn	2.28E-08	6.86E-10	5.12E-10	7.95E-10
<sup>66</sup> Zn	9.96E-08	4.54E-09	2.30E-09	7.43E-09
<sup>67</sup> Zn	2.30E-08	1.08E-09	5.03E-10	1.67E-09
<sup>68</sup> Zn	1.30E-07	5.01E-09	2.30E-09	8.05E-09
<sup>70</sup> Zn	-3.41E-10	-1.15E-11	5.19E-12	6.53E-11
<sup>69</sup> Ga	2.56E-08	7.67E-10	3.16E-10	1.12E-09
<sup>71</sup> Ga	2.85E-08	6.53E-10	2.14E-10	7.67E-10
<sup>70</sup> Ge	4.73E-08	1.24E-09	4.43E-10	1.60E-09
<sup>72</sup> Ge	5.24E-08	1.34E-09	4.07E-10	1.57E-09
<sup>73</sup> Ge	1.46E-08	3.92E-10	1.17E-10	4.64E-10
<sup>74</sup> Ge	7.23E-08	1.76E-09	4.79E-10	2.02E-09
<sup>76</sup> Ge	-4.78E-10	-2.07E-11	2.56E-12	5.17E-11
<sup>75</sup> As	6.33E-09	1.45E-10	4.19E-11	1.77E-10
<sup>76</sup> Se	2.64E-08	6.20E-10	1.50E-10	6.62E-10
<sup>77</sup> Se	1.05E-08	2.29E-10	5.71E-11	2.56E-10
<sup>78</sup> Se	3.97E-08	8.80E-10	1.98E-10	9.26E-10
<sup>79</sup> Se	4.14E-09	3.92E-11	9.47E-12	1.28E-10
<sup>80</sup> Se	7.99E-08	1.81E-09	3.64E-10	1.90E-09
<sup>82</sup> Se	-3.00E-10	-8.36E-12	2.64E-13	2.33E-11
<sup>79</sup> Br	6.74E-09	2.98E-10	6.66E-11	2.35E-10

Isotope	$Z = 1.5 \times 10^{-2}$	$Z = 1 \times 10^{-3}$	$Z = 1 \times 10^{-4}$ ( <i>st</i> )	$Z = 1 \times 10^{-4}$ ( <i>test</i> )
<sup>81</sup> Br	1.40E-08	2.55E-10	4.80E-11	2.54E-10
<sup>80</sup> Kr	7.80E-09	3.36E-11	3.85E-12	1.64E-11
<sup>81</sup> Kr	1.12E-09	5.37E-12	5.46E-13	1.80E-12
<sup>82</sup> Kr	5.32E-08	1.11E-09	1.64E-10	8.58E-10
<sup>83</sup> Kr	1.71E-08	3.64E-10	5.46E-11	2.99E-10
<sup>84</sup> Kr	1.08E-07	2.56E-09	3.71E-10	2.27E-09
<sup>86</sup> Kr	2.39E-08	1.53E-09	2.45E-10	2.66E-09
<sup>85</sup> Rb	1.89E-08	6.46E-10	1.12E-10	7.13E-10
<sup>87</sup> Rb	8.17E-09	6.30E-10	1.27E-10	1.18E-09
<sup>86</sup> Sr	5.66E-08	8.49E-10	7.94E-11	5.02E-10
<sup>87</sup> Sr	3.65E-08	5.86E-10	4.62E-11	3.08E-10
<sup>88</sup> Sr	7.52E-07	1.83E-08	1.20E-09	1.17E-08
<sup>89</sup> Y	1.50E-07	4.56E-09	3.22E-10	3.30E-09
<sup>90</sup> Zr	1.62E-07	4.52E-09	2.67E-10	2.81E-09
<sup>91</sup> Zr	3.84E-08	1.44E-09	9.46E-11	1.03E-09
<sup>92</sup> Zr	6.28E-08	2.35E-09	1.65E-10	1.80E-09
<sup>93</sup> Zr	1.66E-08	6.52E-10	4.92E-11	4.61E-10
<sup>94</sup> Zr	8.65E-08	3.06E-09	1.95E-10	2.21E-09
<sup>96</sup> Zr	2.60E-09	5.25E-10	7.62E-11	9.17E-10
<sup>93</sup> Nb	4.76E-09	1.18E-10	5.07E-12	1.38E-10
<sup>92</sup> Mo	-3.48E-11	-2.48E-12	-2.47E-13	-1.40E-12
<sup>94</sup> Mo	7.68E-10	5.29E-12	-9.36E-14	1.92E-14
<sup>95</sup> Mo	8.49E-09	3.54E-10	2.31E-11	2.76E-10
<sup>96</sup> Mo	1.79E-08	5.96E-10	3.61E-11	4.05E-10
<sup>97</sup> Mo	6.19E-09	2.03E-10	1.32E-11	1.50E-10
<sup>98</sup> Mo	2.22E-08	7.23E-10	3.87E-11	4.55E-10
<sup>100</sup> Mo	1.93E-10	5.62E-11	4.54E-12	6.47E-11
<sup>99</sup> Tc	7.70E-10	3.41E-11	2.61E-12	1.95E-11
<sup>96</sup> Ru	-1.24E-11	-8.32E-13	-7.35E-14	-4.21E-13

Isotope	$Z = 1.5 \times 10^{-2}$	$Z = 1 \times 10^{-3}$	$Z = 1 \times 10^{-4}$ ( <i>st</i> )	$Z = 1 \times 10^{-4}$ ( <i>test</i> )
<sup>98</sup> Ru	-2.87E-12	-2.41E-13	-2.47E-14	-1.40E-13
<sup>99</sup> Ru	2.28E-09	6.49E-11	2.55E-12	4.30E-11
<sup>100</sup> Ru	1.11E-08	3.55E-10	1.73E-11	2.07E-10
<sup>101</sup> Ru	2.39E-09	8.03E-11	4.02E-12	5.01E-11
<sup>102</sup> Ru	1.21E-08	4.27E-10	2.16E-11	2.64E-10
<sup>104</sup> Ru	1.93E-10	5.54E-11	3.92E-12	5.62E-11
<sup>103</sup> Rh	2.53E-09	8.95E-11	4.50E-12	5.63E-11
<sup>104</sup> Pd	8.36E-09	2.71E-10	1.36E-11	1.60E-10
<sup>105</sup> Pd	2.14E-09	7.53E-11	3.90E-12	4.82E-11
<sup>106</sup> Pd	9.73E-09	3.51E-10	1.87E-11	2.24E-10
<sup>107</sup> Pd	1.83E-09	6.70E-11	3.65E-12	4.16E-11
<sup>108</sup> Pd	1.20E-08	4.49E-10	2.38E-11	2.81E-10
<sup>110</sup> Pd	1.80E-10	6.25E-11	4.58E-12	6.53E-11
<sup>107</sup> Ag	7.12E-11	5.96E-13	-9.76E-14	1.62E-12
<sup>109</sup> Ag	3.10E-09	1.14E-10	6.00E-12	7.08E-11
<sup>108</sup> Cd	5.79E-11	2.12E-13	-9.65E-15	-4.76E-14
<sup>110</sup> Cd	1.01E-08	3.63E-10	1.86E-11	2.12E-10
<sup>111</sup> Cd	3.41E-09	1.33E-10	7.11E-12	8.43E-11
<sup>112</sup> Cd	1.24E-08	5.17E-10	2.76E-11	3.25E-10
<sup>113</sup> Cd	3.64E-09	1.51E-10	8.02E-12	9.46E-11
<sup>114</sup> Cd	1.77E-08	7.68E-10	4.08E-11	4.78E-10
<sup>116</sup> Cd	3.01E-10	1.35E-10	1.30E-11	1.75E-10
<sup>113</sup> In	-1.33E-12	-7.69E-14	-6.60E-15	-3.78E-14
<sup>115</sup> In	3.49E-09	1.55E-10	8.30E-12	9.85E-11
<sup>114</sup> Sn	-2.80E-12	-2.21E-13	-2.10E-14	-1.19E-13
<sup>115</sup> Sn	-1.41E-12	-1.12E-13	-1.08E-14	-6.16E-14
<sup>116</sup> Sn	2.40E-08	1.02E-09	5.09E-11	5.78E-10
<sup>117</sup> Sn	7.27E-09	3.28E-10	1.78E-11	2.09E-10
<sup>118</sup> Sn	3.11E-08	1.60E-09	8.86E-11	1.04E-09

Isotope	$Z = 1.5 \times 10^{-2}$	$Z = 1 \times 10^{-3}$	$Z = 1 \times 10^{-4}$ ( <i>st</i> )	$Z = 1 \times 10^{-4}$ ( <i>test</i> )
<sup>119</sup> Sn	9.48E-09	4.74E-10	2.62E-11	3.07E-10
<sup>120</sup> Sn	4.76E-08	2.70E-09	1.52E-10	1.81E-09
<sup>122</sup> Sn	3.19E-10	2.36E-10	3.29E-11	4.71E-10
<sup>124</sup> Sn	-1.68E-11	3.32E-12	1.60E-12	4.87E-11
<sup>121</sup> Sb	3.61E-09	2.08E-10	1.18E-11	1.43E-10
<sup>123</sup> Sb	1.97E-10	5.90E-11	5.07E-12	7.06E-11
<sup>122</sup> Te	6.14E-09	3.04E-10	1.68E-11	1.98E-10
<sup>123</sup> Te	2.22E-09	1.02E-10	5.59E-12	6.47E-11
<sup>124</sup> Te	1.19E-08	6.29E-10	3.60E-11	4.31E-10
<sup>125</sup> Te	4.01E-09	2.08E-10	1.16E-11	1.41E-10
<sup>126</sup> Te	2.17E-08	1.23E-09	6.30E-11	7.61E-10
<sup>128</sup> Te	2.36E-09	1.96E-10	1.46E-11	2.27E-10
<sup>130</sup> Te	-1.55E-10	-7.07E-12	-9.25E-13	-4.87E-12
<sup>127</sup> I	2.71E-09	1.57E-10	7.64E-12	9.77E-11
<sup>129</sup> I	3.12E-11	5.87E-12	5.44E-13	6.97E-12
<sup>128</sup> Xe	6.75E-09	3.82E-10	1.91E-11	2.27E-10
<sup>129</sup> Xe	2.62E-09	1.51E-10	7.36E-12	9.79E-11
<sup>130</sup> Xe	1.43E-08	8.44E-10	4.21E-11	5.04E-10
<sup>131</sup> Xe	5.08E-09	3.17E-10	1.53E-11	1.88E-10
<sup>132</sup> Xe	2.61E-08	1.78E-09	8.83E-11	1.06E-09
<sup>134</sup> Xe	2.43E-10	2.44E-10	3.20E-11	4.62E-10
<sup>136</sup> Xe	-2.38E-11	1.58E-12	9.37E-13	3.85E-11
<sup>133</sup> Cs	3.40E-09	2.53E-10	1.27E-11	1.56E-10
<sup>135</sup> Cs	8.91E-10	2.51E-10	1.75E-11	2.07E-10
<sup>134</sup> Ba	9.63E-09	5.23E-10	2.50E-11	2.91E-10
<sup>135</sup> Ba	3.50E-09	1.80E-10	8.05E-12	1.14E-10
<sup>136</sup> Ba	2.42E-08	1.83E-09	8.81E-11	1.06E-09
<sup>137</sup> Ba	1.87E-08	1.70E-09	1.05E-10	1.22E-09
<sup>138</sup> Ba	1.39E-07	2.68E-08	1.36E-09	1.71E-08

Isotope	$Z = 1.5 \times 10^{-2}$	$Z = 1 \times 10^{-3}$	$Z = 1 \times 10^{-4}$ ( <i>st</i> )	$Z = 1 \times 10^{-4}$ ( <i>test</i> )
<sup>139</sup> La	1.56E-08	3.42E-09	1.70E-10	2.15E-09
<sup>140</sup> Ce	3.55E-08	1.17E-08	5.28E-10	6.46E-09
<sup>142</sup> Ce	9.59E-11	5.14E-10	5.72E-11	7.85E-10
<sup>141</sup> Pr	2.75E-09	1.23E-09	6.23E-11	7.96E-10
<sup>142</sup> Nd	7.98E-09	2.87E-09	1.17E-10	1.41E-09
<sup>143</sup> Nd	1.04E-09	4.89E-10	2.47E-11	3.16E-10
<sup>144</sup> Nd	3.24E-09	1.59E-09	8.29E-11	1.07E-09
<sup>145</sup> Nd	5.73E-10	2.96E-10	1.53E-11	1.99E-10
<sup>146</sup> Nd	3.08E-09	1.47E-09	7.42E-11	9.40E-10
<sup>148</sup> Nd	7.57E-11	2.64E-10	1.66E-11	2.27E-10
<sup>150</sup> Nd	-8.25E-12	9.24E-12	8.50E-13	1.56E-11
<sup>144</sup> Sm	-1.19E-12	-8.68E-14	-8.44E-15	-4.79E-14
<sup>146</sup> Sm	8.08E-14	5.23E-15	1.38E-16	9.57E-16
<sup>147</sup> Sm	3.21E-10	1.72E-10	8.61E-12	1.11E-10
<sup>148</sup> Sm	1.00E-09	3.72E-10	1.73E-11	2.06E-10
<sup>149</sup> Sm	1.32E-10	7.26E-11	3.81E-12	4.94E-11
<sup>150</sup> Sm	6.07E-10	3.16E-10	1.64E-11	2.05E-10
<sup>151</sup> Sm	3.59E-17	3.38E-15	4.04E-16	1.28E-15
<sup>152</sup> Sm	4.21E-10	2.72E-10	1.44E-11	1.81E-10
<sup>154</sup> Sm	2.39E-11	1.24E-10	7.80E-12	1.11E-10
<sup>151</sup> Eu	7.41E-11	4.37E-11	2.23E-12	2.96E-11
<sup>153</sup> Eu	7.01E-11	5.00E-11	2.65E-12	3.42E-11
<sup>152</sup> Gd	1.86E-11	3.32E-12	1.58E-13	2.05E-12
<sup>154</sup> Gd	1.57E-10	7.54E-11	3.90E-12	4.84E-11
<sup>155</sup> Gd	9.25E-11	7.08E-11	4.01E-12	5.26E-11
<sup>156</sup> Gd	3.80E-10	2.23E-10	1.24E-11	1.58E-10
<sup>157</sup> Gd	1.78E-10	1.02E-10	5.72E-12	7.31E-11
<sup>158</sup> Gd	7.80E-10	4.01E-10	2.25E-11	2.82E-10
<sup>160</sup> Gd	9.61E-12	9.03E-11	6.17E-12	9.07E-11

Isotope	$Z = 1.5 \times 10^{-2}$	$Z = 1 \times 10^{-3}$	$Z = 1 \times 10^{-4}$ ( <i>st</i> )	$Z = 1 \times 10^{-4}$ ( <i>test</i> )
<sup>159</sup> Tb	1.65E-10	8.96E-11	5.02E-12	6.39E-11
<sup>160</sup> Dy	2.71E-10	1.29E-10	7.13E-12	8.72E-11
<sup>161</sup> Dy	1.12E-10	6.72E-11	3.88E-12	5.02E-11
<sup>162</sup> Dy	5.56E-10	2.87E-10	1.62E-11	2.04E-10
<sup>163</sup> Dy	1.73E-10	8.91E-11	4.98E-12	6.36E-11
<sup>164</sup> Dy	1.02E-09	4.78E-10	2.44E-11	3.03E-10
<sup>163</sup> Ho	8.98E-14	2.73E-13	2.56E-14	1.86E-13
<sup>165</sup> Ho	2.14E-10	1.21E-10	6.42E-12	8.12E-11
<sup>164</sup> Er	7.84E-11	5.03E-11	2.83E-12	3.67E-11
<sup>166</sup> Er	4.14E-10	1.82E-10	9.45E-12	1.15E-10
<sup>167</sup> Er	1.87E-10	8.45E-11	4.48E-12	5.60E-11
<sup>168</sup> Er	7.96E-10	3.61E-10	1.79E-11	2.22E-10
<sup>170</sup> Er	6.07E-11	1.91E-10	1.03E-11	1.46E-10
<sup>169</sup> Tm	1.97E-10	9.68E-11	4.79E-12	6.14E-11
<sup>170</sup> Yb	2.67E-10	1.14E-10	5.27E-12	6.45E-11
<sup>171</sup> Yb	2.63E-10	1.70E-10	8.15E-12	1.08E-10
<sup>172</sup> Yb	7.90E-10	4.24E-10	2.01E-11	2.52E-10
<sup>173</sup> Yb	3.60E-10	1.96E-10	9.38E-12	1.20E-10
<sup>174</sup> Yb	1.70E-09	9.40E-10	4.47E-11	5.67E-10
<sup>176</sup> Yb	3.54E-11	2.04E-10	1.33E-11	1.88E-10
<sup>175</sup> Lu	2.24E-10	1.32E-10	6.27E-12	8.09E-11
<sup>176</sup> Lu	4.00E-11	2.33E-11	1.10E-12	1.40E-11
<sup>176</sup> Hf	3.08E-10	1.65E-10	7.79E-12	9.70E-11
<sup>177</sup> Hf	1.74E-10	1.14E-10	5.71E-12	7.41E-11
<sup>178</sup> Hf	8.22E-10	5.14E-10	2.61E-11	3.28E-10
<sup>179</sup> Hf	2.78E-10	1.75E-10	8.88E-12	1.12E-10
<sup>180</sup> Hf	1.56E-09	9.58E-10	4.74E-11	5.79E-10
<sup>182</sup> Hf	1.64E-11	1.26E-10	8.67E-12	1.18E-10
<sup>180</sup> Ta	4.39E-14	3.54E-14	1.85E-15	2.94E-14

Isotope	$Z = 1.5 \times 10^{-2}$	$Z = 1 \times 10^{-3}$	$Z = 1 \times 10^{-4}$ ( <i>st</i> )	$Z = 1 \times 10^{-4}$ ( <i>test</i> )
<sup>181</sup> Ta	3.12E-10	2.04E-10	1.00E-11	1.25E-10
<sup>180</sup> W	-4.55E-14	-2.74E-15	-2.36E-16	-1.35E-15
<sup>182</sup> W	7.63E-10	3.43E-10	1.58E-11	1.89E-10
<sup>183</sup> W	4.54E-10	2.53E-10	1.23E-11	1.52E-10
<sup>184</sup> W	1.17E-09	6.95E-10	3.16E-11	3.83E-10
<sup>186</sup> W	1.80E-10	4.85E-10	2.38E-11	3.05E-10
<sup>185</sup> Re	2.17E-10	1.37E-10	6.27E-12	7.76E-11
<sup>187</sup> Re	-1.80E-11	9.44E-11	3.32E-12	6.13E-11
<sup>186</sup> Os	4.71E-10	2.30E-10	9.85E-12	1.14E-10
<sup>187</sup> Os	2.03E-10	6.57E-11	4.19E-12	3.16E-11
<sup>188</sup> Os	5.65E-10	4.15E-10	2.06E-11	2.56E-10
<sup>189</sup> Os	1.31E-10	1.13E-10	5.64E-12	7.20E-11
<sup>190</sup> Os	7.48E-10	5.52E-10	2.85E-11	3.59E-10
<sup>192</sup> Os	1.45E-12	1.56E-10	8.30E-12	1.13E-10
<sup>191</sup> Ir	1.02E-10	1.17E-10	5.95E-12	7.70E-11
<sup>193</sup> Ir	8.86E-11	1.45E-10	7.49E-12	9.91E-11
<sup>192</sup> Pt	3.48E-10	1.55E-10	7.91E-12	9.27E-11
<sup>194</sup> Pt	8.99E-10	6.68E-10	3.72E-11	4.70E-10
<sup>195</sup> Pt	2.66E-10	2.50E-10	1.31E-11	1.66E-10
<sup>196</sup> Pt	1.46E-09	9.98E-10	4.84E-11	5.81E-10
<sup>198</sup> Pt	-7.63E-12	1.17E-10	9.27E-12	1.44E-10
<sup>197</sup> Au	3.51E-10	2.78E-10	1.30E-11	1.60E-10
<sup>198</sup> Hg	1.22E-09	8.23E-10	3.62E-11	4.18E-10
<sup>199</sup> Hg	5.19E-10	4.11E-10	1.87E-11	2.29E-10
<sup>200</sup> Hg	1.79E-09	1.44E-09	6.57E-11	7.97E-10
<sup>201</sup> Hg	7.25E-10	6.28E-10	2.88E-11	3.51E-10
<sup>202</sup> Hg	3.03E-09	2.46E-09	1.13E-10	1.32E-09
<sup>204</sup> Hg	7.83E-13	8.14E-11	8.93E-12	1.56E-10
<sup>203</sup> Tl	1.33E-09	1.28E-09	6.06E-11	7.22E-10

Isotope	$Z = 1.5 \times 10^{-2}$	$Z = 1 \times 10^{-3}$	$Z = 1 \times 10^{-4}$ ( <i>st</i> )	$Z = 1 \times 10^{-4}$ ( <i>test</i> )
<sup>205</sup> Tl	3.60E-09	2.88E-09	1.20E-10	1.42E-09
<sup>204</sup> Pb	2.33E-09	1.57E-09	6.47E-11	7.50E-10
<sup>205</sup> Pb	1.70E-10	1.30E-10	4.44E-12	5.31E-11
<sup>206</sup> Pb	1.18E-08	1.62E-08	9.14E-10	8.22E-09
<sup>207</sup> Pb	1.36E-08	2.81E-08	1.55E-09	1.32E-08
<sup>208</sup> Pb	1.84E-08	4.93E-07	5.85E-08	1.48E-07
<sup>209</sup> Bi	8.34E-11	7.80E-09	1.37E-09	3.64E-09
<sup>210</sup> Po	3.19E-18	8.53E-15	4.19E-15	6.30E-14



# Appendix B

## Surface enrichments

Hereafter we report the pulse by pulse surface enrichments, in the usual spectroscopic notation<sup>1</sup>, for a star with initial mass  $M=2M_{\odot}$  and different metallicities:  $Z=Z_{\odot}$  (corresponding to  $1.5 \times 10^{-2}$ , see Section 7.1),  $Z=1 \times 10^{-3}$  (see Section 7.2) and  $Z=1 \times 10^{-4}$  (the *st* case described in Section 7.2 and the *test* case presented in Section 8.1). In the first column we report the element labels, while in the others columns we tabulate the pulse by pulse  $[X_i/Fe]$  (the first row identify the number of TP followed by TDU).

### B.1 Solar metallicity case ( $Z=1.5 \times 10^{-2}$ )

El.	1	2	3	4	5	6	7	8	9	10	11
C	-1.9E-01	-1.5E-01	-5.2E-02	6.7E-02	1.8E-01	2.8E-01	3.7E-01	4.4E-01	5.1E-01	5.6E-01	5.6E-01
N	3.1E-01	3.1E-01	3.1E-01	3.1E-01	3.1E-01	3.1E-01	3.1E-01	3.1E-01	3.0E-01	3.0E-01	3.0E-01
O	-5.9E-04	-5.6E-04	-1.0E-05	9.3E-04	1.9E-03	2.7E-03	3.1E-03	3.2E-03	2.8E-03	2.1E-03	2.1E-03
F	-8.2E-03	-2.0E-03	2.5E-02	7.3E-02	1.4E-01	2.1E-01	2.8E-01	3.5E-01	4.3E-01	4.9E-01	4.9E-01
Ne	-2.3E-03	1.4E-03	1.4E-02	3.4E-02	6.0E-02	8.9E-02	1.2E-01	1.6E-01	1.9E-01	2.2E-01	2.2E-01
Na	7.5E-02	7.7E-02	8.2E-02	9.0E-02	1.0E-01	1.1E-01	1.3E-01	1.4E-01	1.6E-01	1.7E-01	1.7E-01
Mg	0.0E+00	3.8E-05	2.4E-04	6.3E-04	1.3E-03	2.2E-03	3.4E-03	5.0E-03	7.0E-03	9.0E-03	9.1E-03
Al	2.3E-04	5.2E-04	9.7E-04	1.8E-03	2.9E-03	4.3E-03	5.7E-03	7.3E-03	9.0E-03	1.0E-02	1.0E-02
Si	0.0E+00	2.9E-05	1.4E-04	2.9E-04	4.6E-04	6.2E-04	7.8E-04	9.4E-04	1.1E-03	1.2E-03	1.2E-03
P	0.0E+00	3.6E-04	1.9E-03	4.3E-03	7.2E-03	1.0E-02	1.3E-02	1.6E-02	1.8E-02	2.0E-02	2.0E-02
S	0.0E+00	-3.2E-06	1.3E-05	5.1E-05	1.1E-04	1.7E-04	2.4E-04	3.1E-04	3.6E-04	4.1E-04	4.1E-04

<sup>1</sup> $[El/Fe]=\log(N(El)/N(Fe))-\log(N(El)/N(Fe))_{\odot}$ ; the label El stands for the generic element.

El.	1	2	3	4	5	6	7	8	9	10	11
Cl	5.4E-06	1.0E-04	5.2E-04	1.2E-03	2.0E-03	2.9E-03	3.8E-03	4.8E-03	5.8E-03	6.6E-03	6.6E-03
Ar	0.0E+00	1.3E-05	6.4E-05	1.3E-04	2.0E-04	2.5E-04	3.1E-04	3.5E-04	3.8E-04	4.1E-04	4.2E-04
K	-2.6E-04	-1.2E-04	4.1E-04	1.2E-03	2.0E-03	3.0E-03	4.1E-03	5.0E-03	6.0E-03	7.0E-03	7.4E-03
Ca	1.4E-05	-3.7E-05	-1.5E-04	-2.7E-04	-3.5E-04	-4.3E-04	-5.0E-04	-5.5E-04	-6.3E-04	-7.0E-04	-7.3E-04
Sc	8.2E-06	2.1E-03	6.4E-03	1.1E-02	1.7E-02	2.2E-02	2.7E-02	3.2E-02	3.8E-02	4.2E-02	4.2E-02
Ti	6.0E-07	6.0E-05	4.6E-04	1.2E-03	2.2E-03	3.3E-03	4.4E-03	5.5E-03	6.5E-03	7.2E-03	7.2E-03
V	2.5E-06	-1.3E-04	-3.4E-04	-4.6E-04	-3.9E-04	-1.2E-04	3.2E-04	8.8E-04	1.5E-03	2.1E-03	2.1E-03
Cr	0.0E+00	-3.7E-06	7.8E-07	1.8E-05	4.7E-05	7.6E-05	1.1E-04	1.4E-04	1.6E-04	1.8E-04	1.9E-04
Mn	4.6E-06	-1.0E-04	-2.3E-04	-2.1E-04	6.1E-05	6.2E-04	1.5E-03	2.6E-03	4.0E-03	5.1E-03	5.2E-03
Fe	0.0E+00										
Co	1.6E-05	3.5E-03	1.2E-02	2.1E-02	2.9E-02	3.6E-02	4.3E-02	4.7E-02	5.3E-02	5.9E-02	6.2E-02
Ni	-2.9E-06	8.3E-05	5.6E-04	1.2E-03	1.7E-03	2.2E-03	2.6E-03	2.9E-03	3.1E-03	3.2E-03	3.1E-03
Cu	2.7E-06	4.5E-03	1.6E-02	3.0E-02	4.2E-02	5.3E-02	6.3E-02	7.1E-02	7.9E-02	8.5E-02	8.5E-02
Zn	-1.1E-06	5.8E-04	4.1E-03	9.9E-03	1.7E-02	2.4E-02	3.2E-02	3.8E-02	4.5E-02	5.0E-02	5.0E-02
Ga	3.8E-06	3.9E-03	2.0E-02	4.8E-02	8.1E-02	1.2E-01	1.5E-01	1.8E-01	2.1E-01	2.3E-01	2.3E-01
Ge	1.2E-06	4.1E-03	2.1E-02	4.9E-02	8.4E-02	1.2E-01	1.6E-01	1.9E-01	2.2E-01	2.4E-01	2.4E-01
As	-6.6E-06	2.4E-03	1.3E-02	3.0E-02	5.3E-02	7.7E-02	1.0E-01	1.2E-01	1.4E-01	1.6E-01	1.6E-01
Se	0.0E+00	5.7E-03	3.0E-02	6.7E-02	1.1E-01	1.5E-01	2.0E-01	2.3E-01	2.7E-01	2.9E-01	2.9E-01
Br	-6.9E-03	-4.4E-03	7.8E-03	3.1E-02	6.4E-02	9.9E-02	1.4E-01	1.7E-01	2.0E-01	2.2E-01	2.3E-01
Kr	1.5E-03	1.0E-02	4.5E-02	1.0E-01	1.6E-01	2.2E-01	2.8E-01	3.2E-01	3.7E-01	4.0E-01	4.0E-01
Rb	-2.0E-06	2.2E-02	8.3E-02	1.4E-01	2.0E-01	2.5E-01	2.9E-01	3.3E-01	3.6E-01	3.8E-01	3.9E-01
Sr	2.5E-06	2.2E-02	2.1E-01	4.6E-01	6.8E-01	8.4E-01	9.6E-01	1.1E+00	1.1E+00	1.2E+00	1.2E+00
Y	-3.1E-06	2.3E-02	2.0E-01	4.3E-01	6.3E-01	7.9E-01	9.0E-01	9.9E-01	1.1E+00	1.1E+00	1.1E+00
Zr	0.0E+00	1.7E-02	1.9E-01	4.3E-01	6.4E-01	7.9E-01	9.1E-01	9.9E-01	1.1E+00	1.1E+00	1.1E+00
Nb	-8.3E-06	-2.0E-04	8.1E-04	2.6E-02	8.8E-02	1.8E-01	3.0E-01	3.5E-01	4.3E-01	5.0E-01	5.7E-01
Mo	1.1E-06	5.2E-03	1.1E-01	3.0E-01	4.8E-01	6.2E-01	7.3E-01	8.2E-01	8.8E-01	9.2E-01	9.2E-01
Ru	-3.1E-06	1.5E-03	6.8E-02	2.1E-01	3.6E-01	4.9E-01	5.9E-01	6.7E-01	7.3E-01	7.7E-01	7.7E-01
Rh	-8.2E-06	6.0E-04	3.6E-02	1.2E-01	2.2E-01	3.1E-01	3.8E-01	4.4E-01	4.9E-01	5.2E-01	5.2E-01
Pd	4.2E-06	2.2E-03	1.1E-01	3.1E-01	5.0E-01	6.4E-01	7.5E-01	8.3E-01	9.0E-01	9.4E-01	9.4E-01

El.	1	2	3	4	5	6	7	8	9	10	11
Ag	-1.2E-05	3.7E-04	3.0E-02	1.0E-01	1.9E-01	2.7E-01	3.4E-01	4.0E-01	4.4E-01	4.7E-01	4.8E-01
Cd	3.6E-06	2.8E-03	1.2E-01	3.4E-01	5.4E-01	6.9E-01	8.0E-01	8.9E-01	9.5E-01	9.9E-01	9.9E-01
In	-7.1E-06	1.6E-03	8.1E-02	2.4E-01	4.0E-01	5.4E-01	6.4E-01	7.1E-01	7.7E-01	8.1E-01	8.1E-01
Sn	0.0E+00	2.8E-03	1.2E-01	3.4E-01	5.4E-01	7.0E-01	8.1E-01	8.9E-01	9.5E-01	9.9E-01	9.9E-01
Sb	-6.8E-06	1.3E-03	6.1E-02	1.8E-01	3.0E-01	4.1E-01	5.0E-01	5.6E-01	6.2E-01	6.5E-01	6.5E-01
Te	0.0E+00	4.6E-04	3.8E-02	1.3E-01	2.5E-01	3.5E-01	4.2E-01	4.8E-01	5.3E-01	5.6E-01	5.6E-01
I	-1.3E-05	-6.0E-05	1.2E-02	4.5E-02	9.1E-02	1.4E-01	1.8E-01	2.1E-01	2.4E-01	2.5E-01	2.6E-01
Xe	3.5E-06	4.4E-04	4.8E-02	1.7E-01	3.0E-01	4.1E-01	4.9E-01	5.6E-01	6.1E-01	6.4E-01	6.4E-01
Cs	-7.7E-06	8.0E-04	7.9E-02	1.8E-01	2.8E-01	3.7E-01	4.4E-01	5.0E-01	5.5E-01	5.8E-01	5.8E-01
Ba	0.0E+00	7.2E-04	1.1E-01	3.6E-01	5.9E-01	7.5E-01	8.7E-01	9.5E-01	1.0E+00	1.0E+00	1.0E+00
La	0.0E+00	2.7E-04	8.3E-02	3.0E-01	5.1E-01	6.7E-01	7.8E-01	8.6E-01	9.2E-01	9.5E-01	9.5E-01
Ce	0.0E+00	1.7E-04	6.3E-02	2.6E-01	4.6E-01	6.2E-01	7.3E-01	8.1E-01	8.7E-01	9.0E-01	9.1E-01
Pr	-2.5E-06	4.5E-05	3.9E-02	1.5E-01	2.9E-01	4.1E-01	5.1E-01	5.8E-01	6.4E-01	6.7E-01	6.7E-01
Nd	0.0E+00	3.7E-05	3.4E-02	1.6E-01	3.2E-01	4.5E-01	5.6E-01	6.3E-01	6.9E-01	7.2E-01	7.2E-01
Sm	-3.3E-06	-4.6E-05	1.5E-02	8.2E-02	1.8E-01	2.7E-01	3.5E-01	4.2E-01	4.6E-01	4.9E-01	4.9E-01
Eu	-1.6E-05	-2.1E-04	1.9E-03	1.3E-02	3.3E-02	5.6E-02	7.9E-02	1.0E-01	1.2E-01	1.3E-01	1.3E-01
Gd	4.2E-06	-7.6E-05	7.2E-03	4.2E-02	9.8E-02	1.6E-01	2.1E-01	2.5E-01	2.8E-01	3.0E-01	3.0E-01
Tb	-1.6E-03	-1.8E-03	1.5E-03	2.1E-02	5.4E-02	9.2E-02	1.3E-01	1.6E-01	1.8E-01	1.9E-01	1.9E-01
Dy	2.5E-04	1.3E-04	6.3E-03	4.1E-02	9.7E-02	1.6E-01	2.2E-01	2.6E-01	2.9E-01	3.1E-01	3.1E-01
Ho	-9.6E-06	-3.6E-05	4.4E-03	2.5E-02	6.3E-02	9.4E-02	1.1E-01	1.4E-01	1.7E-01	1.7E-01	1.7E-01
Er	5.0E-06	-6.3E-05	7.1E-03	4.4E-02	1.1E-01	1.7E-01	2.3E-01	2.8E-01	3.2E-01	3.4E-01	3.4E-01
Tm	-3.6E-03	-3.8E-03	1.1E-03	3.0E-02	8.1E-02	1.4E-01	1.9E-01	2.4E-01	2.8E-01	3.0E-01	3.0E-01
Yb	5.7E-04	6.4E-04	1.8E-02	9.3E-02	2.0E-01	3.1E-01	4.0E-01	4.7E-01	5.2E-01	5.5E-01	5.6E-01
Lu	-1.2E-03	-1.3E-03	6.5E-03	4.7E-02	1.1E-01	1.9E-01	2.5E-01	3.1E-01	3.5E-01	3.7E-01	3.7E-01
Hf	2.9E-04	6.5E-04	2.5E-02	1.3E-01	2.7E-01	4.0E-01	5.1E-01	5.8E-01	6.4E-01	6.8E-01	6.8E-01
Ta	-4.9E-06	1.5E-04	1.6E-02	9.1E-02	2.1E-01	3.2E-01	4.2E-01	4.9E-01	5.5E-01	5.8E-01	5.8E-01
W	-1.1E-06	4.3E-04	2.1E-02	1.1E-01	2.5E-01	3.7E-01	4.8E-01	5.5E-01	6.1E-01	6.5E-01	6.5E-01
Re	-6.8E-02	-6.8E-02	-6.1E-02	-3.5E-02	1.5E-02	7.4E-02	1.3E-01	1.8E-01	2.2E-01	2.4E-01	2.4E-01
Os	4.9E-03	4.8E-03	7.3E-03	2.4E-02	5.4E-02	9.0E-02	1.3E-01	1.5E-01	1.8E-01	1.9E-01	1.9E-01

El.	1	2	3	4	5	6	7	8	9	10	11
Ir	-1.3E-05	-2.0E-04	-3.0E-04	1.7E-03	6.1E-03	1.2E-02	1.8E-02	2.3E-02	2.7E-02	2.9E-02	2.9E-02
Pt	7.4E-06	-8.1E-05	1.5E-03	1.3E-02	3.5E-02	6.2E-02	8.8E-02	1.1E-01	1.3E-01	1.4E-01	1.4E-01
Au	-5.9E-06	-1.5E-04	9.8E-04	9.4E-03	2.6E-02	4.9E-02	7.2E-02	9.3E-02	1.1E-01	1.2E-01	1.2E-01
Hg	1.2E-05	4.1E-04	1.6E-02	9.6E-02	2.2E-01	3.5E-01	4.5E-01	5.3E-01	5.9E-01	6.3E-01	6.3E-01
Tl	-7.7E-07	9.2E-04	1.7E-02	1.1E-01	2.7E-01	4.2E-01	5.4E-01	6.2E-01	6.9E-01	7.2E-01	7.2E-01
Pb	9.0E-07	1.7E-04	4.8E-03	5.1E-02	1.5E-01	2.6E-01	3.6E-01	4.4E-01	4.9E-01	5.3E-01	5.3E-01
Bi	-1.0E-06	-4.8E-06	8.5E-05	1.7E-03	6.5E-03	1.4E-02	2.4E-02	3.3E-02	4.2E-02	4.7E-02	4.7E-02

## B.2 Intermediate metallicity case ( $Z=1\times 10^{-3}$ )

El.	1	2	3	4	5	6	7	8	9	10
C	-1.3E-01	5.0E-01	8.9E-01	1.1E+00	1.3E+00	1.4E+00	1.5E+00	1.6E+00	1.7E+00	1.7E+00
N	4.0E-01	4.1E-01								
O	-9.9E-03	1.4E-03	2.6E-02	5.6E-02	8.6E-02	1.1E-01	1.3E-01	1.5E-01	1.7E-01	1.8E-01
F	-4.1E-02	1.8E-01	4.7E-01	7.1E-01	8.8E-01	1.0E+00	1.1E+00	1.2E+00	1.3E+00	1.4E+00
Ne	-4.9E-03	4.1E-02	1.4E-01	2.6E-01	3.8E-01	4.9E-01	5.9E-01	6.8E-01	7.7E-01	8.0E-01
Na	1.5E-01	1.6E-01	1.7E-01	2.0E-01	2.4E-01	2.8E-01	3.3E-01	3.7E-01	4.2E-01	4.4E-01
Mg	7.4E-05	5.8E-04	2.9E-03	8.3E-03	1.7E-02	2.9E-02	4.5E-02	6.4E-02	8.7E-02	9.8E-02
Al	3.0E-03	1.1E-02	2.3E-02	3.7E-02	4.8E-02	5.7E-02	6.4E-02	7.1E-02	7.6E-02	7.9E-02
Si	6.3E-06	1.5E-04	4.2E-04	7.8E-04	1.2E-03	1.6E-03	2.1E-03	2.6E-03	3.1E-03	3.3E-03
P	2.0E-06	2.0E-03	7.6E-03	1.6E-02	2.4E-02	3.3E-02	4.0E-02	4.7E-02	5.3E-02	5.5E-02
S	4.8E-07	8.8E-06	6.9E-05	1.7E-04	2.6E-04	3.3E-04	3.6E-04	3.6E-04	3.4E-04	3.3E-04
Cl	1.2E-05	3.2E-04	8.6E-04	1.5E-03	2.2E-03	2.9E-03	3.6E-03	4.3E-03	5.0E-03	5.2E-03
Ar	0.0E+00	2.1E-05	5.9E-05	1.1E-04	1.5E-04	2.1E-04	2.8E-04	3.6E-04	4.7E-04	5.3E-04
K	-1.9E-04	1.9E-04	8.4E-04	1.7E-03	2.8E-03	3.9E-03	5.2E-03	6.6E-03	8.2E-03	9.1E-03
Ca	1.0E-05	-1.1E-04	-2.7E-04	-4.4E-04	-6.4E-04	-9.1E-04	-1.2E-03	-1.6E-03	-2.0E-03	-2.2E-03
Sc	3.9E-05	3.7E-03	8.8E-03	1.5E-02	2.4E-02	3.4E-02	4.5E-02	5.7E-02	7.1E-02	7.7E-02

El.	1	2	3	4	5	6	7	8	9	10
Ti	8.7E-07	3.4E-04	1.2E-03	2.4E-03	3.8E-03	5.1E-03	6.4E-03	7.6E-03	8.8E-03	9.3E-03
V	1.1E-05	-2.1E-04	-2.3E-04	6.0E-05	4.8E-04	7.9E-04	9.1E-04	7.9E-04	5.3E-04	3.8E-04
Cr	0.0E+00	7.9E-06	4.8E-05	1.1E-04	1.9E-04	2.7E-04	3.5E-04	4.4E-04	5.3E-04	5.7E-04
Mn	2.5E-05	-6.2E-05	1.6E-04	9.1E-04	2.0E-03	3.2E-03	4.2E-03	5.1E-03	5.7E-03	5.9E-03
Fe	0.0E+00	0.0E+00	0.0E+00	0.0E+00	0.0E+00	4.8E-17	0.0E+00	0.0E+00	4.8E-17	4.8E-17
Co	2.6E-05	6.6E-03	1.6E-02	2.5E-02	3.7E-02	5.1E-02	6.9E-02	9.1E-02	1.2E-01	1.3E-01
Ni	-4.3E-06	1.4E-04	3.9E-04	6.4E-04	8.0E-04	9.4E-04	1.1E-03	1.4E-03	1.8E-03	2.0E-03
Cu	1.6E-05	8.0E-03	1.8E-02	2.9E-02	4.0E-02	5.2E-02	6.8E-02	8.6E-02	1.1E-01	1.2E-01
Zn	-1.6E-06	6.2E-04	3.1E-03	6.4E-03	1.0E-02	1.4E-02	1.7E-02	2.1E-02	2.5E-02	2.7E-02
Ga	1.6E-05	4.7E-03	1.5E-02	2.8E-02	4.1E-02	5.3E-02	6.6E-02	7.9E-02	9.2E-02	9.8E-02
Ge	1.8E-06	4.5E-03	1.5E-02	2.8E-02	4.2E-02	5.5E-02	6.8E-02	8.1E-02	9.3E-02	9.8E-02
As	-2.6E-05	2.3E-03	7.9E-03	1.5E-02	2.4E-02	3.2E-02	3.9E-02	4.6E-02	5.4E-02	5.6E-02
Se	0.0E+00	5.5E-03	1.7E-02	3.3E-02	4.9E-02	6.5E-02	8.0E-02	9.4E-02	1.1E-01	1.1E-01
Br	-6.9E-03	-4.0E-03	3.5E-03	1.5E-02	3.0E-02	4.4E-02	5.9E-02	7.3E-02	8.5E-02	9.4E-02
Kr	1.5E-03	9.7E-03	3.0E-02	5.7E-02	8.5E-02	1.1E-01	1.4E-01	1.6E-01	1.8E-01	1.9E-01
Rb	-3.0E-06	1.5E-02	3.8E-02	7.0E-02	1.1E-01	1.5E-01	2.0E-01	2.4E-01	2.8E-01	3.0E-01
Sr	1.1E-05	6.6E-02	2.1E-01	3.6E-01	4.7E-01	5.6E-01	6.2E-01	6.7E-01	7.1E-01	7.3E-01
Y	0.0E+00	7.4E-02	2.2E-01	3.7E-01	4.8E-01	5.8E-01	6.5E-01	7.1E-01	7.5E-01	7.7E-01
Zr	0.0E+00	8.2E-02	2.4E-01	4.0E-01	5.2E-01	6.1E-01	6.9E-01	7.4E-01	7.9E-01	8.1E-01
Nb	-3.6E-05	6.2E-04	7.3E-03	2.5E-02	5.8E-02	9.2E-02	1.3E-01	1.8E-01	2.2E-01	2.6E-01
Mo	6.5E-06	4.8E-02	1.7E-01	3.0E-01	4.1E-01	4.8E-01	5.5E-01	5.9E-01	6.3E-01	6.5E-01
Ru	-1.2E-05	2.8E-02	1.1E-01	2.1E-01	3.0E-01	3.7E-01	4.3E-01	4.7E-01	5.0E-01	5.2E-01
Rh	-3.9E-05	1.4E-02	6.0E-02	1.2E-01	1.8E-01	2.2E-01	2.6E-01	2.9E-01	3.1E-01	3.2E-01
Pd	2.1E-05	5.2E-02	1.8E-01	3.2E-01	4.3E-01	5.2E-01	5.8E-01	6.3E-01	6.7E-01	6.9E-01
Ag	-4.5E-05	1.4E-02	5.4E-02	1.1E-01	1.6E-01	2.0E-01	2.3E-01	2.6E-01	2.9E-01	2.9E-01
Cd	1.6E-05	7.1E-02	2.3E-01	3.8E-01	5.1E-01	6.0E-01	6.8E-01	7.3E-01	7.8E-01	7.9E-01
In	-2.5E-05	4.6E-02	1.6E-01	2.8E-01	3.8E-01	4.7E-01	5.3E-01	5.8E-01	6.2E-01	6.3E-01
Sn	1.7E-06	8.7E-02	2.6E-01	4.3E-01	5.6E-01	6.6E-01	7.4E-01	8.0E-01	8.5E-01	8.7E-01
Sb	-2.9E-05	4.5E-02	1.4E-01	2.5E-01	3.6E-01	4.4E-01	5.2E-01	5.7E-01	6.2E-01	6.4E-01

El.	1	2	3	4	5	6	7	8	9	10
Te	-2.6E-06	2.9E-02	1.0E-01	1.9E-01	2.7E-01	3.3E-01	3.8E-01	4.2E-01	4.6E-01	4.7E-01
I	-5.2E-05	8.5E-03	3.5E-02	7.1E-02	1.1E-01	1.4E-01	1.7E-01	1.9E-01	2.1E-01	2.1E-01
Xe	1.3E-05	4.2E-02	1.5E-01	2.6E-01	3.6E-01	4.4E-01	5.1E-01	5.6E-01	6.0E-01	6.1E-01
Cs	-2.6E-05	6.7E-02	1.7E-01	3.0E-01	4.3E-01	5.3E-01	6.1E-01	6.8E-01	7.3E-01	7.5E-01
Ba	6.0E-06	2.3E-01	5.7E-01	8.3E-01	1.0E+00	1.1E+00	1.2E+00	1.3E+00	1.3E+00	1.4E+00
La	0.0E+00	2.4E-01	6.0E-01	8.6E-01	1.0E+00	1.2E+00	1.3E+00	1.3E+00	1.4E+00	1.4E+00
Ce	0.0E+00	3.1E-01	7.1E-01	9.8E-01	1.2E+00	1.3E+00	1.4E+00	1.5E+00	1.5E+00	1.5E+00
Pr	-1.2E-05	2.2E-01	5.4E-01	8.0E-01	9.8E-01	1.1E+00	1.2E+00	1.3E+00	1.4E+00	1.4E+00
Nd	-2.5E-06	2.5E-01	6.2E-01	8.8E-01	1.1E+00	1.2E+00	1.3E+00	1.3E+00	1.4E+00	1.4E+00
Sm	-1.4E-05	1.7E-01	4.6E-01	6.9E-01	8.5E-01	9.7E-01	1.1E+00	1.1E+00	1.2E+00	1.2E+00
Eu	-6.4E-05	3.7E-02	1.3E-01	2.3E-01	3.3E-01	4.1E-01	4.7E-01	5.2E-01	5.7E-01	5.8E-01
Gd	1.3E-05	1.0E-01	2.9E-01	4.7E-01	6.1E-01	7.3E-01	8.1E-01	8.8E-01	9.4E-01	9.6E-01
Tb	-1.6E-03	5.5E-02	1.8E-01	3.1E-01	4.2E-01	5.1E-01	5.8E-01	6.4E-01	6.9E-01	7.1E-01
Dy	2.4E-04	9.4E-02	2.9E-01	4.6E-01	6.0E-01	6.9E-01	7.7E-01	8.3E-01	8.9E-01	9.1E-01
Ho	-3.5E-05	5.1E-02	1.8E-01	3.1E-01	4.1E-01	5.0E-01	5.7E-01	6.1E-01	6.6E-01	6.7E-01
Er	2.4E-05	1.1E-01	3.3E-01	5.3E-01	6.8E-01	7.9E-01	8.7E-01	9.3E-01	9.8E-01	1.0E+00
Tm	-3.6E-03	7.1E-02	2.8E-01	4.6E-01	5.9E-01	6.8E-01	7.5E-01	8.1E-01	8.6E-01	8.7E-01
Yb	5.9E-04	2.1E-01	5.5E-01	8.1E-01	9.8E-01	1.1E+00	1.2E+00	1.3E+00	1.3E+00	1.3E+00
Lu	-9.1E-04	1.1E-01	3.6E-01	5.8E-01	7.4E-01	8.5E-01	9.3E-01	9.9E-01	1.0E+00	1.1E+00
Hf	2.3E-04	3.2E-01	7.0E-01	9.8E-01	1.2E+00	1.3E+00	1.4E+00	1.5E+00	1.5E+00	1.5E+00
Ta	-2.3E-05	2.4E-01	6.1E-01	8.7E-01	1.1E+00	1.2E+00	1.3E+00	1.3E+00	1.4E+00	1.4E+00
W	-1.6E-06	3.0E-01	7.0E-01	9.7E-01	1.2E+00	1.3E+00	1.4E+00	1.4E+00	1.5E+00	1.5E+00
Re	-6.4E-02	6.8E-02	3.1E-01	5.4E-01	7.2E-01	8.4E-01	9.3E-01	9.9E-01	1.0E+00	1.1E+00
Os	4.6E-03	7.2E-02	2.2E-01	3.8E-01	5.0E-01	6.0E-01	6.8E-01	7.4E-01	7.9E-01	8.0E-01
Ir	-5.5E-05	1.2E-02	4.6E-02	9.1E-02	1.4E-01	1.8E-01	2.2E-01	2.5E-01	2.8E-01	2.9E-01
Pt	2.8E-05	4.8E-02	1.7E-01	3.0E-01	4.0E-01	4.9E-01	5.6E-01	6.1E-01	6.6E-01	6.8E-01
Au	-1.4E-05	3.9E-02	1.5E-01	2.7E-01	3.8E-01	4.6E-01	5.2E-01	5.7E-01	6.1E-01	6.3E-01
Hg	5.7E-05	3.1E-01	7.2E-01	1.0E+00	1.2E+00	1.3E+00	1.4E+00	1.5E+00	1.5E+00	1.6E+00
Tl	-2.3E-06	3.9E-01	8.6E-01	1.2E+00	1.3E+00	1.5E+00	1.6E+00	1.6E+00	1.7E+00	1.7E+00

El.	1	2	3	4	5	6	7	8	9	10
Pb	6.6E-07	1.1E+00	1.7E+00	2.0E+00	2.2E+00	2.3E+00	2.4E+00	2.5E+00	2.5E+00	2.6E+00
Bi	-1.5E-06	6.7E-01	1.2E+00	1.5E+00	1.7E+00	1.8E+00	1.9E+00	2.0E+00	2.1E+00	2.1E+00

## B.3 Low metallicity cases

### B.3.1 $Z=1 \times 10^{-4}$ (*st case*)

El.	1	2	3	4	5	6	7	8	9
C	1.4E+00	1.8E+00	2.1E+00	2.2E+00	2.4E+00	2.5E+00	2.6E+00	2.6E+00	2.6E+00
N	4.9E-01	4.9E-01	5.0E-01	5.1E-01	5.2E-01	5.4E-01	5.6E-01	5.9E-01	6.4E-01
O	4.5E-02	2.0E-01	3.5E-01	4.7E-01	5.6E-01	6.4E-01	7.0E-01	7.4E-01	7.5E-01
F	3.3E-01	1.3E+00	1.7E+00	1.9E+00	2.1E+00	2.2E+00	2.3E+00	2.4E+00	2.4E+00
Ne	1.1E-02	4.2E-01	7.5E-01	9.9E-01	1.2E+00	1.3E+00	1.4E+00	1.5E+00	1.6E+00
Na	2.2E-01	2.4E-01	3.5E-01	5.1E-01	6.6E-01	8.0E-01	9.1E-01	1.0E+00	1.0E+00
Mg	1.1E-04	3.6E-03	3.1E-02	8.6E-02	1.6E-01	2.5E-01	3.5E-01	4.3E-01	4.5E-01
Al	6.4E-03	2.2E-02	5.6E-02	1.0E-01	1.5E-01	1.9E-01	2.3E-01	2.6E-01	2.8E-01
Si	2.0E-03	4.2E-03	6.5E-03	9.0E-03	1.2E-02	1.5E-02	1.8E-02	2.0E-02	2.1E-02
P	6.9E-03	2.1E-02	4.4E-02	7.3E-02	1.0E-01	1.3E-01	1.6E-01	1.8E-01	1.8E-01
S	9.8E-05	3.2E-04	6.5E-04	1.0E-03	1.4E-03	1.8E-03	2.2E-03	2.4E-03	2.5E-03
Cl	2.9E-04	8.7E-04	1.6E-03	2.3E-03	3.1E-03	3.9E-03	4.6E-03	5.4E-03	5.5E-03
Ar	2.3E-04	4.9E-04	7.1E-04	8.9E-04	1.1E-03	1.3E-03	1.5E-03	1.7E-03	1.8E-03
K	9.9E-04	2.5E-03	3.9E-03	5.3E-03	6.7E-03	8.3E-03	1.0E-02	1.2E-02	1.3E-02
Ca	-1.7E-04	-3.6E-04	-5.7E-04	-8.4E-04	-1.2E-03	-1.5E-03	-2.0E-03	-2.4E-03	-2.5E-03
Sc	1.0E-02	2.1E-02	3.3E-02	4.4E-02	5.7E-02	7.3E-02	8.9E-02	1.1E-01	1.1E-01
Ti	8.1E-04	2.1E-03	3.5E-03	4.8E-03	6.0E-03	7.4E-03	8.7E-03	9.7E-03	9.9E-03
V	-1.5E-04	-1.3E-04	-8.0E-05	-1.8E-04	-4.6E-04	-8.1E-04	-1.3E-03	-2.0E-03	-2.1E-03
Cr	1.9E-05	7.7E-05	1.5E-04	2.4E-04	3.4E-04	4.6E-04	5.7E-04	6.8E-04	7.1E-04
Mn	-2.3E-04	-1.8E-04	1.4E-04	4.7E-04	6.2E-04	5.6E-04	2.8E-04	-9.4E-05	-1.5E-04

El.	1	2	3	4	5	6	7	8	9
Fe	0.0E+00	0.0E+00	0.0E+00	0.0E+00	0.0E+00	0.0E+00	0.0E+00	0.0E+00	0.00E+00
Co	1.7E-02	3.5E-02	5.2E-02	7.1E-02	9.5E-02	1.2E-01	1.6E-01	1.9E-01	2.0E-01
Ni	2.3E-03	4.9E-03	6.9E-03	8.3E-03	9.4E-03	1.1E-02	1.2E-02	1.4E-02	1.5E-02
Cu	6.6E-02	1.2E-01	1.6E-01	1.9E-01	2.2E-01	2.5E-01	2.8E-01	3.1E-01	3.2E-01
Zn	1.2E-02	3.4E-02	5.6E-02	7.2E-02	8.2E-02	9.1E-02	9.8E-02	1.1E-01	1.1E-01
Ga	3.9E-02	8.9E-02	1.4E-01	1.8E-01	2.1E-01	2.3E-01	2.5E-01	2.7E-01	2.7E-01
Ge	3.1E-02	7.4E-02	1.1E-01	1.5E-01	1.8E-01	2.0E-01	2.2E-01	2.4E-01	2.4E-01
As	1.5E-02	3.8E-02	6.1E-02	8.1E-02	9.8E-02	1.1E-01	1.3E-01	1.4E-01	1.4E-01
Se	2.3E-02	5.8E-02	9.2E-02	1.2E-01	1.4E-01	1.7E-01	1.9E-01	2.0E-01	2.1E-01
Br	3.3E-03	2.5E-02	5.4E-02	8.3E-02	1.1E-01	1.3E-01	1.5E-01	1.7E-01	1.8E-01
Kr	2.1E-02	6.0E-02	1.0E-01	1.3E-01	1.6E-01	2.0E-01	2.3E-01	2.5E-01	2.5E-01
Rb	3.3E-02	9.0E-02	1.6E-01	2.2E-01	2.8E-01	3.4E-01	4.0E-01	4.4E-01	4.5E-01
Sr	1.4E-02	1.3E-01	2.4E-01	3.3E-01	4.0E-01	4.9E-01	5.5E-01	5.9E-01	6.0E-01
Y	8.7E-03	1.1E-01	2.3E-01	3.3E-01	4.2E-01	5.3E-01	6.0E-01	6.5E-01	6.6E-01
Zr	6.7E-03	1.0E-01	2.2E-01	3.3E-01	4.1E-01	5.4E-01	6.2E-01	6.7E-01	6.8E-01
Nb	-5.1E-04	-5.7E-04	3.5E-03	1.5E-02	3.0E-02	5.0E-02	8.6E-02	1.2E-01	1.5E-01
Mo	3.8E-03	6.4E-02	1.4E-01	2.1E-01	2.8E-01	3.8E-01	4.4E-01	4.9E-01	5.0E-01
Ru	2.3E-03	4.2E-02	9.6E-02	1.5E-01	1.9E-01	2.5E-01	3.0E-01	3.4E-01	3.4E-01
Rh	8.9E-04	2.2E-02	5.1E-02	7.9E-02	1.0E-01	1.4E-01	1.7E-01	1.9E-01	2.0E-01
Pd	4.0E-03	7.3E-02	1.6E-01	2.3E-01	2.9E-01	3.9E-01	4.4E-01	4.9E-01	5.0E-01
Ag	5.3E-04	1.9E-02	4.4E-02	6.9E-02	9.2E-02	1.3E-01	1.6E-01	1.8E-01	1.8E-01
Cd	4.4E-03	9.1E-02	2.0E-01	2.9E-01	3.7E-01	4.8E-01	5.4E-01	5.9E-01	6.0E-01
In	2.3E-03	5.9E-02	1.4E-01	2.0E-01	2.6E-01	3.5E-01	4.0E-01	4.4E-01	4.5E-01
Sn	4.6E-03	1.0E-01	2.2E-01	3.3E-01	4.2E-01	5.5E-01	6.2E-01	6.7E-01	6.8E-01
Sb	2.0E-03	5.1E-02	1.2E-01	2.0E-01	2.7E-01	3.8E-01	4.5E-01	5.0E-01	5.1E-01
Te	1.1E-03	3.3E-02	7.9E-02	1.2E-01	1.7E-01	2.4E-01	2.9E-01	3.2E-01	3.3E-01
I	-2.7E-05	1.0E-02	2.6E-02	4.2E-02	5.9E-02	8.8E-02	1.1E-01	1.2E-01	1.3E-01
Xe	2.6E-03	5.1E-02	1.2E-01	1.8E-01	2.4E-01	3.4E-01	3.9E-01	4.4E-01	4.4E-01
Cs	3.6E-03	6.9E-02	1.6E-01	2.5E-01	3.3E-01	4.6E-01	5.2E-01	5.7E-01	5.8E-01

El.	1	2	3	4	5	6	7	8	9
Ba	1.9E-02	2.5E-01	4.8E-01	6.4E-01	7.7E-01	9.5E-01	1.0E+00	1.1E+00	1.1E+00
La	1.8E-02	2.6E-01	4.9E-01	6.5E-01	7.9E-01	9.8E-01	1.1E+00	1.1E+00	1.1E+00
Ce	2.5E-02	3.1E-01	5.8E-01	7.5E-01	9.0E-01	1.1E+00	1.2E+00	1.2E+00	1.2E+00
Pr	1.5E-02	2.3E-01	4.6E-01	6.2E-01	7.7E-01	9.6E-01	1.0E+00	1.1E+00	1.1E+00
Nd	2.2E-02	2.6E-01	5.0E-01	6.6E-01	8.0E-01	9.8E-01	1.1E+00	1.1E+00	1.1E+00
Sm	1.7E-02	1.7E-01	3.5E-01	4.9E-01	6.3E-01	8.0E-01	8.9E-01	9.4E-01	9.5E-01
Eu	2.6E-03	3.4E-02	8.6E-02	1.4E-01	2.0E-01	3.0E-01	3.6E-01	3.9E-01	4.0E-01
Gd	9.7E-03	9.8E-02	2.3E-01	3.4E-01	4.6E-01	6.2E-01	7.0E-01	7.5E-01	7.6E-01
Tb	3.4E-03	5.1E-02	1.3E-01	2.0E-01	2.8E-01	4.1E-01	4.8E-01	5.2E-01	5.3E-01
Dy	9.6E-03	8.6E-02	2.0E-01	3.0E-01	4.0E-01	5.5E-01	6.4E-01	6.9E-01	6.9E-01
Ho	4.7E-03	5.0E-02	1.2E-01	1.8E-01	2.6E-01	3.9E-01	4.4E-01	4.8E-01	4.8E-01
Er	1.2E-02	1.1E-01	2.4E-01	3.5E-01	4.6E-01	6.2E-01	7.1E-01	7.6E-01	7.6E-01
Tm	4.9E-03	7.8E-02	1.8E-01	2.7E-01	3.6E-01	5.0E-01	5.8E-01	6.3E-01	6.4E-01
Yb	2.8E-02	2.3E-01	4.4E-01	5.9E-01	7.3E-01	9.1E-01	1.0E+00	1.1E+00	1.1E+00
Lu	1.4E-02	1.3E-01	2.8E-01	3.9E-01	5.0E-01	6.5E-01	7.4E-01	7.8E-01	7.9E-01
Hf	4.8E-02	3.2E-01	5.9E-01	7.5E-01	9.1E-01	1.1E+00	1.2E+00	1.3E+00	1.3E+00
Ta	3.6E-02	2.6E-01	4.9E-01	6.4E-01	7.9E-01	9.7E-01	1.1E+00	1.1E+00	1.1E+00
W	4.6E-02	3.1E-01	5.7E-01	7.3E-01	8.8E-01	1.1E+00	1.2E+00	1.2E+00	1.2E+00
Re	-3.4E-01	-1.2E-01	1.2E-01	2.7E-01	4.2E-01	6.0E-01	6.9E-01	7.4E-01	7.5E-01
Os	2.7E-02	8.8E-02	1.8E-01	2.6E-01	3.4E-01	4.6E-01	5.3E-01	5.7E-01	5.7E-01
Ir	1.0E-03	1.2E-02	3.3E-02	5.3E-02	8.0E-02	1.3E-01	1.6E-01	1.7E-01	1.8E-01
Pt	6.1E-03	5.0E-02	1.2E-01	1.8E-01	2.6E-01	3.7E-01	4.4E-01	4.7E-01	4.8E-01
Au	5.1E-03	4.4E-02	1.0E-01	1.6E-01	2.2E-01	3.1E-01	3.7E-01	4.0E-01	4.1E-01
Hg	5.8E-02	3.5E-01	6.1E-01	7.8E-01	9.3E-01	1.1E+00	1.2E+00	1.2E+00	1.2E+00
Tl	5.6E-02	4.1E-01	7.0E-01	8.8E-01	1.0E+00	1.2E+00	1.3E+00	1.3E+00	1.3E+00
Pb	1.2E+00	1.8E+00	2.1E+00	2.3E+00	2.4E+00	2.5E+00	2.6E+00	2.6E+00	2.6E+00
Bi	1.0E+00	1.4E+00	1.7E+00	1.9E+00	2.1E+00	2.2E+00	2.3E+00	2.3E+00	2.3E+00

**B.3.2**  $Z=1 \times 10^{-4}$  (*test case*)

El.	1	5	10	15	20	25	30	40	49
C	1.4E+00	2.5E+00	2.8E+00	3.0E+00	3.1E+00	3.2E+00	3.2E+00	3.3E+00	3.3E+00
N	4.9E-01	5.3E-01	6.2E-01	7.2E-01	8.5E-01	9.4E-01	1.0E+00	1.3E+00	1.5E+00
O	4.5E-02	6.6E-01	9.0E-01	1.0E+00	1.1E+00	1.1E+00	1.2E+00	1.3E+00	1.3E+00
F	3.3E-01	2.2E+00	2.7E+00	3.0E+00	3.3E+00	3.4E+00	3.5E+00	3.6E+00	3.7E+00
Ne	1.1E-02	1.4E+00	2.0E+00	2.3E+00	2.6E+00	2.7E+00	2.8E+00	3.0E+00	3.0E+00
Na	2.2E-01	8.4E-01	1.5E+00	1.8E+00	2.1E+00	2.3E+00	2.4E+00	2.7E+00	2.8E+00
Mg	1.1E-04	2.7E-01	8.9E-01	1.3E+00	1.6E+00	1.8E+00	1.9E+00	2.1E+00	2.2E+00
Al	6.4E-03	1.9E-01	4.5E-01	6.4E-01	8.2E-01	9.1E-01	9.8E-01	1.1E+00	1.2E+00
Si	2.0E-03	1.6E-02	3.9E-02	6.1E-02	8.6E-02	1.0E-01	1.1E-01	1.5E-01	1.6E-01
P	6.9E-03	1.3E-01	2.9E-01	3.6E-01	4.1E-01	4.4E-01	4.7E-01	5.2E-01	5.4E-01
S	9.8E-05	1.8E-03	3.8E-03	4.6E-03	5.1E-03	5.4E-03	5.8E-03	6.7E-03	7.1E-03
Cl	2.9E-04	4.5E-03	1.0E-02	1.5E-02	2.0E-02	2.3E-02	2.6E-02	3.3E-02	3.5E-02
Ar	2.3E-04	1.4E-03	3.1E-03	4.7E-03	6.1E-03	7.0E-03	7.6E-03	9.3E-03	1.0E-02
K	9.9E-04	9.1E-03	2.2E-02	3.4E-02	4.6E-02	5.2E-02	5.8E-02	7.0E-02	7.5E-02
Ca	-1.7E-04	-1.6E-03	-4.6E-03	-7.6E-03	-1.0E-02	-1.2E-02	-1.3E-02	-1.6E-02	-1.7E-02
Sc	1.0E-02	8.3E-02	2.0E-01	2.8E-01	3.5E-01	3.8E-01	4.0E-01	4.5E-01	4.7E-01
Ti	8.1E-04	8.8E-03	1.9E-02	2.8E-02	3.7E-02	4.3E-02	4.8E-02	6.0E-02	6.5E-02
V	-1.5E-04	-6.3E-04	-2.8E-03	-5.4E-03	-7.5E-03	-8.1E-03	-8.4E-03	-8.4E-03	-8.5E-03
Cr	1.9E-05	5.2E-04	1.5E-03	2.3E-03	3.2E-03	3.7E-03	4.1E-03	5.2E-03	5.6E-03
Mn	-2.3E-04	2.2E-04	-3.3E-04	-3.8E-04	1.2E-03	2.7E-03	4.3E-03	8.4E-03	1.1E-02
Fe	0.0E+00								
Co	1.7E-02	1.3E-01	3.2E-01	4.5E-01	5.4E-01	5.8E-01	6.1E-01	6.7E-01	6.9E-01
Ni	2.3E-03	1.2E-02	2.3E-02	3.3E-02	4.3E-02	4.8E-02	5.2E-02	6.1E-02	6.5E-02
Cu	6.6E-02	2.7E-01	4.4E-01	5.6E-01	6.5E-01	6.8E-01	7.1E-01	7.7E-01	7.9E-01
Zn	1.2E-02	1.0E-01	1.6E-01	2.0E-01	2.4E-01	2.6E-01	2.8E-01	3.2E-01	3.4E-01
Ga	3.9E-02	2.7E-01	3.9E-01	4.8E-01	5.5E-01	5.8E-01	6.1E-01	6.8E-01	7.1E-01
Ge	3.1E-02	2.4E-01	3.6E-01	4.5E-01	5.1E-01	5.5E-01	5.8E-01	6.6E-01	6.9E-01
As	1.5E-02	1.5E-01	2.3E-01	2.9E-01	3.5E-01	3.7E-01	4.0E-01	4.7E-01	5.0E-01

El.	1	5	10	15	20	25	30	40	49
Se	2.3E-02	2.2E-01	3.5E-01	4.4E-01	5.1E-01	5.5E-01	5.9E-01	6.7E-01	7.1E-01
Br	3.3E-03	1.7E-01	3.1E-01	3.7E-01	4.2E-01	4.6E-01	4.9E-01	5.6E-01	5.9E-01
Kr	2.1E-02	2.7E-01	4.5E-01	5.6E-01	6.6E-01	7.2E-01	7.7E-01	9.0E-01	9.5E-01
Rb	3.3E-02	4.6E-01	7.5E-01	8.9E-01	1.0E+00	1.1E+00	1.1E+00	1.2E+00	1.3E+00
Sr	1.4E-02	6.7E-01	9.9E-01	1.1E+00	1.2E+00	1.3E+00	1.4E+00	1.6E+00	1.6E+00
Y	8.7E-03	7.3E-01	1.1E+00	1.2E+00	1.3E+00	1.4E+00	1.5E+00	1.6E+00	1.7E+00
Zr	6.7E-03	7.4E-01	1.1E+00	1.3E+00	1.4E+00	1.5E+00	1.5E+00	1.7E+00	1.8E+00
Nb	-5.1E-04	9.6E-02	4.3E-01	6.6E-01	8.2E-01	9.0E-01	9.6E-01	1.1E+00	1.2E+00
Mo	3.8E-03	5.5E-01	9.2E-01	1.1E+00	1.2E+00	1.3E+00	1.3E+00	1.5E+00	1.5E+00
Ru	2.3E-03	3.9E-01	7.0E-01	8.3E-01	9.6E-01	1.0E+00	1.1E+00	1.3E+00	1.3E+00
Rh	8.9E-04	2.4E-01	4.7E-01	5.7E-01	6.9E-01	7.6E-01	8.4E-01	9.9E-01	1.0E+00
Pd	4.0E-03	5.6E-01	9.0E-01	1.0E+00	1.2E+00	1.3E+00	1.3E+00	1.5E+00	1.6E+00
Ag	5.3E-04	2.2E-01	4.3E-01	5.3E-01	6.5E-01	7.2E-01	7.9E-01	9.4E-01	9.9E-01
Cd	4.4E-03	6.6E-01	1.0E+00	1.2E+00	1.3E+00	1.4E+00	1.5E+00	1.6E+00	1.7E+00
In	2.3E-03	5.0E-01	8.3E-01	9.6E-01	1.1E+00	1.2E+00	1.3E+00	1.4E+00	1.5E+00
Sn	4.6E-03	7.3E-01	1.1E+00	1.3E+00	1.4E+00	1.5E+00	1.6E+00	1.8E+00	1.8E+00
Sb	2.0E-03	5.4E-01	9.3E-01	1.1E+00	1.2E+00	1.3E+00	1.4E+00	1.5E+00	1.6E+00
Te	1.1E-03	3.6E-01	6.8E-01	8.0E-01	9.4E-01	1.0E+00	1.1E+00	1.3E+00	1.3E+00
I	-2.7E-05	1.4E-01	3.2E-01	4.0E-01	5.1E-01	5.8E-01	6.5E-01	7.9E-01	8.4E-01
Xe	2.6E-03	4.7E-01	8.3E-01	9.8E-01	1.1E+00	1.2E+00	1.3E+00	1.4E+00	1.5E+00
Cs	3.6E-03	6.0E-01	1.0E+00	1.1E+00	1.3E+00	1.4E+00	1.5E+00	1.6E+00	1.7E+00
Ba	1.9E-02	1.1E+00	1.5E+00	1.7E+00	1.9E+00	2.0E+00	2.1E+00	2.3E+00	2.3E+00
La	1.8E-02	1.1E+00	1.5E+00	1.7E+00	1.9E+00	2.0E+00	2.1E+00	2.3E+00	2.3E+00
Ce	2.5E-02	1.2E+00	1.7E+00	1.9E+00	2.1E+00	2.2E+00	2.3E+00	2.4E+00	2.4E+00
Pr	1.5E-02	1.0E+00	1.5E+00	1.7E+00	1.9E+00	2.0E+00	2.1E+00	2.3E+00	2.3E+00
Nd	2.2E-02	1.1E+00	1.5E+00	1.7E+00	2.0E+00	2.1E+00	2.1E+00	2.3E+00	2.3E+00
Sm	1.7E-02	8.7E-01	1.4E+00	1.6E+00	1.8E+00	1.9E+00	2.0E+00	2.1E+00	2.1E+00
Eu	2.6E-03	3.5E-01	7.3E-01	9.1E-01	1.1E+00	1.2E+00	1.3E+00	1.4E+00	1.4E+00
Gd	9.7E-03	6.8E-01	1.2E+00	1.4E+00	1.6E+00	1.7E+00	1.8E+00	1.9E+00	1.9E+00

El.	1	5	10	15	20	25	30	40	49
Tb	3.4E-03	4.6E-01	8.8E-01	1.1E+00	1.3E+00	1.4E+00	1.4E+00	1.6E+00	1.6E+00
Dy	9.6E-03	6.1E-01	1.1E+00	1.3E+00	1.5E+00	1.6E+00	1.7E+00	1.8E+00	1.8E+00
Ho	4.7E-03	4.6E-01	8.5E-01	1.0E+00	1.2E+00	1.3E+00	1.4E+00	1.5E+00	1.5E+00
Er	1.2E-02	6.8E-01	1.2E+00	1.4E+00	1.6E+00	1.7E+00	1.8E+00	1.9E+00	1.9E+00
Tm	4.9E-03	5.5E-01	1.0E+00	1.2E+00	1.4E+00	1.5E+00	1.6E+00	1.7E+00	1.8E+00
Yb	2.8E-02	9.7E-01	1.5E+00	1.7E+00	1.9E+00	2.0E+00	2.1E+00	2.2E+00	2.3E+00
Lu	1.4E-02	7.0E-01	1.2E+00	1.4E+00	1.6E+00	1.7E+00	1.8E+00	1.9E+00	2.0E+00
Hf	4.8E-02	1.2E+00	1.7E+00	1.9E+00	2.1E+00	2.2E+00	2.3E+00	2.4E+00	2.5E+00
Ta	3.6E-02	1.0E+00	1.5E+00	1.8E+00	2.0E+00	2.1E+00	2.2E+00	2.3E+00	2.3E+00
W	4.6E-02	1.1E+00	1.6E+00	1.8E+00	2.0E+00	2.2E+00	2.2E+00	2.4E+00	2.4E+00
Re	-3.4E-01	6.4E-01	1.2E+00	1.4E+00	1.6E+00	1.7E+00	1.8E+00	1.9E+00	2.0E+00
Os	2.7E-02	5.0E-01	9.3E-01	1.1E+00	1.3E+00	1.4E+00	1.5E+00	1.6E+00	1.7E+00
Ir	1.0E-03	1.4E-01	3.9E-01	5.3E-01	6.9E-01	7.8E-01	8.5E-01	9.6E-01	9.9E-01
Pt	6.1E-03	4.1E-01	8.3E-01	1.0E+00	1.2E+00	1.3E+00	1.4E+00	1.5E+00	1.5E+00
Au	5.1E-03	3.4E-01	7.1E-01	9.0E-01	1.1E+00	1.2E+00	1.3E+00	1.4E+00	1.4E+00
Hg	5.8E-02	1.1E+00	1.6E+00	1.9E+00	2.1E+00	2.2E+00	2.3E+00	2.4E+00	2.4E+00
Tl	5.6E-02	1.2E+00	1.7E+00	2.0E+00	2.2E+00	2.3E+00	2.4E+00	2.5E+00	2.5E+00
Pb	1.2E+00	2.5E+00	2.9E+00	3.0E+00	3.0E+00	3.1E+00	3.1E+00	3.1E+00	3.1E+00
Bi	1.0E+00	2.2E+00	2.6E+00	2.7E+00	2.7E+00	2.7E+00	2.8E+00	2.8E+00	2.8E+00

# Appendix C

## My publications

- [1] Cristallo, S., Straniero, O., Gallino, R., Herwig, F., Chieffi, A., Limongi, M., Busso, M.: 2001, *Nucl. Phys. A* **688**, 217.
- [2] Gallino, R., Pignatari, M., Cristallo, S., Straniero, O., Travaglio, C., Busso, M.: 2003, *IAUJD* **4**, 27.
- [3] Straniero, O., Domínguez, I., Cristallo, S., Gallino, R.: 2003, *PASA* **20**, 389.
- [4] Gallino, R., Käppeler, F., Reifarth, R., Straniero, O., Cristallo, S., Davis, A.M., Domínguez, I.: 2003, *EAEJA* **13716**
- [5] Gallino, R., Arnone, E., Cristallo, S., Masera, S., Travaglio, C., Lambert, D.L., Lugaro, M., Käppeler, F., van Winckel, H., Reyniers, M., Straniero, O., Davis, A.M.: 2003, *Nucl. Phys. A* **718**, 181.
- [6] Cristallo, S., Gallino, R., Straniero, O.: 2004, *Mem. S.A.It.* **75**, 174.
- [7] Abia, C., de Laverny, P., Domínguez, I., Straniero, O., Cristallo, S., Plez, B.: 2004, *Mem. S.A.It.* **75**, 607.
- [8] Straniero, O., Cristallo, S., Gallino, R., Domínguez, I.: 2004, *Mem. S.A.It.* **75**, 665.
- [9] Cristallo, S., Straniero, O., Gallino, R.: 2004, *Mem. S.A.It.* **75**, 676.
- [10] Delaude, D., Gallino, R., Cristallo, S., Straniero, O., Husti, L., Ryan, S.: 2004, *Mem. S.A.It.* **75**, 706.
- [11] Domínguez, I., Abia, C., Straniero, O., Cristallo, S., Pavlenko, Ya.V.: 2004, *A&A* **442**, 1045.
- [12] Cristallo, S., Straniero, O., Gallino, R., Piersanti, L., Domínguez, I.: 2005, *IAUS* **228**, 483.
- [13] Gallino, R., Delaude, D., Husti, L., Cristallo, S., Straniero, O., Ryan, S.: *Nucl. Phys. A* **758**, 485.
- [14] Cristallo, S., Straniero, O., Gallino, R.: 2005, *Nucl. Phys. A* **758**, 509.

[15] Straniero, O., Gallino, R., Cristallo, S.: *Nucl. Phys. A* in press

[16] Cristallo, S., Gallino, R., Straniero, O., Piersanti, L., Domínguez, I.: *Mem. S.A.It.*  
in press